

UNIVERSITÄT
BAYREUTH

Strukturaufklärung von
triazin- und heptazinbasierten Photokatalysatoren
mittels NMR-Kristallographie

DISSERTATION

zur Erlangung des akademischen Grades eines Doktors der Naturwissenschaften (Dr. rer. nat.)

im Promotionsprogramm Materialchemie und Katalyse

an der Bayreuther Graduiertenschule für Mathematik und Naturwissenschaften (BayNAT)

der Universität Bayreuth

vorgelegt von

Maria Barbara Mesch

geboren in Schrobenhausen

Bayreuth, 2016

Die vorliegende Arbeit wurde in der Zeit von Januar 2012 bis März 2016 in Bayreuth am Lehrstuhl für Anorganische Chemie III unter Betreuung von Herrn Professor Dr. Jürgen Senker angefertigt.

Vollständiger Abdruck der von der Bayreuther Graduiertenschule für Mathematik und Naturwissenschaften (BayNAT) der Universität Bayreuth genehmigten Dissertation zur Erlangung des akademischen Grades eines Doktors der Naturwissenschaften (Dr. rer. nat.).

Dissertation eingereicht am: 30.03.2016

Zulassung durch die Promotionskommission: 19.04.2016

Wissenschaftliches Kolloquium: 12.08.2016

Amtierender Direktor: Prof. Dr. Stephan Kümmel

Prüfungsausschuss:

Prof. Dr. Jürgen Senker (Erstgutachter)

Prof. Dr. Hans-Werner Schmidt (Zweitgutachter)

Prof. Dr. Birgit Weber (Vorsitz)

JProf. Dr. Sven Hüttner

*Es gibt ein Licht ganz am Ende des Tunnels.
Ist man im Tunnel drin, dann sieht man es nicht,
jedoch am Ende des Tunnels scheint ein Licht.*

aus Starlight Express

Inhaltsverzeichnis

INHALTSVERZEICHNIS	V
ABKÜRZUNGSVERZEICHNIS.....	VII
1 ZUSAMMENFASSUNG/SUMMARY	1
1.1 Zusammenfassung.....	1
1.2 Summary	3
2 EINLEITUNG.....	5
2.1 Motivation und Zielsetzung	5
2.2 Photokatalytisch aktive CN-Materialien	7
2.3 Photokatalyse	8
2.4 Steigerung der photokatalytischen Aktivität	10
2.4.1 Modifizierung Bandlücke.....	10
2.4.2 Beeinflussung der Ladungstrennung, -stabilisierung und -mobilität.....	11
2.4.3 Katalytisch aktive Zentren und Oberfläche.....	12
2.5 NMR-Kristallographie	13
2.6 Strukturlösung triazin- und heptazin-basierter Materialien.....	15
3 SYNOPSIS.....	21
3.1 Bestimmung der Länge von Phenyl-Triazin-Oligomeren mittels 1D-Spektren.....	22
3.2 Bestimmung der Länge von Heptazin-Oligomeren mittels 1D Spektren.....	24
3.3 Strukturaufklärung heptazin-basierter Netzwerke mittels 1D Spektren.....	26
3.4 Spectral-editing zur Strukturlösung eines PTI-Derivates.....	29
3.5 Strukturaufklärung von PTI Nanoschichten: 1D und 2D Spektren.....	31
3.6 Bestimmung von Atompositionen am Beispiel von PTI/LiCl	33
3.7 Schlussfolgerung	38
4 QUELLEN	41
5 DARSTELLUNG DES EIGENANTEILS.....	49
6 ERGEBNISSE.....	53
6.1 Bestimmung der Länge von Phenyl-Triazin-Oligomeren mittels 1D-Spektren.....	53
6.1.1 Phenyl-Triazine Oligomers for Light-Driven Hydrogen Evolution.....	55
6.1.2 Supporting Information	64
6.2 Bestimmung der Länge von Heptazin-Oligomeren mittels 1D Spektren.....	93
6.2.1 Low-Molecular-Weight Carbon Nitrides for Solar Hydrogen Evolution	95
6.2.2 Supporting Information.....	104

6.3	Strukturaufklärung eines heptazin-basierten Netzwerks mittels 1D Spektren	123
6.3.1	Donor-Acceptor Type Heptazine-Based Polymer Networks for Photocatalytic Hydrogen Evolution	125
6.3.2	Supporting Information	132
6.4	Spectral-editing zur Strukturlösung eines PTI-Derivates	143
6.4.1	Triazine-based Carbon Nitrides for Visible-Light-Driven Hydrogen Evolution ...	145
6.4.2	Supporting Information	150
6.5	Strukturaufklärung von PTI Nanoschichten: 1D und 2D Spektren	161
6.5.1	Crystalline Carbon Nitride Nanosheets for Improved Visible-Light Hydrogen Evolution	163
6.5.2	Supporting Information	167
6.6	Bestimmung von Atompositionen am Beispiel von PTI/LiCl	181
6.6.1	Solving the Hydrogen and Lithium Substructure of Poly (Triazine Imide)/LiCl Using NMR Crystallography	183
6.6.2	Supporting Information	196
7	PUBLIKATIONSLISTE	219
8	DANKSAGUNG	221
9	ERKLÄRUNG DES VERFASSERS	223

Abkürzungsverzeichnis

*	Rotationsseitenbande im Spektrum
1D	eindimensional
2D	zweidimensional
3D	dreidimensional
4AP	4-Amino-2,6-dihydroxypyrimidin
Å	Ångström (Einheit) [10^{-10} m]
aPTI	amorphes Poly(triazinimid)
AFM	Rasterkraftmikroskop von engl. atomic force microscope
CN	Kohlenstoffnitrid
CP	Kreuzpolarisation von engl. cross-polarization
CPPI	Kreuzpolarisation mit Polarisationsinversion von engl. cross-polarization with polarization inversion
CTF	kovalentes Triazinnetzwerk von engl. covalent triazine framework
DMSO	Dimethylsulfoxid
EA	Elementaranalyse
ED	Elektronendiffraktion
engl.	englisch
EPR	Elektronenspinresonanz von engl. electron paramagnetic resonance
eV	Elektronenvolt (Einheit)
FK	Festkörper
HMP	heptazin-basiertes mikroporöses Polymer
HOMO	höchstes besetztes Orbital von engl. highest occupied molecular orbital

IR	Infrarot
LG	Lee-Goldburg
LUMO	niedrigstes unbesetztes Orbital von engl. lowest unoccupied molecular orbital
MALDI-TOF	Matrix unterstützte Laser-Desorption/Ionisation mit Flugzeitmassenspektrometer-Detektion von engl. time of flight
MAS	Rotation im magischen Winkel von engl. magic angle spinning
N _c	zentrales Stickstoffatom im Heptazinring
NMR	Kernspinresonanz von engl. nuclear magnetic resonance
N _{tert}	tertiäres Stickstoffatom
ppm	Teile einer Million von engl. parts per million (Einheit) [10 ⁻⁶]
PTI	Poly(triazinimid)
PTO	Phenyl-Triazin-Oligomer
PXRD	Röntgenpulverdiffraktion von engl. powder x-ray diffraction
RCF	relative Zentrifugalkraft (Einheit der Rotation) von engl. relative centrifugal force
REDOR	NMR-Pulssequenz von engl. rotational-echo double-resonance
rpm	Umdrehungen pro Minute (Einheit der Rotation) von engl. rounds per minute
UV-Vis	ultraviolett und sichtbar von engl. ultraviolet and visible
TEM	Transelectronenmikroskop
TGA	thermogravimetrische Analyse
V	Volt (Einheit)
XRD	Röntgendiffraktion von engl. x-ray diffraction
XPS	Röntgenphotoelektronenspektroskopie von engl. x-ray photoelectron spectroscopy

1 Zusammenfassung/Summary

1.1 Zusammenfassung

Die vorliegende Arbeit befasst sich mit der Strukturaufklärung von wasserstoffhaltigen Kohlenstoffnitriden, die aus Triazin- oder Heptazineinheiten aufgebaut und aktiv bezüglich der photokatalytischen Wasserstofferzeugung aus Wasser sind. Durch Kooperationen mit synthetisch arbeitenden Gruppen konnte eine Vielzahl unterschiedlicher Proben mittels NMR-kristallographischen Methoden untersucht werden. Auf diese Weise wurde ein wertvoller Beitrag zur Erarbeitung von Struktureigenschafts-Beziehungen geleistet, um in Zukunft aktivere Photokatalysatoren zu entwickeln.

Mithilfe von 1D ^{13}C und ^{15}N Spektren konnten Polymerarchitekturen bestimmt werden. Dabei war für jede Probe ein eigener Lösungsansatz nötig, da die charakteristischen Gruppen, welche eine spektrale Auflösung aufwiesen, für jedes Material neu identifiziert werden mussten. Durch Einpuls ^{13}C Spektren wurde die Kettenlänge von Phenyl-Triazin-Oligomeren bestimmt, was basierend auf einer genauen Bestimmung der ^{13}C Relaxationszeiten möglich war. Eine analoge Fragestellung für heptazin-basierte Oligomere wurde mit 1D ^{15}N Spektren untersucht. Da aufgrund der geringen natürlichen Häufigkeit Kreuzpolarisationsspektren verwendet werden mussten und somit keine quantitativen Spektren zugänglich waren konnte nur die relative Kettenlänge bestimmt werden. In einem Copolymer aus Heptazinchlorid und Di(aminobenzol)benzothiazol wurde durch ^{15}N Spektren nachgewiesen, dass die Verknüpfung über sekundäre und nicht über tertiäre Amine erfolgt. Desweiteren wurde über quantitative ^{13}C Spektren die Anzahl der Endgruppen und damit der Vernetzungsgrad dieser Polymere bestimmt.

Neben Fragen zur Polymerarchitektur wurden auch die monomeren Einheiten untersucht, welche für diese Materialien in der Regel Triazin- oder Heptazineinheiten sind. Die Unterscheidung der monomeren Strukturen wurde erst durch die Verwendung von CPPI möglich, da die relevanten Signale teilweise überlagern. Im CPPI Spektrum werden Signale bestimmter chemischer Gruppen selektiv gedämpft, wodurch darunterliegende, entscheidende Signale sichtbar werden und eine eindeutige Unterscheidung zwischen Triazin- und Heptazineinheit zulassen.

An Poly(triazinimid)/LiCl wurde die Morphologie nach Delaminierung untersucht. Zum einen konnte durch 1D Spektren der Kerne ^1H , ^{13}C und ^{15}N nachgewiesen werden, dass der erste Schritt des Delaminierungsprozesses den Lithiumgehalt des Produkts bestimmt. Zum anderen verdeutlichten ^1H - ^1H 2D Spindiffusionsspektren, dass Wasser stark mit der Probe wechselwirkt. Dies weist darauf hin, dass Nanoschichten entstehen, die von Wassermonolagen umgeben sind. Mithilfe quantitativer ^1H Spektren und der Dichte einer Wassermonolage konnte so die Dicke der Nanoschichten aus NMR-Daten bestimmt werden.

Durch Erweitern des bisher angewendeten Methodenrepertoires um weitere 2D Spektren und Abstandsmessungen konnte zudem die Lithium- und Protonenstruktur von PTI/LiCl geklärt werden. Dazu wurde aus 1D und 2D Spektren zunächst ein Konnektivitätenschema entwickelt, woraus Strukturmodelle abgeleitet wurden. Aus dem Zusammenspiel von quantenmechanischen Strukturrechnungen, gemessenen und berechneten NMR-Parametern sowie Abstandsmessungen und deren Simulationen (^1H - ^7Li und ^{13}C - ^7Li) konnte mithilfe einer Kostenfunktion eine Modellklasse identifiziert werden. Eine weitere Verfeinerung innerhalb dieser Modellklasse auf eine Struktur wurde durch ^1H - ^{13}C und ^{13}C - ^7Li Abstandsmessungen erreicht.

In ihrer Gesamtheit demonstrieren die dargestellten Arbeiten wie wertvoll und aussagekräftig die NMR-Kristallographie für die Strukturlösung von CN-Materialien ist. Durch eine geschickte Auswahl der Experimente kann von der Morphologie, über die Polymerarchitektur und die monomeren Bausteine bis hin zur atomaren Ebene auf allen Größenskalen ein Beitrag geleistet werden.

Da die Arbeit kumulativ verfasst wurde, befindet sich eine ausführlichere Zusammenfassung in Kapitel 3, die vollständigen Publikationen sind in Kapitel 6 abgedruckt.

1.2 Summary

The presented thesis addresses the structural analysis of hydrogen containing carbon nitrides, which are composed of triazine or heptazine units. The materials are photocatalytically active concerning the hydrogen evolution from water. Through cooperations with synthetically working groups, a number of different samples could be studied by NMR crystallography. Thereby a valuable contribution to the development of structure-property-relationships was made, in order to develop more active catalysts in the future.

Using 1D ^{13}C and ^{15}N spectra the architecture of polymers could be determined. A separate approach was needed for each sample, due to the fact that the characteristic groups with spectral resolution needed to be identified for each material. For phenyl-triazine oligomers the chain length was determined by onepulse ^{13}C spectra. Therefore an accurate knowledge of the ^{13}C relaxation times was necessary. A similar question was investigated on heptazine-based oligomers using ^{15}N spectra. As a result of the low natural abundance a cross-polarization sequence had to be used, making quantitative integrals inaccessible. Thereby only the relative chain lengths could be determined. Furthermore a copolymer of heptazine chloride and di(aminobenzo)benzothiadiazole was studied using ^{15}N spectra. It could be proofed that the linking occurs only via secondary and not via tertiary amines. Additionally, quantitative ^{13}C spectra revealed the amount of end groups resulting in an exact knowledge of the degree of condensation.

Besides the question about the architecture of polymers also the monomeric units, which are triazine or heptazine units for these materials, were studied. For a differentiation between the monomeric units CPPI was needed, as the relevant signals overlap. In a CPPI spectrum the signals of certain groups are selectively dampened whereby relevant, underlying groups rise and allow for the differentiation between triazine and heptazine.

Furthermore, the morphology of delaminated Poly(triazineimide)/LiCl was studied. On the one hand, using 1D ^1H , ^{13}C and ^{15}N spectra, it could be proofed that the first step of the delamination determines the lithium content of the sample. On the other hand, ^1H - ^1H 2D spindiffusion experiments revealed an intense interaction between water and the sample. This indicates that nanosheets, which are surrounded by water monolayers, were formed. Using quantitative ^1H spectra and the density of a water monolayer the thickness of the nanosheets could be determined.

Expanding the experimental repertoire by other 2D spectra and distance measurements the lithium and proton structure of PTI/LiCl was revealed. Therefore, a connectivity pattern was derived from 1D and 2D spectra. Based on this, structure models were developed. By the combination of quantum chemical calculations, measured and calculated NMR parameters as well as distance measurements

and their simulations (^1H - ^7Li and ^{13}C - ^7Li) one class of models could be identified using a cost function. Further refinement was accomplished using ^{13}C - ^7Li and ^1H - ^{13}C distance measurements and revealed one preferable structure.

In their entirety the displayed projects demonstrate that NMR crystallography is a valuable and meaningful method to derive the structure of CN materials. Subtle choosing of the experiments allows the determination from morphologies, over polymer architectures and monomeric units to the atomic level on all scales.

This thesis was written cumulative. A more detailed summary is given in chapter 3, the full publications are reprinted in chapter 6.

2 Einleitung

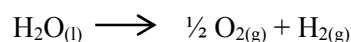
2.1 Motivation und Zielsetzung

Aktuellen Prognosen zufolge wird der globale Energiebedarf bis zum Jahr 2040 um 37% steigen,^[1] während die Menge an leicht zugänglichen fossilen Rohstoffe limitiert ist.^[2] Zudem ist der Verbrauch fossiler Rohstoffe immer mit der Emission des Treibhausgases CO₂ verbunden, die zu den bekannten Problemen, wie globaler Erderwärmung, beiträgt.^[2] Um die Herausforderung des steigenden Energiebedarfs nachhaltig zu bewältigen, werden neue Ansätze benötigt, den Energiebedarf unabhängig von fossilen Rohstoffen zu decken. Dabei liegt das Augenmerk auf erneuerbaren Energien, wie beispielsweise Biomasse, Wind- und Solarenergie, die 2014 in Deutschland 11,1% des Primärenergiebedarfs deckten.^[3]

Die vielseitigste Ressource, die zudem den Vorteil eines unerschöpflichen Vorrats hat, ist dabei die Sonnenenergie.^[2] Dementsprechend sind solar-basierte Methoden in den Fokus der Forschung gerückt. Dabei unterscheidet man zwischen drei verschiedenen Bereichen: Photovoltaik, Photothermik und Photochemie.^[2] Mithilfe von Photovoltaik kann Sonnenstrahlung in elektrische Energie umgewandelt werden. In der Photothermik wird die Wärmeenergie direkt genutzt, wodurch zum Beispiel Warmwasser erzeugt werden kann. Im photochemischen Bereich wird die Sonnenenergie in Form von chemischer Energie gespeichert. Unter chemischer Energie versteht man in diesem Fall die Speicherung der Energie in Form chemischer Verbindungen wie etwa Wasserstoff, Brennstoffe oder chemischer Rohstoffe.^[2]

Der Vorteil von Wasserstoff ist, dass er bei der Verbrennung nur Wasser bildet und keine weitere Emission von Schadstoffen, wie beispielsweise dem Treibhausgas CO₂ oder Feinstaub verursacht.^[4] Zudem besitzt er eine hohe Energiedichte^[5] und kann außerdem durch den Einsatz in Brennstoffzellen wieder in elektrische Energie umgewandelt werden.^[6] Damit hat Wasserstoff ein hohes Potential in der Zukunft als grüner und sauberer Energieträger eingesetzt zu werden.^[7,8] Als Zukunftsvision taucht dabei der Begriff der solaren Raffinerie auf.^[6] Diese beschreibt die Gewinnung von Wasserstoff mithilfe von Sonnenenergie aus Wasser und die anschließende nachhaltige Synthese von Brennstoffen und Basischemikalien.^[6,9] Die aktuell größte Herausforderung dieser Technologie ist die Wasserstoffgewinnung.

Bisher wird Wasserstoff überwiegend aus fossilen Rohstoffen, zum Beispiel durch Methoden wie Dampfreformierung, gewonnen.^[10,11] Die Gewinnung aus Wasser stellt dabei eine attraktive Alternative dar, da Wasser eine günstige, umweltschonende und in großem Maß zur Verfügung stehende Ressource ist.^[9,12] Die Bildung von Wasserstoff erfolgt dabei nach der Gleichung



mit der freien Reaktionsenthalpie $\Delta G^0 = +237 \text{ kJ/mol}$.^[4] Dies zeigt bereits den großen Nachteil dieser Methode: Die Reaktion ist stark endergonisch und damit ist der Prozess der Wasserspaltung, aufgrund des kleinen Einflusses der Entropiezunahme, energieaufwendig.^[13] Seit jedoch Fujishima und Honda 1972 mit einer TiO_2 -Elektrode unter Lichteinfluss Wasser in Wasserstoff und Sauerstoff spalten konnten,^[14] wird die Photokatalyse als erfolgversprechende Methode zur Wasserstoffgewinnung erforscht. Dabei muss jedoch mehr Energie aufgewendet werden, als die Thermodynamik rechtfertigt, was auf kinetische Effekte zurückzuführen ist.^[13] Daher muss in photokatalytischen Materialien vor allem die kinetische Reaktionshemmung verringert werden.^[13]

Neben der Verbesserung der Aktivität müssen die Katalysatormaterialien auch in Bezug auf Stabilität, Zugänglichkeit und Wirtschaftlichkeit erforscht und verbessert werden, um die Photokatalyse kommerziell nutzbar zu machen.^[15] Dabei wurden viele Materialien untersucht, was durch zahlreiche Reviews belegt wird.^[4,10,11,16,17] Die Klasse der Kohlenstoffnitride, die neben der photokatalytischen Aktivität weitere günstige Eigenschaften besitzen, wurde 2009 von Wang *et al.* entdeckt.^[15] Sie sind einfach und günstig herzustellen, nicht toxisch sowie thermisch und chemisch stabil, was sie für eine industrielle Anwendung attraktiv macht.^[18] Bisher sind die Aktivitäten jedoch für eine kommerzielle Nutzung nicht ausreichend hoch, wodurch deren Steigerung in den Fokus der Forschung gerückt ist.^[19,20] Durch die systematische Charakterisierung photokatalytisch aktiver CN-Materialien kann auf lange Sicht eine Struktur-Eigenschafts-Beziehung abgeleitet werden, die dann ein gezieltes Katalysatordesign und eine Erhöhung der Aktivität ermöglicht.

In dieser Arbeit werden daher die Strukturen verschiedener, polymerer, wasserstoffhaltiger Kohlenstoffnitride, die überwiegend an den Lehrstühlen von Prof. Lotsch und Prof. Schnick synthetisiert wurden, aufgeklärt. Da die katalytische Aktivität dieser Materialien stark von den Synthesebedingungen und damit auch den Strukturen abhängt, bieten sie die Möglichkeit die Struktur-Eigenschafts-Beziehung zu untersuchen. Dabei spielen Aspekte wie die Einstellung der Bandlücke durch strukturelle Änderungen eine wichtige Rolle. Auch Materialien, die als Modellsubstanz für photokatalytisch aktive Materialien fungieren werden betrachtet.

Die „klassische“ Strukturaufklärung dieser CN-Materialien durch Diffraktionsmethoden ist häufig schwierig oder unmöglich, da viele dieser Materialien amorph sind, oder die Struktur leichter Atome wie ^1H oder ^7Li untersucht werden muss. Als mögliche Alternative hat sich die NMR-Kristallographie etabliert.^[21] In der NMR-Kristallographie wird NMR-Spektroskopie als lokale Methode mit Diffraktions- und Computermethoden ergänzt,^[21] wobei das Hauptaugenmerk dieser Arbeit auf der NMR-Spektroskopie liegt.

Dabei sollen beispielsweise Charakteristika wie die Kettenlänge, die Anzahl und Art der Endgruppen, die Monomereinheit oder das Verknüpfungsmuster eines CN-Polymers bestimmt werden. Auch der strukturelle Unterschied zwischen Nanoschichten und Bulkmaterial, sowie die Position einzelner

^1H und ^7Li Atome wird untersucht. Diese Ergebnisse werden dann im Zusammenhang mit der photokatalytischen Aktivität der Materialien betrachtet. Je nach Fragestellung werden entsprechende Lösungsansätze erarbeitet, wobei ein breites Methodenrepertoire angewendet wird, das von 1D-Messungen über spectral-editing Methoden und 2D Spektren bis hin zu quantitativen Abstandsmessungen reicht.

2.2 Photokatalytisch aktive CN-Materialien

CN-Materialien werden erst seit 2009 für die Photokatalyse erforscht.^[15] Die Vorteile von CN-Materialien sind neben der geeigneten Bandlücke, dass sie in der Regel einfach aus leicht zugänglichen, nicht-toxischen, günstigen Ausgangsubstanzen hergestellt werden können.^[18] Dies ist unter anderem für eine großtechnische Anwendung von enormer Bedeutung.^[18] Entscheidend ist auch ihre hohe Stabilität gegenüber Temperatur, Wasser und Strahlung. Zudem sind CN-Materialien leicht modifizierbar, wodurch ihre Funktionalität gut angepasst werden kann.^[22–31] In Summe besitzen sie daher ein hohes Potential als Photokatalysatoren für die Wasserspaltung Anwendung zu finden.^[31,32]

Das erste CN-Material wurden von Berzelius entdeckt und von Liebig 1834 als Melon bezeichnet.^[33] Melon stellt dabei eines der ersten synthetischen Polymere dar, dessen Strukturaufklärung erst im letzten Jahrzehnt gelang (siehe auch 2.6).^[34,35] Dies belegt, dass CN-Materialien lange Zeit nicht wissenschaftlich relevant waren, bis 1989 Liu und Cohen theoretisch vorhersagten, dass die Verbindung $\beta\text{-C}_3\text{N}_4$ härter als Diamant sei.^[36–40] Dadurch entwickelte sich ein intensives Forschungsfeld, welches durch die Entdeckung, dass CN-Materialien aktiv in der Photokatalyse sind, aktuell nochmal einen Aufschwung erfährt. Dies bestätigt die Recherche in SciFinder® nach den Schlagwörtern „carbon nitride“ und „photocat“, welche 150 Publikationen für das Jahr 2013 und bereits 534 Publikationen für 2015 ergab. Zudem erschienen bis heute zahlreiche Reviews.^[20,22,31,32,41–45]

CN-Materialien werden aus stickstoffreichen Ausgangsverbindungen, wie Cyanamid,^[46] Dicyandiamid^[47] oder Melamin,^[48,49] durch thermische Kondensation hergestellt (Abbildung 1).^[24,45,50] Die Substanzen unterscheiden sich vor allem aufgrund des Kondensationsgrads, des C/N-Verhältnis, des Wasserstoffgehalts, der Kristallinität und der Morphologie.^[24,25,34,50–52]

Die CN-Materialien basieren auf Heptazin (Tri-s-triazin)- oder Triazineinheiten (Abbildung 1). Theoretische Studien zeigen grundsätzlich, dass heptazin-basierte Strukturen energetisch günstiger als Triazin-basierte sind.^[53,54] Dies wurde auch experimentell nachgewiesen, da bei der Pyrolyse von Cyanamid, Dicyandiamid oder Melamin eine heptazin-basierte Struktur entsteht.^[22,32] Triazin-basierte Netzwerke konnten dagegen erstmals 2001 in einer Hochdrucksynthese^[55,56] und 2011 in einer Salzschnmelze^[47] synthetisiert werden, da dort zusätzliche Stabilisierungsmechanismen auftreten. Das aus der Salzschnmelze synthetisierte Poly(triazinimid) hat verbleibendes LiCl in der Struktur eingelagert.

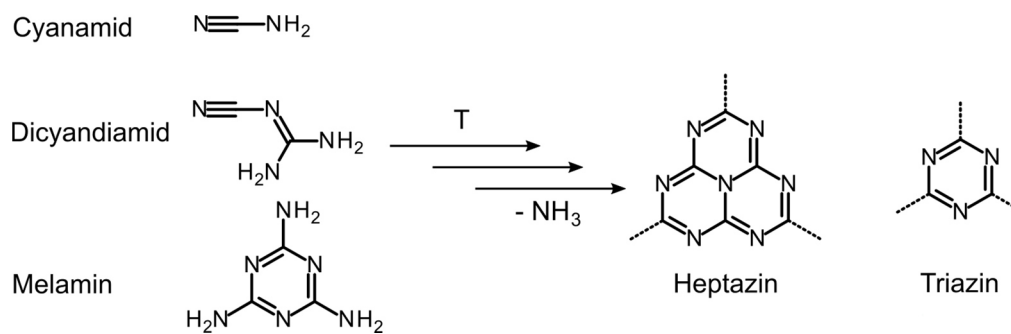


Abbildung 1. Strukturformel von Heptazin und Triazin.

Unabhängig von der Baueinheit, Heptazin oder Triazin, sind CN-Materialien photokatalytisch aktiv.^[15,46,57] Darauf aufbauend wurden neben Kohlenstoffnitriden, auch andere stickstoffreiche Verbindungen für die Photokatalyse entdeckt, nachdem sich herauskristallisierte, dass ein hoher Stickstoffanteil gut für die photokatalytische Aktivität ist.^[31,32,57–59] Zudem sind poröse Polymere photokatalytisch aktiv,^[60] weshalb versucht wurde die Vorteile der Kohlenstoffnitride mit denen mikroporöser Netzwerke zu kombinieren.^[61] Die neuen Verbindungen enthalten ebenfalls Triazin oder Heptazineinheiten, die jedoch nun durch organische Linker verbunden werden.^[58] Obwohl diese Materialien gerade bezüglich der Flexibilität und Modifizierung Vorteile aufweisen,^[62] ist die photokatalytische Wasserspaltung mithilfe dieser Materialklasse noch ein sehr junges Gebiet.^[58,61,63–65]

2.3 Photokatalyse

Der photokatalytische Prozess kann schematisch in drei Reaktionsschritte unterteilt werden^[11,18]: 1) Lichtabsorption und Ladungsträgerbildung, 2) Ladungstrennung und -rekombination und 3) katalytische Reaktion (Abbildung 2). Im ersten Schritt wird Sonnenlicht absorbiert, wobei sich Elektronen und Löcher bilden. In Schritt zwei müssen sich diese trennen und zur Oberfläche diffundieren. Alternativ dazu und für die Katalyse unerwünscht, können die Elektronen und Löcher miteinander reagieren. Die Rekombination findet vorzugsweise an Partikelgrenzen und Defekten, welche als katalytisch aktive Zentren fungieren, statt. Der dritte Schritt, ist die eigentliche katalytische Reaktion und findet an den aktiven Zentren der Partikeloberfläche statt.

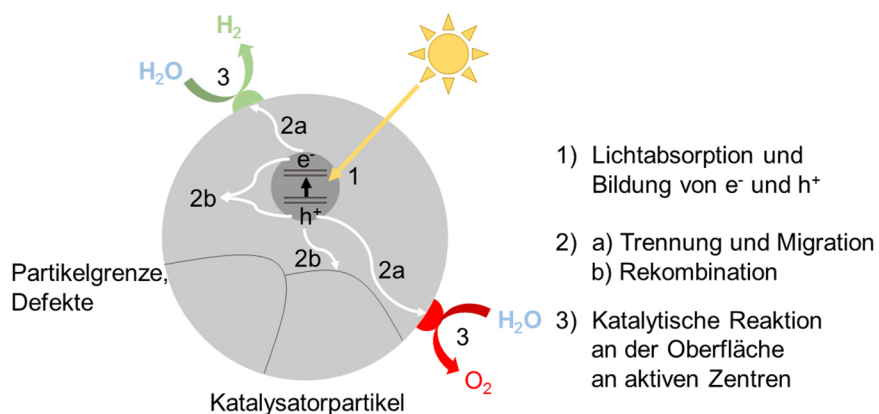


Abbildung 2. Schematische Darstellung der Reaktionsschritte im photokatalytischen Prozess in Anlehnung an [11].

Daraus ergeben sich folgende Bedingungen für eine photokatalytische Aktivität: ^[4,11,12]

- ➔ Die Bandlücke sollte so klein sein ($< 3,0$ eV), dass sichtbares Licht, welches circa 46% des Sonnenlichts ausmacht, absorbiert werden kann. Zudem muss die Bandlücke $> 1,23$ eV sein, um die Wasserspaltung zu katalysieren, was der Reaktionsenthalpie der Wasserspaltung entspricht. Zusätzlich spielt die Position der Bänder eine entscheidende Rolle. Das unterste Level des Leitungsbandes muss unter 0 V (Potential für H^+/H_2) und das oberste Level des Valenzbandes muss über 1,23 V (Potential für O_2/H_2O) liegen.
- ➔ Eine effektive Ladungstrennung und ausreichend hohe Ladungsmobilität sind nötig, um die Elektronen und Löcher an die reaktive Oberfläche zu transportieren, wobei die Lebensdauer ausreichend lang sein muss. Das heißt die Rekombination von Elektronen und Löchern muss möglichst unterdrückt werden.
- ➔ Die Anzahl der katalytisch aktiven Zentren an der Oberfläche muss möglichst hoch sein, wobei die Zentren für die H_2 - und O_2 -Bildung getrennt sein sollten, um die Rückreaktion zu H_2O zu vermeiden.

Viele der CN-Materialien können, aufgrund ihrer Bandlücke, Wasser theoretisch vollständig in Wasserstoff und Sauerstoff spalten. Die vollständige Wasserspaltung stellt jedoch eine äußerst komplexe Reaktion dar, weshalb oftmals nur eine Halbreaktion in Gegenwart von geeigneten Opferreagentien untersucht wird. Bei diesen handelt es sich um leicht zu oxidierende oder reduzierende Substanzen, die stöchiometrisch verbraucht werden. Dadurch läuft eine Teilreaktion an der Oberfläche schnell ab. Wird die Halbreaktion der Wasserstofferzeugung betrachtet, kann zum Beispiel Methanol als Opferreagenz eingesetzt werden, welches dann anstelle von Wasser oxidiert wird. Daher muss zwischen Wasserspaltung, Wasser wird in Wasserstoff und Sauerstoff gespalten, und Wasserstofferzeugung, Wasserstoff wird in Gegenwart eines Opferreagenz erzeugt, unterschieden werden. Durch die Untersuchung einer der Teilreaktionen der Wasserspaltung können bereits die kinetischen und thermodynamischen Voraussetzungen des Katalysatorsystems betrachtet werden.^[11,66] Zudem kann durch eine Kombination zweier Photokatalysatoren, die jeweils eine Teilreaktion katalysieren, eine Wasserspaltung erfolgen.^[67,68] Dabei wird mit einem flüssigen Redox-Vermittler gearbeitet und diese Systeme werden als Z-Schema Katalysatorsysteme bezeichnet.^[69]

Um effektive Katalysatoren, auch für einzelne Teilreaktionen zu erhalten, müssen die Kohlenstoffnitride und stickstoffreichen Polymere weiterentwickelt werden. Die entsprechend wichtigsten Konzepte werden im nachfolgenden Kapitel beschrieben.

2.4 Steigerung der photokatalytischen Aktivität

Die photokatalytische Aktivität der CN-Materialien ist trotz vielversprechender Ansätze bisher nicht ausreichend hoch für eine kommerzielle Anwendung. Dementsprechend wird momentan versucht, die Aktivität durch Modifizierung der Substanzen zu erhöhen. Dabei können die Materialien bezüglich ihrer Bandlücke, der Ladungstrennung, -mobilität und -stabilisierung sowie ihrer katalytisch aktiven Zentren verändert werden (siehe auch 2.3).^[11,42,70]

2.4.1 Modifizierung Bandlücke

Um eine Erhöhung der katalytischen Aktivität durch eine Veränderung der Bandlücke zu erreichen, muss diese so modifiziert werden, dass mehr Anteile des sichtbaren Lichtes absorbiert werden können. Mithilfe gezielter Dotierungen können neue Niveaus eingeführt werden, wodurch die Bandlücke verkleinert und dadurch die absorbierte Lichtmenge vergrößert werden kann (Abbildung 3).



Abbildung 3. Schematische Darstellung der Reduzierung der Bandlücke bei einer Dotierung. Angelehnt an [32].

Einige Dotierungsmöglichkeiten wurden 2012 zusammengefasst.^[31,32] Man unterscheidet dabei zwischen Metall- und Nichtmetall-Dotierungen, wobei erstere Wang *et al.* 2009 einführt. Inspiriert durch Porphyrin-Komplexe in der Natur, dotierten sie graphitisches- C_3N_4 ($g-C_3N_4$) mit Eisen.^[71] Analog konnte $g-C_3N_4$ auch mit Zink dotiert werden.^[72] Beide Dotierungen hatten eine Verringerung der Bandlücke und damit eine erhöhte photokatalytische Aktivität zur Folge. Alternativ können CN-Materialien auch mit Nichtmetallen dotiert werden, um die Bandlücke zu verändern. Durch Fluorierung^[73], Sulfonierung^[74] und der Dotierung mit Bor^[75] wurde die Bandlücke angepasst und die photokatalytische Aktivität ebenfalls erhöht.

Eine weitere Methode ist sogenanntes molekulares Doping. Dabei werden CN-Materialien in Gegenwart eines Comonomers synthetisiert. Als Comonomere werden dabei strukturverwandte Moleküle zu Melamin wie Barbitursäure^[76] oder Triaminopyrimidin^[59,77] eingesetzt. Diese konnten sowohl in triazin-, als auch in heptazin-basierte Strukturen eingebaut werden. Aber auch Moleküle wie Aminobenzonitril, Anilin, Benzonitril^[78] oder Poly(hexylthiophen)^[79] konnten mit gewünschtem Effekt copolymerisiert werden.

Daneben gibt es auch noch andere Möglichkeiten die Bandlücke zu verändern beziehungsweise die Lichtabsorption zu verbessern. Dazu wurden zum Beispiel das CN-Material mit organischen Farbstoffen wie Magnesium-Phthalocyanin modifiziert.^[80] Auch durch zusätzliche Protonierung konnte die Bandlücke verändert werden^[81] oder durch die Sensibilisierung des Katalysators mithilfe von Tantalsäure oder Kaliumtantalat.^[82]

Dabei ist zu beachten, dass durch die jeweiligen Modifizierungen nicht ausschließlich die Bandlücke beeinflusst wird, sondern häufig eine Änderung der Materialien bezüglich der Kristallinität, Oberfläche und Partikelgröße damit verbunden ist. Dadurch ist die Erhöhung der katalytischen Aktivität oftmals ein kooperativer Effekt und kann nicht vollständig auf die geänderte Bandlücke zurückgeführt werden.

2.4.2 Beeinflussung der Ladungstrennung, -stabilisierung und -mobilität

Neben der Bandlücke ist das Verhalten der Elektronen und Löcher im Halbleitermaterial für die photokatalytische Aktivität von entscheidender Bedeutung.^[83] Dieses ist jedoch hochkomplex und hängt von vielen verschiedenen Parametern wie der Kristallstruktur, der Kristallitgröße, der Art und Anzahl von Defekten und den Oberflächeneigenschaften ab.^[66] Erstmals konnte 2014 der komplexe Vorgang der Ladungstrennung und des -transfers durch EPR Spektroskopie visualisiert werden.^[7] Um photokatalytisch aktiv zu sein, müssen die Ladungsträger an die Oberfläche des Katalysators gelangen und dort reagieren. Dafür benötigen sie eine ausreichend lange Lebensdauer, das bedeutet eine gute Trennung und damit verbunden eine kleine Rekombinationsrate, und ausreichend hohe Mobilität.^[84]

Wie bereits im letzten Abschnitt erwähnt konnte durch eine Sensibilisierung des CN-Photokatalysators mit Tantsäure die Bandlücke beeinflusst werden. Zudem wurde dadurch aber auch eine bessere Trennung der Elektronen und Löcher erreicht, da die Elektronen auf das Leitungsband der Tantal-Komponente abfließen können und damit die Rekombination unterdrückt wird. Der vorgeschlagene Mechanismus ist in Abbildung 4 dargestellt.^[82]

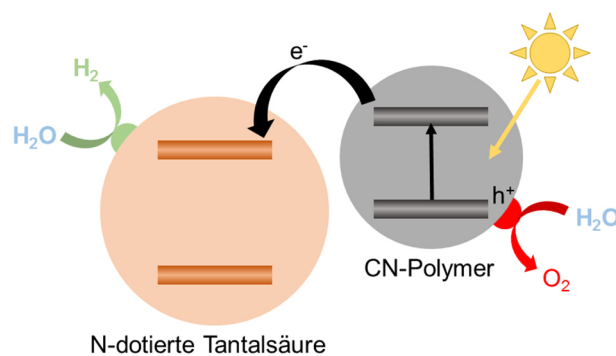


Abbildung 4. Vorgeschlagener Reaktionsmechanismus für die Wasserstoffentwicklung eines mit Tantsäure modifizierten CN-Polymeren. Angelehnt an [82].

Ein ähnlicher Effekt konnte 2012 durch ein organisch-anorganisches Kompositmaterial erreicht werden. Dabei können in der Regel die Elektronen gut auf das Kompositmaterial übergehen, wodurch die Rekombination erschwert wird. Das erste Kompositmaterial war dabei $\text{SrTiO}_3:\text{Rh}$, wobei die Steigerung der Aktivität auf die verbesserte Ladungstrennung zurückgeführt werden konnte.^[85] Dieser Ansatz wurde dann auf verschiedene Kompositmaterialien wie zum Beispiel Graphen^[86] und

Phosphate^[87] übertragen. Einen Überblick über CN-Kompositmaterialien gibt auch das 2015 erschienene Review von Zhao *et al.*^[88]

Ein ähnliches Prinzip gilt, wenn zwei Halbleitermaterialien oder ein Halbleitermaterial mit einem Metall, in diesem Fall spricht man von Cokatalysatoren, kombiniert werden. Dabei wird neben der verbesserten Ladungstrennung in der Regel auch die Bandlücke beeinflusst und es werden zusätzliche reaktive Zentren eingeführt. Dennoch ist die verbesserte Ladungstrennung ein entscheidender Punkt. Dies wurde 2010 durch das Aufbringen von Goldnanopartikeln auf die CN-Katalysatoroberfläche erstmals demonstriert.^[89] Analog dazu konnte auch durch Heterostrukturen mit ZnWO₄ Nanostäbchen^[90] und Nickel Nanodrähten^[91] die photokatalytische Aktivität verbessert werden. Ein bei CN-Materialien häufig eingesetzter Cokatalysator ist Platin.^[57,61,76,92,93]

Ein weiterer Ansatzpunkt ist die Kristallinität und die Kristallitgröße. Die Kristallinität ist wichtig, da Defekte im Material in der Regel Rekombinationszentren darstellen, während Defekte an der Oberfläche meist reaktive Zentren für die gewünschte katalytische Reaktion sind und daher die Aktivität unterstützen (siehe auch 2.4.3).^[66,94] Die Kristallitgröße beeinflusst einerseits die Oberfläche und die Bandlücke, da diese von der Partikelgröße abhängt (siehe auch 2.4.3 und 2.4.1).^[66] Andererseits ist in kleinen Kristalliten die Weglänge, die bis an die Oberfläche zurückgelegt werden muss, klein, wodurch die Wahrscheinlichkeit auf eine Rekombination sinkt und die photokatalytische Aktivität steigt.^[66] Dies konnte bereits mehrfach, vor allem durch Nanoschichten gezeigt werden.^[94-99] Das große Potential dieser Methode wird auch in den beiden Reviews, die 2015 erschienen sind, bestätigt.^[100,101] Neben Nanoschichten wurden auch Nanostäbchen synthetisiert, die ebenfalls eine erhöhte photokatalytische Aktivität aufgrund einer besseren Ladungsträgertrennung besitzen.^[102]

2.4.3 Katalytisch aktive Zentren und Oberfläche

Damit die katalytische Reaktion stattfindet, werden aktive Zentren an der Oberfläche benötigt an denen die Elektronen und Löcher auf das Wasser beziehungsweise das Opferreagenz übertragen werden können.^[66] Hierzu gibt es zwei mögliche Ansätze: einerseits eine Vergrößerung der Oberfläche und andererseits eine Vermehrung der aktiven Zentren.

Die häufigste Methode die Oberfläche zu vergrößern ist die Nanostrukturierung und wurde unter einem anderen Gesichtspunkt bereits im vorherigen Abschnitt diskutiert. In den letzten Jahren ist der Fokus dabei auf Nanoschichten gerückt.^[95-98] Alternativ dazu wird die Oberfläche größer, wenn die Porosität zunimmt. Über alternative Syntheserouten, wie Templatmethoden,^[103,104] können poröse CN-Materialien synthetisiert werden, die eine erhöhte katalytische Aktivität aufweisen. Auch durch das Einbringen von organischen Linkern, als Abstandhalter zwischen die CN-Einheiten, kann die Porosität erhöht werden.^[61]

Auch für die photokatalytische Wasserspaltung wird, wie in den meisten heterogenen Katalysen, vermutet, dass Endgruppen und Defekte an der Oberfläche die aktiven Zentren sind.^[31] Dementsprechend könnten durch unvollständige Polymerisation und die Einführung von Defekten die Anzahl der aktiven Zentren erhöht werden (Abbildung 5). Eine weitere Methode sind die im letzten Abschnitt erwähnten Heterostrukturen. Dadurch wird einerseits die Elektron-Loch Trennung verbessert, andererseits die Anzahl an aktiven Zentren vermehrt. Bei der vollständigen Wasserspaltung ist dabei zu beachten, dass an den aktiven Zentren möglicherweise neben den Teilreaktionen auch die Rückreaktion von H_2 und O_2 zu Wasser ablaufen kann. Daher muss das Material und die eingesetzte Menge mit Bedacht gewählt werden.

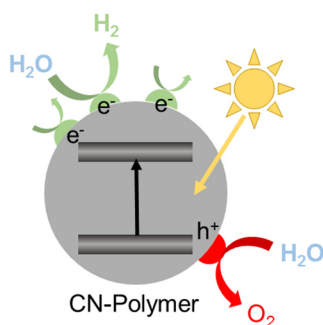


Abbildung 5. Schematische Darstellung der Erhöhung der Anzahl an katalytisch aktiven Zentren.

2.5 NMR-Kristallographie

Bereits bei der Entwicklung der unter 2.3 genannten Faktoren zur Verbesserung der photokatalytischen Aktivität spielte die Strukturaufklärung der Photokatalysatoren eine große Rolle. Nur auf diesem Weg kann eine Struktur-Eigenschafts-Beziehung abgeleitet werden. Zudem wäre es erstrebenswert Eigenschaften, wie die Bandlücke oder die Ladungsträgermobilität ebenfalls mit strukturellen Eigenschaften verknüpfen zu können, um ein gezieltes Design von Photokatalysatoren zu ermöglichen.

Da viele der molekularen und polymeren CN-Materialien keine Einkristalle bilden, kann die Strukturlösung nur anhand des Pulvers durchgeführt werden. Dies stellt eine große Herausforderung für Diffraktionsmethoden dar, die oft nicht vollständig oder nicht eindeutig zu bewältigen ist.^[105] In den letzten zehn Jahren hat sich daher als Alternative die NMR-Kristallographie etabliert.^[21,106] Sie verbindet NMR-Spektroskopie mit Pulverdiffraktion und quantenmechanischen Rechnungen. Je nach Fragestellung und Notwendigkeit können die Methoden entsprechend kombiniert werden, wobei beispielweise auch eine Kristallstrukturlösung basierend ausschließlich auf NMR-Daten möglich ist.^[107,108] Daher liegt der Schwerpunkt der NMR-Kristallographie in dieser Arbeit auf der FK-NMR-Spektroskopie, die wenn nötig komplementär durch Diffraktions- und Computermethoden ergänzt wird. Aus dem Zusammenspiel der Informationen aus den verschiedenen Methoden (Abbildung 6) kann dann eine möglichst vollständige Strukturlösung erarbeitet werden.^[109] Mittlerweile kommt die

NMR-Kristallographie folglich immer dann zum Einsatz, wenn die Strukturlösung über Diffraktionsmethoden zum Beispiel aufgrund von Fehlordnung schwierig bis unmöglich ist, wenn die Materialien amorph sind oder leichte Atome, wie Wasserstoff und Lithium, die eine geringe Streukraft besitzen, untersucht werden sollen. Eine Vielzahl an Fragestellungen konnte dadurch bereits adressiert werden und wurde in diversen Reviews und „Special Issues“ zusammengefasst.^[21,106,109,110]

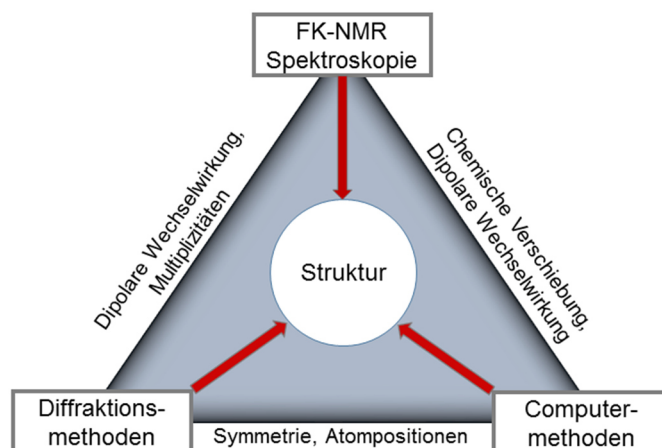


Abbildung 6. Zusammenspiel der unterschiedlichen Methoden der NMR-Kristallographie.

Die NMR-Spektroskopie ist dabei eine sehr vielseitige Methode, aus der viele Informationen über die lokale Umgebung NMR-aktiver Kerne gewonnen werden können. Es können beispielsweise chemische Gruppen zugeordnet, Fehlordnungen detektiert, Dynamik untersucht, Abstände und Orientierungen bestimmt werden. Die zugrunde liegenden Wechselwirkungen sind die chemische Verschiebung, die dipolare Kopplung und die quadrupolare Wechselwirkung.^[106] In dieser Arbeit werden vor allem die ersten Beiden für die Untersuchung struktureller Aspekte herangezogen (Abbildung 7). Dafür haben sich eine Vielzahl an Methoden etabliert,^[111] wobei nachfolgend kurz auf die in dieser Arbeit verwendeten und ihren Informationsgehalt eingegangen wird.

Aus 1D Spektren können neben der chemischen Verschiebung und damit der Information über die lokale Umgebung einer Spezies auch die Intensitätsverhältnisse bestimmt werden. Dafür müssen jedoch Kerne mit geringer natürlicher Häufigkeit, wie zum Beispiel ^{15}N , angereichert werden, um in umsetzbarer Messzeit die gewünschten Ergebnisse zu erhalten. Neben den höheren Kosten, entsteht dadurch aber auch viel Potential. Durch selektive Anreicherung werden mehr Informationen zugänglich, indem zum Beispiel gezielt einzelne funktionelle Gruppen und deren Wechselwirkungen betrachtet werden können. Wenn aus der chemischen Verschiebung die chemische Umgebung nicht direkt abgeleitet werden kann, können sogenannte spectral-editing Methoden verwendet werden. Dadurch kann die Anzahl an gebundenen Protonen eines Heteroatoms bestimmt werden.

Eine ausführlichere Information über die Konnektivitäten in den Verbindungen liefern verschiedene 2D Spektren. Es können in Abhängigkeit von der Pulssequenz, sowohl homonukleare, als auch heteronukleare Konnektivitäten direkt über Bindungen oder durch den Raum gemessen werden. Die

Information über Abstände, welche in den 2D Spektren qualitativ zur Bestimmung von Konnektivitäten genutzt wird, kann auch quantitativ verwendet werden. Dadurch können Abstände zwischen verschiedenen Spezies bestimmt werden. Auch in diesem Fall kann eine selektive Anreicherung sinnvoll sein.

Aus diesen Informationen können dann Strukturmodelle erstellt werden. Darauf basierend werden dann die relevanten NMR-Parameter berechnet und die entsprechenden Abstandsmessungen simuliert und mit den experimentellen Daten verglichen. Häufig ist bereits jetzt eine Strukturlösung möglich. Falls diese jedoch nicht eindeutig ist, werden weitere Methoden hinzugenommen.

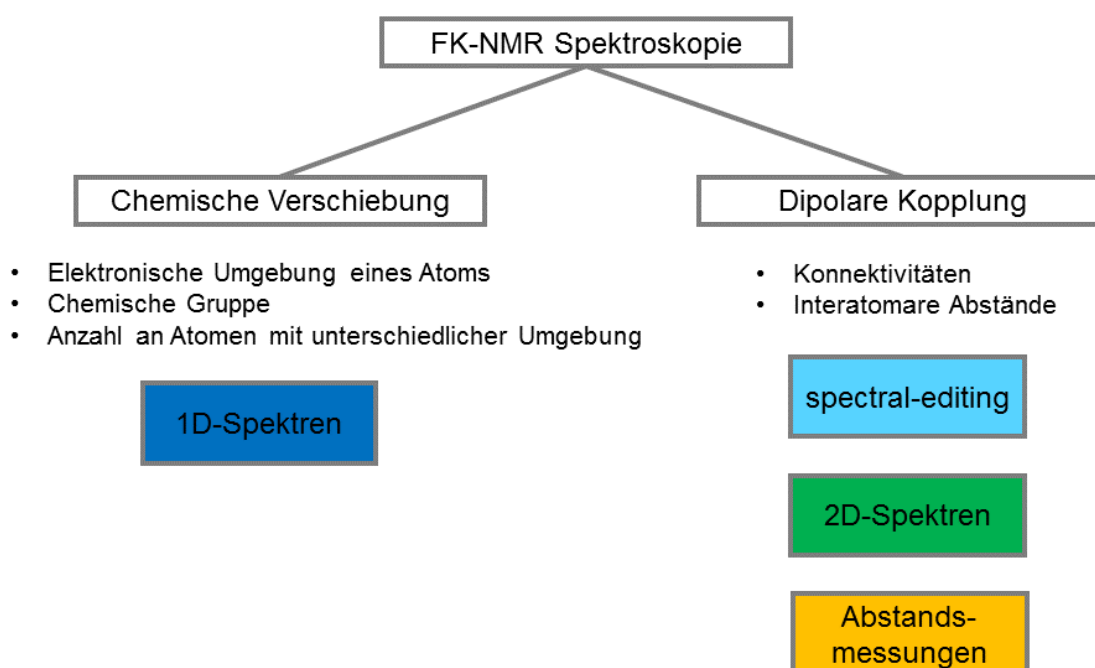


Abbildung 7. Verwendete Wechselwirkungen und Informationsgewinn für die Strukturlösung durch FK-NMR Spektroskopie.

2.6 Strukturlösung triazin- und heptazin-basierter Materialien

Die Strukturaufklärung von stickstoffreichen Materialien, wie Melam, Melem oder Melon (Abbildung 8), erwies sich, unter anderem aufgrund deren schlechter Löslichkeit, lange Zeit als schwierig.^[25] Auch der amorphe Charakter und der unterschiedliche Wasserstoffgehalt in Abhängigkeit von der gewählten Synthesemethode erschwerten die Strukturaufklärung.^[112] Durch die Suche nach β - C_3N_4 und der Verwendung von CN-Materialien als Photokatalysatoren und der damit verbundenen Notwendigkeit einer Strukturlösung, ist dieses Forschungsfeld wieder in den Vordergrund gerückt. Nachfolgend werden nun die wichtigsten Eckpunkte der Strukturlösung von CN-Materialien kurz dargestellt und auf den Beitrag, den die NMR-Kristallographie hierbei leisten kann, anhand einiger Beispiele eingegangen.

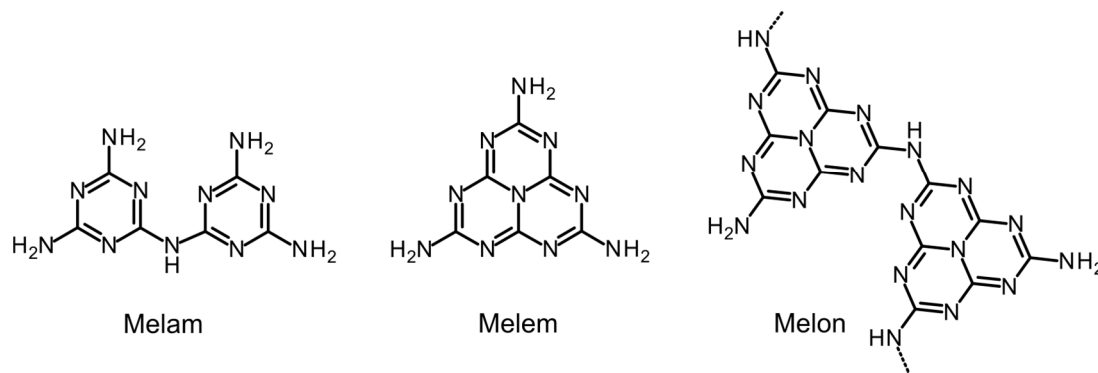


Abbildung 8. Strukturformeln von Melam, Melem und Melon.

Die ersten Strukturvorschläge für CN-Materialien basierten in der Regel auf Triazineinheiten^[53] in hexagonalen^[39] und orthorhombischen^[113,114] Strukturen. Neben triazin-basierten Modellen wurden ab 2001 dann erste heptazin-basierte Strukturen veröffentlicht.^[115–117] Obwohl Pauling und Sturdivant Heptazin bereits 1937 postulierten,^[118] war die Struktur bis 1982 unbekannt.^[119,120] Da jedoch theoretische Studien aus 2002 und 2007 besagen, dass heptazin-basierte Strukturen energetisch günstiger als triazin-basierte sind^[53,54] ist der Fokus zunehmend auf heptazin-basierte Strukturen gerückt.^[24] Häufig konnten jedoch keine Einkristalle gezüchtet werden weshalb die Charakterisierung weiterhin schwierig war. So wurde zum Beispiel 2008 von Bojdys *et al.* ein CN-Material aus Dicyandiamid in einer LiCl/KCl Salzschnmelze hergestellt und als heptazin-basiert publiziert.^[121] Erst 2011 gelang mithilfe von NMR-Kristallographie die eindeutige Unterscheidung von Triazin- und Heptazineinheiten.^[47] Dabei konnte gezeigt werden, dass sich aus Dicyandiamid in der Salzschnmelze anstelle eines Heptazinnetzwerkes ein triazin-basiertes Netzwerk bildet.^[47]

Bereits 1997^[122] und 1998^[123] wurden erste NMR-Rechnungen an CN-Materialien durchgeführt und die NMR-Spektroskopie als vielversprechende Methode zur Charakterisierung dieser Materialien vorgeschlagen. Sehnert *et al.* bestätigten dies 2007, indem sie die NMR-Parameter vieler CN-Modellvorschläge berechneten.^[54] Sie bewiesen zudem, dass eine Unterscheidung von Triazin- und Heptazineinheiten 1D ¹⁵N Spektren möglich ist, da triazin-basierte Strukturen je ein Signal weniger als Heptazin-basierte haben.

Mithilfe von NMR-Kristallographie, genauer der Kombination von Pulverdiffraktion, NMR-Spektroskopie und theoretische Methoden wurde dies auch experimentell, am Beispiel von Melem gezeigt.^[52] Die Signale der 1D ¹³C und ¹⁵N NMR-Messungen konnten mittels spectral-editing durch Kreuzpolarisation mit Polarisationsinversion (CPPI) zugeordnet und mit Melamin verglichen werden (Abbildung 9).^[52] Dadurch war neben der Signalzuordnung auch die Bestimmung der tautomeren Form möglich, da ausschließlich NH₂ beziehungsweise N_{tert} und keine NH-Gruppen in der Probe vorlagen. Zusammen mit Pulverdiffraktionsdaten konnte dadurch die Melem-Struktur gelöst werden, während die Strukturaufklärung ausschließlich durch Diffraktionsmethoden erst drei Jahre später möglich war, als die Synthese von Einkristallen gelang. Die Einkristallstrukturlösung bestätigte die

NMR-kristallographische Struktur und verfeinert sie weiter,^[124] wobei die Wasserstoffbrückenbindungen nicht exakt definiert waren, da Wasserstoff eine sehr geringe Streukraft besitzt. Diese wurden jedoch basierend auf der Kristallstruktur wiederum mithilfe eines NMR-kristallographischen Ansatzes charakterisiert.^[125] Durch den Abgleich von quantitativen ^1H - ^{15}N Lee-Goldburg Kreuzpolarisation (LG-CP) und ^1H - ^1H Doppelquanten (DQ) Aufbaukurven mit Simulationen gelang die Geometriebestimmung der NH_2 -Gruppe. Der Strukturvorschlag wurde anschließend durch ^1H - ^{13}C CP Aufbaukurven und deren Auswertung mittels zweiter Momente bestätigt und stimmt gut mit der Einkristallstrukturlösung überein. Somit konnte basierend auf einer Kristallstruktur, für die die Protonenpositionen nicht bekannt sind, diese durch FK-NMR-Spektroskopie und quantenmechanische Rechnungen bestimmt werden.^[125]

Auch die Struktur der Cyamelursäure wurde 2008 mit NMR-Kristallographie gelöst,^[126,127] während die Strukturlösung allein mit Diffraktionsmethoden bis dato nicht gelang. Zunächst musste ebenfalls die tautomere Form bestimmt werden. Bereits durch die Informationen aus 1D ^1H und ^{15}N Spektren und ^{15}N CPPI Messungen konnte die Anzahl von 17 theoretisch möglichen Tautomeren auf vier reduziert werden. Quantenmechanische Rechnungen und ^{13}C NMR-Messungen reduzierten weiter bis auf ein Tautomer (Abbildung 9), welches die NMR-Messungen erklärt. Dabei muss jedoch der Einfluss der Wasserstoffbrückenbindungen auf die Anisotropie und die Asymmetrie der Verschiebung berücksichtigt werden. Basierend auf diesen Ergebnissen konnte dann mit Pulverdiffraktion die Kristallstruktur gelöst werden, wobei zwei mögliche Strukturen resultieren, die sich nur durch das Wasserstoffbrückenbindungsmuster unterscheiden. Durch den Vergleich der gemessenen ^{13}C NMR-Parameter der chemischen Verschiebung mit quantenmechanisch berechneten Werten, konnte dann eine der beiden möglichen Protonenstrukturen favorisiert werden. Grundlage hierfür war ebenfalls die Sensitivität des chemischen Verschiebungstensors bezüglich der Wasserstoffbrückenbindungen.

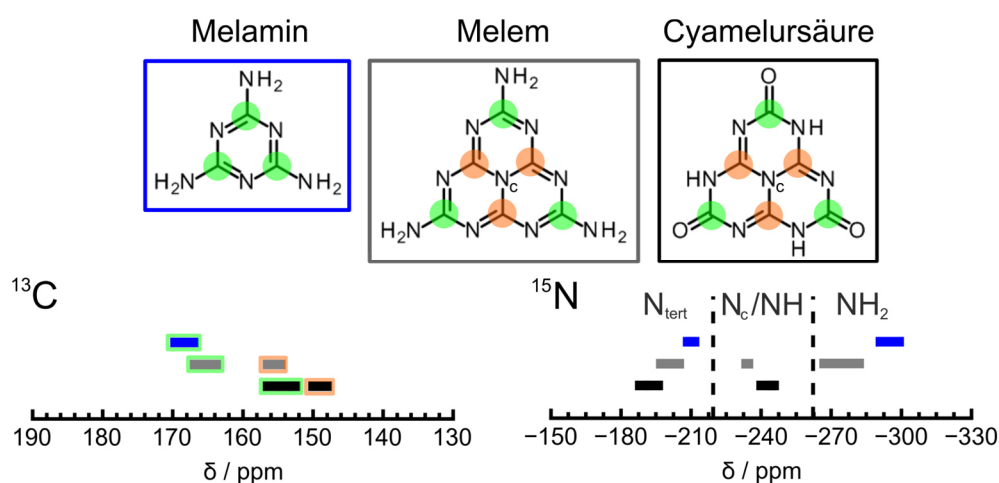


Abbildung 9. Übersicht über die gemessenen chemischen Verschiebungen und die Signaluordnung von Melamin (blau), Melem (grau) und Cyamelursäure (schwarz).^[52,127]

Parallel zur Betrachtung monomerer Heptazinmoleküle erfolgte die Untersuchung polymerer Materialien. Bis 2006 konnte jedoch nicht eindeutig geklärt werden, ob diese aus Triazin- oder Heptazineinheiten aufgebaut sind.^[112,128] Lotsch und Schnick bewiesen 2006 mittels 1D ^{15}N FK-NMR-Spektren und spectral-editing Methoden,^[112] dass aus einem triazin-basierten Ausgangsmaterial, Tricyanomelaminat, ein heptazin-basiertes Polymer entsteht. Holst und Gillan bestätigten dies, indem sie ein Kohlenstoffnitrid aus Trichlormelamin herstellten und charakterisierten. Dabei bildete sich ebenfalls ein heptazin-basiertes Netzwerk.^[129]

Ein weiterer Schritt in Richtung Charakterisierung von CN-Materialien erfolgte 2007, als Melon 137 Jahre nach seiner ersten Erwähnung, durch NMR-Kristallographie charakterisiert wurde.^[34] Bereits ^{15}N 1D und CPPI Messungen zeigten, dass kein vollständig polymerisiertes Netzwerk vorlag, da sowohl NH als auch NH_2 Gruppen nachgewiesen werden konnten (Abbildung 10). Die Vermutung, dass es sich um ein heptazin-basiertes Polymer handelt lag nahe, da das Signal bei -225 ppm einem tertiären Stickstoff zugeordnet wurde und damit auf einen zentralen Heptazinstickstoff (N_c) hindeutet. Zudem entspricht der Signalbereich nicht dem Erwarteten für eine triazin-basierte Struktur. Durch quantitative ^{15}N Spektren an einer angereicherten Probe konnte aus dem NH_2/NH Verhältnis der Polymerisationsgrad bestimmt werden, der annähernd ein unendliches Kettenpolymer nahelegte. Aufgrund der Anreicherung konnte die Phasenreinheit durch ein ^{15}N - ^{15}N Spindiffusionsexperiment nachgewiesen werden.

Darauf basierend wurde die 2D Struktur mithilfe von Elektronendiffraktion geklärt, wonach sich 1D Zick-Zack Ketten bilden, die durch Wasserstoffbrückenbindungen zu Schichten in einem Abstand von 3.2 Å verbunden sind. Die berechneten NMR-Parameter dieses Modells stimmen gut mit den experimentellen Ergebnissen überein. Darauf aufbauend konnte durch NMR-Spektroskopie und Kraftfeldrechnungen die 3D Struktur geklärt werden.^[35] Dazu wurden quantitative ^1H - ^{13}C CP Aufbaukurven und deren Auswertung mithilfe von zweiten Momenten verschiedener 3D Strukturmodelle angewendet. Diese Methode basiert jedoch auf einer exakt bestimmten Protonenstruktur, die wie schon bei Melem durch ^1H - ^{15}N Lee-Goldburg CP und ^1H - ^1H -Doppelquantenexperimente bestimmt wird. Anhand eines ^{15}N - ^{13}C 2D Korrelationsspektrums wurde zusätzlich die Signalzuordnung der ^{13}C Signale bestimmt, um die Genauigkeit der Methode zu erhöhen. Aus den ^1H - ^{13}C CP Aufbaukurven konnten dann favorisierte Strukturen bestimmt werden. Zusätzlich wurden für alle Modelle Energien durch Kraftfeldmethoden berechnet. Mithilfe des Abgleichs der Energien mit den bevorzugten Modellen aus der NMR-Analytik ergaben sich zwei Strukturen, die gemein haben, dass die Heptazineinheiten in benachbarten Schichten möglichst wenig überlappen. Dies wurde schließlich 2015 durch Röntgen- und Neutronendiffraktion bestätigt.^[130]

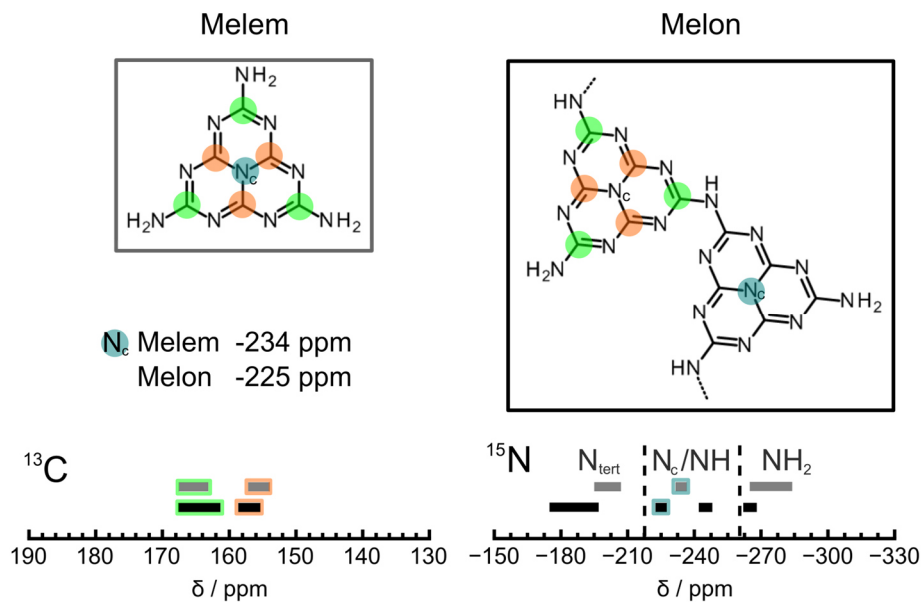


Abbildung 10. Vergleich der experimentell bestimmten chemischen Verschiebungen von Melem (Monomer, grau) und Melon (Polymer, schwarz).

Weiter kondensiert als Melon ist das von Döblinger *et al.* synthetisierte Poly(heptazinimid), welches mittels Elektronendiffraktion charakterisiert wurde.^[131] Durch Kondensation von Melamin bildet sich ein 2D Netzwerk, in dem Heptazineinheiten über Imid-Gruppen verbunden sind. Dabei entstehen Kavitäten, in die verbleibendes Melamin eingelagert wird.

Ein ähnliches Netzwerk, jedoch auf Triazineinheiten basierend konnte 2008 synthetisiert^[121] und 2011 als Poly(triazinimid) (PTI) charakterisiert werden.^[47] Durch Elementaranalyse wurde neben Kohlen-, Stick- und Wasserstoff auch Lithium und Chlor nachgewiesen, welche aus der Synthese in der Salzschnmelze verbleiben. Eine ^{15}N CPPI Messung ermöglichte die eindeutige Zuordnung der beiden ^{15}N Signalgruppen zu NH-Gruppen und tertiären Stickstoffatomen N_{tert} . Zusätzlich wurde Heptazin als Baueinheit ausgeschlossen, da das charakteristische Signal, bei ungefähr -230 ppm, für den zentralen Stickstoff nicht nachgewiesen werden konnte. Dass es, aufgrund einer ähnlichen Verschiebung, nicht von den NH-Gruppen überdeckt wurde, bestätigte ein CPPI Spektrum, bei dem das Signal der NH-Gruppen unterdrückt ist. Dies belegte eindeutig, dass PTI aus Triazineinheiten aufgebaut ist. Da kein Signal für NH_2 -Gruppen zu sehen war, wird ein vollständig polymerisiertes 2D Netzwerk vermutet. Die Phasenreinheit der Probe wurde auch hier durch ein 2D ^{15}N - ^{15}N Spindiffusionsspektrum einer angereicherten Probe nachgewiesen. Mithilfe von Elektronen- und Pulverdifferfraktion konnte die Kristallstruktur geklärt werden, wobei die Lithiumpositionen nur zu 2/3 besetzt sind. Das Verhältnis $\text{NH}/\text{N}_{\text{tert}}$ zeigte, dass eine von drei NH-Gruppen des Netzwerkes deprotoniert vorliegt, was eine Protonen-Lithium Fehlordnung nahelegt. Dies wird durch die Aufspaltung im ^{13}C Spektrum in drei Signale unterstützt. Diese Fehlordnung konnte aber nicht geklärt werden und ist unter anderem Ziel dieser Arbeit.

Da vermutet wird, dass die photokatalytische Aktivität unter anderem auf die Triazin- und Heptazineinheiten zurückzuführen ist, wurden in den letzten Jahren auch andere polymere Netzwerke

auf Triazin- und Heptazin-Basis synthetisiert und in Bezug auf eine photokatalytische Aktivität untersucht. Ein Beispiel ist das kovalente Triazin-Netzwerk CTF-1, welches 2008 durch Trimerisierung von Cyaniden synthetisiert wurde.^[132,133] Mittels Variation der eingesetzten Cyanide kann eine Vielzahl an Polymeren hergestellt werden.^[134–137] Durch einen ähnlichen Ansatz konnten 2010 von Boudrys *et al.* heptazin-basierte Netzwerke hergestellt werden.^[138] Ein weiteres photokatalytisch aktives, heptazin-basiertes Netzwerk wurde 2013 von Kailasam *et al.* publiziert.^[61] Auch für diese Polymere ist die Strukturaufklärung für das Verständnis der photokatalytischen Aktivität von großer Bedeutung. Da die meisten dieser Polymere wenig kristallin sind, kann auch hier die NMR-Kristallographie einen wesentlichen Beitrag zur Strukturklärung leisten. Dabei können die bereits auf CN-Materialien etablierten Methoden verwendet werden.

3 Synopsis

Diese kumulative Dissertation besteht aus sechs Einzelpublikationen. Alle Publikationen befassen sich mit der Strukturaufklärung von photokatalytisch aktiven triazin- und heptazin-basierten Materialien. Die Triazin- bzw. Heptazineinheiten dienen in den Strukturen als Monomere für Oligomere und Polymere.

Als Methode wurde dabei die FK-NMR-Spektroskopie verwendet, da die CN-Materialien entweder einen amorphen Charakter aufweisen und damit für kristallographische Methoden unzugänglich sind, oder leichte Atome untersucht werden, die in Diffraktionsmethoden aufgrund ihrer geringen Streukraft schlecht unterscheidbar sind. Aber auch für die FK-NMR Spektroskopie sind diese Materialien herausfordernd. Der natürlich häufig vorkommende Kern ^1H hat eine hohe Sensitivität. Durch die damit verbundenen starken Wechselwirkungen und den geringen Verschiebungsbereich ist die Auflösung oft schlecht. Erst die Anwendung spezieller Methoden kann diese erhöhen, wodurch der Informationsgewinn steigt. Die NMR-aktiven Kerne ^{13}C und ^{15}N haben eine geringe natürliche Häufigkeit von 1% und 0,4% und zudem eine geringe Sensitivität, zeigen jedoch für unterschiedliche chemische Gruppen in der Regel charakteristische Verschiebungen. Aufgrund der geringen Signalintensität sind die Messzeiten, trotz der Anwendung von Methoden zur Signalverstärkung, wie Kreuzpolarisation, jedoch lang. Wird die quantitative Information der NMR-Spektren benötigt, können jedoch diese Methoden nicht angewendet werden. Zusätzlich muss auch noch die lange Relaxationszeit dieser Kerne berücksichtigt werden, wodurch die Messzeit extrem verlängert wird.

In den ersten drei Kapiteln (6.1-6.3) dieser Arbeit wird gezeigt, wie trotz dieser Komplikationen quantitative Informationen über die Struktur der betrachteten CN-Materialien aus 1D Spektren gewonnen werden können und wie mit geringer Intensität und langen Messzeiten sowie geringer Auflösung umgegangen wird.

Im nächsten Schritt (Kapitel 6.4) wird durch die Methode des spectral-editing die Auflösung erhöht, indem selektiv Signale bestimmter Gruppen gedämpft werden. Als Basis dafür musste eine Flipback-Pulssequenz zur Erhöhung der Signalintensität bei gleichbleibender Messzeit angewendet werden.

In Kapitel 6.5 werden zusätzlich hochaufgelöste ^1H Spektren verwendet und es wird gezeigt welche weiteren Informationen dadurch aus ^1H 2D Spektren gewonnen werden können. Zudem wird erstmals mit ^{15}N -angereicherten Proben gearbeitet, um ^{15}N Spektren trotz extrem kleinen Probenmengen zugänglich zu machen.

Die Arbeit, die in Kapitel 6.6 dargestellt ist, zeichnet sich durch ein breites Messrepertoire aus. Dabei werden die bisher erwähnten Methoden zusammengeführt und um weitere hetero- und homonukleare 2D Spektren und quantitative Abstandsmessungen erweitert.

Einen schematischen Überblick über den Aufbau dieser Arbeit gibt nachfolgende Graphik.

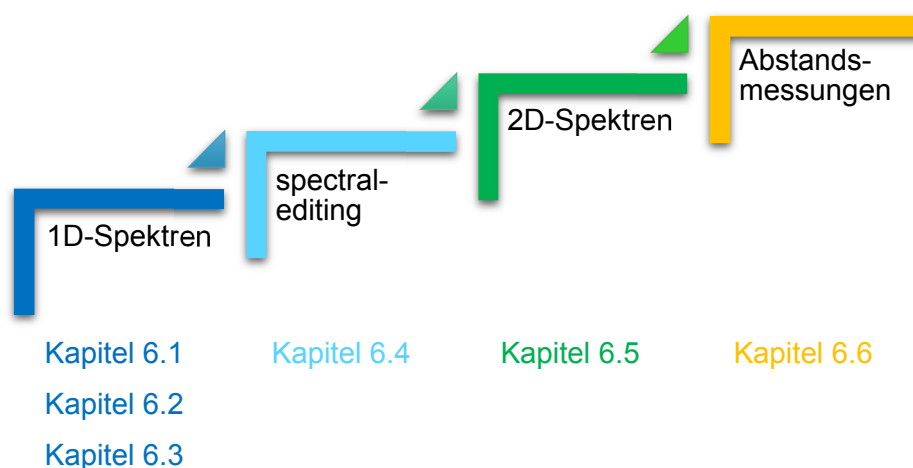


Abbildung 11. Schematischer Überblick über die in dieser Arbeit dargestellten Methoden und Kapitel.

3.1 Bestimmung der Länge von Phenyl-Triazin-Oligomeren mittels 1D-Spektren

Im ersten Projekt wurden Phenyl-Triazin-Oligomere untersucht. Diese basieren auf dem bereits publizierten, kovalenten, triazin-basierten Netzwerk CTF-1^[132] welches durch Trimerisierung von 1,4-Dicyanobenzol bei 400°C in einer ZnCl₂-Schmelze entsteht. Dabei bildet sich ein 2D Netzwerk mit einer hexagonalen Struktur, das abwechselnd aus Phenyl- und Triazinringen aufgebaut ist. Das schwarze, poröse Material ist kaum photokatalytisch aktiv. Weitere Publikationen zeigten jedoch, dass auf CTF-1 basierende Strukturen vielversprechende Eigenschaften für die Photokatalyse besitzen.^[64,65,136] Daher wurde in der in Kapitel 6.1 abgedruckten Publikation die Synthese modifiziert, um eine Zersetzung, die in der CTF-1 Synthese durch hohe Temperaturen einsetzt, zu umgehen.

Die untersuchten Phenyl-Triazin-Oligomere (PTO) werden daher, ähnlich wie CTF-1, in einer ZnCl₂-Schmelze aus 1,4-Dicyanobenzol synthetisiert, jedoch bei einer niedrigeren Synthesetemperatur (300-350°C) und längerer Reaktionszeit. Zusätzlich wurde die Menge an ZnCl₂ zwischen 1 und 15 Äquivalenten relativ zu 1,4-Dicyanobenzol variiert. Es entstehen unlösliche helle Pulver, die weiter charakterisiert werden.

Durch PXRD, IR, XPS und ¹³C und ¹⁵N CP FK-NMR-Spektren konnten sowohl Triazinringe, als auch Nitril-Endgruppen nachgewiesen werden. Besonders in den ¹³C CP Spektren (Abbildung 12) ist das charakteristische Signal für Triazin-Kohlenstoffe bei 169 ppm (Signal 6) und das der Endgruppen bei ~115 ppm (Signal 1) deutlich sichtbar. Dies bestätigte die erfolgreiche Trimerisierung der Nitrile zu Triazinringen bei 300°C, wobei diese nicht vollständig ablief und daher eine oligomere Struktur nahe legt.

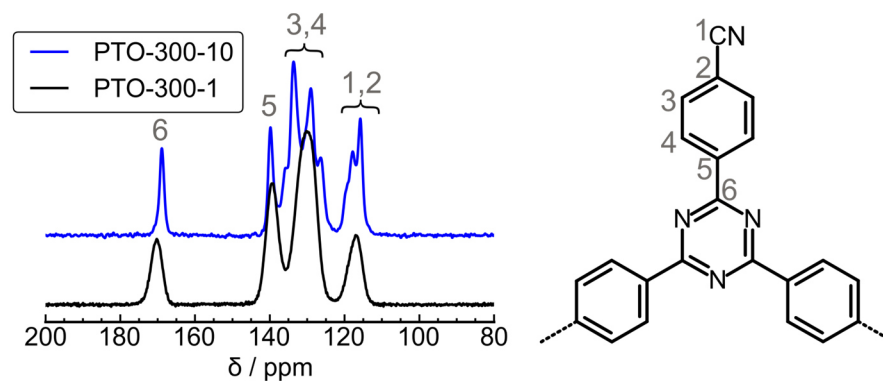


Abbildung 12. ^{13}C CP MAS NMR-Spektren von zwei unterschiedlichen PTOs (links) und Strukturformel einer Baueinheit (rechts). Die PTOs sind wie folgt benannt: PTO-Synthesetemperatur-Äquivalente ZnCl_2 .

Durch MALDI-TOF Analysen konnte qualitativ nachgewiesen werden, dass mit höherem ZnCl_2 -Gehalt kürzere Oligomere entstehen. IR Spektren bestätigten diesen Zusammenhang, was darauf hindeutet, dass der entscheidende Unterschied zwischen den Proben der Polymerisationsgrad ist. Um den Polymerisationsgrad quantitativ zu bestimmen wurde Einpuls ^{13}C FK-NMR-Spektroskopie verwendet.

Damit jedoch Quantität gewährleistet werden kann, müssen die verschiedenen Spins zwischen den Pulsen vollständig relaxieren. Daher müssen zunächst die Relaxationszeiten der unterschiedlichen Signale untersucht werden, weshalb Einpuls Spektren mit verschiedenen T_1 -Zeiten gemessen und integriert wurden (Abbildung 13). Durch die langen T_1 -Zeiten von Kernen mit geringer natürlicher Häufigkeit werden lange Messzeiten nötig, da erst ab einer Wiederholzeit von 5 T_1 die Magnetisierung zu $>99\%$ relaxiert ist. Die Notwendigkeit wird dadurch bestätigt, dass trotz einer Relaxationszeit von 6000 s, was ungefähr 3 T_1 entspricht, die Intensität des Triazin Signals um circa 5% unterschätzt wurde.

Da die Kettenlänge aus dem Verhältnis von Nitril zu Triazin (κ) bestimmt wird, welches für Trimere 0,50 ist und mit steigender Kettenlänge sinkt, wird dadurch auch die Kettenlänge tendenziell unterschätzt. Für die beiden Proben wird dieses Verhältnis durch Entfaltung des Spektrums mit der längsten Relaxationszeit bestimmt. Dabei überlagert sich das Signal der Nitril-Gruppe mit einem Signal des Phenylrings (Signale 1 und 2) und kann nicht getrennt, sondern nur in Summe integriert werden. Dies wird dann bei der Berechnung des Nitril-Triazin Verhältnis aus den Intensitäten berücksichtigt. Für die Probe mit einem hohen ZnCl_2 -Gehalt ergibt sich ein Nitril-Triazin Verhältnis κ von 0,46 was auf Trimere ($\kappa = 0,50$) und kurze Oligomere ($\kappa < 0,50$) schließen lässt. Bei niedrigem ZnCl_2 -Gehalt sinkt κ auf 0,21, was auf längere und eventuell verzweigte Oligomere hindeutet.

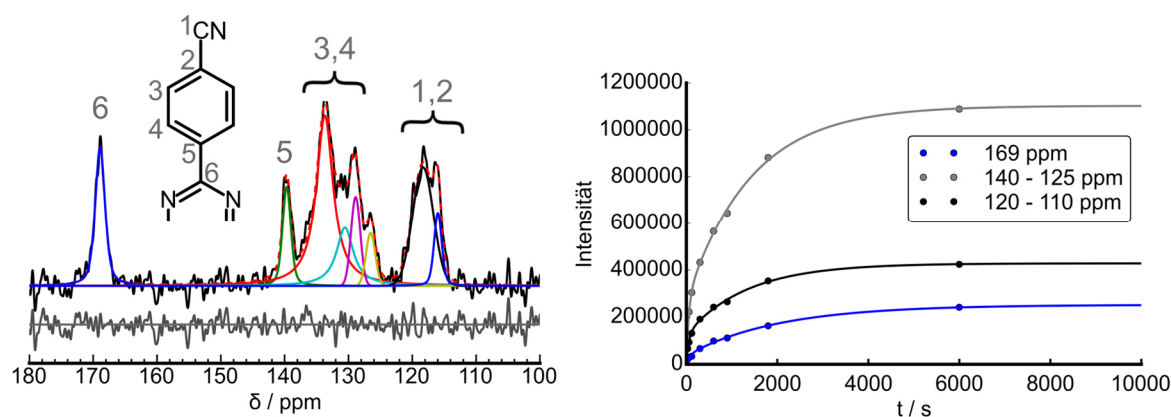


Abbildung 13. Entfaltetes ^{13}C MAS Einpuls Spektrum von PTO-300-10 mit einer Wiederholzeit von $t = 6000$ s (links) und Relaxationskurve (rechts).

Die anschließenden photokatalytischen Studien zeigen, dass die kürzeren Oligomere eine höhere Aktivität aufweisen, was unter anderem auf die größere Anzahl an Endgruppen zurückzuführen ist, die als aktive Zentren fungieren können. Oberflächenmessungen bewiesen, dass die erhöhte Aktivität nicht ausschließlich durch die größere Oberfläche verursacht wird. Im Vergleich zu anderen Photokatalysatoren fällt hier besonders die hohe Langzeitstabilität, und deren Aktivität, auch in Abwesenheit eines Cokatalysators positiv auf.

3.2 Bestimmung der Länge von Heptazin-Oligomeren mittels 1D Spektren

Im folgenden Absatz wurde ebenfalls die Oligomerlänge, diesmal jedoch einer heptazin-basierten Strukturen untersucht. Dabei wurden bewusst aktiver Zentren, hier Endgruppen, eingeführt, um die photokatalytische Aktivität zu steigern (Kapitel 6.2).

Das Heptazin-Polymer Melon^[34] (Abbildung 14) ist, ähnlich wie das Polymer CTF-1, kaum katalytisch aktiv. Durch Erniedrigung der Synthesetemperatur auf 450°C , im Vergleich zur Synthese von Melon bei $\sim 600^\circ\text{C}$, wird eine unvollständige Polymerisierung erreicht. Die entstandene Substanz besitzt deutlich erhöhte photokatalytische Aktivität. XRD, IR und UV-Vis Analytik deuten auf ein Gemisch von Melem^[52], dem Monomer, und Heptazin-Oligomeren hin. Dieses Gemisch wurde in DMSO gelöst und durch Zentrifugation bei 10000 und 60000 RCF in drei Fraktionen (DMSO-löslich, RCF 10000 und RCF 60000) aufgetrennt. Alle drei Fraktionen wurden mithilfe XRD, IR, UV-Vis, MALDI-TOF und FK-NMR charakterisiert.

Für die lösliche Fraktion konnte durch alle Methoden im Zusammenspiel gezeigt werden, dass es sich um Melem oder Melem-Hydrat handelt. Dabei sind sowohl im ^{13}C CP, als auch im ^{15}N CP Spektrum die charakteristischen Signale erkennbar. Den deutlichsten Hinweis auf die Präsenz von Melem oder Melem-Hydrat gibt die Verschiebung des zentralen Stickstoffatoms im Heptazinring. Dieser wandert mit zunehmendem Polymerisationsgrad von -234 ppm für Melem zu größeren Werten (Abbildung 14). In der löslichen Fraktion liegt er jedoch bei -234 ppm, wodurch eine monomere Melemeinheit nachgewiesen werden konnte.

Mithilfe von XRD, IR, UV-Vis und MALDI-TOF wurde für die anderen beiden Fraktionen eine Ähnlichkeit zu Melon festgestellt, wodurch eine oligomere Struktur vermutet wurde. Jedoch konnten die beiden Fraktionen nicht eindeutig unterschieden werden. Die im Abschnitt 3.1 zum Ergebnis führenden strukturellen Charakteristika sind in diesen Oligomeren nicht enthalten, weshalb ein anderer Ansatz verwendet werden muss. Da die ^{13}C CP Spektren in diesem Fall wenig Anhaltspunkte lieferten, wurden ^{15}N CP Spektren näher betrachtet. Über zwei unabhängige Charakteristika konnte dabei nachgewiesen werden, dass die Oligomere in der RCF 60000 Fraktion kürzer als die in der RCF 10000 Fraktion sind. Zum einen stellt die chemische Verschiebung des zentralen Stickstoffatoms (N_c), wie in Abschnitt 2.6 beschrieben, eine sensible Größe für die Umgebung des Heptazinmoleküls dar. Dies zeigt sich zum Beispiel daran, dass N_c in Melem eine chemische Verschiebung von -234 ppm aufweist, während N_c in Melon zu -225 ppm verschiebt. In den beiden Proben ist das Signal für den zentralen Stickstoff sehr breit, was auf eine Verteilung schließen lässt. Das Maximum der beiden Fraktionen verschiebt sich jedoch in Richtung -234 ppm für RCF 60000 (Abbildung 14), wodurch auf unterschiedliche durchschnittliche Oligomerlängen geschlossen werden kann, wobei RCF 60000 die kürzeren Oligomere besitzt.

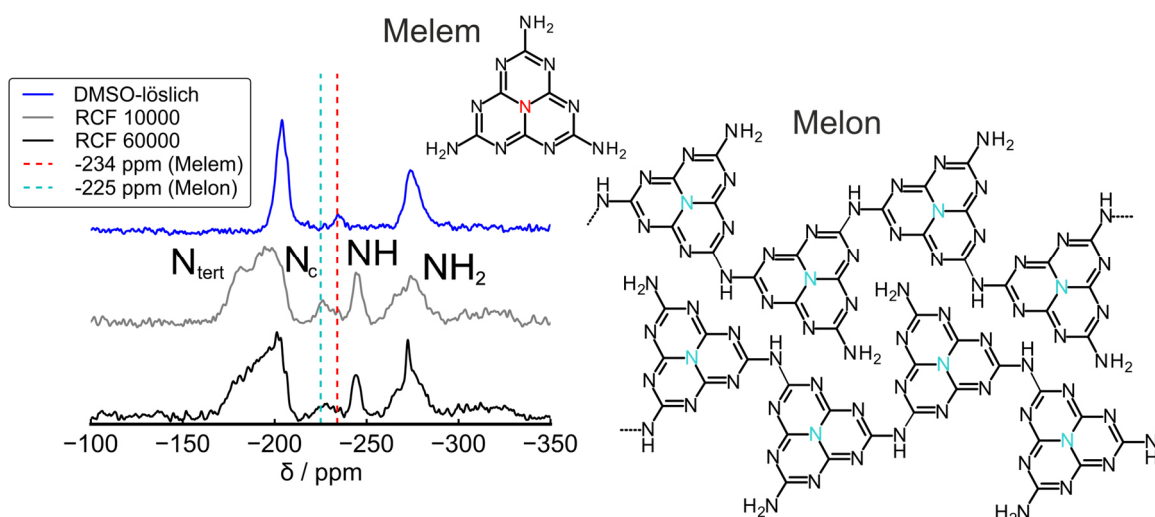


Abbildung 14. ^{15}N CP MAS Spektren (links) und Strukturformel von Melem und Melon (rechts).

Zum anderen kann die Oligomerlänge n aus dem Verhältnis von NH_2 - zu NH -Gruppen (-245 ppm zu -255 bis -290 ppm) bestimmt werden (Abbildung 15 (links)). Dieses sinkt mit steigender Oligomerlänge (Abbildung 15 (rechts)). Dabei ist zu beachten, dass die Werte hier nur relativ zueinander und nicht quantitativ betrachtet werden können, da aufgrund der geringen natürlichen Häufigkeit von ^{15}N nur Kreuzpolarisationsspektren gemessen werden konnten. Die Fraktion RCF 10000 hat ein NH_2 - zu NH -Verhältnis von 2,4 und RCF 60000 von 3,3. Dadurch wurde bestätigt, dass RCF 60000 aus kürzeren und RCF 10000 aus längeren Oligomere besteht. Tendenziell handelt es sich dabei überwiegend um Dimere (RCF 60000) beziehungsweise Trimere (RCF 10000).

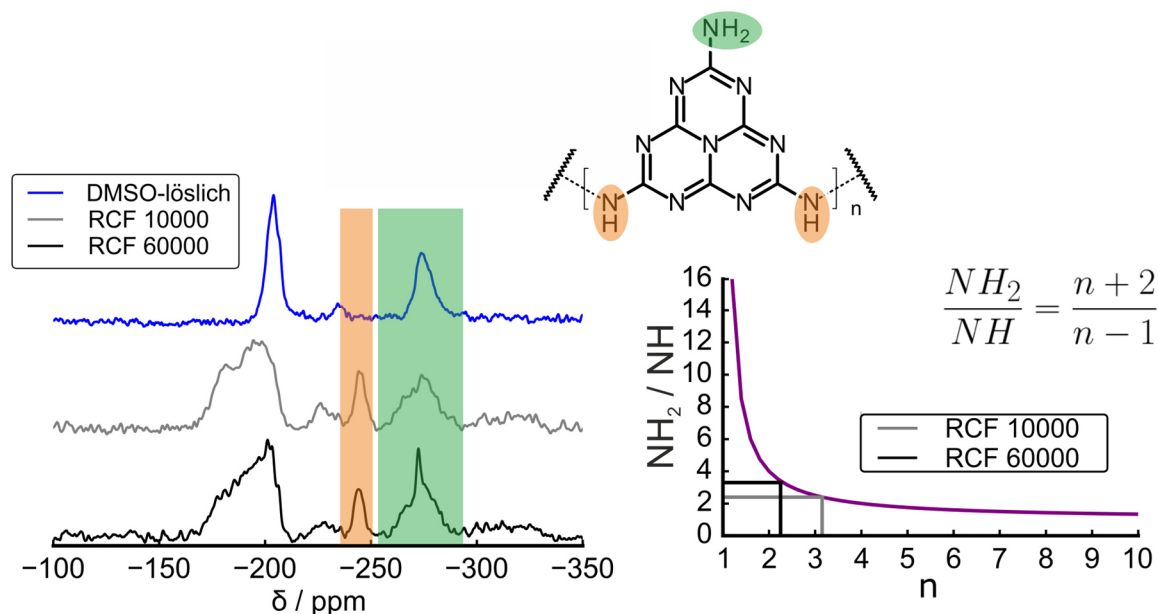


Abbildung 15. ^{15}N CP MAS Spektren der 3 Fraktionen (links) mit Kennzeichnung der NH- (orange) und NH_2 -Gruppen (grün). NH_2/NH -Verhältnis aufgetragen gegen die Oligomerlänge n und zugehörige Formel (rechts).

Die Fraktion RCF 60000, mit den kürzesten Oligomeren, ist katalytisch am aktivsten. Dies gilt auch, wenn der Einfluss der größeren Oberfläche berücksichtigt wird. Um die erhöhte Aktivität besser erklären zu können, wurden DFT Rechnungen in Abhängigkeit der Oligomerlänge durchgeführt. Dabei wird die Bandlücke mit abnehmender Oligomerlänge größer, da sich die Position des LUMO verändert, während die des HOMO nahezu unverändert bleibt. Diese Veränderung rechtfertigt jedoch nicht die beobachtete photokatalytische Aktivität. Zusätzlich wurde festgestellt, dass das LUMO bei längeren Oligomeren deutlich weniger delokalisiert ist als bei kürzeren, wodurch es in längeren Oligomeren weniger zugänglich ist. Da es oft auch als Näherung für die reduzierend wirkenden Stellen verwendet wird, sind kürzere Oligomere photokatalytisch aktiver. Dies unterstützt die These, dass primäre und/oder sekundäre Amine als reduzierende Stellen agieren und unterstreicht damit die Wichtigkeit der Defekte, in diesem Fall Endgruppen, für die Photokatalyse.

3.3 Strukturaufklärung heptazin-basierter Netzwerke mittels 1D Spektren

Im Kapitel 6.3 werden ebenfalls heptazin-basierte Substanzen untersucht. In diesem Fall handelt es sich jedoch um polymere, mikroporöse Netzwerke (heptazine-based microporous polymer networks, HMP) die aus Heptazinchlorid und Di(aminobenzol)benzothiadiazol in zwei unterschiedlichen Verhältnissen (4:3 bzw. 2:3) synthetisiert werden (HMP-3_4:3 und HMP-3_2:3, Abbildung 16). Ziel ist eine Erhöhung der photokatalytischen Aktivität durch die Stabilisierung der Ladungsträger. Um diese zu verbessern wird eine Elektronen-Donor-Akzeptor Struktur eingebaut, indem die Heptazineinheit mit einem Donor-Akzeptor-Molekül copolymerisiert wird. Die für diese Eigenschaften ausschlaggebenden funktionellen Gruppen sind nur bei niedrigen Synthesetemperaturen zugänglich. Daher stellt sich auch hier die Frage nach der Vollständigkeit der Reaktion und damit den Endgruppen und der Architektur des Polymers.

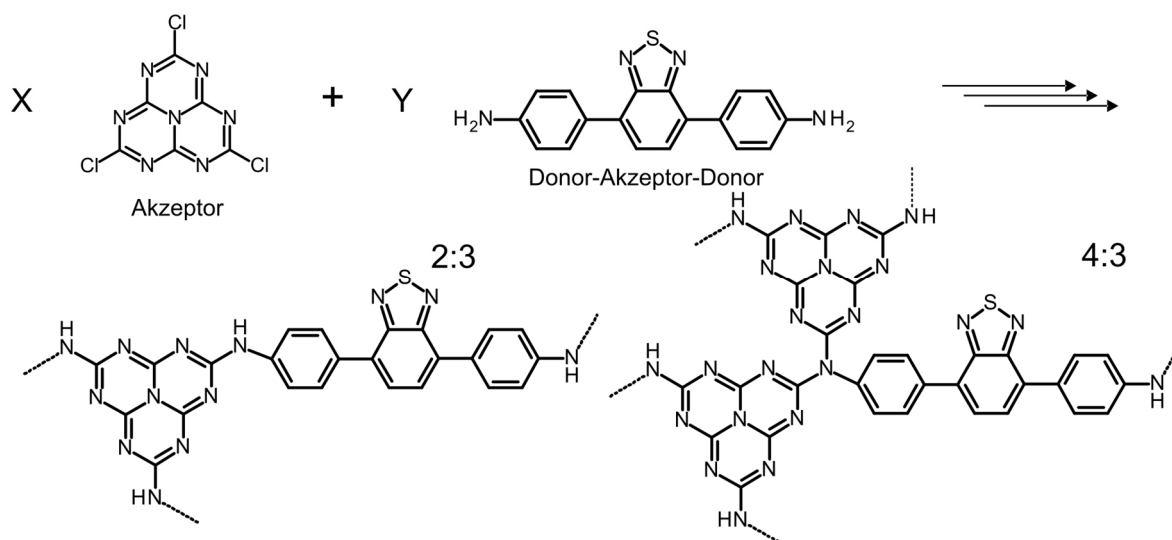


Abbildung 16. Edukte der heptazin-basierten Polymere HMP-3_4:3 und HMP-3_2:3 und mögliche Verknüpfungsmuster.

Beide Polymere wurden zunächst mit EA charakterisiert. Dabei liegt der Stickstoffgehalt deutlich unter dem erwarteten Gehalt, was bei CN-Materialien häufig beobachtet wird. Zudem sind aufgrund unvollständiger Ausbeuten noch Endgruppen in den Polymeren enthalten, welche im Falle des Heptazinchlorids hydrolysieren können. Dies macht eine Charakterisierung mittels EA unzuverlässig. Eine TGA der Polymere zeigte eine hohe thermische Stabilität für HMP-3_2:3 (500°C in inerter Atmosphäre) während die für HMP-3_4:3 niedriger war. Da HMP-3_4:3 theoretisch den höheren Vernetzungsgrad hat, kann dies zunächst nicht erklärt werden. Für die weitere Charakterisierung wurde FK-NMR gewählt, da die Proben wenig kristallin sind.

Wie bereits in Absatz 3.2 beschrieben, reagiert die Verschiebung des zentralen Stickstoffs der Heptazinringe (N_c) empfindlich auf seine Umgebung. Demnach wurden zunächst ^{15}N Spektren gemessen (Abbildung 17), wodurch sowohl der Heptazinring (N_c bei -227 ppm), als auch die Thiazol-Einheit (-55 ppm) in beiden Proben nachgewiesen werden konnte. Die chemische Verschiebung von -227 ppm für N_c ist ein klares Indiz für eine NH-Verbrückung zwischen den Monomeren. Dies wird auch durch das Signal zwischen -250 ppm und -260 ppm bestätigt, welches NH Gruppen zugeordnet werden kann. Darüber hinaus konnte in HMP-3_4:3 Cyamelursäure als Nebenprodukt identifiziert werden.

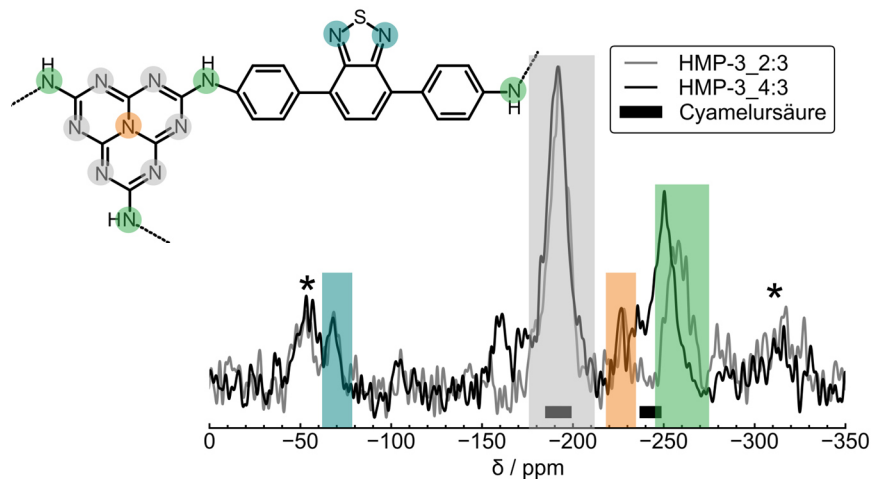


Abbildung 17. ^{15}N CP MAS Spektren von HMP-3_2:3 und HMP-3_4:3. Die chemischen Verschiebungen von Melon und Cyamelursäure sind durch Balken markiert.

Für eine quantitative Aussage wurden in diesem Fall zusätzlich Einpuls ^{13}C Spektren verwendet. Die Signalzuordnung im ^{13}C Spektrum erwies sich als komplex, da die Signale der beiden Monomere und der Cyamelursäure zum Teil überlappen (Abbildung 18).

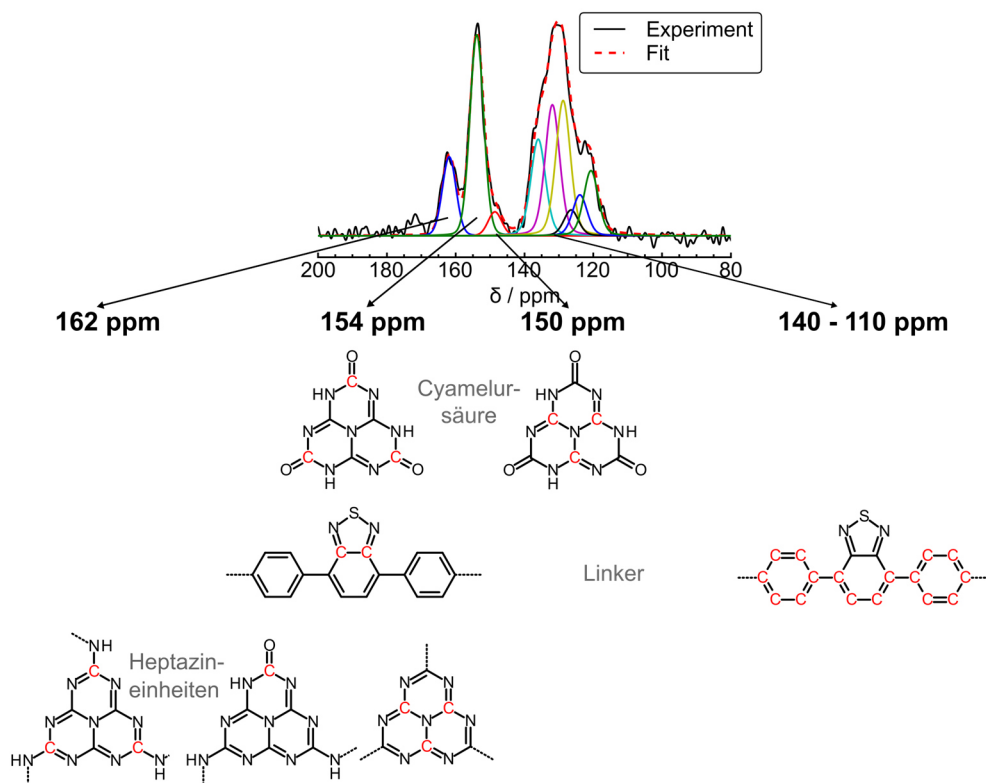


Abbildung 18. Signalzuordnung des ^{13}C NMR-Spektrums für HMP-3_4:3.

Dennoch konnten das Verhältnis von Heptazin- zu Linker-Einheiten und der Anteil an Cyamelursäure bestimmt werden, wodurch sich die Verknüpfungsmuster im Polymer ergaben. Weiterhin wurde die Vollständigkeit der Polymerisation und der Anteil an Endgruppen berechnet. Aus diesen Informationen ergab sich eine Summenformel für die beiden Polymere (Abbildung 19). HMP-3_2:3

besitzt deutlich weniger unreaktierte Endgruppen (0,24 pro Linker) und bildet damit ein dichteres Netzwerk aus, während in HMP-3_4:3 neben unreaktierte Cyamelursäure (0,21 pro Linker) auch ein deutlich höherer Anteil an Endgruppen (0,57 pro Linker) enthalten ist. Dadurch ist der Vernetzungsgrad von HMP-3_4:3 niedriger als der von HMP-3_2:3, während dies aus den Synthesebedingungen nicht erwartet wurde. Dadurch kann auch die zuvor erwähnte höhere thermische Stabilität von HMP-3_2:3 erklärt werden.

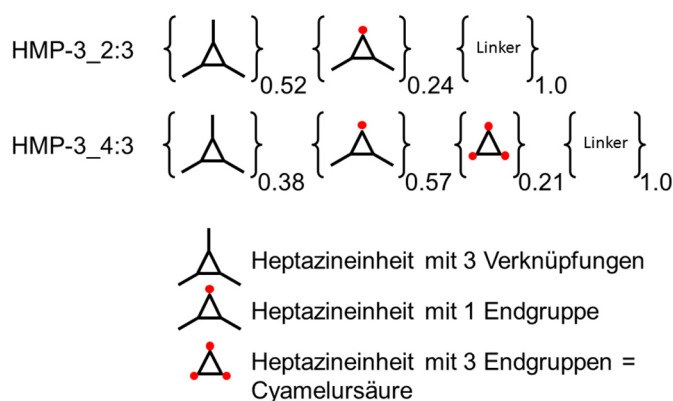


Abbildung 19. Summenformel für die beiden Polymere.

Außerdem wurde die photokatalytische Aktivität der Polymere untersucht. Trotz geringer Porosität konnte eine hohe Aktivität festgestellt werden, die dank der ausführlichen Charakterisierung auf die verbesserte Ladungsseparation durch die eingeführten Donor-Akzeptor-Einheiten zurückgeführt wurde.

3.4 Spectral-editing zur Strukturlösung eines PTI-Derivates

Die im Folgenden untersuchte Substanz besteht aus dem triazin-basierten Netzwerk PTI/LiCl, welches durch das Einbringen eines Comonomers (4-Amino-2,6-dihydroxypyrimidin (4AP)) während der Synthese modifiziert wurde. Ziel der Copolymerisation war, die photokatalytische Aktivität durch den Einbau von Defekten, die als aktive Zentren wirken, zu erhöhen. Um auf eine Struktur-Eigenschafts-Beziehung schließen zu können ist es jedoch essentiell, die Struktur aufzuklären. Hierbei ist es von besonderem Interesse zu wissen, ob das Triazinnetzwerk auch in Gegenwart eines Comonomers gebildet wird, beziehungsweise ob das Comonomer überhaupt eingebaut wird (Abbildung 20). Mithilfe von spectral-editing kann zwischen einem Triazin- und Heptazinnetzwerk unterschieden werden (Kapitel 6.4).

Amorphes PTI (aPTI) wurde in Gegenwart des Comonomers 4AP synthetisiert. IR und EA Daten legen nahe, dass 4AP eingebaut ist, da im IR-Spektrum sowohl eine CH-Schwingung, als auch Hinweise auf CN-Endgruppen und Gruppen, die Sauerstoff enthalten, sichtbar wurden. Durch EA wird ein erhöhter Kohlenstoff- und Sauerstoffgehalt nachgewiesen, was ebenso für einen Einbau des Comonomers spricht.

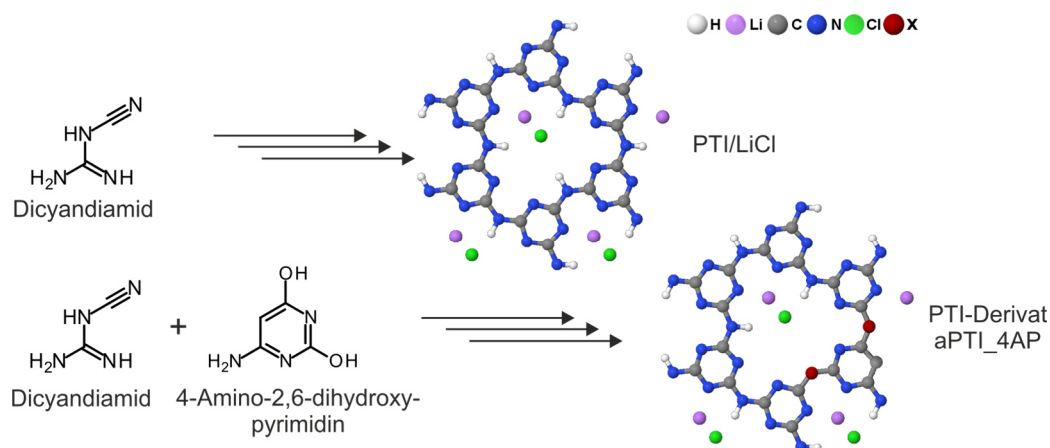


Abbildung 20. Synthese von PTI aus Dicyandiamid und dessen idealisierte Struktur (oben) und Synthese des PTI-Derivats aPTI_4AP aus Dicyandiamid und dem Comonomer 4-Amino-2,6-dihydroxypyrimidin (4AP) und dessen vorgeschlagene Struktur (unten).

Durch ^{13}C und ^{15}N NMR-Spektren wurde der Einbau des Comonomers und die Baueinheit des Netzwerks weiter untersucht. Im ^{13}C Spektrum ist ein breites Signal zwischen 152 und 170 ppm zu sehen, während PTI/LiCl drei aufgelöste Signale in diesem Bereich besitzt (Abbildung 21 (links)). Die deutlich größere Linienbreite verglichen mit PTI/LiCl bestätigt den amorphen Charakter, macht jedoch weitere Aussagen schwieriger. Zudem kann die Linienbreite durch eine ungleichmäßige Verteilung des 4AP in der Struktur zustande kommen, was auf einen Einbau hindeutet.

Das ^{15}N CP ist ähnlich dem Spektrum von PTI/LiCl und zeigt ein breites Signal bei circa -180 ppm, das tertiären Stickstoffatomen zugeordnet wurde und ein Signal im Bereich der NH-Gruppen (Abbildung 21 (rechts)). Vor allem letzteres besitzt, wie schon das ^{13}C Signal, eine deutlich höhere Linienbreite und eine geringere Auflösung. Aus dem Spektrum kann jedoch nicht mit Sicherheit bestätigt werden, dass Triazin- und nicht Heptazinringe entstehen, da das charakteristische Signal für den zentralen Stickstoff des Heptazinrings (siehe auch Abschnitt 3.2 und 3.3) im selben Verschiebungsbereich wie das der NH Gruppen liegt. Durch ein CPPI Experiment können jedoch NH-Gruppen von tertiären Stickstoffatomen eindeutig unterschieden werden. Dazu wird ein CPPI Spektrum mit einer Depolarisationszeit aufgenommen, bei der das Signal der NH Gruppen unterdrückt wird, während das von tertiären Stickstoffatomen erhalten bleibt. Da in dem experimentellen Spektrum kein Signal in diesem Bereich und damit kein Heptazinring in der Struktur ist, konnte nachgewiesen werden, dass auch unter Zugabe des Comonomers ein Triazingerüst entsteht. Die ^{15}N Spektren wurden erst durch eine Flipback-Pulssequenz ermöglicht, die die natürliche Relaxationszeit der Protonen verkürzt, indem die Magnetisierung mithilfe eines 90° Pulses zurück in die z-Achse gebracht wird. Dadurch kann eine Verkürzung der Messzeit bei gleicher Signalintensität erreicht werden.

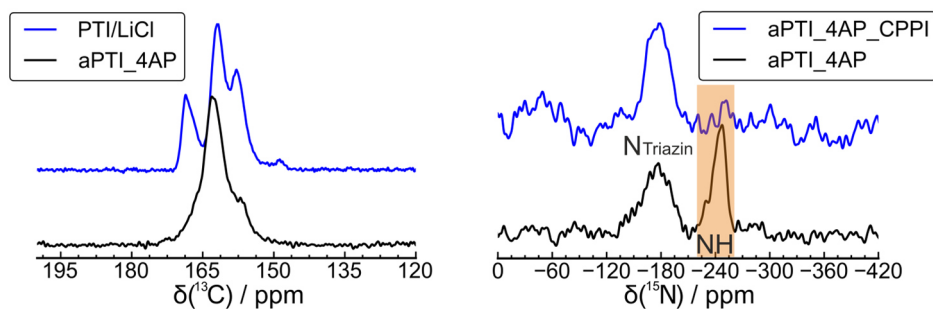


Abbildung 21. ^{13}C CP MAS Spektren (links) und ^{15}N CP MAS Spektrum (schwarz, rechts) und CPPI Spektrum (blau, rechts) mit einer Inversionszeit von $400\ \mu\text{s}$ gemessen bei einer Rotationsfrequenz von 10 bzw. 6 kHz.

In den photokatalytischen Studien besitzt aPTI_4AP eine deutlich erhöhte Aktivität. Durch den Nachweis, dass 4AP eingebaut wurde, ist die Erhöhung der Aktivität auf die Dotierung mit Kohlenstoff zurückzuführen. Weder PTI/LiCl, noch das amorphe PTI selbst, sind ähnlich photokatalytisch aktiv.

3.5 Strukturaufklärung von PTI Nanoschichten: 1D und 2D Spektren

In der bereits erschienenen Veröffentlichung (Kapitel 6.5) wird, wie in Kapitel 3.4, ebenfalls eine auf PTI/LiCl basierende Struktur untersucht. Das PTI wurde mittels eines Sonoverfahrens mit dem Ziel Nanoschichten zu erzeugen, delaminiert. Aufgrund der Erhöhung der Oberfläche sollen daher mehr reaktive Zentren zugänglich werden, wodurch die photokatalytische Aktivität steigt. Die Struktur der Proben wird mittels 1D und 2D Spektren näher untersucht.

Um die PTI Nanoschichten herzustellen wurde PTI in Wasser suspendiert, durch Ultraschall behandelt, und anschließend bei 3000 rpm zentrifugiert (Abbildung 22). Die überstehende Lösung (Lösung 1) wurde dann nochmal bei 5000 rpm und darauffolgend (Lösung 2) bei 25000 rpm zentrifugiert. Durch AFM, TEM, XRD und XPS konnte nachgewiesen werden, dass die PTI Struktur erhalten bleibt, die van-der-Waals- und elektrostatischen Kräfte jedoch aufgebrochen werden und vor allem im letzten Schritt Nanoschichten zurückbleiben, die aufgrund der Zentrifugation wieder agglomerieren. Weiterhin wurde durch EA nachgewiesen, dass infolge der Ultraschallbehandlung der Lithium-Gehalt sinkt, während das C/N Verhältnis weitestgehend konstant blieb.

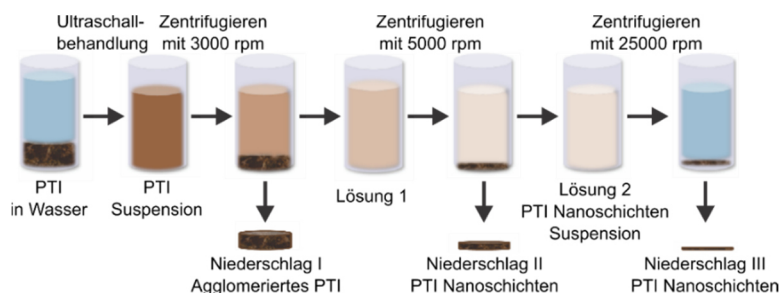


Abbildung 22. Schematische Darstellung der Synthese der PTI Nanoschichten.

Um weitere Informationen über den Unterschied zwischen den Nanoschichten im Vergleich zu PTI/LiCl zu erfahren, wurden FK-NMR-Messungen an ^{15}N angereicherten Proben durchgeführt. Der

Vergleich von 1D NMR-Spektren (^1H , ^{13}C und ^{15}N , Abbildung 23) der Niederschläge I-III mit PTI/LiCl bestätigte, dass die PTI Grundstruktur erhalten bleibt. Weiterhin konnte nachgewiesen werden, dass sich der Lithiumgehalt bei der initialen Ultraschallbehandlung einstellt und dann in allen drei Niederschlägen konstant bleibt, was durch die gleichbleibenden Intensitätsverhältnissen zwischen den Signalen in den ^1H , ^{13}C und ^{15}N Spektren deutlich wird.

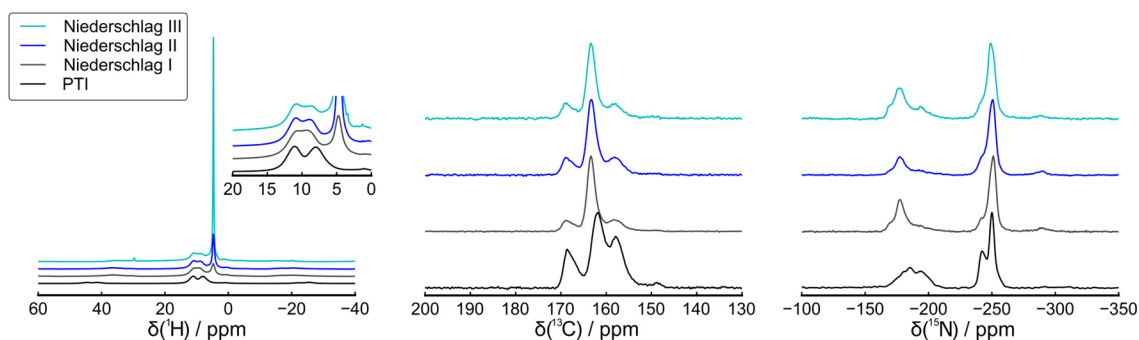


Abbildung 23. ^1H MAS NMR-Spektrum (links), ^{13}C (mitte) und ^{15}N (rechts) CP MAS Spektren der Niederschläge I-III.

Die hochaufgelösten ^1H Spektren, die bei 62,5 kHz Rotation in einem 1,3 mm Rotor gemessen wurden, zeigten zwei Wassersignale bei 4,6 und 6,2 ppm (Abbildung 24, blaue Signale), die bei Niederschlag III am intensivsten sind. Durch 2D ^1H - ^1H Spindiffusionsspektren mit dieser hohen Auflösung, konnte gezeigt werden, dass zwischen Wasser und PTI eine sehr starke Kopplung besteht (Abbildung 24, blaue Quadrate), welche stärker als zwischen den unterschiedlichen Protonen (Abbildung 24, oranges Quadrat) in PTI ist. Zusammen mit dem Wissen um eine Schichtstruktur, lässt dies vermuten, dass sich das Wasser auf den Oberflächen anlagert und damit der Wasser-PTI Abstand sehr klein ist. Daher kann aus dem Verhältnis von Wasser- zu PTI-Signalintensität unter der Annahme einer Wasser-Monolagendichte, die Dicke der Nanoschichten abgeschätzt werden. Diese Schichtdicke von 2-4 PTI-Lagen stimmt sehr gut mit der aus AFM Messungen erhaltenen überein. Demnach war es in diesem Fall durch NMR-Messungen möglich, neben Fragen zur Struktur auch die Schichtdicke der Nanoschichten näher zu betrachten.

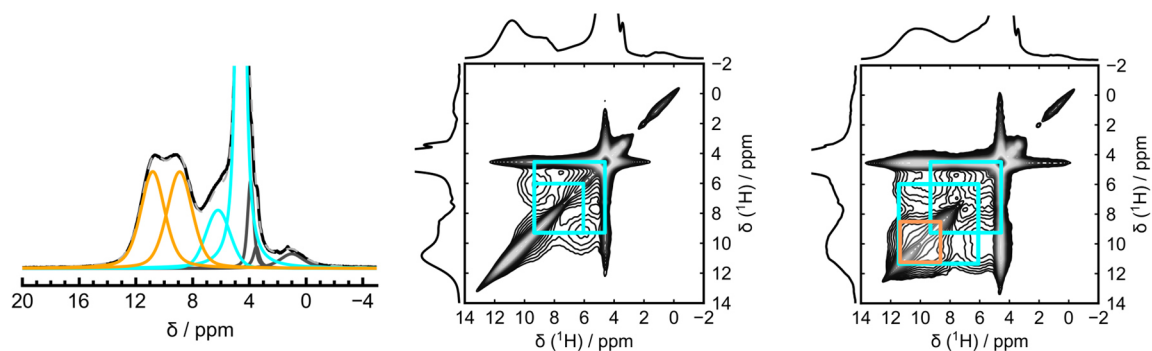


Abbildung 24. Entfaltung des ^1H MAS NMR-Spektrums (links) und der ^1H - ^1H 2D Spindiffusionsspektren mit einer Mischzeit von 10 ms (mitte) und 200 ms (rechts) des Niederschlags III bei $\nu_{\text{rot}} = 62,5\text{kHz}$. Die Signale des Wassers und die Kopplung zwischen Wasser- und PTI-Protonen sind blau gekennzeichnet, PTI-Signale und die Kopplung zwischen den unterschiedlichen PTI-Protonen orange.

Durch die niedrige Schichtdicke und damit große Oberfläche wurde eine Erhöhung der photokatalytischen Aktivität vermutet, da mehr aktive Zentren zugänglich sein können. Dies konnte durch photokatalytische Experimente bestätigt werden, die eine Abhängigkeit der photokatalytischen Aktivität von der Schichtdicke bestätigte. Die Probe mit der geringsten Dicke wies eine 18-fach höhere Aktivität verglichen mit PTI/LiCl auf.

3.6 Bestimmung von Atompositionen am Beispiel von PTI/LiCl

Die detaillierteste NMR-kristallographische Untersuchung wurde, wie in Kapitel 6.6 dargestellt, an PTI/LiCl durchgeführt. Wie in den vorherigen Kapiteln (3.4 und 3.5) bereits verdeutlicht, stellt PTI eine Modellsubstanz für CN-Photokatalysatoren dar. Dabei ist die Netzwerkstruktur bereits gut charakterisiert,^[47] während die Positionen der leichten Atome, Wasserstoff und Lithium, noch nicht untersucht wurden, da sie durch Diffraktionsmethoden nahezu nicht zugänglich sind. Photokatalytische Studien und Berechnungen der Bandstruktur zeigten, dass der Lithiumgehalt, und damit auch die Lithiumsubstruktur, eine entscheidende Rolle in der Photokatalyse spielen.^[57,139] Da die Lithium- mit der Protonensubstruktur korreliert, müssen beide untersucht werden. Um die einzelnen Atompositionen aufzuklären, wurde ein neuer NMR-kristallographischer Ansatz verwendet, indem NMR-Spektroskopie mit chemischer Modellierung, Elektronendiffraktion und der Analyse der Paarverteilungsfunktion kombiniert wurde.

Zunächst wurde eine ^{15}N -angereicherte Probe aus ^{15}N -Dicyandiamid nach der Vorschrift von Wirnhier *et al.* synthetisiert^[47] und mittels 1D Spektren der NMR-aktiven Kerne ^1H , ^{13}C , ^{15}N und ^7Li charakterisiert (Abbildung 25).

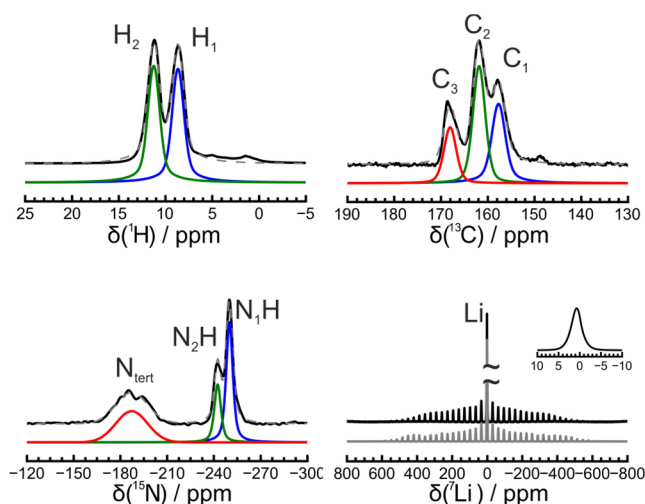


Abbildung 25. 1D ^1H , ^{13}C , ^{15}N und ^7Li MAS NMR Spektrum von PTI/LiCl (von links nach rechts).

Anschließend wurden 2D Spektren aufgenommen, die dipolare Kopplung und damit räumlich Nähe zeigen (Abbildung 26). Anhand der intensivsten Signale, die für die kürzesten Abstände und damit stärksten Wechselwirkungen auftreten, wurde ein Konnektivitätenschema entwickelt (Abbildung 26, unten). Aus dem ^1H - ^{15}N und dem ^{15}N - ^{13}C Korrelationsspektrum konnten die kovalenten Bindungen

abgeleitet werden. (Abbildung 26, schwarze Linien im Konnektivitätenschema). Die weiteren heteronuklearen Nachbarschaften ergaben sich aus ^{13}C - ^1H und ^7Li - ^1H Spektren (Abbildung 26, orange gestrichelte Linien im Konnektivitätenschema). Dabei wurde deutlich, dass in der Probe zwei verschiedene $\text{N}_{\text{tert}}\text{-C-NH-C-N}_{\text{tert}}$ Gruppen auftreten müssen, die sich unter anderem durch verschiedene Lithiumabstände unterscheiden und über tertiäre Stickstoffatome N_{tert} verbunden sind. Darüber hinaus wurden homonukleare Kopplungen (Abbildung 26, blau gestrichelte Linien im Konnektivitätenschema) untersucht. Es zeigt sich, dass die Abstände zwischen den Protonen von zwei unterschiedlichen Gruppen ($\text{H}_1\text{-H}_2$) kürzer sind, als bei zwei gleichen Gruppen ($\text{H}_1\text{-H}_1$ oder $\text{H}_2\text{-H}_2$). Eine direkte Nachbarschaft von NH-Gruppen, die dann über nur ein C getrennt wären, kann aufgrund der fehlenden NH-NH-Kopplung ausgeschlossen werden.

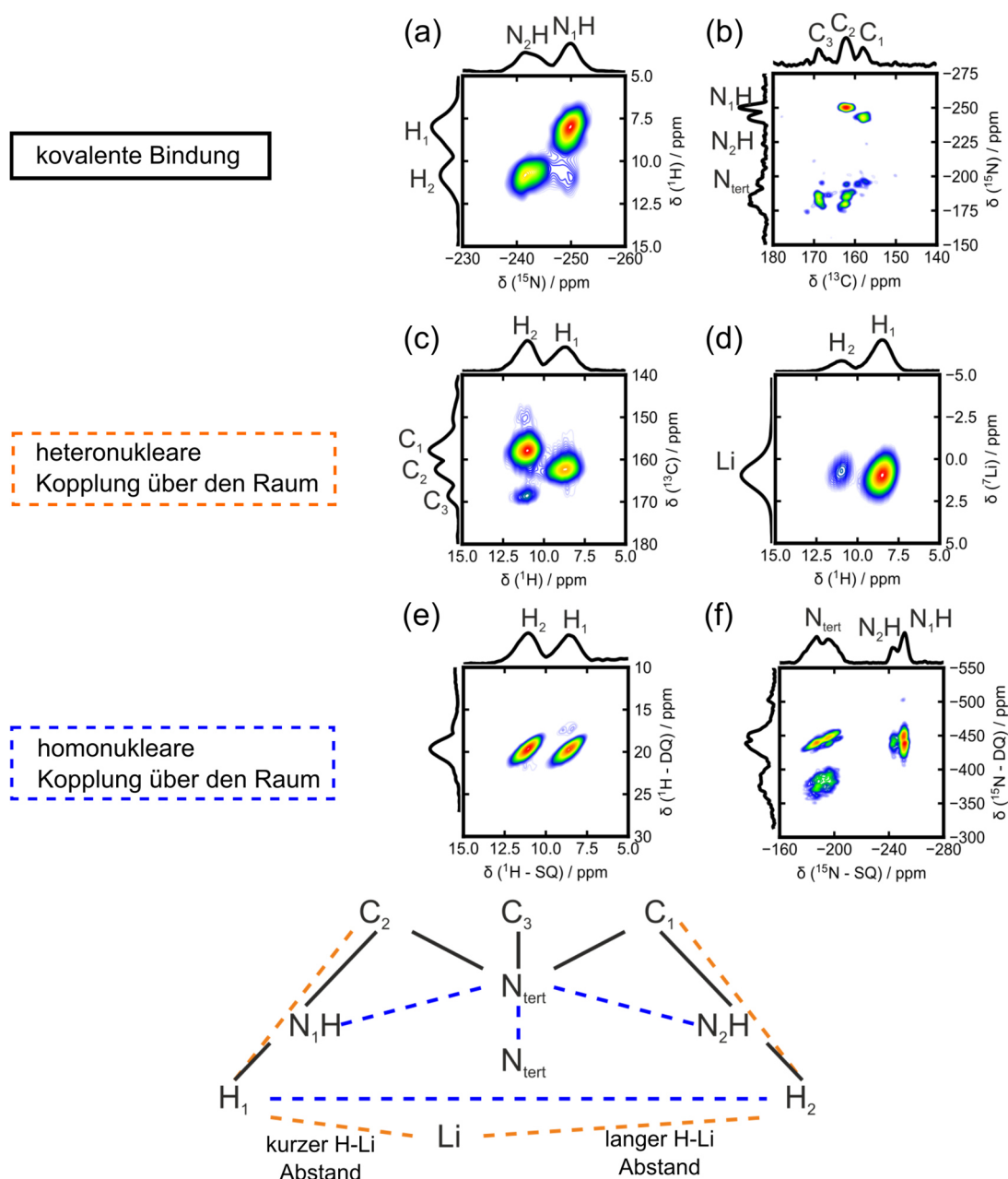


Abbildung 26. 2D Spektren von PTI/LiCl: a) ^1H - ^{15}N b) ^{15}N - ^{13}C c) ^{13}C - ^1H d) ^7Li - ^1H e) ^1H - ^1H -homonuklear f) ^{15}N - ^{15}N homonuklear. Abgeleitetes Konnektivitätenschema (unten). Schwarze Linien symbolisieren eine kovalente Bindung, während orangene Linien heteronukleare und blau homonukleare räumliche Nähe zeigen.

Auf Basis dieses Schemas (Abbildung 26, unten) und der Netzwerkstruktur wurden Strukturmodelle erarbeitet. In den homogenen Modellen sind pro Kavität zwei Lithium und zwei Protonen platziert. Dabei entstehen drei Modellklassen: I) 112 hom2b, beide Protonen sitzen an einem Brücken-Stickstoffatom, II) 112 hombr, ein Proton an einem Brücken-, das anderen an einem Ring-Stickstoffatom und III) 112 hom2r, beide Protonen sind an ein Ring-Stickstoffatom gebunden. Innerhalb der Klassen wurden alle theoretisch möglichen Modelle aufgestellt. Für die Lithiumionen sind bereits in der Struktur von Wirnhier *et al.* drei favorisierte Positionen in einer Schicht angegeben, so dass ein Lithiumion von zwei Stickstoffatomen koordiniert werden kann (Abbildung 27 Li-Kavität).^[47] In den Strukturen nehmen die Ionen, wenn die Protonensubstruktur dies zulässt, diese favorisierten Positionen ein. Anschließend wurden die Strukturen geometrieoptimiert und in jeder Klasse, die Struktur mit dem energetischen Minimum verwendet. Diese sind in Abbildung 27 dargestellt.

Weiterhin wurden heterogene Modelle entworfen. Dabei ist eine Kavität mit vier Protonen, eine andere zum Ladungsausgleich mit vier Lithium besetzt. Die Positionen der vier Protonen entsprechen ebenfalls denen des Energieminimums aller möglichen Permutationen, was in einer getrennten Publikation veröffentlicht wird. Die Lithiumatome besetzen die drei favorisierten Stellen in einer Kavität und das vierte Lithium wurde zwischen zwei dieser Ionen, jedoch entlang *c* in den Zwischenschichtraum verschoben, positioniert. Dadurch entstehen drei zueinander um 120° gedrehte Strukturen (*m0*, *m1*, *m2*). Diese Kavitäten wurden entweder so zu Schichten angeordnet, dass alle Kavitäten einer Schicht protoniert sind (116, Abbildung 27), oder dass innerhalb einer Schicht protonierte und lithiierte Kavitäten nach einem bestimmten Muster auftreten (226, Abbildung 27). Die benachbarten Schichten sind dann jeweils invers bezüglich der protonierten und lithiierten Kavitäten. Alle Modelle wurden geometrieoptimiert und entsprechend ihrer Energie sortiert. Nur die energetisch günstigsten Modelle wurden für die weitere Untersuchung in Betracht gezogen. Dies sind 112 hom2b, 112 hombr, 112 hom2r, 116 *m2* und 226 *m2* (Abbildung 27).

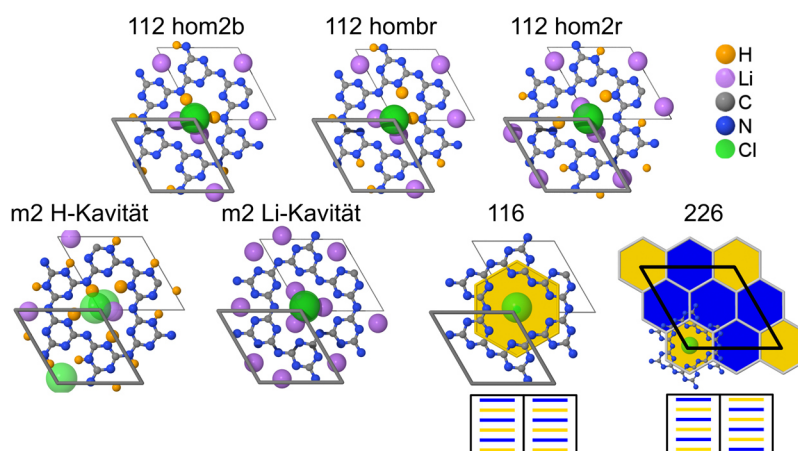


Abbildung 27. Darstellung der energetisch günstigsten Strukturmodelle: Oben: Homogene Modelle 112 hom2b, 112 hombr und 112 hom2r (von links nach rechts). Unten: Kavitäten im heterogenen Modell *m2* mit einer lithiierten und einer protonierten Kavität und deren Anordnung innerhalb der Schicht. Abwechselnd protonierte und lithiierte Schichten in Modell 116 und gemischte Schichten in Modell 226. Lithiierte Kavitäten sind in gelb dargestellt, Protonierte in blau.

Da die chemischen Verschiebungen für diese komplexen Modelle nicht bekannt sind, können sie nicht direkt mit dem Konnektivitätenschema abgeglichen werden. Jedoch können durch quantenmechanische Rechnungen die chemischen Verschiebungen bestimmt, daraus mithilfe der experimentell bestimmten Halbwertsbreiten die theoretischen Spektren berechnet und mit den experimentellen Spektren verglichen werden (Abbildung 28). Eine gemeinsame Zuordnung der chemischen Verschiebungen für alle Modelle war jedoch nicht möglich.

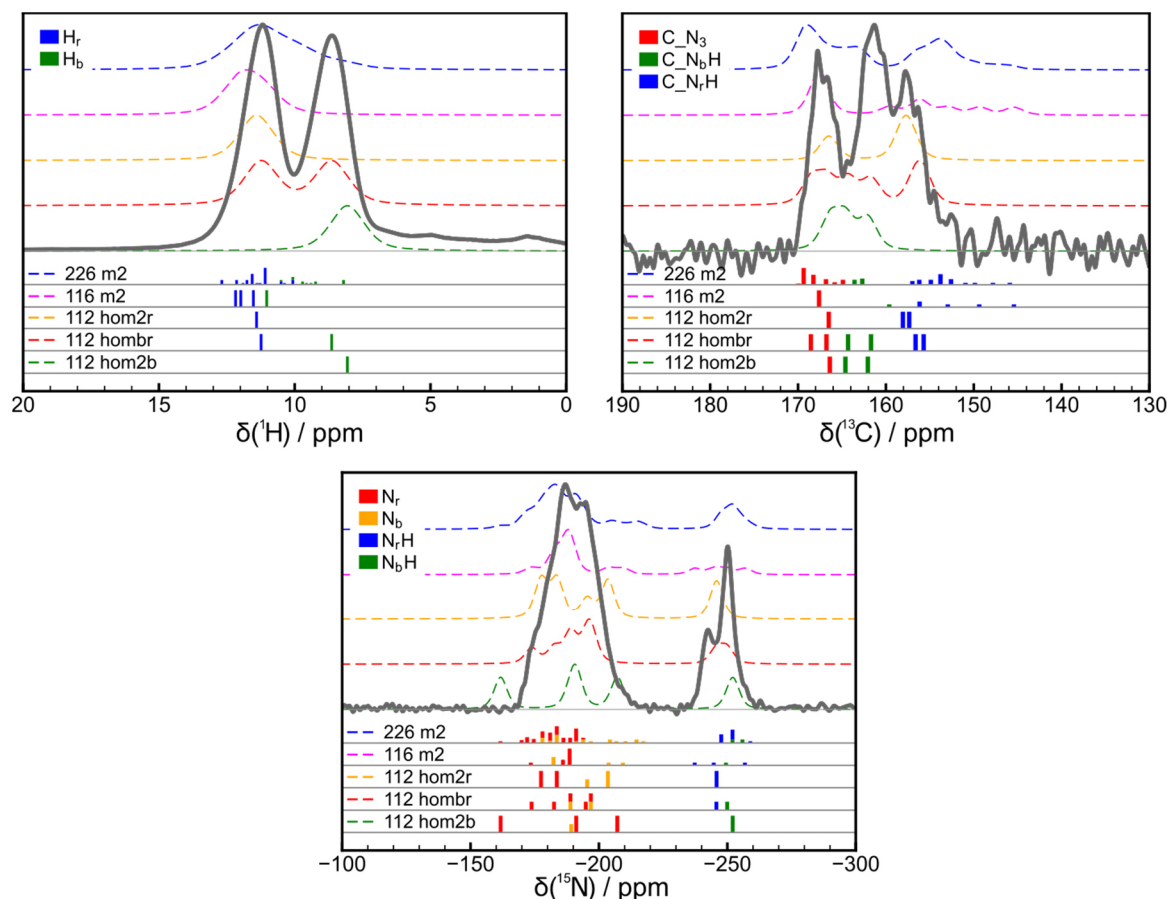


Abbildung 28. Berechnete chemische Verschiebungen und Spektren für ^1H (oben links), ^{13}C (oben rechts) und ^{15}N (unten). Mithilfe experimentell bestimmter Halbwertsbreiten wurden theoretische Spektren für alle Modelle berechnet (gestrichelte Linien). Die chemischen Gruppen sind jeweils farblich markiert: blau: Protonierung am Ring-Stickstoff (H_r , $C_{N_r}H$ und N_rH), grün: Protonierung am Brücken-Stickstoff (H_b , $C_{N_b}H$ und N_bH), rot: keine Protonierung am Ring, gelb: keine Protonierung an der Brücke.

Da aus den berechneten Spektren kein Modell eindeutig bestimmt werden konnte, mussten weitere Kriterien hinzugezogen werden. Dazu wurden $^1\text{H}\{^7\text{Li}\}$ und $^{13}\text{C}\{^7\text{Li}\}$ REDOR Abstandsmessungen mit den Simulationen aus den Modellen verglichen. Durch ein Zusammenführen aller Methoden mithilfe einer Kostenfunktion konnte das Strukturmodell 112 hombr als Wahrscheinlichstes bestimmt werden.

Auf Basis dieses Modells, konnten dann eine Korrelation zwischen chemischer Verschiebung und struktureller Baueinheit erarbeitet werden. Das entscheidende Kriterium für die Verschiebung im ^1H Spektrum ist dabei die Position der Protonierung, die am Ring (H_r) oder der Brücke (H_b) erfolgen

kann. Dies wirkt sich dann auch auf die Verschiebungen im ^{13}C und ^{15}N Spektrum aus, wo das Protonierungsmuster in der Nachbarschaft im Fall von ^{13}C , beziehungsweise am Kern direkt für ^{15}N , den größten Einfluss hat. Dieses Modell stimmt auch vollständig mit dem zuvor aus 2D Spektren abgeleiteten Konnektivitätenschema überein.

Aus Elektronendiffraktionsdaten wurden die Lithiumpositionen bestätigt und zudem eine Symmetrierniedrigung von hexagonal auf eine orthorhombische $C222_1$ Symmetrie detektiert. Da die Wasserstoffpositionen für Elektronendiffraktion jedoch unzugänglich sind, wurde das Modell 112 o hombr orthorhombisch aufgestellt (112 o hombr I) und die Protonenpositionen durch ein weiteres Modell 112 o hombr II (Abbildung 29) verfeinert. Diese Modelle wurden ebenfalls geometrieoptimiert und mit Abstandsmessungen untersucht. Neben $^1\text{H}\{^7\text{Li}\}$ und $^{13}\text{C}\{^7\text{Li}\}$ REDOR (Abbildung 29) wurden auch ^1H - ^{13}C CP-Aufbaukurven verwendet, die wiederum über eine Kostenfunktion zusammengeführt wurden.

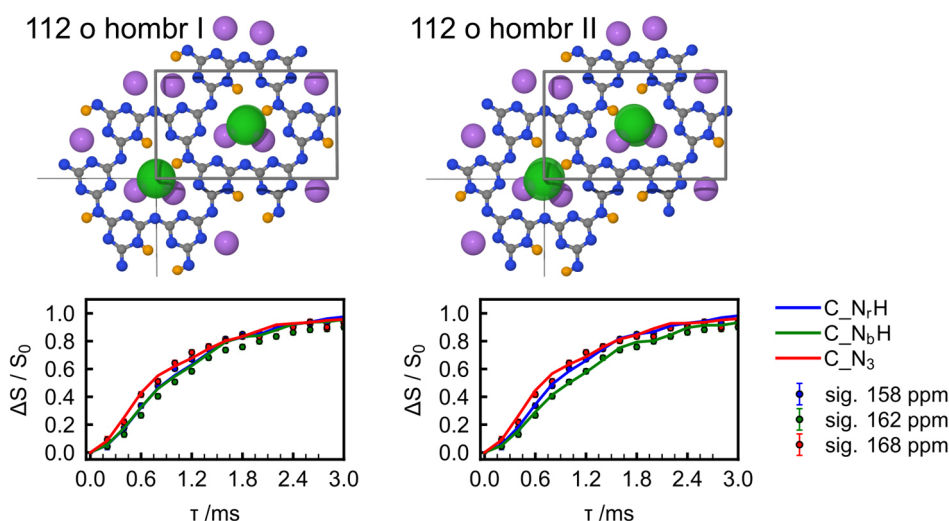


Abbildung 29. Strukturmodelle 112 o hombr I (links) und 112 o hombr II (rechts) sowie gemessene (Punkte) und simulierte (Linien) $^{13}\text{C}\{^7\text{Li}\}$ REDOR Kurven.

Übereinstimmend favorisieren alle drei Methoden Modell 112 o hombr II. Der durchschnittliche R -Wert sinkt von 0,10 auf 0,08. Vor allem für die Simulationen der $^{13}\text{C}\{^7\text{Li}\}$ REDOR Kurven ist dies auch qualitativ sichtbar, da die Aufspaltung zwischen den Kurven besser reproduziert werden konnte (Abbildung 29 unten). Durch eine anschließende Auswertung der Paarverteilungsfunktion konnte eine Wellung der Schichten mit einer Kohärenzlänge unter 4 nm nachgewiesen werden, die auf verbleibende Dipolmomente in der Struktur zurückzuführen ist.

Das finale Strukturmodell 112 o hombr II besitzt eine $P2_12_12_1$ Symmetrie und ist daher in guter Übereinstimmung (Abbildung 31) mit der aus Elektronendiffraktion bestimmten Raumgruppe $C222_1$, wobei die C-Zentrierung aufgehoben wurde.

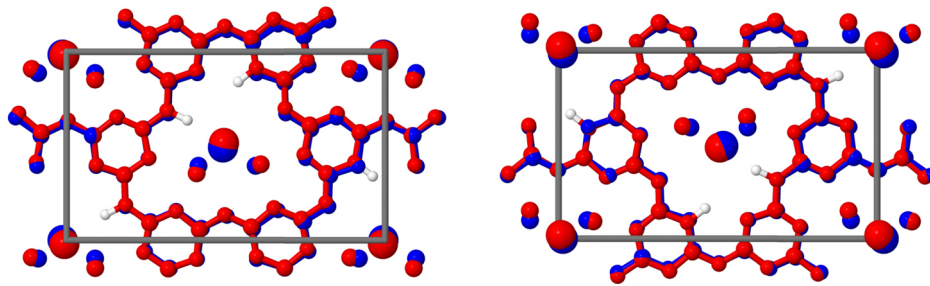


Abbildung 30. Modelle 112 o hombr II (rot) im Vergleich mit der Strukturlösung aus Elektronendiffraktion (blau). Schicht bei $c = 1/4$ (links) und bei $3/4$ (rechts).

Demnach konnte an PTI/LiCl demonstriert werden, dass durch einen neuen NMR-kristallographischen Ansatz, der NMR-Spektroskopie, chemische Modellierung, Elektronendiffraktion und Analyse der Paarverteilungsfunktion verbindet, die Protonen- und Lithiumsubstruktur gelöst werden konnte.

3.7 Schlussfolgerung

In den letzten sechs Kapiteln wurde die Untersuchung unterschiedlicher struktureller Fragestellungen von CN-Materialien mit NMR-Kristallographie dargestellt.

Ähnlich wie die Proteinstruktur in verschiedene Ebenen, die Primär-, Sekundär-, Tertiär- und Quartärstruktur gegliedert ist, kann auch die Strukturlösung von Polymeren auf mehrere Ebenen unterteilt werden. Die kleinste Baueinheit und damit unterste Ebene sind dabei einzelne Atome, deren Position innerhalb einer Struktur geklärt werden muss. Auf der nächsthöheren Ebene sind die Atome bereits zu Verbindungen, den Monomeren verknüpft, wobei die Verknüpfungsmuster und die Baueinheiten charakterisiert werden müssen. Sind diese bekannt, wird übergeordnet die Polymerarchitektur untersucht. Darunter versteht man neben der Art der Verknüpfung der Monomere, Charakteristika wie die Kettenlänge sowie die Art und Anzahl der Endgruppen. Abschließend muss dann noch die Morphologie, als übergeordnete Struktur der Polymere untersucht werden. Dementsprechend kann die Strukturlösung von Polymeren allgemein als Pyramide wie in Abbildung 31 dargestellt werden.

Überträgt man diese Systematik nun auf die vorgestellte Strukturaufklärung von CN-Materialien wird deutlich, dass NMR-Kristallographie auf allen Ebenen dazu beigetragen kann (Abbildung 31).

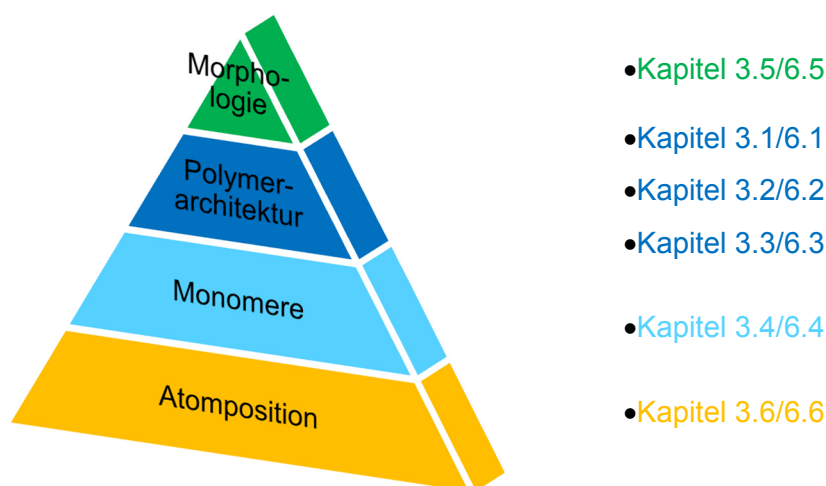


Abbildung 31. Schematische Darstellung der Strukturaufklärung an polymeren Materialien und die Zuordnung, in welchem Kapitel dieser Arbeit die entsprechend Fragestellung adressiert wurde

In Kapitel 3.6 wurde die Protonen-Lithium-Struktur in reinem PTI anhand einer ausführlichen NMR-kristallographischen Arbeit gelöst. Dabei wurde aus 1D und 2D FK-NMR-Spektren ein Konnektivitätenschema abgeleitet. Anschließend wurde durch das Zusammenspiel mit quantenmechanischen Rechnungen, NMR-Abstandsmessungen, Elektronendiffraktion sowie der Analyse der Paarverteilungsfunktion, die Positionen der Protonen und Lithiumionen, vollständig geklärt.

Die Frage nach den Monomeren wurde in Kapitel 3.4 untersucht. Es wurde zur Erhöhung der photokatalytischen Aktivität von PTI ein Comonomer eingebaut. Durch FK-NMR-Spektroskopie konnte die erfolgreiche Synthese des Copolymers unter Erhalt der triazin-basierten Struktur bestätigt werden.

In den Kapiteln 3.1 und 3.2 wurden Oligomere hinsichtlich ihrer Kettenlänge untersucht. Abhängig von den charakteristischen Gruppen und damit den untersuchten Kernen konnte aus ^{13}C oder ^{15}N Spektren eine absolute, beziehungsweise relative Kettenlänge bestimmt werden. Kapitel 3.3 befasste sich ebenfalls mit einer polymeren Struktur, wobei die Frage nach den Endgruppen und damit dem Verknüpfungsmuster untersucht wurde. Zusammenfassend wurde in den Kapiteln 3.1 - 3.3 demnach die Polymerarchitektur mit 1D Spektren untersucht, wobei das Problem der Auflösung und des Messens quantitativer Spektren von Kernen mit geringer natürlicher Häufigkeit bei jeder Fragestellung neu gelöst werden musste.

Dass auch die Morphologie durch NMR-Messungen zugänglich ist, zeigt die Arbeit in Kapitel 3.5. Dabei wurden PTI-Nanoschichten mittels 1D und 2D Spektren charakterisiert, wobei nachgewiesen werden konnte, dass die Struktur erhalten bleibt. Darüber hinaus konnte die Schichtdicke der delaminierten Probe bestimmt werden.

Obwohl die NMR-Kristallographie eine sehr wertvolle Methode zur Strukturaufklärung von CN-Materialien ist, muss auch der methodische und zeitliche Aufwand berücksichtigt werden. Vor allem die in CN-Materialien relevanten Kerne ^1H , ^{13}C und ^{15}N haben jeweils spezielle Anforderungen.

^1H Spektren sind, aufgrund der hohen natürlichen Häufigkeit und des hohen gyromagnetischen Verhältnisses, relativ einfach zu messen. Die starke dipolare Wechselwirkung, die aus dem gyromagnetischen Verhältnis resultiert, verringert jedoch häufig die Auflösung. Daher werden spezielle Methoden, wie komplexe Pulssequenzen oder ultra-hohes MAS benötigt, um aussagekräftige Spektren zu erhalten. Für Messungen der Kerne ^{13}C und ^{15}N ist die natürliche Häufigkeit von 1% beziehungsweise 0,4% eine Herausforderung. 1D ^{13}C Kreuzpolarisationsspektren sind noch in wenigen Stunden Messzeit zugänglich, wohingegen quantitative Experimente oder 2D Spektren spezielle Pulssequenzen oder Messzeiten von mehreren Tagen erfordern beziehungsweise eine Anreicherung notwendig machen. Eine Messzeit von mehreren Tagen ist für ^{15}N bereits bei 1D Kreuzpolarisationsspektren unumgänglich. Quantitative ^{15}N Messungen und 2D Experimente werden erst durch eine Isotopenanreicherung möglich.

Daher steht die NMR-Kristallographie mit bewährten Methoden, wie der Einkristallstrukturlösung, nicht in Konkurrenz, sondern widmet sich den durch diese Methoden unzugänglichen Strukturen.

4 Quellen

- [1] International Energy Agency. *World Energy Outlook 2014 Factsheet*, 2014.
- [2] Haeßner, C.; Köhler, K.; Wussow, K. Umwandlung und Speicherung von Sonnenenergie. *Chemie Unserer Zeit* **2014**, *48*, 246–259.
- [3] Arbeitsgemeinschaft Energiebilanzen e.V. *Pressedienst 01/2015 Jahresbericht*; 2015.
- [4] Chen, X.; Shen, S.; Guo, L.; Mao, S. S. Semiconductor-based Photocatalytic Hydrogen Generation. *Chem. Rev.* **2010**, *110*, 6503–6570.
- [5] Lee, J. S. Photocatalytic water splitting under visible light with particulate semiconductor catalysts. *Catal. Surv. Asia* **2005**, *9*, 217–227.
- [6] Marschall, R. Mit Sonnenlicht zum Wasserstoff. *Nachrichten aus der Chemie* **2015**, *6*, 631–635.
- [7] Hollmann, D.; Karnahl, M.; Tschierlei, S.; Kailasam, K.; Schneider, M.; Radnik, J.; Grabow, K.; Bentrup, U.; Junge, H.; Beller, M.; et al. Structure-activity relationships in bulk polymeric and sol-gel-derived carbon nitrides during photocatalytic hydrogen production. *Chem. Mater.* **2014**, *26*, 1727–1733.
- [8] Gust, D.; Moore, T. A.; Moore, A. L. Realizing artificial photosynthesis. *Faraday Discuss.* **2012**, *155*, 9–26.
- [9] Schlögl, R. Chemistry's Role in Regenerative Energy. *Angew. Chem. Int. Ed.* **2011**, *50*, 6424–6426.
- [10] Abe, R. Recent progress on photocatalytic and photoelectrochemical water splitting under visible light irradiation. *J. Photochem. Photobiol. C* **2010**, *11*, 179–209.
- [11] Kudo, A.; Miseki, Y. Heterogeneous photocatalyst materials for water splitting. *Chem. Soc. Rev.* **2009**, *38*, 253–278.
- [12] Lewis, N. S. Light work with water. *Nature* **2001**, *414*, 589–590.
- [13] Bowker, M. Sustainable hydrogen production by the application of ambient temperature photocatalysis. *Green Chem.* **2011**, *13*, 2235–2246.
- [14] Fujishima, A.; Honda, K. Electrochemical photolysis of water at a semiconductor electrode. *Nature* **1972**, *238*, 37–38.
- [15] Wang, X.; Maeda, K.; Thomas, A.; Takanabe, K.; Xin, G.; Carlsson, J. M.; Domen, K.; Antonietti, M. A metal-free polymeric photocatalyst for hydrogen production from water under visible light. *Nat. Mater.* **2009**, *8*, 76–80.
- [16] Maeda, K.; Domen, K. Photocatalytic Water Splitting: Recent Progress and Future Challenges. *J. Phys. Chem. Lett.* **2010**, *1*, 2655–2661.
- [17] Ohtani, B. Photocatalysis A to Z—What we know and what we do not know in a scientific sense. *J. Photochem. Photobiol. C* **2010**, *11*, 157–178.
- [18] Tachibana, Y.; Vayssieres, L.; Durrant, J. R. Artificial photosynthesis for solar water-splitting. *Nat. Photonics* **2012**, *6*, 511–518.
- [19] Yin, S.; Han, J.; Zhou, T.; Xu, R.; Yin, S.; Han, J.; Zhou, T.; Xu, R. Recent Progress in g-C₃N₄ based low cost photocatalytic system: activity enhancement and emerging applications. *Catal. Sci. Technol.* **2015**, *5*, 5048–5061.
- [20] Zheng, Y.; Lin, L.; Wang, B.; Wang, X. Graphitic Carbon Nitride Polymers toward Sustainable Photoredox Catalysis. *Angew. Chem. Int. Ed.* **2015**, *54*, 12868–12884.

- [21] Martineau, C.; Senker, J.; Taulelle, F. NMR Crystallography. *Annu. Reports NMR Spectrosc.* **2014**, *82*, 1–57.
- [22] Wang, X.; Blechert, S.; Antonietti, M. Polymeric graphitic carbon nitride for heterogeneous photocatalysis. *ACS Catal.* **2012**, *2*, 1596–1606.
- [23] Vinu, A. Two-dimensional hexagonally-ordered mesoporous carbon nitrides with tunable pore diameter, surface area and nitrogen content. *Adv. Funct. Mater.* **2008**, *18*, 816–827.
- [24] Schwarzer, A.; Saplinova, T.; Kroke, E. Tri-s-triazines (s-heptazines)—From a “mystery molecule” to industrially relevant carbon nitride materials. *Coord. Chem. Rev.* **2013**, *257*, 2032–2062.
- [25] Kroke, E. Novel group 14 nitrides. *Coord. Chem. Rev.* **2004**, *248*, 493–532.
- [26] Xia, X.; Zhou, C.; Tong, D.; Liu, M.; Zhang, D.; Fang, M.; Yu, W. Preparation of magnetic graphitic carbon nitride nanocomposites. *Mater. Lett.* **2010**, *64*, 2620–2623.
- [27] Jiang, G.; Zhou, C. H.; Xia, X.; Yang, F.; Tong, D.; Yu, W.; Liu, S. Controllable preparation of graphitic carbon nitride nanosheets via confined interlayer nanospace of layered clays. *Mater. Lett.* **2010**, *64*, 2718–2721.
- [28] Benard, D. J.; Linnen, C.; Harker, A.; Michels, H. H.; Addison, J. B. Dissociation of Cyanogen Azide: An Alternative Route to Synthesis of Carbon Nitride. *J. Phys. Chem. B* **1998**, *5647*, 6010–6019.
- [29] Bian, S.-W.; Ma, Z.; Song, W.-G. Preparation and Characterization of Carbon Nitride Nanotubes and Their Applications as Catalyst Supporter. *J. Phys. Chem. C* **2009**, *113*, 8668–8672.
- [30] Byers, J. C.; Tamiasso-Martinhon, P.; Deslouis, C.; Paillet, A.; Semenikhin, O. A. Atomic Force Microscopy Studies of Carbon Nitride (CN_x) Films Deposited on a Conducting Polymer Substrate. *J. Phys. Chem. C* **2010**, *114*, 18474–18480.
- [31] Wang, Y.; Wang, X.; Antonietti, M. Polymeric graphitic carbon nitride as a heterogeneous organocatalyst: from photochemistry to multipurpose catalysis to sustainable chemistry. *Angew. Chem. Int. Ed.* **2012**, *51*, 68–89.
- [32] Zheng, Y.; Liu, J.; Liang, J.; Jaroniec, M.; Qiao, S. Z. Graphitic carbon nitride materials: controllable synthesis and applications in fuel cells and photocatalysis. *Energy Environ. Sci.* **2012**, *5*, 6717–6731.
- [33] Liebig, J. Ueber einige Stickstoff - Verbindungen. *Liebigs Ann. Pharm.* **1834**, *10*, 1–47.
- [34] Lotsch, B. V.; Döblinger, M.; Sehnert, J.; Seyfarth, L.; Senker, J.; Oeckler, O.; Schnick, W. Unmasking melon by a complementary approach employing electron diffraction, solid-state NMR spectroscopy, and theoretical calculations-structural characterization of a carbon nitride polymer. *Chem. Eur. J.* **2007**, *13*, 4969–4980.
- [35] Seyfarth, L.; Seyfarth, J.; Lotsch, B. V.; Schnick, W.; Senker, J. Tackling the stacking disorder of melon--structure elucidation in a semicrystalline material. *Phys. Chem. Chem. Phys.* **2010**, *12*, 2227–2237.
- [36] Liu, A. Y.; Wentzcovitch, R. M. Carbon Nitride. *Phys. Rev. B* **1994**, *50*, 10362–10365.
- [37] Sung, C.-M.; Sung, M. Carbon nitride and other speculative superhard materials. *Mater. Chem. Phys.* **1996**, *43*, 1–18.
- [38] Liu, A. Y.; Cohen, M. L. Structural properties and electronic structure of low-compressibility materials; β -Si₃N₄ and hypothetical β -C₃N₄. *Phys. Rev. B* **1990**, *41*, 10727–10734.
- [39] Teter, D. M.; Hemley, R. J. Low-Compressibility Carbon Nitrides. *Science* **1996**, *271*, 53–55.

- [40] Liu, A. Y.; Cohen, M. L. Prediction of new low compressibility solids. *Science* **1989**, *245*, 841–842.
- [41] Wang, E. G. Research on carbon nitrides. *Prog. Mater. Sci.* **1997**, *41*, 241–298.
- [42] Dong, G.; Zhang, Y.; Pan, Q.; Qiu, J. A fantastic graphitic carbon nitride (g-C₃N₄) material: Electronic structure, photocatalytic and photoelectronic properties. *J. Photochem. Photobiol. C* **2014**, *20*, 33–50.
- [43] Zhu, J.; Xiao, P.; Li, H.; Carabineiro, S. A. C. Graphitic carbon nitride: synthesis, properties, and applications in catalysis. *ACS Appl. Mater. Interfaces* **2014**, *6*, 16449–16465.
- [44] Ye, S.; Wang, R.; Wu, M.-Z.; Yuan, Y.-P. A review on g-C₃N₄ for photocatalytic water splitting and CO₂ reduction. *Appl. Surf. Sci.* **2015**, *358*, 15–27.
- [45] Cao, S.; Low, J.; Yu, J.; Jaroniec, M. Polymeric photocatalysts based on graphitic carbon nitride. *Adv. Mater.* **2015**, *27*, 2150–2176.
- [46] Maeda, K.; Wang, X.; Nishihara, Y.; Lu, D.; Antonietti, M.; Domen, K. Photocatalytic activities of graphitic carbon nitride powder for water reduction and oxidation under visible light. *J. Phys. Chem. C* **2009**, *113*, 4940–4947.
- [47] Wirthner, E.; Döblinger, M.; Gunzelmann, D.; Senker, J.; Lotsch, B. V.; Schnick, W. Poly(triazine imide) with Intercalation of Lithium and Chloride Ions [(C₃N₃)₂((NH)_xLi(1-x))₃·LiCl]: A Crystalline 2D Carbon Nitride Network. *Chem. Eur. J.* **2011**, *17*, 3213–3221.
- [48] May, H. Pyrolysis of Melamine. *J. Appl. Chem.* **1959**, *9*, 340–344.
- [49] Yan, S. C.; Li, Z. S.; Zou, Z. G. Photodegradation performance of g-C₃N₄ fabricated by directly heating melamine. *Langmuir* **2009**, *25*, 10397–10401.
- [50] Thomas, A.; Fischer, A.; Goettmann, F.; Antonietti, M.; Müller, J.-O.; Schlögl, R.; Carlsson, J. M. Graphitic carbon nitride materials: variation of structure and morphology and their use as metal-free catalysts. *J. Mater. Chem.* **2008**, *18*, 4893–4908.
- [51] Semencha, A. V.; Blinov, L. N. Theoretical prerequisites, problems, and practical approaches to the preparation of carbon nitride: A Review. *Glas. Phys. Chem.* **2010**, *36*, 199–208.
- [52] Jürgens, B.; Irran, E.; Senker, J.; Kroll, P.; Müller, H.; Schnick, W. Melem (2,5,8-Triamino-tri-s-triazine), an Important Intermediate during Condensation of Melamine Rings to Graphitic Carbon Nitride: Synthesis, Structure Determination by X-ray Powder Diffractometry, Solid-State NMR, and Theoretical Studies. *J. Am. Chem. Soc.* **2003**, *125*, 10288–10300.
- [53] Kroke, E.; Schwarz, M.; Horath-Bordon, E.; Kroll, P.; Noll, B.; Norman, A. D. Tri-s-triazine derivatives. Part I. From trichloro-tri-s-triazine to graphitic C₃N₄ structures. *New J. Chem.* **2002**, *26*, 508–512.
- [54] Sehnert, J.; Baerwinkel, K.; Senker, J. Ab initio calculation of solid-state NMR spectra for different triazine and heptazine based structure proposals of g-C₃N₄. *J. Phys. Chem. B* **2007**, *111*, 10671–10680.
- [55] McMillan, P. F.; Lees, V.; Quirico, E.; Montagnac, G.; Sella, A.; Reynard, B.; Simon, P.; Bailey, E.; Deifallah, M.; Corà, F. Graphitic carbon nitride C₆N₉H₃·HCl: Characterisation by UV and near-IR FT Raman spectroscopy. *J. Solid State Chem.* **2009**, *182*, 2670–2677.
- [56] Zhang, Z.; Leinenweber, K.; Bauer, M.; Garvie, L. A. J.; McMillan, P. F.; Wolf, G. H. High-Pressure Bulk Synthesis of Crystalline C₆N₉H₃*HCl: A Novel C₃N₄ Graphitic Derivative. *J. Am. Chem. Soc.* **2001**, *123*, 7788–7796.
- [57] Ham, Y.; Maeda, K.; Cha, D.; Takanabe, K.; Domen, K. Synthesis and Photocatalytic Activity of Poly(triazine imide). *Chem. Asian J.* **2013**, *8*, 218–224.

- [58] Stegbauer, L.; Schwinghammer, K.; Lotsch, B. V. A hydrazone-based covalent organic framework for photocatalytic hydrogen production. *Chem. Sci.* **2014**, *5*, 2789–2793.
- [59] Bhunia, M. K.; Yamauchi, K.; Takanabe, K. Harvesting Solar Light with Crystalline Carbon Nitrides for Efficient Photocatalytic Hydrogen Evolution. *Angew. Chem. Int. Ed.* **2014**, *53*, 11001–11005.
- [60] Vyas, V. S.; Lotsch, B. V. Materials chemistry: Organic polymers form fuel from water. *Nature* **2015**, *521*, 41–42.
- [61] Kailasam, K.; Schmidt, J.; Bildirir, H.; Zhang, G.; Blechert, S.; Wang, X.; Thomas, A. Room temperature synthesis of heptazine-based microporous polymer networks as photocatalysts for hydrogen evolution. *Macromol. Rapid Commun.* **2013**, *34*, 1008–1013.
- [62] Ockwig, N. W.; Co, A. P.; Keeffe, M. O.; Matzger, A. J.; Yaghi, O. M. Porous, Crystalline, Covalent Organic Frameworks. *Science* **2005**, *310*, 1166–1171.
- [63] Bi, J.; Fang, W.; Li, L.; Wang, J.; Liang, S.; He, Y.; Liu, M.; Wu, L. Covalent Triazine-Based Frameworks as Visible Light Photocatalysts for the Splitting of Water. *Macromol. Rapid Commun.* **2015**, *36*, 1799–1805.
- [64] Butchosa, C.; McDonald, T. O.; Cooper, A. I.; Adams, D. J.; Zwiijnenburg, M. A. Shining a Light on s-Triazine-Based Polymers. *J. Phys. Chem. C* **2014**, *118*, 4314–4324.
- [65] Jiang, X.; Wang, P.; Zhao, J. 2D covalent triazine framework: a new class of organic photocatalyst for water splitting. *J. Mater. Chem. A* **2015**, *3*, 7750–7758.
- [66] Navarro Yerga, R. M.; Álvarez Galván, M. C.; del Valle, F.; Villoria de la Mano, J. A.; Fierro, J. L. G. Water Splitting on Semiconductor Catalysts under Visible-Light Irradiation. *ChemSusChem* **2009**, *2*, 471–485.
- [67] Maeda, K. Z - Scheme Water Splitting Using Two Different Semiconductor Photocatalysts. *ACS Catal.* **2013**, *2*, 1486–1503.
- [68] Martin, D. J.; Reardon, P. J. T.; Moniz, S. J. a; Tang, J. Visible Light-Driven Pure Water Splitting by a Nature-Inspired Organic Semiconductor-Based System. *J. Am. Chem. Soc.* **2014**, *2*–5.
- [69] Zhou, P.; Yu, J.; Jaroniec, M. All-Solid-State Z-Scheme Photocatalytic Systems. *Adv. Mater.* **2014**, *26*, 4920–4935.
- [70] Cao, S.; Yu, J. G-C₃N₄-Based Photocatalysts for Hydrogen Generation. *J. Phys. Chem. Lett.* **2014**, *5*, 2101–2107.
- [71] Wang, X.; Chen, X.; Thomas, A.; Fu, X.; Antonietti, M. Metal-Containing Carbon Nitride Compounds: A New Functional Organic-Metal Hybrid Material. *Adv. Mater.* **2009**, *21*, 1609–1612.
- [72] Yue, B.; Li, Q.; Iwai, H.; Kako, T.; Ye, J. Hydrogen production using zinc-doped carbon nitride catalyst irradiated with visible light. *Sci. Technol. Adv. Mater.* **2011**, *12*, 034401/1–7.
- [73] Wang, Y.; Di, Y.; Antonietti, M.; Li, H.; Chen, X.; Wang, X. Excellent Visible-Light Photocatalysis of Fluorinated Polymeric Carbon Nitride Solids. *Chem. Mater.* **2010**, *22*, 5119–5121.
- [74] Liu, G.; Niu, P.; Sun, C.; Smith, S. C.; Chen, Z.; Lu, G. Q.; Cheng, H. M. Unique electronic structure induced high photoreactivity of sulfur-doped graphitic C₃N₄. *J. Am. Chem. Soc.* **2010**, *132*, 11642–11648.
- [75] Lin, Z.; Wang, X. Nanostructure Engineering and Doping of Conjugated Carbon Nitride Semiconductors for Hydrogen Photosynthesis. *Angew. Chem. Int. Ed.* **2013**, *52*, 1735–1738.

- [76] Zhang, J.; Chen, X.; Takane, K.; Maeda, K.; Domen, K.; Epping, J. D.; Fu, X.; Antonietti, M.; Wang, X. Synthesis of a Carbon Nitride Structure for Visible-Light Catalysis by Copolymerization. *Angew. Chem. Int. Ed.* **2010**, *49*, 441–444.
- [77] Ho, W.; Zhang, Z.; Lin, W.; Huang, S.; Zhang, X.; Wang, X.; Huang, Y. Copolymerization with 2,4,6-Triaminopyrimidine for the Rolling-up the Layer Structure, Tunable Electronic Properties, and Photocatalysis of g-C₃N₄. *ACS Appl. Mater. Interfaces* **2015**, *7*, 5497–5505.
- [78] Zhang, J.; Zhang, G.; Chen, X.; Lin, S.; Möhlmann, L.; Dołęga, G.; Lipner, G.; Antonietti, M.; Blechert, S.; Wang, X. Co-Monomer Control of Carbon Nitride Semiconductors to Optimize Hydrogen Evolution with Visible Light. *Angew. Chem. Int. Ed.* **2012**, *51*, 3183–3187.
- [79] Yan, H.; Huang, Y. Polymer composites of carbon nitride and poly(3-hexylthiophene) to achieve enhanced hydrogen production from water under visible light. *Chem. Commun.* **2011**, *47*, 4168–4170.
- [80] Takane, K.; Kamata, K.; Wang, X.; Antonietti, M.; Kubota, J.; Domen, K. Photocatalytic hydrogen evolution on dye-sensitized mesoporous carbon nitride photocatalyst with magnesium phthalocyanine. *Phys. Chem. Chem. Phys.* **2010**, *12*, 13020–13025.
- [81] Zhang, Y.; Thomas, A.; Antonietti, M.; Wang, X. Activation of carbon nitride solids by protonation: Morphology changes, enhanced ionic conductivity, and photoconduction experiments. *J. Am. Chem. Soc.* **2009**, *131*, 50–51.
- [82] Li, Q.; Yue, B.; Iwai, H.; Kako, T.; Ye, J. Carbon nitride polymers sensitized with N-doped tantalum acid for visible light-induced photocatalytic hydrogen evolution. *J. Phys. Chem. C* **2010**, *114*, 4100–4105.
- [83] Zhang, L.; Mohamed, H. H.; Dillert, R.; Bahnemann, D. Kinetics and mechanisms of charge transfer processes in photocatalytic systems: A review. *J. Photochem. Photobiol. C* **2012**, *13*, 263–276.
- [84] Hoffmann, M. R.; Martin, S. T.; Choi, W.; Bahnemann, D. W. Environmental Applications of Semiconductor Photocatalysis. *Chem. Rev.* **1995**, *95*, 69–96.
- [85] Kang, H. W.; Lim, S. N.; Song, D.; Park, S. B. Organic-inorganic composite of g-C₃N₄-SrTiO₃:Rh photocatalyst for improved H₂ evolution under visible light irradiation. *Int. J. Hydrogen Energy* **2012**, *37*, 11602–11610.
- [86] Xiang, Q.; Yu, J.; Jaroniec, M. Preparation and Enhanced Visible-Light Photocatalytic H₂ - Production Activity of Graphene / C₃N₄ Composites. *J. Phys. Chem. C* **2011**, 7355–7363.
- [87] Zhong, J.; Li, J.; Liu, X.; Hu, W.; Song, J.; Liu, K.; Jin, T.; Ding, J. Enhanced photo-induced charge separation and sun light-driven photocatalytic performance of g-C₃N₄ modified by phosphate. *Appl. Phys. A* **2015**, *120*, 829–833.
- [88] Zhao, Z.; Sun, Y.; Dong, F. Graphitic carbon nitride based nanocomposites: a review. *Nanoscale* **2015**, *7*, 15–37.
- [89] Di, Y.; Wang, X.; Thomas, A.; Antonietti, M. Making Metal-Carbon Nitride Heterojunctions for Improved Photocatalytic Hydrogen Evolution with Visible Light. *ChemCatChem* **2010**, *2*, 834–838.
- [90] Sun, L.; Zhao, X.; Jia, C.-J.; Zhou, Y.; Cheng, X.; Li, P.; Liu, L.; Fan, W. Enhanced visible-light photocatalytic activity of g-C₃N₄-ZnWO₄ by fabricating a heterojunction: investigation based on experimental and theoretical studies. *J. Mater. Chem.* **2012**, *22*, 23428–23438.
- [91] Cao, S.-W.; Yuan, Y.-P.; Barber, J.; Loo, S. C. J.; Xue, C. Noble-metal-free g-C₃N₄/Ni(dmgh)₂ composite for efficient photocatalytic hydrogen evolution under visible light irradiation. *Appl. Surf. Sci.* **2014**, *319*, 344–349.

- [92] Xincheng Wang; Kazuhiko Maeda; Xiufang Chen; Kazuhiro Takanabe; Kazunari Domen; Yidong Hou; Xianzhi Fu; Antonietti, M. Polymer Semiconductors for Artificial Photosynthesis: Hydrogen Evolution by Mesoporous Graphitic Carbon Nitride with Visible Light. *J. Am. Chem. Soc.* **2009**, *131*, 1680–1681.
- [93] Martha, S.; Nashim, A.; Parida, K. M. Facile synthesis of highly active g-C₃N₄ for efficient hydrogen production under visible light. *J. Mater. Chem. A* **2013**, *1*, 7816–7824.
- [94] Li, X.; Hartley, G.; Ward, A. J.; Young, P. A.; Masters, A. F.; Maschmeyer, T. Hydrogenated Defects in Graphitic Carbon Nitride Nanosheets for Improved Photocatalytic Hydrogen Evolution. *J. Phys. Chem. C* **2015**, *119*, 14938–14946.
- [95] Niu, P.; Zhang, L.; Liu, G.; Cheng, H. M. Graphene-like carbon nitride nanosheets for improved photocatalytic activities. *Adv. Funct. Mater.* **2012**, *22*, 4763–4770.
- [96] Yang, S.; Gong, Y.; Zhang, J.; Zhan, L.; Ma, L.; Fang, Z.; Vajtai, R.; Wang, X.; Ajayan, P. M. Exfoliated Graphitic Carbon Nitride Nanosheets as Efficient Catalysts for Hydrogen Evolution Under Visible Light. *Adv. Mater.* **2013**, *25*, 2452–2456.
- [97] Ma, L.; Fan, H.; Li, M.; Tian, H.; Fang, J.; Dong, G. A simple melamine-assisted exfoliation of polymeric graphitic carbon nitrides for highly efficient hydrogen production from water under visible light. *J. Mater. Chem. A* **2015**, *3*, 22404–22412.
- [98] Tong, J.; Zhang, L.; Li, F.; Li, M.; Cao, S. An efficient top-down approach for the fabrication of large-aspect-ratio g-C₃N₄ nanosheets with enhanced photocatalytic activities. *Phys. Chem. Chem. Phys.* **2015**, *17*, 23532–23537.
- [99] Tong, J.; Zhang, L.; Li, F.; Wang, K.; Han, L.; Cao, S. Rapid and high-yield production of g-C₃N₄ nanosheets via chemical exfoliation for photocatalytic H₂ evolution. *RSC Adv.* **2015**, *5*, 88149–88153.
- [100] Dong, X.; Cheng, F. Recent development in exfoliated two-dimensional g-C₃N₄ nanosheets for photocatalytic applications. *J. Mater. Chem. A* **2015**, *3*, 23642–23652.
- [101] Zhang, J.; Chen, Y.; Wang, X. Two-dimensional covalent carbon nitride nanosheets: synthesis, functionalization, and applications. *Energy Environ. Sci.* **2015**, *8*, 3092–3108.
- [102] Li, H.-J.; Qian, D.-J.; Chen, M. Templateless Infrared Heating Process for Fabricating Carbon Nitride Nanorods with Efficient Photocatalytic H₂ Evolution. *ACS Appl. Mater. Interfaces* **2015**, *7*, 25162–25170.
- [103] Chen, X.; Jun, Y.-S.; Takanabe, K.; Maeda, K.; Domen, K.; Fu, X.; Antonietti, M.; Wang, X. Ordered Mesoporous SBA-15 Type Graphitic Carbon Nitride: A Semiconductor Host Structure for Photocatalytic Hydrogen Evolution with Visible Light. *Chem. Mater.* **2009**, *21*, 4093–4095.
- [104] Cui, Y.; Zhang, J.; Zhang, G.; Huang, J.; Liu, P.; Antonietti, M.; Wang, X. Synthesis of bulk and nanoporous carbon nitride polymers from ammonium thiocyanate for photocatalytic hydrogen evolution. *J. Mater. Chem.* **2011**, *21*, 13032–13039.
- [105] Harris, K. D.; Cheung, E. Y. How to determine structures when single crystals cannot be grown: opportunities for structure determination of molecular materials using powder diffraction data. *Chem. Soc. Rev.* **2004**, *33*, 526–538.
- [106] *NMR Crystallography*; Harris, R. K., Wasylishen, R. E., Duer, M. J., Eds.; John Wiley & Sons Ltd, Chichester, UK, 2009.
- [107] Brouwer, D. H.; Darton, R. J.; Morris, R. E.; Levitt, M. H. A solid-state NMR method for solution of zeolite crystal structures. *J. Am. Chem. Soc.* **2005**, *127*, 10365–10370.
- [108] Brouwer, D. H. Structure solution of network materials by solid-state NMR without knowledge of the crystallographic space group. *Solid State Nucl. Magn. Reson.* **2013**, *51-52*, 37–45.

- [109] Harris, R. K. NMR studies of organic polymorphs & solvates. *Analyst* **2006**, *131*, 351–373.
- [110] Ripmeester, J. A.; Wasylishen, R. E. NMR crystallography. *CrystEngComm* **2013**, No. 15, 8598.
- [111] Seyfarth, L. Dissertation, NMR Kristallographie in der Strukturaufklärung von mikro- und semikristallinen Materialien: Entwicklung und Anwendung, 2008.
- [112] Lotsch, B. V.; Schnick, W. From Triazines to Heptazines: Novel Nonmetal Tricyanomelaminates as Precursors for Graphitic Carbon Nitride Materials. *Chem. Mater.* **2006**, *18*, 1891–1900.
- [113] Alves, I.; Demazeau, G.; Tanguy, B.; Weill, F. On a new model of the graphitic form of C₃N₄. *Solid State Commun.* **1999**, *109*, 697–701.
- [114] Mattesini, M.; Matar, S. F.; Etourneau, J. Stability and electronic property investigations of the graphitic C₃N₄ system showing an orthorhombic unit cell. *J. Mater. Chem.* **2000**, *10*, 709–713.
- [115] Komatsu, T.; Nakamura, T. Polycondensation/pyrolysis of tris-s-triazine derivatives leading to graphite-like carbon nitrides. *J. Mater. Chem.* **2001**, *11*, 474–478.
- [116] Komatsu, T. Prototype carbon nitrides similar to the symmetric triangular form of melon. *J. Mater. Chem.* **2001**, *11*, 802–805.
- [117] Komatsu, T. The first synthesis and characterization of cyameluric high polymers. *Macromol. Chem. Phys.* **2001**, *202*, 19–25.
- [118] Pauling, L.; Sturdivant, J. The Structure of Cyameluric Acid, Hydromelonic Acid and Related Substances. *Proc. Natl. Acad. Sci. U. S. A.* **1937**, *23*, 616–620.
- [119] Hosmane, R. S.; Rossman, M. A.; Leonard, N. J. Synthesis and structure of tri-s-triazine. *J. Am. Chem. Soc.* **1982**, *104*, 5497–5499.
- [120] Shahbaz, M.; Urano, S.; LeBreton, P. R.; Rossman, M. A.; Hosmane, R. S.; Leonard, N. J. Tri-s-triazine: synthesis, chemical behavior, and spectroscopic and theoretical probes of valence orbital structure. *J. Am. Chem. Soc.* **1984**, *106*, 2805–2811.
- [121] Bojdys, M. J.; Müller, J.-O.; Antonietti, M.; Thomas, A. Ionothermal synthesis of crystalline, condensed, graphitic carbon nitride. *Chem. Eur. J.* **2008**, *14*, 8177–8182.
- [122] Tossell, J. A. Second-Nearest-Neighbor Effects upon N NMR Shieldings in Models for Solid Si₃N₄ and C₃N₄. *J. Magn. Reson.* **1997**, *53*, 49–53.
- [123] Yoon, Y.-G.; Pfrommer, B. G.; Mauri, F.; Louie, S. G. NMR Chemical Shifts in Hard Carbon Nitride Compounds. *Phys. Rev. Lett.* **1998**, *80*, 3388–3391.
- [124] Sattler, A.; Schnick, W. Zur Kenntnis der Kristallstruktur von Melem C₆N₇(NH₂)₃. *Zeitschrift für Anorg. und Allg. Chemie* **2006**, *632*, 238–242.
- [125] Seyfarth, L.; Senker, J. An NMR crystallographic approach for the determination of the hydrogen substructure of nitrogen bonded protons. *Phys. Chem. Chem. Phys.* **2009**, *11*, 3522–3531.
- [126] El-Gamel, N. E. A.; Seyfarth, L.; Wagler, J.; Ehrenberg, H.; Schwarz, M.; Senker, J.; Kroke, E. The tautomeric forms of cyameluric acid derivatives. *Chem. Eur. J.* **2007**, *13*, 1158–1173.
- [127] Seyfarth, L.; Sehnert, J.; El-Gamel, N. E. A.; Milius, W.; Kroke, E.; Brey, J.; Senker, J. Structure elucidation of cyameluric acid by combining solid-state NMR spectroscopy, molecular modeling and direct-space methods. *J. Mol. Struct.* **2008**, *889*, 217–228.
- [128] Tragl, S.; Gibson, K.; Glaser, J.; Duppel, V.; Simon, A.; Meyer, H. J. Template assisted formation of micro- and nanotubular carbon nitride materials. *Solid State Commun.* **2007**, *141*, 529–534.

- [129] Holst, J. R.; Gillan, E. G. From triazines to heptazines: Deciphering the local structure of amorphous nitrogen-rich carbon nitride materials. *J. Am. Chem. Soc.* **2008**, *130*, 7373–7379.
- [130] Fina, F.; Callear, S. K.; Carins, G. M.; Irvine, J. T. S. Structural Investigation of Graphitic Carbon Nitride via XRD and Neutron Diffraction. *Chem. Mater.* **2015**, *27*, 2612–2618.
- [131] Döblinger, M.; Lotsch, B. V.; Wack, J.; Thun, J.; Senker, J.; Schnick, W. Structure elucidation of polyheptazine imide by electron diffraction - A templated 2D carbon nitride network. *Chem. Commun.* **2009**, No. 12, 1541–1543.
- [132] Kuhn, P.; Antonietti, M.; Thomas, A. Porous, Covalent Triazine-Based Frameworks Prepared by Ionothermal Synthesis. *Angew. Chem. Int. Ed.* **2008**, *47*, 3450–3453.
- [133] Kuhn, P.; Forget, A.; Su, D.; Thomas, A.; Antonietti, M. From microporous regular frameworks to mesoporous materials with ultrahigh surface area: Dynamic reorganization of porous polymer networks. *J. Am. Chem. Soc.* **2008**, *130*, 13333–13337.
- [134] Kuhn, P.; Thomas, A.; Antonietti, M. Toward tailorable porous organic polymer networks: A high-temperature dynamic polymerization scheme based on aromatic nitriles. *Macromolecules* **2009**, *42*, 319–326.
- [135] Ren, S.; Dawson, R.; Laybourn, A.; Jiang, J.; Khimiyak, Y.; Adams, D. J.; Cooper, A. I. Functional conjugated microporous polymers: from 1,3,5-benzene to 1,3,5-triazine. *Polym. Chem.* **2012**, *3*, 928–934.
- [136] Ren, S.; Bojdys, M. J.; Dawson, R.; Laybourn, A.; Khimiyak, Y. Z.; Adams, D. J.; Cooper, A. I. Porous, fluorescent, covalent triazine-based frameworks via room-temperature and microwave-assisted synthesis. *Adv. Mater.* **2012**, *24*, 2357–2361.
- [137] Katekomol, P.; Roeser, J.; Bojdys, M.; Weber, J.; Thomas, A. Covalent triazine frameworks prepared from 1,3,5-tricyanobenzene. *Chem. Mater.* **2013**, *25*, 1542–1548.
- [138] Bojdys, M. J.; Wohlgemuth, S. A.; Thomas, A.; Antonietti, M. Ionothermal Route to Layered Two-Dimensional Polymer-Frameworks Based on Heptazine Linkers. *Macromolecules* **2010**, *43*, 6639–6645.
- [139] McDermott, E. J.; Wirnhier, E.; Schnick, W.; Viridi, K. S.; Scheu, C.; Kauffmann, Y.; Kaplan, W. D.; Kurmaev, E. Z.; Moewes, A. Band Gap Tuning in Poly(triazine imide), a Nonmetallic Photocatalyst. *J. Phys. Chem. C* **2013**, *117*, 8806–8812.

5 Darstellung des Eigenanteils

1. Phenyl-Triazine Oligomers for Light-Driven Hydrogen Evolution

Schwinghammer, K.; Hug, S.; Mesch, M. B.; Senker, J.; Lotsch, B. V. *Energy Environ. Sci.* **2015**, *8*, 3345.

K. Schwinghammer und Dr. S Hug sind gleichberechtigte Autoren dieser Publikation. Sie haben unter der Betreuung von Prof. B. V. Lotsch das Konzept der Publikation erarbeitet und Literaturrecherche, Synthese und Photokatalyse und den Großteil der Charakterisierung durchgeführt. Das Konzept für die NMR-Charakterisierung wurde von mir unter der Betreuung von Prof. J. Senker erarbeitet. Alle ^{15}N NMR- und direkten ^{13}C NMR-Messungen habe ich durchgeführt und ausgewertet. ^{13}C CP Messungen wurden teilweise von C. Minke und teilweise von mir gemessen.

Die Publikation wurde weitestgehend von K. Schwinghammer, Dr. S Hug und Prof. B. V. Lotsch verfasst. Der NMR-Teil verfasste ich in Zusammenarbeit mit Prof. J. Senker. Alle Autoren haben bei der Überarbeitung des Manuskripts mitgewirkt.

Diese Publikation ist auch Teil der Doktorarbeiten von K. Schwinghammer und Dr. S. Hug.

Mein Eigenanteil beläuft sich auf circa 20%.

2. Low-Molecular-Weight Carbon Nitrides for Solar Hydrogen Evolution

Lau, V. W.; Mesch, M. B.; Duppel, V.; Blum, V.; Senker, J.; Lotsch, B. V. *J. Am. Chem. Soc.* **2015**, *137*, 1064.

Das Konzept der Publikation wurde von Dr. V. W. Lau und Prof. B. V. Lotsch erarbeitet. Dr. V. W. Lau führte die Synthesen durch und charakterisierte die Substanzen mit Unterstützung von V. Duppel (TEM). Die Strukturaufklärung mittels NMR wurde von mir unter Betreuung von Prof. J. Senker erarbeitet. Die Messungen führte ich durch und wertete sie aus. Die HOMO/LUMO Orbitale wurden von Prof. V. Blum berechnet.

Den NMR-Teil verfasste ich in Zusammenarbeit mit Prof. J. Senker. Die Berechnung der HOMO/LUMO Orbitale wurde von Prof. V. Blum beschrieben. Die restliche Publikation wurde überwiegend von Dr. V. W. Lau und Prof. B.V. Lotsch verfasst und von mir und Prof. J. Senker mit überarbeitet.

Mein Eigenanteil beläuft sich auf circa 25%.

3. Donor-Acceptor Type Heptazine-Based Polymer Networks for Photocatalytic Hydrogen Evolution

Kailasam, K.; Mesch, M. B.; Möhlmann, L.; Baar, M.; Blechert, S.; Schwarze, M.; Schörder, M.; Schomäcker, R.; Senker, J.; Thomas, A. *Energy Technol.* **2016** DOI: 10.1002/ente.201500478

Das Konzept der Publikation wurde am Lehrstuhl von Prof. A. Thomas erarbeitet. Prof. K. Kailasam synthetisierte und charakterisierte die Polymere. Alle NMR-Messungen führte ich unter Betreuung von Prof. J. Senker durch und wertete sie aus. Dabei wurde das Konzept der Auswertung von mir entwickelt. Dr. L. Möhlmann und M. Baar synthetisierten am Lehrstuhl von Prof. S. Blechert die Ausgangsverbindungen. Dr. M. Schwarze und M. Schröder führten am Lehrstuhl von Prof. R. Schomäcker die photokatalytischen Messungen durch.

Die Publikation verfasste überwiegend Prof. K. Kailasam, während ich und Prof. J. Senker sie überarbeiteten. Der vollständige NMR-spektroskopische Teil wurde von mir in Zusammenarbeit mit Prof. J. Senker verfasst.

Diese Publikation ist auch Teil der Doktorarbeit von Dr. M. Baar.

Mein Eigenanteil beläuft sich auf circa 35 %.

4. Triazine-based Carbon Nitrides for Visible-Light-Driven Hydrogen Evolution

Schwinghammer, K.; Tuffy, B.; Mesch, M. B.; Wirnhier, E.; Martineau, C.; Taulelle, F.; Schnick, W.; Senker, J.; Lotsch, B. V. *Angew. Chem. Int. Ed.* **2013**, 52 (9), 2435.

Das Konzept der Veröffentlichung wurde am Lehrstuhl von Prof. B. V. Lotsch erarbeitet. Die Substanz und Synthese basiert auf der Publikation von Dr. E. Zeuner (geb. Wirnhier) und Prof. W. Schnick. Die Synthesen dieser Publikation führten K. Schwinghammer und B. Tuffy durch. Die Auswahl der erforderlichen NMR-spektroskopischen Untersuchungen erfolgte von mir in Zusammenarbeit mit Dr. C. Martineau und Prof. J. Senker. Die Messungen wurden von mir in Frankreich in der Arbeitsgruppe von Prof. F. Taulelle durchgeführt. Die weitere Charakterisierung und die Untersuchung der photokatalytischen Aktivität führte K. Schwinghammer durch.

Die Publikation wurde größtenteils von K. Schwinghammer in Zusammenarbeit mit Prof. B. V. Lotsch verfasst. Mein Hauptbeitrag besteht aus dem NMR-spektroskopischen Teil, der von mir und Prof. J. Senker geschrieben wurde.

Diese Publikation ist auch Teil der Doktorarbeiten von K. Schwinghammer, B. Tuffy und Dr. E. Zeuner (geb. Wirnhier).

Mein Eigenanteil beläuft sich auf circa 30%.

5. Crystalline Carbon Nitride Nanosheets for Improved Visible-Light Hydrogen Evolution

Schwinghammer, K.; Mesch, M. B.; Duppel, V.; Ziegler, C.; Senker, J.; Lotsch, B. V. *J. Am. Chem. Soc.* **2014**, *136* (5), 1730.

Das Konzept der Publikation wurde am Lehrstuhl von Prof. B. V. Lotsch erarbeitet. Die Synthesen und photokatalytischen Versuche führte K. Schwinghammer durch. Die NMR-Charakterisierung erfolgte von mir. Die Experimente und Analysemethoden, sowie die Berechnung der Wassermonolagen wurden von mir in Zusammenarbeit mit Prof. J. Senker erarbeitet. Die weitere Charakterisierung erfolgte von K. Schwinghammer in Zusammenarbeit mit V. Duppel (TEM) und C. Ziegler (AFM).

Die Publikation verfassten hauptsächlich K. Schwinghammer und Prof. B. V. Lotsch, wobei der NMR-spektroskopische Teil von mir und Prof. J. Senker ergänzt wurde. Anschließend überarbeiteten alle Autoren die Publikation.

Diese Publikation ist auch Teil der Doktorarbeit von K. Schwinghammer.

Mein Eigenanteil beläuft sich auf circa 35%.

6. Solving the Hydrogen and Lithium Substructure of Poly (Triazine Imide)/LiCl Using NMR Crystallography

Mesch, M. B.; Bärwinkel, K.; Krysiak, Y.; Martineau, C.; Taulelle, F.; Neder, R.; Kolb, U.; Senker, J. *to be submitted to Chem. Eur. J.*

Dieses Projekt wurde in einer lehrstuhlinternen Kooperation durchgeführt. Dabei war ich für alle NMR-spektroskopischen Aspekte und K. Bärwinkel für die quantenmechanischen Rechnungen zuständig. Das Konzept der Publikation wurde von K. Bärwinkel und mir in Zusammenarbeit mit Prof. J. Senker erarbeitet. Alle NMR-Messungen führte ich durch. Das ^1H - ^{15}N 2D Spektrum und die ^1H - ^1H Doppelquanten-Singlequanten Spektren habe ich unter Betreuung von Dr. C. Martineau am Lehrstuhl von Prof. F. Taulelle gemessen. Die Geometrieoptimierungen, sowie Energie- und Shiftrechnungen wurden von K. Bärwinkel durchgeführt. Die Simulationen der Abstandsmessungen erfolgten ebenso wie alle weiteren Auswertungen, Interpretationen und die Darstellung der Daten in Zusammenarbeit. Y. Krysiak, betreut von Prof. U. Kolb, führte die Elektronendiffraktionsexperimente durch und wertete sie aus. Die Analyse der Paarverteilungsfunktion wurde von Prof. R. Neder durchgeführt.

Die Publikation wurde von mir verfasst und von K. Bärwinkel und Prof. J. Senker ergänzt und korrigiert. Y. Krysiak ergänzte zusammen mit Prof. U. Kolb den Abschnitt über Diffraction.

Diese Publikation ist auch Teil der Doktorarbeiten von K. Bärwinkel und Y. Krysiak.

Mein Eigenanteil beläuft sich auf circa 50%.

6 Ergebnisse

6.1 Bestimmung der Länge von Phenyl-Triazin-Oligomeren mittels 1D-Spektren

Phenyl-Triazine Oligomers for Light-Driven Hydrogen Evolution

K. Schwinghammer,^{†,||} S. Hug,^{†,||} M. B. Mesch,[‡] J. Senker,[‡] B. V. Lotsch^{*,†}

Erschienen in:

Energy & Environmental Science 2015, 8, 3345

Abdruck mit Genehmigung, Copyright (2013) The Royal Society of Chemistry

[†] Max Planck Institute for Solid State Research, Heisenbergstr. 1, 70569 Stuttgart, Germany
Department of Chemistry, University of Munich, LMU, Butenandtstr. 5-13, 81377 Munich, Germany

Nanosystems Initiative Munich (NIM) and Center for Nanoscience, Schellingstr. 4, 80799 Munich, Germany

[‡] Department of Inorganic Chemistry III, University of Bayreuth, Universitätsstr. 30, 95447 Bayreuth, Germany

^{||} These authors contributed equally.

^{*} B.Lotsch@fkf.mpg.de

6.1.1 Phenyl-Triazine Oligomers for Light-Driven Hydrogen Evolution

Energy &
Environmental
Science

PAPER

View Article Online
View Journal | View IssueCite this: *Energy Environ. Sci.*,
2015, 8, 3345Phenyl-triazine oligomers for light-driven
hydrogen evolution†K. Schwinghammer,^{‡,abc} S. Hug,^{‡,abc} M. B. Mesch,^d J. Senker^d and B. V. Lotsch^{*abc}

The design of stable, yet highly tunable organic photocatalysts which orchestrate multi-step electron transfer reactions is at the heart of the newly emerging field of polymer photocatalysis. Covalent triazine frameworks such as the archetypal CTF-1 have been theorized to constitute a new class of photocatalytically active polymers for light-driven water splitting. Here, we revisit the ionothermal synthesis of CTF-1 by trimerization of 1,4-dicyanobenzene catalyzed by the Lewis acid zinc chloride and demonstrate that the microporous black polymer CTF-1 is essentially inactive for hydrogen evolution. Instead, highly photoactive phenyl-triazine oligomers (PTOs) with higher crystallinity as compared to CTF-1 are obtained by lowering the reaction temperature to 300 °C and prolonging the reaction time to >150 hours. The low reaction temperature of the PTOs largely prevents incipient carbonization and thus results in a carbon-to-nitrogen weight ratio close to the theoretical value of 3.43. The oligomers were characterized by MALDI-TOF and quantitative solid-state NMR spectroscopy, revealing variations in size, connectivity and thus nitrile-to-triazine ratios depending on the initial precursor dilution. The most active PTO samples efficiently and stably reduce water to hydrogen with an average rate of 1076 (± 278) $\mu\text{mol h}^{-1} \text{g}^{-1}$ under simulated sunlight illumination, which is competitive with the best carbon nitrile-based and purely organic photocatalysts. The photocatalytic activity of the PTOs is found to sensitively depend on the polymerization degree, thus suggesting a prominent role of the unreacted nitrile moieties in the photocatalytic process. Notably, PTOs even show moderate hydrogen production without the addition of any co-catalyst.

Received 19th August 2015,
Accepted 7th September 2015

DOI: 10.1039/c5ee02574e

www.rsc.org/ees

Broader context

The increasing demand of renewable energy resources, such as hydrogen generated by photocatalytic water reduction, necessitates the exploration of efficient, stable, non-toxic and abundant photocatalysts. While organic photocatalysts fulfil these requirements, rational catalyst design remains challenging both experimentally and computationally due to the scarcity of structure–property–activity insights, particularly in disordered polymeric systems. This case in point is illustrated by the archetypal covalent triazine framework CTF-1, which was computationally predicted to satisfy the (thermodynamic) criteria for exhibiting activity for photocatalytic hydrogen evolution, but shown to be nearly inactive here. We demonstrate further that triazine-based oligomers populated with terminal nitrile groups, rather than the extended framework, are highly active photocatalysts for the hydrogen evolution reaction. The nitrile groups likely act as solubilizing agents and conduits for charge transfer between the oligomer, co-catalyst and reactants, which puts the role of functional groups embedded in the carbon nitrile backbone in the spotlight. This work thus illustrates the potential of well-defined oligomeric systems as a new generation of metal-free photocatalysts and provides a guideline for the rational design of novel organic photocatalysts by molecular engineering.

^a Max Planck Institute for Solid State Research, Heisenbergstr. 1, 70569 Stuttgart, Germany. E-mail: b.lotsch@fkf.mpg.de

^b Department of Chemistry, University of Munich, LMU, Butenandstr. 5-13, 81377 Munich, Germany

^c Nanosystems Initiative Munich and Center of Nanoscience, Schellingstr. 4, 80799 Munich, Germany

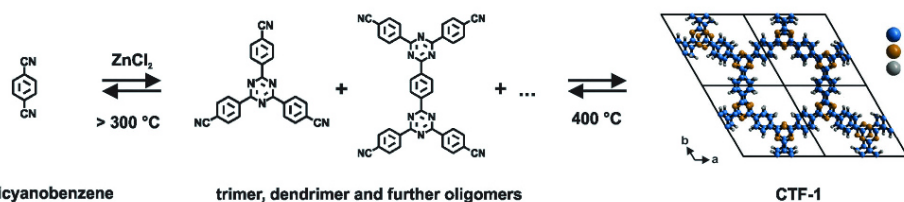
^d Inorganic Chemistry III, University of Bayreuth, Universitätsstr. 30, 95447 Bayreuth, Germany

† Electronic supplementary information (ESI) available: Experimental details (methods and syntheses), characterization data of the organic phase of PTO and further XRD, XPS, NMR, TEM, BET, MALDI-TOF, IR, ICP, EDX and photocatalytic measurements as well as elemental analyses. See DOI: 10.1039/c5ee02574e

‡ These authors contributed equally.

Introduction

The direct conversion of solar energy to chemical energy, exemplified by light-induced water splitting into hydrogen and oxygen, enables the sustainable generation of storable chemical fuels and is hence a green energy cycle.¹ However, the development of a cost-effective process for the generation of hydrogen from water has yet to be developed.¹ Since the discovery of water splitting on an n-type semiconducting TiO₂ electrode by Fujishima and Honda in 1972,² research largely focused on inorganic semiconductors that often entail costly and environmentally critical



Scheme 1 Reaction mechanism of CTF-1 starting from 1,4-dicyanobenzene, which leads to the formation of oligomers via trimerization and, ultimately, to an extended 2D CTF (right). The idealized crystal structure of fully condensed, crystalline CTF-1 is shown in an AA-type eclipsed configuration (viewed along the *c*-direction).

fabrication steps.³ The development of carbon-based photocatalysts has become an active research field, which has produced the first promising examples of polymers,⁴ graphite oxide,⁵ carbon nitrides^{6–8} and COFs⁹ as predominantly carbon-based photocatalysts. In particular, the incorporation of triazine units into polymeric systems has been shown to correlate with efficient hydrogen evolution as the triazine nitrogen, with its free electron pair and electron poor character, may act as the active site.^{6,7,9–12} An example of such a triazine system is the covalent triazine framework CTF-1 (see Scheme 1) which was first synthesized in 2008 by Kuhn *et al.*¹³ CTF-1 is built from alternating triazine and phenyl building blocks forming a 12-membered hexagonal ring system, resulting in layers which are stacked in a close-to-eclipsed AA-type fashion.¹³ The black colored and highly porous product is obtained from 1,4-dicyanobenzene by a trimerization reaction under inert ionothermal conditions at 400 °C for 40 hours.¹³ However, incipient carbonization occurs due to the elevated reaction temperature, as evidenced by the larger carbon content and the dark color of the product.¹³ In 2012, Ren *et al.*¹⁴ achieved the synthesis of yellow colored and thus largely carbon-free, but non-porous CTF-1 through a super acid-catalyzed (microwave-assisted) synthesis.

Such colored compounds may be capable of light-induced hydrogen evolution drawing on recent experimental and theoretical results delineating the structural and photophysical properties of CTF-1-type materials.^{14,15} Moreover, based on first principles calculations, Zhao and co-workers¹⁶ predicted that certain CTFs including CTF-1 should be promising visible-light photocatalysts according to the suitable band gap of CTF-1 (2.42 eV) and the position of its band potentials which are dependent on the nitrogen content of the CTFs, the number of ring systems, and the extent of π - π interactions.

Here, we revisit the synthesis of CTF-1 and demonstrate that conditions circumventing the formation of amorphous carbon invariably yield low molecular weight triazine-based compounds, henceforth referred to as phenyl-triazine oligomers (PTO), with intriguing optical and electronic properties. These oligomers are studied with respect to their photocatalytic activity for hydrogen evolution and compared to the archetypal CTF-1 and the related molecular model system 2,4,6-tris(*p*-cyanophenyl)-1,3,5-triazine, henceforth referred to as “the trimer”.

In contrast to black CTF-1 which shows negligible catalytic activity, the most active PTO samples exhibit an average, but non-optimized

hydrogen evolution rate of $1076 (\pm 278) \mu\text{mol h}^{-1} \text{g}^{-1}$. Thus, PTOs are competitive with the commonly used Melon ($\text{g-C}_3\text{N}_4$) and other purely organic photocatalysts^{6–11,17–19} with regards to hydrogen evolution under simulated sunlight, and long-term stability. Notably, PTOs are even active without the addition of any co-catalyst.¹⁹ Their high activity and potential to act in a Pt-free environment ($121 \mu\text{mol h}^{-1} \text{g}^{-1}$) renders triazine-based photocatalysts and PTOs in particular promising candidates for truly abundant photocatalysts.

Results and discussion

CTF-1 synthesized according to literature protocols was tested for hydrogen evolution under simulated sunlight (for experimental details see below and Table S8, ESI†) but was found to show very low activity. We rationalize the low activity of CTF-1 with the large carbon content in the sample, as the synthesis of CTF-1 seems to be a delicate balance between incomplete polymerization resulting mostly in oligomers, and the competitive formation and degradation of the framework yielding amorphous carbon at elevated temperatures. At the originally applied synthesis temperature of 400 °C, a large amount of carbon is formed, which may well hinder light penetration to the photocatalyst.¹³

In addition, the thermodynamic driving force for electron transfer in the extended system may be too low to support efficient hydrogen evolution.

Synthesis

We therefore attempted to synthesize non-carbonized CTF-1. While the synthesis of yellow colored CTF-1 according to Ren *et al.*¹⁴ requires water-free conditions, we modified the original ionothermal approach,¹³ thereby obtaining PTOs rather than the extended CTF-1 polymer. The syntheses of the PTOs were carried out in a fashion analogous to the original ionothermal synthesis using zinc chloride melts, as established by Antonietti and co-workers.¹³ As already stated in that work, syntheses at temperatures below 350 °C yielded mainly soluble products after two days of reaction time. Due to the slow reaction kinetics at 350 °C we prolonged the reaction times to increase the conversion, in accordance with van't Hoff's law.²⁰ Indeed, reaction times

Table 1 Synthesis conditions used for the PTOs and the reference material CTF-1

Sample	Eq. ZnCl ₂	Synthesis temperature/°C	Synthesis time ^a /h
PTO-300-1	1	300	168
PTO-300-2.5	2.5	300	168
PTO-300-5	5	300	168
PTO-300-10	10	300	168
PTO-300-15	15	300	168
PTO-350-1	1	350	96
PTO-350-10	10	350	96
CTF-1 ^b	1	400	48

^a Heating at a rate of 60 °C h⁻¹ and cooling at 10 °C h⁻¹. ^b Synthesized according to Kuhn *et al.*¹³

of 96 h for syntheses at 350 °C and of 168 h at 300 °C led to oligomeric products which were insoluble in organic solvents (THF, acetone, ethanol, chloroform and dichloromethane), water and hot 1 M HCl. During the organic washing procedure (and later on by Soxhlet extraction) with THF, smaller oligomers and unreacted starting material were washed off (organic phase of PTO, see Fig. S3 and S4, ESI†). The detailed synthesis conditions are shown in Table 1. The products are identified by adding to the prefix PTO first the synthesis temperature and then the equivalents of zinc chloride with respect to 1,4-dicyanobenzene used in the synthesis.

Characterization

First, we analyzed the crystallinity of the as-obtained materials by powder XRD measurements and compared the results with CTF-1 (Fig. 1a and c). The diffraction patterns of PTO-350-1 and the as-prepared CTF-1 sample are largely reminiscent of CTF-1,¹³ albeit with less intense reflections. At the lower reaction temperature of 300 °C and prolonged reaction time, materials with

higher crystallinity are obtained which differ from the reference and cannot simply be assigned to the precursors. While PTO-300-1 still shows similarities to the framework due to the presence of the prominent 100 reflection, the samples synthesized with a larger amount of ZnCl₂ (*e.g.* PTO-300-15) display diffraction patterns completely different from CTF-1, yet faintly resembling the trimer. We believe that the powder diffraction patterns of the PTO samples differ from the one of CTF-1 due to the formation of oligomers. These oligomers exhibit a decreased layer distance compared to CTF-1 (Table S1, ESI†). Furthermore, it seems that the oligomers formed at a one-to-one precursor to ZnCl₂ ratio (PTO-300-1) differ from the ones synthesized in an excess of zinc chloride (>1 equivalent).

We used IR spectroscopy as a tool to survey the progress of the trimerization reaction based on the characteristic IR signals of the nitrile groups of the starting material, which are expected to form triazine rings. The IR spectra are depicted in Fig. 1b and d. The materials synthesized between 300–350 °C show the same prominent bands as CTF-1 and the trimer. The characteristic bands for the triazine unit are found at 1506 cm⁻¹ (C–N stretching mode)^{21,22} and 1355 cm⁻¹ (in-plane ring stretching vibrations),^{23,24} confirming the successful formation of triazine rings under these synthesis conditions. The lower temperature clearly leads to incomplete polymerization as indicated by the additional signal at 2227 cm⁻¹ representing unreacted nitrile groups in the sample.

To further confirm the formation of CTF-1-like materials, we conducted elemental analysis (Table S2, ESI†). The elemental analysis (EA) data of the as-synthesized PTOs synthesized at 300 °C reveal values very close to the theoretical ones for CTF-1 and the ones reported by Ren *et al.*¹⁴ for yellow colored CTF-1. The results are in sharp contrast to the materials synthesized above 300 °C and the ones found by Antonietti and co-workers¹³ where a higher carbon content (and C/N ratio) is observed due to partial carbonization of the products.¹³ An incipient carbonization can also be detected for the materials synthesized in an excess of zinc chloride (PTO-300-15). No statement on the extent of trimerization of the PTOs and thus the amount of unreacted nitrile groups can be made based on EA because the precursor of the synthesis (1,4-dicyanobenzene) has the same elemental composition and, hence, C/N ratio as one formula unit of CTF-1 or any intermediate oligomer.

To gain more insights into the local chemical environment in the different materials, XPS measurements were conducted (Fig. S5 and S6, ESI†). The nitrogen environments of the low temperature products (PTO-300-1 and 15) are in agreement with the as-synthesized CTF-1 sample showing a dominant N 1s peak at around 398.9 eV. According to the literature,^{25,26} this as well as the weak signal at 400.3 eV observed for CTF-1 can be assigned to nitrogen atoms within the triazine units (C–N=C) as well as terminal nitrile groups. More likely, however, the signal at 400.3 eV arises from pyrrolic nitrogen containing decomposition products since this signal is more prominent in the CTF-1 sample. The C 1s XPS measurements of the three samples reveal two peaks. The first signal at 284.6 eV is attributed to the carbon atoms of the phenyl rings as well as adventitious carbon (C–C)

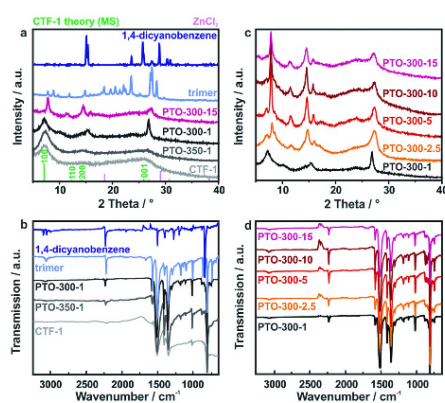


Fig. 1 (a) PXRD patterns and (b) IR spectra of the PTOs: PTO-350-1, PTO-300-1 and PTO-300-15 in comparison to the as-synthesized CTF-1, the trimer and 1,4-dicyanobenzene. The diffraction patterns of ZnCl₂ and the simulated pattern of CTF-1¹³ are added for clarity. (c) PXRD patterns and (d) IR spectra of the PTOs synthesized at 300 °C with different amounts of ZnCl₂.

which is used for calibration.²⁷ The second one appearing at around 286.8 eV for CTF-1 and PTO-300-1 and at 286.3 eV for PTO-300-15 is assigned to the carbon atoms in the triazine (N=C-N) and nitrile moieties (C≡N).²⁸ The C-C carbon signal of CTF-1 is more dominant in comparison to the triazine/nitrile peak due to a higher amorphous carbon content which was already verified by elemental analysis. For the different samples, no obvious shifts of the binding energy of C 1s and N 1s core electrons are observable, suggesting that the chemical states of both carbon and nitrogen atoms in the PTOs are the same as in the more highly condensed CTF-1 sample.

The results obtained by IR and XPS were further supported by ¹³C and ¹⁵N solid-state (ss) NMR spectroscopy. The ¹³C CP MAS ssNMR spectra of PTO-300-1, PTO-300-10 as well as CTF-1 (Fig. 2, left) show strong signals at 169, 138, 130 and 115 ppm. The signal at 169 ppm is assigned to triazine ring carbon atoms,²⁹ while the signals at 138 and 130 ppm correspond to the phenyl ring. The signal at 115 ppm is characteristic for nitrile groups as well as the carbon of the phenyl ring to which the nitrile groups are bound. Although it is significantly weaker in CTF-1 it indicates residual nitrile groups in all materials. The ¹⁵N CP MAS ssNMR spectra of all samples (Fig. 2, right) show only one signal at around -125 ppm. From the chemical shift alone it is not possible to distinguish between the triazine unit and terminal nitrile groups, as their signals appear in the same region.^{30,31} Note that in PTO-300-10 the carbon peaks at 130 and 115 ppm as well as the nitrogen peak show a fine structure,

indicating better crystallinity. This is also supported by the XRD measurements shown above. To summarize, the results from IR and ssNMR spectroscopy strongly suggest the successful formation of triazine rings already at a reaction temperature of 300 °C, while the phenyl rings are maintained. In addition, unreacted nitrile groups are found in all products, with higher relative quantities of free nitriles for the PTO samples. Whereas at 400 °C the polymerization process is almost complete, incomplete polymerization and the formation of oligomers are detected at lower temperatures.

Porosity data were calculated from argon sorption measurements and are summarized in Table S2 (ESI†). According to Kuhn *et al.*¹³ CTF-1 displays a relatively high surface area (SA) of 791 m² g⁻¹ due to microporosity, which is confirmed by sorption measurements of our CTF-1 sample (610 m² g⁻¹). In contrast, the PTOs synthesized below 400 °C show significantly lower values in the range of 6–116 m² g⁻¹, suggesting that either no distinct continuous 1D pore system is formed or pore blocking occurs. Similarly low surface areas (2–4 m² g⁻¹) were reported by Ren *et al.*¹⁴ for their yellow colored CTF-1s synthesized by a super acid-catalyzed (microwave-assisted) procedure. The surface areas of PTO-300 samples are slightly increased compared to the ones synthesized at 350 °C, whereas a higher salt concentration (> 1 eq.) leads to lower surface areas irrespective of how much excess of salt melt was used.

Estimation of the degree of polymerization

While the chemical environments of the PTOs are similar to CTF-1 based on IR, ssNMR and XPS, appreciable differences between the samples are discernible, even in PXRD and EA. We assumed that these differences result from different degrees of polymerization and, hence, nitrile content of the PTOs synthesized at 300 °C compared to CTF-1 and PTO-350. Therefore, MALDI-TOF measurements were performed with PTO-300-1 and PTO-300-15 to further analyze the molecular sizes of the synthesized PTOs (Fig. S7 and S8, ESI†). No mass signal was detected for the starting material 1,4-dicyanobenzene (*m/z* = 128) and the polymer CTF-1 itself. For the PTOs, multiples of masses of 1,4-dicyanobenzene ($n \times 128$ for $n = 0, 1, 2, 3, \dots$) are expected since the polymerization up to CTF-1 proceeds without the formation of side products. Taking into account the rules of the trimerization reaction—three nitrile groups forming one triazine unit—fragments of 1,4-dicyanobenzene triplets (trimers) with a mass of 384 *m/z* should be observable. Furthermore, the formation of chains or dendrimers (of the trimer units) leads to $(3 + 2n)$ multiples of the mass of 1,4-dicyanobenzene (Fig. 3b, Tables S4 and S5, ESI†). A ring closure would lead to $(12 + 7n)$ multiples of the 1,4-dicyanobenzene mass (Fig. 3b and Table S6, ESI†). In contrast to CTF-1, we obtained signals in the mass spectra for the PTO samples (Table S3 and Fig. S6 and S7, ESI†) which, in principle, already suggests that the molecular sizes of the PTOs are smaller than CTF-1 and more susceptible to ablation by ionization. The recorded mass spectra of PTO-300-1 and PTO-300-15 differ from each other in that they show small fragments ($m/z \leq 12 \times 128$) for the sample synthesized with a high zinc chloride content (PTO-300-15) and additionally larger

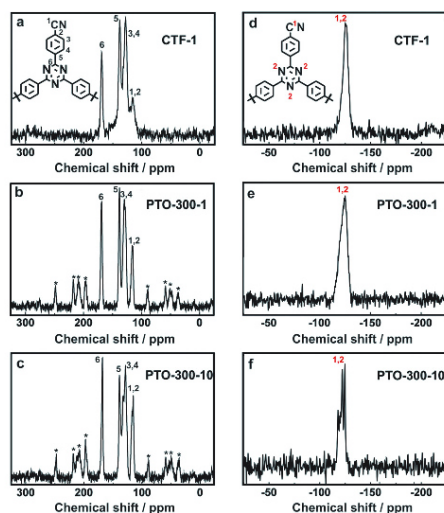


Fig. 2 ¹³C CP MAS ssNMR spectra of (a) CTF-1, (b) PTO-300-1 and (c) PTO-300-10. ¹⁵N CP MAS ssNMR spectra of (d) CTF-1, (e) PTO-300-1 and (f) PTO-300-10. Asterisks mark rotational spinning side bands. A contact time of 5 ms was used for all measurements and the spinning speed was set to 10 kHz (all PTO measurements), 20 kHz (¹³C of CTF-1) and 5 kHz (¹⁵N of CTF-1), respectively.

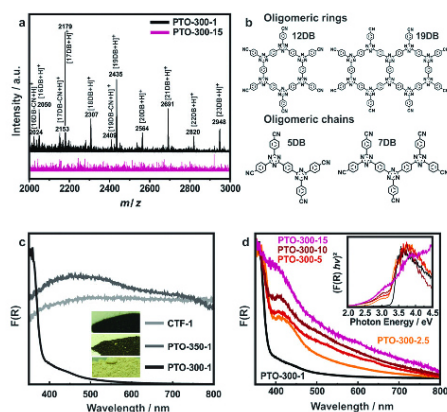


Fig. 3 (a) MALDI-TOF spectra of PTO-300-1 compared to PTO-300-15, measured in positive mode and in the mass range of 2000–3000. For both PTO materials signals have been detected in the mass spectra below the mass range of 2000. DB represents the mass of the precursor 1,4-dicyanobenzene ($m/z = 128$). (b) Examples of possible ring and chain-like oligomers with their calculated masses. (c) UV-Vis spectra and product color (inset) of the PTO samples synthesized at different temperatures compared to CTF-1. (d) UV-Vis spectra of the PTO samples synthesized at 300 °C with different precursor ratios from low (bottom) to high $ZnCl_2$ content (top) and their corresponding Tauc plots (inset).

ones ($m/z > 12 \times 128$) for the PTO synthesized with a 1:1 precursor ratio (PTO-300-1). For both samples, multiples of odd numbers up to 11 of the masses of 1,4-dicyanobenzene were found which can be assigned to chain fragments or small dendrimers (Tables S3–S5, ESI†). Additionally, a signal at 12 times the mass of 1,4-dicyanobenzene was recorded which likely represents a 12-membered ring (Fig. 3b, Tables S3 and S6, ESI†). In the case of PTO-300-1, the mass spectra also show larger fragments of 16–23 multiples of 1,4-dicyanobenzene due to longer chains, larger dendrimers and double ring systems (Fig. 3a, Tables S3–S6, ESI†). It seems that the amount of zinc chloride is crucial for the obtained molecular size of the oligomers as well as the type of oligomeric fragments formed. A high dilution of the starting material leads to smaller, chain-like oligomers (e.g. PTO-300-15) with very low porosities and more favorable stacking interactions (see below and Table S2, ESI†). In contrast, higher concentration of 1,4-dicyanobenzene (PTO-300-1) favors the formation of larger oligomers featuring higher porosities due to the formation of ring-systems (see Table S2, ESI†). The polymerization degree of the PTO samples was also roughly estimated by means of IR spectroscopy. To this end, we relate the IR signal intensities and integrals of the nitrile (2227 cm^{-1}) and triazine bands (1355 cm^{-1}) and compare them with those of the trimer and CTF-1 (Fig. 1c and d and Tables S4–S7, ESI†). In the case of CTF-1, almost no nitrile signal is visible in the IR spectrum, which indicates a near-zero nitrile-to-triazine ratio due to the largely complete conversion to the trimerized product. On the contrary, the highest nitrile-to-triazine ratio is obtained for

the trimer itself (see Tables S4 and S5, ESI†). The PTO samples invariably yielded lower nitrile-to-triazine ratios compared to the trimer. This is consistent with the assumption that the polymerization proceeded further than the trimer in the case of the PTO samples. More precisely, a relatively high nitrile-to-triazine ratio was calculated for PTOs-300 synthesized with large zinc chloride contents (e.g. PTO-300-15), which can only be explained by the formation of short chains or small dendrimers (Tables S4 and S5, ESI†). PTO-300-1 samples reveal lower ratios caused by ring closure or larger dendrimers (Tables S4 and S6, ESI†). To get a more quantitative picture of the degree of polymerization, ^{13}C one pulse ssNMR spectra of PTO-300-1 and PTO-300-10 were recorded (Fig. S11, ESI†). As already described in a previous section the signals for the triazine units and the nitrile groups are well resolved (169 ppm for triazine as well as 120–110 ppm for nitrile groups and the benzene carbons to which the nitrile groups are bound). Using the integrals of the signals, the nitrile-to-triazine ratio can be calculated. Due to the significantly longer spin-lattice relaxation of the triazine carbons compared to the other carbon species the chosen measurement conditions lead to a slight underestimation of around 5% for the intensity of the triazine signal (for further details see the ESI†). The calculated ratio for the PTO-300-10 sample is 0.46, suggesting a mixture of trimers (0.50) and short chains or small dendrimers (< 0.50). For PTO-300-1 it is much lower (0.21) pointing towards a higher degree of polymerization. Therefore, the formation of dendrimers or ring structures is favored under these conditions. This is well in line with the IR and MALDI-TOF data.

Optical properties

Interestingly, the materials showed different colors compared to the samples synthesized at 400 °C (black), as depicted in Fig. 3c. While the samples synthesized at 350 °C are still rather dark and their color is independent of the amount of $ZnCl_2$ used, the synthesis at 300 °C leads to products with yellow (PTO-300-1) or green-greyish complexion (PTO-300-15). The colors of the PTOs differ also from those of the starting materials and the trimer (colorless), which again suggests the formation of oligomeric products.

UV-Vis spectra were recorded in order to evaluate the absorption characteristics of the materials as a function of their polymerization state (Fig. 3c and d). When comparing the samples synthesized at different temperatures, a strong absorption in the UV region (350 nm) is observed for the PTO samples synthesized at 300 °C, with a sharp absorption edge around 370 nm (3.2–3.3 eV, assuming a direct band gap), as well as a weak and broad absorption in the visible light range. According to Butchosa *et al.*¹⁵ these strong absorptions in the UV are caused by $\pi \rightarrow \pi^*$ and $n \rightarrow \pi^*$ excitations, resulting from absorptions within isolated molecular units and oligomer stacking, respectively. The long sloping wavelength tail extending beyond 700 nm in the samples synthesized at higher salt contents (Fig. 3d) likely occurs due to enhanced absorption caused by incipient carbonization. Likewise, the materials synthesized at elevated temperatures ($> 300\text{ °C}$) show broad absorption in the whole visible

region with no distinct absorption edge, which is expected judging from their dark sample color (Fig. 3c). Note, however, that theoretical calculations suggested a band gap of 2.42 eV for CTF-1.¹⁶ When comparing the UV-Vis spectra of the PTO samples synthesized at 300 °C but with different zinc chloride concentrations (Fig. 3d), a second absorption around 410 nm arises, which increases relative to the UV absorption and slightly red-shifts for the materials when synthesized in an excess of salt melt (>1 eq.). This feature may be associated with a reduced interlayer distance for the PTO-300 samples obtained with increasing salt content (Table S1, ESI†), or with more pronounced torsional angles in the otherwise planar systems as suggested by Butchosa *et al.*¹⁵ However, due to the sloping background caused by incipient carbonization,⁷ it is not possible to reliably extract the intensity of this absorption or the position of the absorption edge.

Photocatalytic hydrogen evolution

Since triazine-based organic semiconductors have been reported to reduce water to hydrogen under visible light irradiation, we reasoned that the incorporation of triazine units into organic frameworks may be a viable strategy to rationally design efficient organic photocatalysts.¹² The high chemical and thermal stabilities of the CTFs, together with the suitable optical properties based on theoretical calculations and our experimental findings, should render CTFs suitable photocatalysts for the water-splitting reaction.¹⁶ Platinum-loaded (2.2 wt%) CTF-1 itself ($0.02 \mu\text{mol h}^{-1}$) and the PTO-350 samples ($0.45 \mu\text{mol h}^{-1}$) showed only negligible activity in a buffered (pH 7) aqueous triethanolamine (TEOA) solution when illuminated with simulated sunlight. These low activities may be explained by the large carbon content in the samples which results from incipient carbonization, or by a mismatch in energy levels. The excess of carbon absorbs a significant portion of the light which then cannot penetrate deeply into the photocatalyst. The low crystallinity of the materials may also hinder the photocatalytic process in that the light-induced charge carriers quickly recombine at traps rather than being able to diffuse to the surface of the material.

In contrast, the samples synthesized below 350 °C (PTO-300) exhibit a stable and high hydrogen evolution rate for over 100 hours under the conditions described above (Fig. 4a and b and Fig. S17, ESI†, right). The most active PTO-300 materials were found to produce $10.8 (\pm 2.8) \mu\text{mol h}^{-1}$ hydrogen on average when illuminated with simulated sunlight. The action spectrum of the PTO-300 samples suggest that the highest hydrogen contribution arises from wavelengths with an energy of $400 (\pm 20) \text{ nm}$, revealing average estimated apparent quantum efficiencies of $5.5 (\pm 1.1)\%$ (Fig. 4c). Activities above 450 nm are negligible due to the weaker absorption in this wavelength range. In several cases, not only a constant hydrogen evolution rate was observed but even an increase in activity over time (*e.g.* Fig. S13, ESI†), likely due to the gradually improved wettability of the oligomers and, hence, dispersion. We have analyzed the recovered photocatalyst after operating for over tens of hours and can exclude hydrolysis or any photodegradation of the catalyst (Fig. S22–S24, ESI†). An additional vibration band at 1771 cm^{-1} is observed in the IR spectrum for the photocatalysts

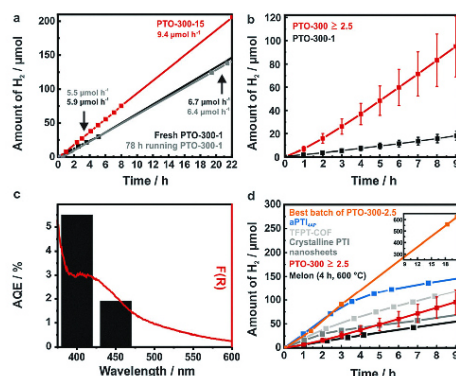


Fig. 4 (a) Stability test of 10 mg Pt-modified PTO-300-15 and PTO-300-1 in 10 vol% buffered (pH 7, 0.5 M, phosphate buffer) TEOA solution under irradiation with simulated sunlight (for PTO-300-15, red) and UV-Vis light ($\geq 250 \text{ nm}$ for PTO-300-1). Stable hydrogen evolution for over 100 h (PTO-300-1) shown as two slopes: the black slope represents a fresh PTO-300-1 suspension within the first 20 h and the grey represents the same suspension after 78 h of photocatalysis, demonstrating stable H_2 evolution for at least 100 h. (b) Average H_2 evolution rate of Pt-modified PTO-300 ≥ 2.5 with standard deviation, compared to PTO-300-1. (c) Action spectrum of Pt-PTO-300-5 (measured with a 40 nm FWHM band pass filter), overlaid on the UV-Vis spectrum of the photocatalyst. (d) Reproducible hydrogen evolution rate of Pt-PTO-300 ≥ 2.5 and of the best performing sample (Pt-PTO-300-2.5) in comparison with literature photocatalysts used as internal standards under identical reactor and illumination conditions (230 mL reactor volume, top-irradiation, equal irradiation surface and intensity 380 mW cm^{-2} , as well as dispersion volume (10 mL of 10 vol% TEOA solution), 10 mg (2 mg for PTI nanosheets) Pt-modified photocatalyst (2.2 wt% Pt) under reported conditions.

treated in a phosphate buffer (Fig. S22, ESI†, right) which can be explained by a possible phosphate coordination. No hydrolysis products are observed in the ^{13}C CP MAS ssNMR spectra (Fig. S24, ESI†).

A factor significantly influencing the variation of activity in the series of PTOs is the ratio of precursor to ZnCl_2 in the syntheses at 300 °C. Higher activities are observed for PTO-300 samples for which an excess of zinc chloride was used in the synthesis (>1 eq.) (Fig. 4b). In line with our previous observations described above, the large zinc chloride content leads to the formation of smaller oligomers, whereas a low zinc chloride environment favors the formation of larger PTO fragments which are photocatalytically less active (Fig. 4b). Similar observations have recently been reported for carbon nitrides,³² where oligomers of Melon showed an increased photocatalytic activity compared to the polymer. Furthermore, the activity of these oligomers depended on their size such that smaller oligomers of Melon showed a higher activity compared to the larger ones.³² We believe that the increased activity of the smaller oligomers compared to their larger relatives or the polymer might be associated with the amount of terminal groups. The terminal groups in the PTO samples are nitrile moieties which appear in larger quantities for the samples synthesized in excess of

zinc chloride. A large nitrile content favors hydrogen bonding and thus, leads to a better dispersion of the photocatalyst during the photocatalytic experiment. Furthermore, it is expected that platinum, which is used as a co-catalyst, preferably coordinates to the terminal nitrile groups and thus promotes improved charge transfer.³³ Another possibility is that the nitrile groups can be considered as active sites themselves, as the photocatalytic activity scales roughly with the relative amount of nitrile groups in the sample. Note, however, that we do not observe a linear correlation between the observed activity and the excess of zinc chloride used. Nevertheless, the interplay between triazines and nitriles or, in other words, a reasonably large conjugated backbone, is decisive since a certain amount of triazines is needed to exhibit a photocatalytic response. For instance, the trimer ($0.08 \mu\text{mol h}^{-1}$) showed only minor activity even with UV-Vis ($\geq 250 \text{ nm}$) illumination (Fig. S14, ESI†). Note that we observe quite significant batch-to-batch variations in the samples with ZnCl_2 -to-precursor ratios of >1 (Table S10 and Fig. S21, ESI†), which we attribute to the dilution and low diffusion of the precursor during the ionothermal reaction at 300°C , and the resulting variations in the oligomer size, indicating that the synthesis is not yet fully optimized. For example, next to average hydrogen evolution rates around $10 \mu\text{mol h}^{-1}$, lower ($3.4 \mu\text{mol h}^{-1}$) and higher hydrogen evolution rates of $30.3 \mu\text{mol h}^{-1}$ were observed, the latter with an estimated apparent quantum efficiency of up to $9.9 (\pm 2.0)\%$. A fine-tuning of the synthesis parameters and the deliberate introduction of additional nitrile groups may therefore further improve the photocatalytic activity of these phenyl-triazine oligomers.

Another important aspect for gauging the intrinsic photocatalytic activities of the samples is to relate them to their specific surface areas, which may correlate with the number of exposed active sites. In this case, however, the PTOs with smaller surface areas showed significantly improved activity and we can therefore exclude surface area effects as dominant factors for the photocatalytic performance (Table S8, ESI†).

Further, the question arises as to whether residual zinc chloride is present as an impurity or quantitatively incorporated into the system and as such may influence the photocatalytic activity of the PTOs. Thomas and co-workers³⁴ reported on possible Zn^{2+} incorporation in CTFs during the synthesis of CTF-0 (derived from 1,3,5-tricyanobenzene) when synthesized in the presence of large zinc chloride quantities. Minor amounts of Zn^{2+} ions within the structure might act as "dopants" as reported previously for carbon nitrides.³⁵ However, this zinc doping procedure (stirring Melon in an acidic ethanol zinc chloride solution) most likely leads to an increased amount of nitrile groups from depolymerization and opening of the triazine rings as seen from the IR spectra. It is therefore doubtful whether the Zn-doping or the formation of nitriles was the reason for the improved activity of the carbon nitrides.³⁵ Here, the presence of zinc chloride in the PTO is $\leq 0.1 \text{ wt}\%$ as established by ICP-AES analysis (Table S2, ESI†). As we cannot completely exclude that minute amounts of impurities may be the reason for the different activities of PTOs-300, we performed two different control experiments. Firstly, zinc chloride (5 mg, 10 mg and 17 mg) was added

to a standardized PTO-300 suspension for photocatalysis, which resulted in a long-term decrease in activity presumably caused by chlorine poisoning of the platinum nanoparticles (Fig. S15, ESI† left). Secondly, a PTO-300 sample was excessively washed with 0.1 M ethylenediaminetetraacetic acid (EDTA), which acts as a complexing agent for zinc ions (Table S9, ESI†), and compared the activities before and after EDTA treatment. Here again, no change in activity was detected after washing (Fig. S15, ESI† left), which implies that Zn^{2+} doping is probably not the reason for the activity differences.

We therefore hypothesize that besides the different nitrile content variations in activity within the oligomers primarily arise from the different optical properties (more well-defined absorption in the visible, see Fig. 3d) as well as more favorable carrier dynamics. The latter may be most facile for oligomers with shorter lengths and smaller interlayer distances, which leads to stronger π -orbital overlap and hence more efficient extraction of the charge carriers at the interfaces. This is supported by the significantly enhanced dispersibility of the smaller oligomers with a higher degree of nitrile moieties.

In addition, several control experiments were performed to ensure that the evolution of hydrogen is indeed photocatalytic and not due to chemical reactions with the catalyst. Most fundamentally, the absence of light resulted in no activity, proving the hydrogen evolution to be photo-induced. Secondly, the activity of the photocatalyst was tested without the addition of the proton reduction catalyst platinum. In fact, unmodified PTO-300 also showed a moderate, yet significant hydrogen evolution rate (PTO-300-15: $1.21 \mu\text{mol h}^{-1}$ or $121 \mu\text{mol h}^{-1} \text{ g}^{-1}$; PTO-300-1: $0.53 \mu\text{mol h}^{-1}$ or $53 \mu\text{mol h}^{-1} \text{ g}^{-1}$), which indicates that PTO-300 acts as an actual photocatalyst rather than just a photosensitizer (Fig. S16, ESI†). Surprisingly, PTO-300 ($121 \mu\text{mol h}^{-1} \text{ g}^{-1}$) significantly outperforms other co-catalyst-free light element photocatalysts (e.g. Melon: $1\text{--}40 \mu\text{mol h}^{-1} \text{ g}^{-1}$,⁸ msp-g- C_3N_4 : $2 \mu\text{mol h}^{-1} \text{ g}^{-1}$,¹⁷ $\text{B}_{4.3}\text{C}$: $14.5 \mu\text{mol h}^{-1} \text{ g}^{-1}$,¹⁹ and PTI: $0 \mu\text{mol h}^{-1} \text{ g}^{-1}$).^{6,7,10} Yet, this modest activity is significantly increased and stabilized by platinum deposition. The absence of an electron donor resulted in negligible activity ($0.01 \mu\text{mol h}^{-1}$) which underlines the importance of a sacrificial donor in the system to avoid recombination of the generated charge carriers and to enhance the driving force for hole collection as compared to the oxidation of pure water. The highest activities were observed when Pt-modified PTO-300 was suspended in an aqueous TEoA solution. However, other electron donors such as oxalic acid and EDTA also led to sustained hydrogen evolution (Fig. S17, ESI†).

We also tested PTOs-300 doped with $3 \text{ wt}\%$ Co_3O_4 nanoparticles and silver nitrate as sacrificial agents for water oxidation. However, no oxygen was detected (within the detection limit), even though triazine-based materials have been predicted to be oxygen evolution catalysts due to their suitable HOMO potential.¹⁶

PTO-300 synthesized from diluted zinc chloride melt is competitive (average rate of $1076 \mu\text{mol h}^{-1} \text{ g}^{-1}$, maximum rate of $3030 \mu\text{mol h}^{-1} \text{ g}^{-1}$) with highly condensed heptazine- and triazine-based carbon nitride photocatalysts, such as Melon

(e.g. msp-g-C₃N₄: 1490 μmol h⁻¹ g⁻¹ or g-C₃N₄ doped with barbituric acid: 294 μmol h⁻¹ g⁻¹),^{17,36} crystalline PFI nanosheets (1750 μmol h⁻¹ g⁻¹),¹⁰ 4-AP doped amorphous PFI (4907 μmol h⁻¹ g⁻¹),⁷ TFPT-COF (1970 μmol h⁻¹ g⁻¹)⁹ and boron carbide (B₄C: 31 μmol h⁻¹ g⁻¹).¹⁹ As differing measurement set-ups (light-sources, irradiation type e.g. inner vs. top-irradiation) may give different results for the same photocatalyst in different laboratories we compare PTO-300 with four of the above reported photocatalysts measured under identical instrumental conditions, namely Melon (g-C₃N₄) synthesized from dicyandiamide for 4 hours at 600 °C,^{8a} crystalline PFI/LiCl nanosheet suspension,¹⁰ 16% 4-AP doped amorphous PFI⁷ and TFPT-COF⁹ (Fig. 4d). While PTO-300-1 (1.5 μmol h⁻¹) is less active than Melon (6.4 μmol h⁻¹), PTOs-300 synthesized in an excess of zinc chloride (10.8 (±2.8) μmol h⁻¹) are superior to Melon and rival TFPT-COF (15.5 μmol h⁻¹). Whereas some photocatalysts tested here (TFPT-COF and (amorphous doped) PFI) exhibit a significant decrease in their hydrogen evolution rate over time within an aqueous TEOA solution, PTO-300 shows long term stability.

Conclusions

We have demonstrated that a lower reaction temperature during ionothermal CTF-1 synthesis gives rise to oligomers of CTF-1 which differ in their length and connectivity. These oligomers are highly efficient hydrogen evolution photocatalysts which show an average hydrogen evolution rate of 10.8 (±2.8) μmol h⁻¹ (10 mg photocatalyst) with simulated sunlight, whereas hardly any activity was observed for the CTF-1 polymer. We hypothesize that the suspicious absence of activity in CTF-1 is due to a reduced thermodynamic driving force for hydrogen evolution or to the incipient carbonization at its synthesis temperature of 400 °C, where light absorption by carbon prevents photon absorption by the framework, thus rendering hydrogen evolution unfeasible. For the triazine-based oligomers obtained at different precursor/zinc chloride ratios, distinct crystallinity, surface area, nitrile content as well as variations in activity were observed. Specifically, PTOs synthesized with an excess of zinc chloride (>1 equivalent relative to the precursor) display higher crystallinity, a reduced layer distance, smaller surface areas, lower hydrophobicity, smaller fragment sizes and a larger amount of terminal nitrile groups. These features were found to contribute to substantially improved photocatalytic activity compared to PTOs obtained with 1:1 precursor/zinc chloride ratio. Since the observed activity enhancement likely correlates with an increased amount of nitrile moieties and improved π-stacking of the oligomers, we believe that by controlling the polymerization progress, we can significantly enhance the charge transfer kinetics, which still is the limiting factor in organic photocatalysts. Finally, the oligomers show the highest activity observed for metal-free organic photocatalysts in the absence of any co-catalyst, thus boding well for the development of earth-abundant organic photocatalysts by controlled polymerization reactions and molecular engineering.^{6-10,17-19}

Acknowledgements

Financial support by the Deutsche Forschungsgemeinschaft (projects LO1801/1-1, SE1417/5-1), the cluster of excellence "Nanosystems Initiative Munich" (NIM), and the Center for NanoScience (CeNS) is gratefully acknowledged. We thank Dr M. Konuma, C. Minke, C. Sondermann, V. Duppel and M.-L. Schreiber for their assistance with the sample characterization and Dr V. Vyas for the synthesis of the trimer. Dr V. W. Lau, F. Haase and L. Stegbauer are gratefully acknowledged for helpful discussions.

References

- X. Chen, S. Shen, L. Guo and S. S. Mao, *Chem. Rev.*, 2010, **110**, 6503.
- A. Fujishima and K. Honda, *Nature*, 1972, **238**, 37.
- H. Tong, S. Ouyang, Y. Bi, N. Umezawa, M. Oshikiri and J. Ye, *Adv. Mater.*, 2012, **24**, 229.
- S. Yanagida, A. Kabumoto, K. Mizumoto, C. Pac and K. Yoshino, *J. Chem. Soc., Chem. Commun.*, 1985, **8**, 474.
- T.-F. Yeh, J.-M. Syu, C. Cheng, T.-H. Chang and H. Teng, *Adv. Funct. Mater.*, 2010, **20**, 2255.
- Y. Ham, K. Maeda, D. Cha, K. Takanabe and K. Domen, *Chem. - Asian J.*, 2013, **8**, 218.
- K. Schwinghammer, B. Tuffy, M. B. Mesch, E. Wirnhier, C. Martineau, F. Taulelle, W. Schnick, J. Senker and B. V. Lotsch, *Angew. Chem., Int. Ed.*, 2013, **52**, 2435.
- (a) X. Wang, K. Maeda, A. Thomas, K. Takanabe, G. Xin, J. M. Carlsson, K. Domen and M. Antonietti, *Nat. Mater.*, 2009, **8**, 76; (b) L. Seyfarth, J. Seyfarth, B. V. Lotsch, W. Schnick and J. Senker, *Phys. Chem. Chem. Phys.*, 2010, **12**, 2227.
- L. Stegbauer, K. Schwinghammer and B. V. Lotsch, *Chem. Sci.*, 2014, **5**, 2789.
- K. Schwinghammer, M. B. Mesch, V. Duppel, C. Ziegler, J. Senker and B. V. Lotsch, *J. Am. Chem. Soc.*, 2014, **136**, 1730.
- M. K. Bhunia, K. Yamauchi and K. Takanabe, *Angew. Chem., Int. Ed.*, 2014, **53**, 11011.
- Y. Wang, X. Wang and M. Antonietti, *Angew. Chem., Int. Ed.*, 2012, **51**, 68.
- P. Kuhn, M. Antonietti and A. Thomas, *Angew. Chem., Int. Ed.*, 2008, **47**, 3450.
- S. Ren, M. J. Bojdys, R. Dawson, A. Laybourn, Y. Z. Khimyak, D. J. Adams and A. I. Cooper, *Adv. Mater.*, 2012, **24**, 2357.
- C. Butchosa, T. O. McDonald, A. I. Cooper, D. J. Adams and M. A. Zwijnenburg, *J. Phys. Chem. C*, 2014, **118**, 4314.
- X. Jiang, P. Wang and J. Zhao, *J. Mater. Chem. A*, 2015, **3**, 7750.
- X. Wang, K. Maeda, X. Chen, K. Takanabe, K. Domen, Y. Hou, X. Fu and M. Antonietti, *J. Am. Chem. Soc.*, 2009, **131**, 1680.
- J. Liu, Y. Liu, N. Liu, Y. Han, X. Zhang, H. Huang, Y. Lifshitz, S.-T. Lee, J. Zhong and Z. Kang, *Science*, 2015, **347**, 970.
- J. Liu, X. Wen, Y. Hou, F. Zuo, G. J. O. Beran and P. Feng, *Angew. Chem., Int. Ed.*, 2013, **52**, 3241.

- 20 J. H. van't Hoff, *Die Gesetze des chemischen Gleichgewichtes für den verdünnten, gasförmigen oder gelösten Zustand*, Engelmann, Leipzig, 2nd edn, 1915, p. 105.
- 21 M. J. Bojdys, J. Jeromenok, A. Thomas and M. Antonietti, *Adv. Mater.*, 2010, **22**, 2202.
- 22 V. G. Manecke and D. Wöhrle, *Makromol. Chem.*, 1968, **120**, 176.
- 23 P. Kuhn, A. Thomas and M. Antonietti, *Macromolecules*, 2009, **42**, 319.
- 24 M. R. Liebl and J. Senker, *Chem. Mater.*, 2013, **25**, 970.
- 25 W. J. Gammon, O. Kraft, A. C. Reilly and B. C. Holloway, *Carbon*, 2003, **41**, 1917.
- 26 G. Beamson and D. Briggs, *High Resolution XPS of Organic Polymers, the Scienta ESCA300 Database*, 1992.
- 27 J. A. Taylor, G. M. Lancaster and J. W. Rabalais, *Appl. Surf. Sci.*, 1978, **1**, 503.
- 28 (a) S. Yang, Y. Gong, J. Zhang, L. Zhan, L. Ma, Z. Fang, R. Vajtai, X. Wang and P. M. Ajayan, *Adv. Mater.*, 2013, **25**, 2452; (b) M. Barber, J. A. Connor, M. F. Guest, I. H. Hillier, M. Schwarz and M. Stacey, *J. Chem. Soc., Faraday Trans. 2*, 1973, **69**, 551; (c) B. A. Sexton and N. R. Avery, *Surf. Sci.*, 1983, **129**, 21.
- 29 B. Jürgens, E. Irran, J. Senker, P. Kroll, H. Müller and W. Schnick, *J. Am. Chem. Soc.*, 2003, **125**, 10288.
- 30 S. Hug, M. Tauchert, S. Li, U. E. Pachmayr and B. V. Lotsch, *J. Mater. Chem.*, 2012, **22**, 13956.
- 31 E. T. Haupt and D. Leibfritz, *Spectrochim. Acta, Part A*, 1989, **45**, 119.
- 32 V. W. Lau, M. B. Mesch, V. Duppel, V. Blum, J. Senker and B. V. Lotsch, *J. Am. Chem. Soc.*, 2015, **137**, 1064.
- 33 (a) B. Y. Kukushkin, *Platinum Met. Rev.*, 1998, **42**, 106; (b) V. W. Lau, I. Moudrakovski, T. Botari, S. Weinburger, M. B. Mesch, V. Duppel, J. Senker, V. Blum, B. V. Lotsch, 2015, submitted.
- 34 P. Katekomol, J. Roeser, M. J. Bojdys, J. Weber and A. Thomas, *Chem. Mater.*, 2013, **25**, 1542.
- 35 B. Yue, Q. Li, H. Iwai, T. Kako and J. Ye, *Sci. Technol. Adv. Mater.*, 2011, **12**, 034401.
- 36 J. Zhang, X. Chen, K. Takanaabe, K. Maeda, K. Domen, J. D. Epping, X. Fu, M. Antonietti and X. Wang, *Angew. Chem., Int. Ed.*, 2010, **49**, 441.

6.1.2 Supporting Information

Electronic Supplementary Material (ESI) for Energy & Environmental Science.
This journal is © The Royal Society of Chemistry 2015

Electronic supplementary information (ESI)

Phenyl-Triazine Oligomers for Light-Driven Hydrogen Evolution

K. Schwinghammer,^{‡a} S. Hug,^{‡a} M. B. Mesch,^b J. Senker,^b and B. V. Lotsch^{a*}

* Author to whom correspondence should be addressed. Tel: +49-711-689-1610, Fax: +49-711-689-1612. E-mail: b.lotsch@fkf.mpg.de

^a Max Planck Institute for Solid State Research, 70569 Stuttgart, Germany. Department of Chemistry, University of Munich, LMU, 81377 Munich, Germany. Nanosystems Initiative Munich (NIM) and Center for NanoScience (CeNS), 80799 Munich, Germany.

^b Inorganic Chemistry III, University of Bayreuth, 95447 Bayreuth, Germany.

[‡] These authors contributed equally

Table of Content

Experimental Section.....	S2
Characterization of the PTO _{organic phase}	S8
XRD Characterization.....	S9
Elemental Analysis and ICP.....	S9
XPS Measurements.....	S10
MALDI-TOF Measurements and IR Analysis.....	S11
Ar-Physisorption Measurements.....	S19
NMR Measurements.....	S21
Photocatalytic Experiments.....	S22
TEM Characterization.....	S30

Experimental Section

Methods

Argon adsorption/desorption measurements were performed at 87 K with an Autosorb-iQ surface analyzer (Quantachrome Instruments, USA). Samples were outgassed in vacuum at 120 °C for 6-12 h to remove all guests. For BET calculations pressure ranges of the Ar isotherms were chosen with the help of the BET Assistant in the ASiQwin software. In accordance with the ISO recommendations multipoint BET tags equal or below the maximum in $V \cdot (1 - P/P_0)$ were chosen.

Infrared (IR) spectroscopy measurements were carried out on a Perkin Elmer Spektrum BX II (Perkin Elmer, USA) with an attenuated total reflectance unit.

Powder X-ray diffraction (PXRD) was measured on a BRUKER D8 Avance (Bruker AXS, USA) in Bragg-Brentano geometry with a Cu-K α_1 -radiation ($\lambda = 1.54051 \text{ \AA}$).

Elemental analysis (EA) was carried out with an Elementarvario EL (Elementar Analysensysteme, Germany).

Energy dispersive X-ray spectroscopy (EDX) was carried out on a JEOL JSM-6500F electron microscope (JEOL, Japan) with a field emission source equipped with an EDX detector (model 7418, Oxford Instruments, UK) and a Tescan Vega TS 5130MM electron microscope equipped with a Si/Li EDX detector (Oxford Instruments, UK).

Inductively coupled plasma atomic emission spectroscopy (ICP-AES) was carried with a pressure digestion system by Berghof, a plasma created on a Vista Pro ICP-AES spectrometer, an Echelle-Polychromator by Fa. Varian Darmstadt and a photomultiplier.

^{13}C magic angle spinning (MAS) solid-state nuclear magnetic resonance (ssNMR) spectra were recorded at ambient temperature on a BRUKER DSX Avance 500 FT and a BRUKER AvanceIII HD 400 NMR spectrometer (Bruker Biospin, Germany) with external magnetic fields of 11.8 T and 9.4 T, respectively. The operating frequencies are 500.1 MHz and 125.7 MHz and 400.1 MHz and 100.6 MHz for ^1H and ^{13}C , respectively, and the spectra were referenced relative to TMS. The samples were contained in 4 or 3.2 mm ZrO_2 rotors and mounted in standard triple resonance BRUKER MAS probes. The spinning speed was set to 10 kHz or 20 kHz (for the photocatalyst after photocatalysis, CTF-1 and quantitative ^{13}C measurements). During acquisition of the spectra ^1H decoupling (approx. 70 kHz RF field) was applied using a SPINAL64 sequence.

For $^1\text{H}^{13}\text{C}$ ramp-amplitude (RAMP) cross-polarization (CP) MAS spectra a contact time of 5 ms and a 90° pulse length of $2.50 \mu\text{s}$ on ^1H was set. The quantitative ^{13}C measurements were recorded using a single pulse (SP) experiment. The recycle delay was varied between 60 and 6000 s for PTO-300-10, to get an idea about the T1. For the final measurements a recycle delay of 6000 s was used and 64 scans were executed. The background signal was recorded using a

recycle delay of 0.5 s to make sure that only the background signal is relaxed and gives a signal. This signal was subtracted from the spectrum.

$^1\text{H}/^{15}\text{N}$ CP MAS ssNMR spectra were measured at ambient temperature on a BRUKER AvanceIII HD 400 NMR (PTO-300-1 und -10) and a BRUKER AvanceII 300 (CTF-1) NMR spectrometer with external magnetic fields of 9.4 T and 7.1 T, respectively. The operating frequencies are 400.1 MHz and 40.6 MHz and 300.1 MHz and 30.4 MHz for ^1H and ^{15}N , respectively.

The samples were contained in 4 or 7 mm ZrO_2 rotors which were mounted in standard double or triple resonance BRUKER MAS probes. The spinning speed was set to 10 or 5 kHz and the chemical shifts were referenced relative to nitromethane. During acquisition of the spectra ^1H decoupling (approx. 70 kHz RF field) was applied using a SPINAL64 sequence.

The spectra were recorded using a RAMP CP pulse on ^1H with a nutation frequency ν_{nut} of 40 kHz and 45 kHz on ^{15}N , respectively. During a contact time of 5 ms the ^1H RF field was linearly varied about 50%. The recycle delay was set to 2 s and 1.5 s. About 120000 and 40000 transients were accumulated for the CP experiments, respectively.

For X-ray photoelectron spectroscopy (XPS), samples were pressed onto indium foil and the spectra were collected on an Axis Ultra (KRATOS Analytical, Manchester) X-ray photoelectron spectrometer with charge neutralization. The spectra were processed using the software OriginPro 8.5.1 and fitted with the Gaussian function. The spectra were referenced to the adventitious carbon 1s peak at 284.600 eV. Binding energies were compared with the NIST Standard Reference Database 30 (Version 4.1) unless otherwise specified.

Matrix-assisted laser deposition/ionization-time of light (MALDI-TOF) was performed on a Shimadzu Axima Resonance mass spectrometer. Calibration was carried out using neat fullerene and using CsI ground with *trans*-2-[3-(4-*tert*-butylphenyl)-2-methyl-2-propenylidene] malononitrile as the matrix. Each sample was ground with dithranol ($m/z = 227$) as the matrix and deposited on a steel sample holder. The spectra were collected in raster mode and the laser power was progressively increased until a suitable signal-to-noise ratio was achieved. The presented spectra are averaged from 100 profiles.

Optical diffuse reflectance spectra of the solids were collected at room temperature with a UV-Vis-NIR diffuse reflectance spectrometer Cary 5000 (Agilent Technologies, USA) at a photometric range of 250-800 nm. Powders were prepared in a sample carrier with a quartz glass window at the edge of the integrating sphere with BaSO_4 as the optical standard. Kubelka-Munk spectra were calculated from the reflectance data.

TEM was performed with a Philips CM 30 ST microscope (LaB₆ cathode, 300 kV, CS = 1.15 mm). Images were recorded with a CCD camera (Gatan) and Digital Micrograph 3.6.1 (Gatan) was used as evaluation software.

Hydrogen evolution experiments in UV and simulated sunlight were carried out in a continuously cooled 230 mL quartz glass reactor (see Fig. S1) with a PTFE septum under argon

atmosphere. The catalyst (10 mg) was suspended in a 0.5 M pH7 phosphate buffer solution (9 mL), triethanolamine (TEoA) was used as the sacrificial electron donor (1 mL), and H_2PtCl_6 (6 μL of 8 wt% in H_2O , ≈ 2.2 wt% Pt, Fig. S25†) was added as precursor for the *in situ* formation of the Pt co-catalyst while stirring. Buffered water conditions lead to higher activities and a more stable hydrogen evolution rate than using non-buffered water (Fig. S18†). The flask was evacuated and purged with argon to remove any dissolved gases in the suspension. Samples were simultaneously top-illuminated (top surface = 15.5 cm^2) at a distance of 22 cm with a 300 W xenon lamp with a water filter and dichroic mirror (Newport Oriel) blocking most of the wavelengths < 420 nm for simulated sunlight (spectral profile see Fig. S2) and < 250 nm for UV-Vis measurements, which amounts to a light intensity of about 380 mW cm^{-2} for the simulated sunlight and 510 mW cm^{-2} for the ≥ 250 nm measurements on the surface of the sample.

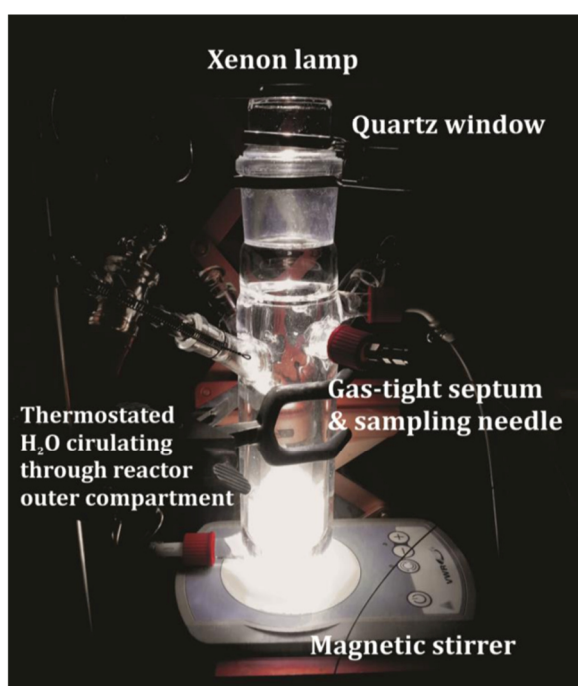


Fig. S1 Reactor set-up used for evaluating photocatalysts for hydrogen evolution.

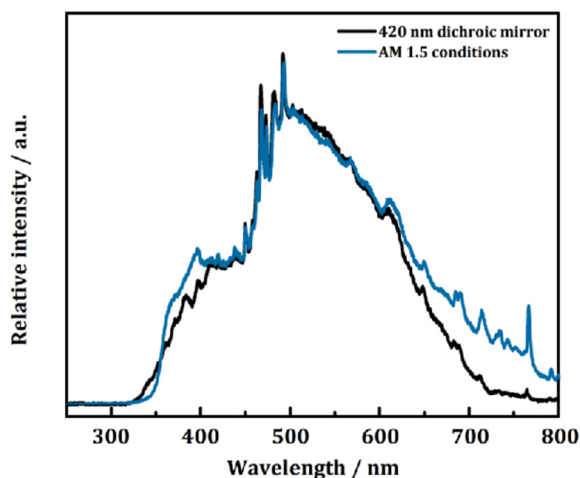


Fig. S2 Light intensity profile of the Xe lamp using the ≥ 420 nm dichroic mirror (simulated sunlight) compared to the AM 1.5 filter (filter and mirror purchased from Newport Oriel). Spectra were recorded with an Ocean Optics USB4000-XR1-ES spectrometer.

The headspace of the reactor was periodically sampled with an online injection system and the gas components were quantified by gas chromatography (thermal conductivity detector, argon as carrier gas). A high hydrophobicity of the CTF-1 and PTO samples was noticed at the beginning which was reduced during the photocatalytic experiment due to a better dispersion of the photocatalyst. Interestingly, the hydrogen evolution rates of the PTO-300s (> 1 eq ZnCl_2) illuminated with simulated sunlight were just slightly lower than for the samples illuminated with ≥ 250 nm. Apparent quantum efficiency calculations were estimated according to $\text{QE}\% = (2 \times H) / P \times 100 / 1$, where H = number of evolved hydrogen molecules and P = incident number of photons on the sample. The incident light was measured with a thermopile power meter with a constant efficiency response across the visible spectrum. Wavelength specific hydrogen evolution experiments were carried out in a 30 mL glass vial also in an argon atmosphere with PTFE/Teflon septa. The samples were top-illuminated for four hours with a full spectrum mirror (≥ 250 nm) and additional 40 nm FWHM light filters (400, 450, 500, 550 or 600 nm) (Thor labs). The irradiation area was 3.6 cm^2 . The hydrogen evolution rates were normalized with respect to an irradiation intensity on the sample surface of 14 mW cm^{-2} . For the internal comparison with other organic photocatalysts (Melon, PTI nanosheets and TFPT-COF), reported conditions for these materials were chosen which means using water instead of the buffered solution.

Four different PTO-300 samples were also tested under AM 1.5 conditions (100 mW cm^{-2}) which is shown in Figure S20.

Materials

All reactions were carried out under an argon atmosphere in flame-dried glassware. 1,4-Dicyanobenzene (98%), DMF (99.8%) and 1,5-bis(diphenylphosphino)pentane (97%) were obtained from Acros Organics. Anhydrous zinc chloride (99.995%, 25 mg product sealed in an ampule), 4-bromobenzonitrile (99%) and Pd(PPh₃)₄ (99%) were purchased from Sigma-Aldrich. Triflic acid and zinc cyanide (98%) were received from Alfa Aesar (98%) and used without further purifications.

Synthesis of photoactive phenyl-triazine oligomers (PTO). In a typical CTF synthesis^{S1} a Duran ampule (1.5 x 12 cm) was charged with finely ground 1,4-dicyanobenzene (500 mg, 3.90 mmol) and ZnCl₂ (1-15 equivalents, see Table 1) within a glove box. The ampule was flame sealed under vacuum and was subjected in a tube oven to temperatures between 300-350 °C for 168-96 h (see Table 1). After cooling to ambient temperature, the ampule was opened and its content ground thoroughly. An inhomogeneous temperature zone in addition to a high zinc chloride content yielded colorless, fiber-like crystals (which are not discussed here). The crude product was stirred in H₂O (75 mL) for 1 h, filtered, and washed with 1 M HCl (2 x 75 mL). The mixture was then stirred at 90 °C in 1 M HCl (75 mL) overnight, filtered, and subsequently washed with 1 M HCl (3 x 75 mL), H₂O (12 x 75 mL), THF (2 x 75 mL), and dichloromethane (1 x 75 mL). Finally, the powder was dried overnight in a desiccator.

Synthesis of CTF-1.^{S1} Similar to the synthesis described above, CTF-1 was obtained starting with 1,4-dicyanobenzene (500 mg, 3.90 mmol) under ZnCl₂ (1 equivalent) conditions at a reaction temperature of 400 °C for 46 hours.

Synthesis of 2,4,6-tris(*p*-bromophenyl)-1,3,5-triazine. This compound was prepared as per a modified literature procedure.^{S2} To a 15 ml Schlenk tube under argon, triflic acid (4.0 ml, 6.7 g, 44.6 mmol) was added and cooled to 0 °C. To this, 4-bromobenzonitrile (1.5 g, 8.2 mmol) was added in portions and the solution was continued to stir for an hour at 0 °C and then 16 hours at room temperature. The workup was done by pouring the reaction mixture in 100 mL ice cold water and neutralizing the resulting suspension with 25% ammonia solution. The precipitate was filtered off, washed with water (2 x 10 mL), acetone (3 x 5 mL) and dried in vacuum to afford the title compound as off-white solid (1.4 g, 94%). ¹H NMR (CDCl₃, 300 MHz): δ ppm 8.59 (d, *J* = 8.4 Hz, 6H), 7.72 (d, *J* = 8.4 Hz, 6H). ¹³C NMR (CDCl₃, 75 MHz): δ ppm 171.37, 135.07, 132.10, 130.55, 127.88.

Synthesis of 2,4,6-tris(*p*-cyanophenyl)-1,3,5-triazine (Trimer). In a microwave vial charged with DMF (10.0 mL), a stream of argon was bubbled for 30 min. To this was then added 2,4,6-tris(*p*-bromophenyl)-1,3,5-triazine (200 mg, 0.37 mmol), Zn(CN)₂ (67 mg, 0.57 mmol), Pd(PPh₃)₄ (25 mg, 0.022 mmol), and 1,5-bis(diphenylphosphino)pentane (10 mg, 0.022 mmol). The vial was sealed and the contents were heated in a microwave for 20 min at 150 °C. The resulting suspension was poured into water (100 mL) and then filtered, washed with water

(20 mL x 2), saturated sodium bicarbonate solution (10 mL x 2) and methanol (20 mL x 2) to obtain the crude product that was purified by flash chromatography (CHCl_3) to obtain 2,4,6-tris(*p*-cyanophenyl)-1,3,5-triazine (Trimer) (120 mg, 85%) as colorless solid. ^1H NMR 300 MHz ($\text{C}_2\text{D}_2\text{Cl}_4$; 70 °C): δ 8.87 (d, J = 8.3 Hz, 6H), 7.93 (d, J = 8.3 Hz, 6H). ^{13}C NMR 75 MHz ($\text{C}_2\text{D}_2\text{Cl}_4$; 70 °C): δ 170.90, 139.14, 132.46, 129.39, 118.09, 116.30. MS (MALDI): m/z : 384.4.

Synthesis of Melon.^{S3} A porcelain crucible was loaded with dicyandiamide and heated in a muffle furnace at 600 °C for 4 hours. The synthesis yielded a yellow colored powder.

Synthesis of 16% 4-AP doped amorphous PTI.^{S4} Dicyandiamide (0.50 g, 5.95 mmol), an eutectic mixture of lithium chloride (59.2 mol%) and potassium chloride (40.8 mol%) and 4-AP (72 mg, 16 % carbon-doping) as doping agent were ground and transferred in open porcelain crucibles, which were heated in a Argon purged horizontal tube furnace at 12 °C min⁻¹ to 550 °C for 6 hours. After grinding the sample, the heating procedure was repeated to gain a homogenous polymerized product. The syntheses yielded in a dark orange colored product which is in accordance with the literature.^{S4}

Synthesis of TFPT-COF and PTI-nanosheets according to the literature.^{S5,6}

Characterization of PTO_{organic phase}

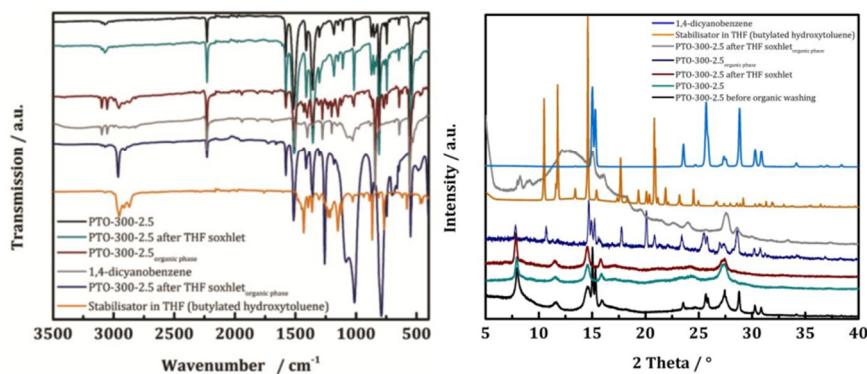


Fig. S3 Exemplary IR spectra (left) and PXRDs (right) of the obtained organic phase after washing PTO-300-2.5 using THF and DCM (PTO-300-2.5_{organic phase}) compared to pristine PTO-300-2.5, after further THF Soxhlet extraction, and of its organic phase from Soxhlet extraction. The IR spectra of the starting material 1,4-dicyanobenzene and of the THF-stabilizer butylated hydroxyl toluene is added for clarity. The first organic phase contains unreacted starting material and most likely smaller oligomers. The organic phase obtained by Soxhlet extraction includes also stabilizer impurities.

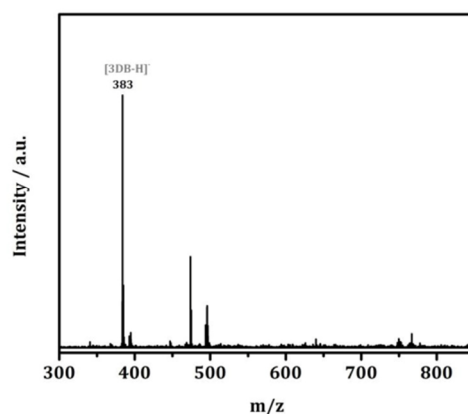


Fig. S4 MALDI-TOF spectrum (negative mode) of PTO-300-15_{organic phase} showing a trimer fragment. No signals were observed in the mass ranges below 300 and above 850.

XRD Characterization

Table S1 Shift of the layer stacking from PTO-300-1 to PTO-300-15 compared to CTF-1.

Sample	2 Theta / °	Layer distance [Å]
CTF-1 ^{S1}	26.2	3.40
PTO-300-1	26.8	3.32
PTO-300-2.5	27.3	3.26
PTO-300-5	27.3	3.26
PTO-300-10	27.3	3.26
PTO-300-15	27.3	3.26

Elemental Analysis and ICP

Table S2 Elemental analysis and BET surface areas of the presented PTOs compared to CTF-1 and calculated theoretical values of the elemental composition of 1,4-dicyanobenzene and the trimer.

Sample	N [wt%]	C [wt%]	H [wt%]	Zn [wt%] ^d	wt.% C/N	BET SA ^a [m ² g ⁻¹]
Calculated	21.86	74.99	3.15	0	3.43	-
1,4-dicyanobenzene and trimer	21.86	74.99	3.15	0	3.43	-
CTF-1 according to Kuhn <i>et al.</i> ^{S1}	19.3	72.8	3.2	-	3.77	791
CTF-1 according to Ren <i>et al.</i> ^{bS7}	20.71	74.49	3.03	-	3.60	2
CTF-1 according to Ren <i>et al.</i> ^{cS7}	22.58	72.93	3.32	-	3.23	4
PTO-300-1	21.61	74.30	3.29	0.03	3.44	116
PTO-300-2.5	21.38	73.53	3.23	0.02	3.44	12
PTO-300-5	21.57	74.25	3.28	0.04	3.44	19
PTO-300-10	21.69	74.45	3.32	0.11	3.43	13
PTO-300-15	20.99	72.75	3.48	0.03	3.47	21
PTO-350-1	21.13	73.59	3.34	0.01	3.48	10
PTO-350-10	20.39	72.93	3.15	0.01	3.58	6
CTF-1 as synthesized	18.60	70.20	3.30	0.21	3.77	610

^aFrom argon physisorption measurements (Figure S21-22). ^bTFMS catalysed synthesis and further heating step at 400 °C for 40 h. ^cTFMS catalysed and microwave-assisted synthesis. ^dMeasured by ICP.

XPS Measurements

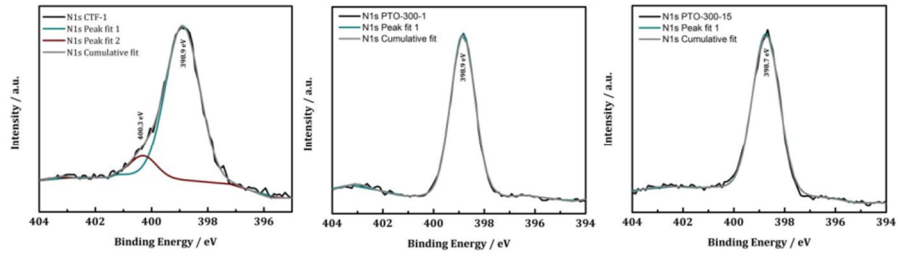


Fig. S5 N1s XPS spectra with applied peak and cumulative fits of CTF-1 (left), PTO-300-1 (middle) and PTO-300-15 (right).

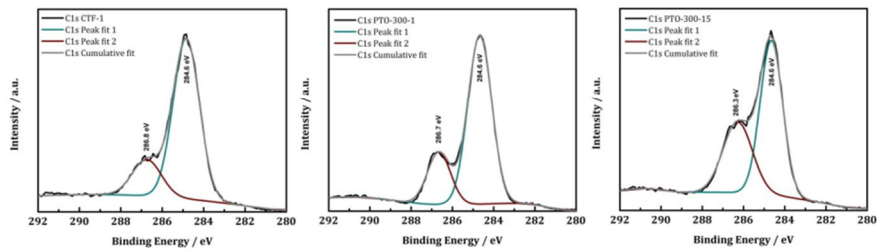


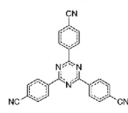
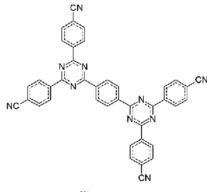
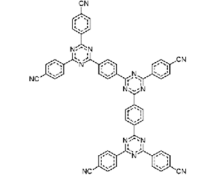
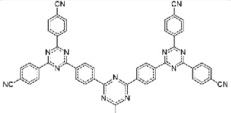
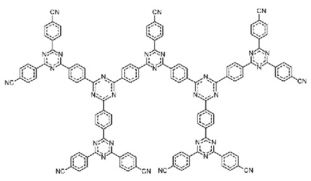
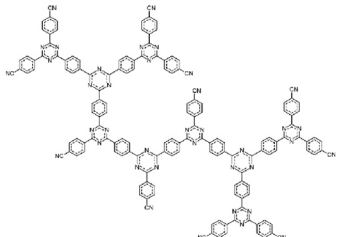
Fig. S6 C1s XPS spectra with applied peak and cumulative fits of CTF-1 (left), PTO-300-1 (middle) and PTO-300-15 (right).

MALDI-TOF Measurements and IR Analysis**Table S3** Summarized mass peaks observed in the MALDI-TOF spectra of PTO-300-1 and PTO-300-15.

PTO-300-1	PTO-300-15	Connectivity
128	128	monomer
256		dimer
384	384	trimer
641	641	pentamer (chain, dendrimer)
897	897	heptamer (chain, dendrimer)
1153	1153	nonamer (chain, dendrimer)
-	1409	endecamer (chain, dendrimer)
1499	1551	dodecamer (chain or ring) without 1CN (PTO-300-1) or with 1N (PTO- 300-15)
2049	-	16mer
2178	-	17mer (chain, dendrimer)
2306	-	18mer
2434	-	19mer (chain, dendrimer or ring)
2563	-	20mer
2690	-	21mer (chain, dendrimer)
2819	-	22mer
2947	-	23mer (chain)

Dendrimers: $(3 + 2n; n = 0, 1, 2, 3, \dots)$ multiples of 1,4-dicyanobenzene mass ($m/z = 128.1$)

Table S4 Observed dendrimeric oligomers of CTF-1 and the specific nitrile-to-triazine ratio.

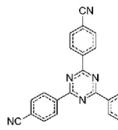
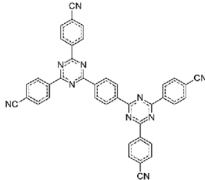
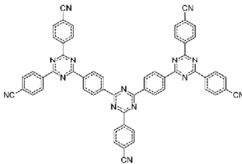
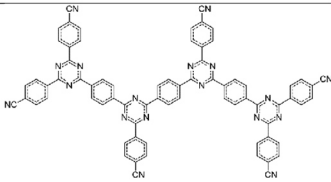
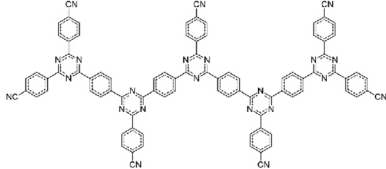
Chain Fragments	n	$(3+2n)$	m/z	Number of $C\equiv N$ / Number of $C=N$ bonds
	0	3	384.4	$3 / 6 \cdot 1 = 0.50$
	1	5	640.7	$4 / 6 \cdot 2 = 0.33$
	2	7	896.9	$5 / 6 \cdot 3 = 0.28$
	3	9	1153.2	$6 / 6 \cdot 4 = 0.25$
	6	15	1922.0	$9 / 6 \cdot 7 = 0.21$
	8	19	2434.5	$11 / 6 \cdot 9 = 0.20$

S12

S13

Chain Fragments: $(3 + 2n; n = 0, 1, 2, 3, \dots)$ multiples of 1,4-dicyanobenzene mass ($m/z = 128.1$)

Table S5 Linear chain fragments (of CTF-1) observable in the mass spectra for the PTO samples and the specific nitrile-to-triazine ratio.

Chain Fragments	n	$(3+2n)$	m/z	Number of C≡N / Number of C=N bonds
	0	3	384.4	$3 / 6 \cdot 1 = 0.50$
	1	5	640.7	$4 / 6 \cdot 2 = 0.33$
	2	7	896.9	$5 / 6 \cdot 3 = 0.28$
	3	9	1153.2	$6 / 6 \cdot 4 = 0.25$
	4	11	1409.4	$7 / 6 \cdot 5 = 0.23$

S14

S15

Ring Fragments: $(12 + 7n; n = 0, 1, 2, 3, \dots)$ multiples of 1,4-dicyanobenzene mass ($m/z = 128.1$)

Table S6 Ring fragments (off CTF-1) observable in the mass spectra for the PTO samples and the specific nitrile-to-triazine ratio.

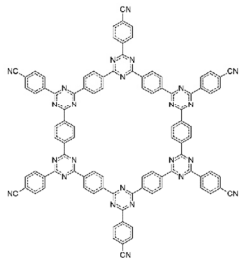
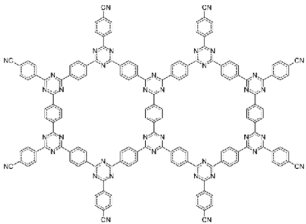
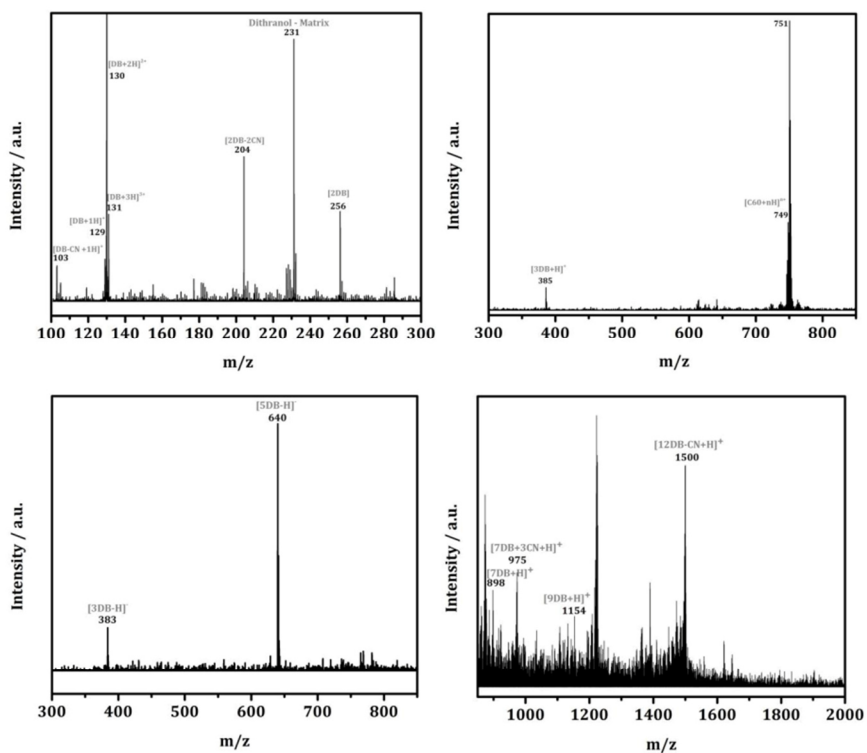
Chain Fragments	n	$(12+7n)$	m/z	Number of C≡N / Number of C=N bonds
	0	12	1537.6	$6 / 6 \cdot 6 = 0.17$
	1	19	2434.5	$8 / 6 \cdot 10 = 0.13$

Table S7 Nitrile-to-triazine ratios calculated from the IR signals (from signal intensities and integral, after background subtraction) of PTO-300-1 and PTO-300 synthesized with higher zinc chloride dilution: PTO-300-2.5, PTO-300-10 and PTO-300-15 in comparison to the trimer.

Sample	Nitrile-to-triazine ratio (intensity)	Nitrile-to-triazine ratio (integral)
PTO-300-1	0.18 (0.18)	0.08 (0.09)
PTO-300-15	0.33 (0.32)	0.18 (0.16)
PTO-300-10	0.38 (0.46)	0.18 (0.23)
PTO-300-2.5	0.41	0.18
Trimer	0.51	0.29

Mass Spectra of PTO-300-1



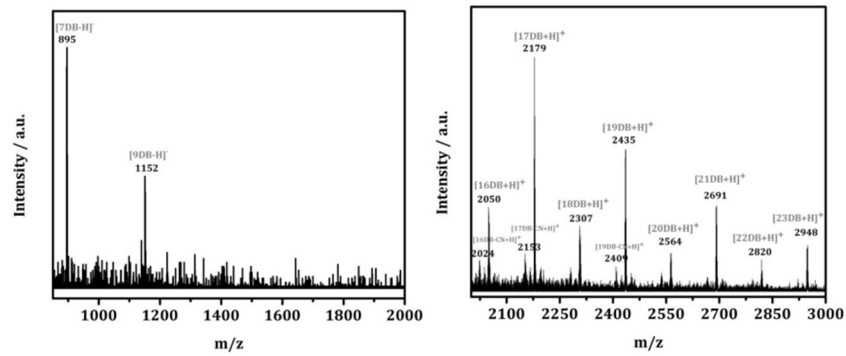
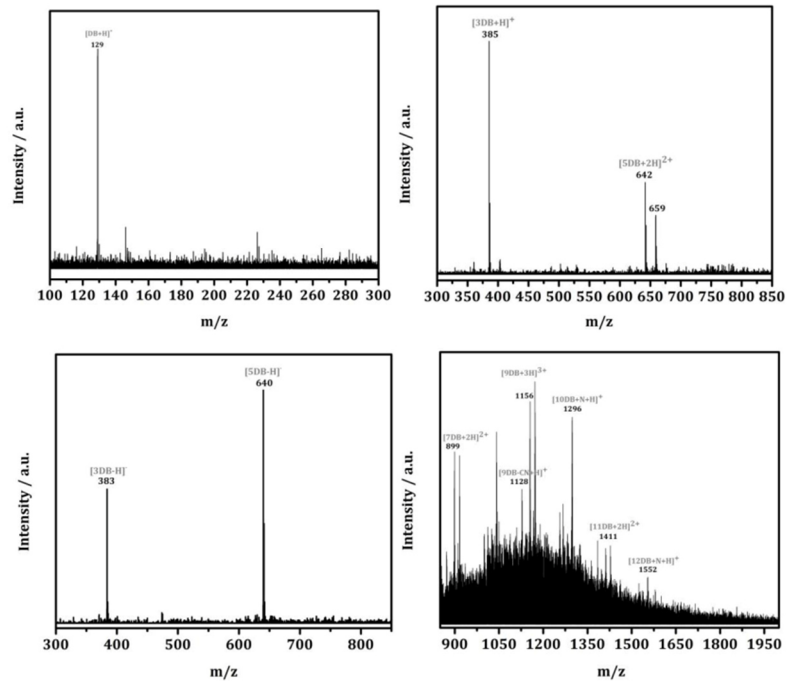


Fig. S7 Representative MALDI-TOF spectra of the PTO-300-1 sample, measured in the mass range > 100 and < 3000 (either in positive or negative mode, indicated with $+H^+$ or $-H^+$, respectively). DB represents the mass of the precursor 1,4-dicyanobenzene ($m/z = 128$). The signals at 230 and 750 correspond to the matrix.

Mass Spectra of PTO-300-15



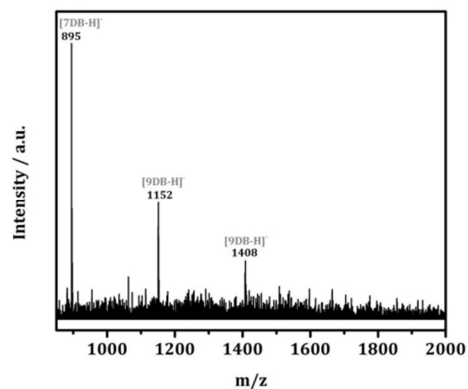
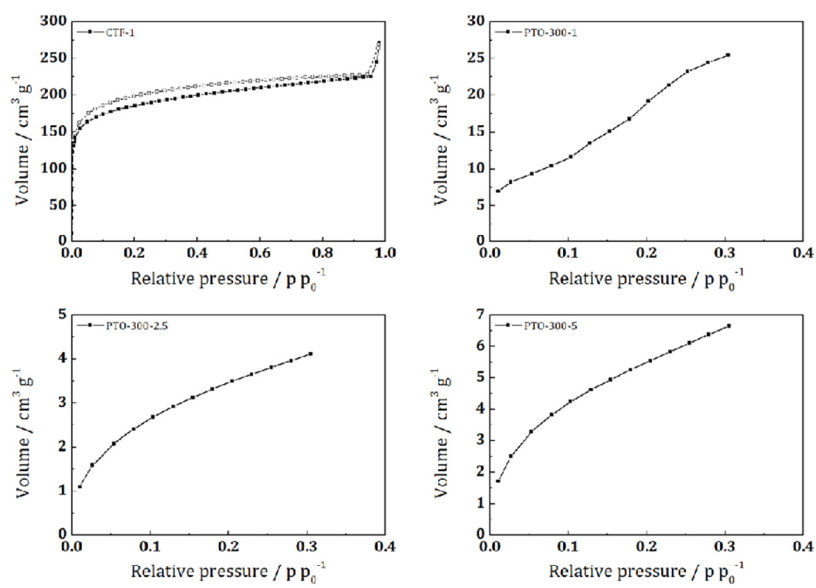


Fig. S8 Representative MALDI-TOF spectra of the PTO-300-15 sample, measured in the mass range > 100 and < 2000 (either in positive or negative mode, indicated with $+H^+$ or $-H^+$, respectively). DB represents the mass of the precursor 1,4-dicyanobenzene ($m/z = 128$). The signals at 230 correspond to the matrix.

Ar-Physisorption Measurements



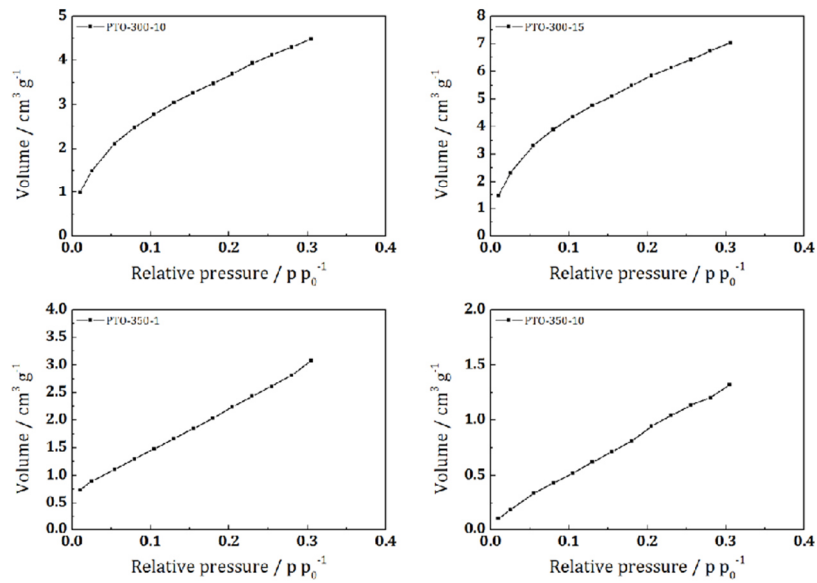
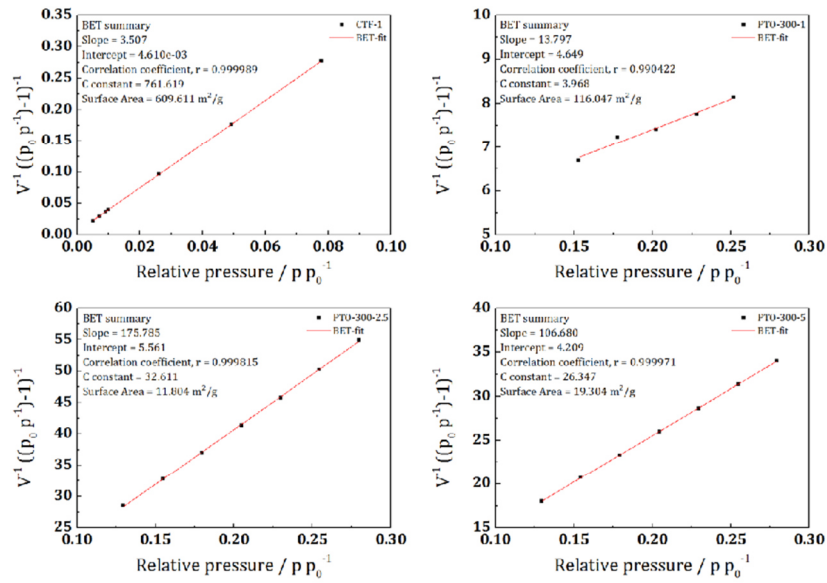


Fig. S9 Argon adsorption (filled squares) and desorption (empty squares) isotherm of CTF-1 and 13-point argon adsorption isotherms of PTO-300s and PTO-350s for BET calculations.



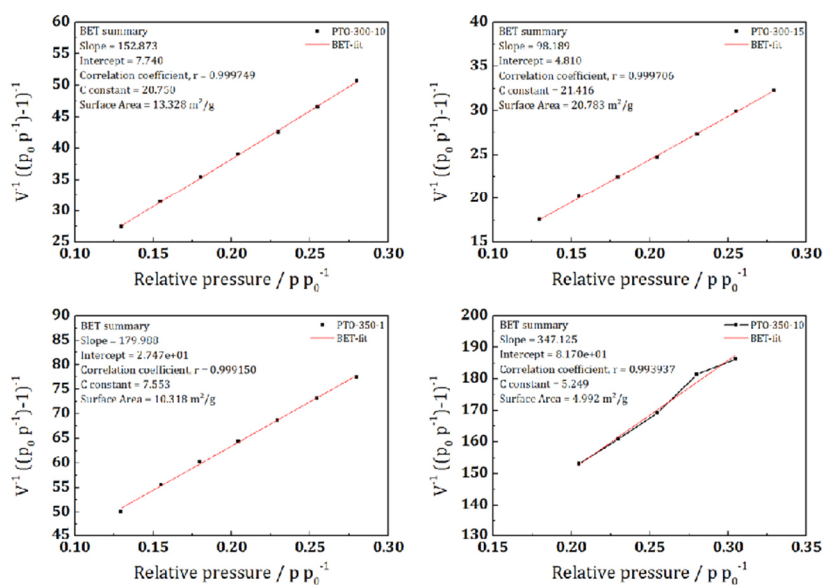


Fig. S10 BET-fits and BET calculation data of CTF-1, PTO-300s and PTO-350s. In accordance with the ISO recommendations multipoint BET tags equal or below the maximum in $V \cdot (1 - P/P_0)$ were chosen.

NMR Measurements

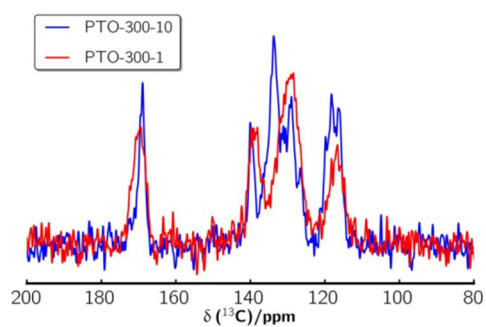


Fig. S11 ^{13}C SP ssNMR spectra of PTO-300-10 and PTO-300-1 recorded with MAS using a rotational frequency of 20 kHz.

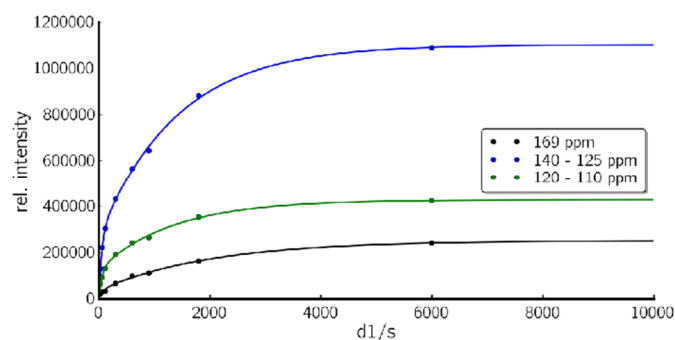


Fig. S12 Recycle delay plotted against signal intensity for ^{13}C SP ssNMR spectra of PTO-300-10 and fitted with the following biexponential function $I(x) = I_{0,1}(1 - \exp(-\frac{x}{T_{1,1}})) + I_{0,2}(1 - \exp(-\frac{x}{T_{1,2}}))$.

The values for I_0 and T_1 are presented in the following table.

	$I_{0,1}$	$T_{1,1} / \text{s}$	$I_{0,2}$	$T_{1,2} / \text{s}$
169 ppm	36716	742	215416	2013
140 – 125 ppm	268771	535	833953	1406
120 – 110 ppm	126903	570	301307	1334

The underestimation of the triazine signal due to the longer spin-lattice relaxation time was calculated from the ratio of the measured intensity at 6000 s to $I_{0,1} + I_{0,2}$ and gives about 5%. For the other signals this deviation is only about 1%.

Photocatalytic Experiments

Hydrogen Evolution Experiments

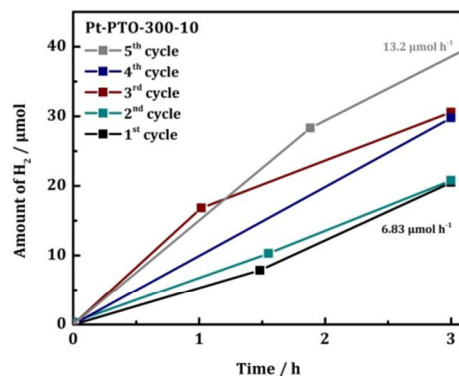


Fig. S13 Cyclic measurements with platinum-modified PTO-300-10 irradiated with simulated sunlight for three hours for each cycle. After each cycle the reactor was evacuated and purged with argon and irradiation was restarted.

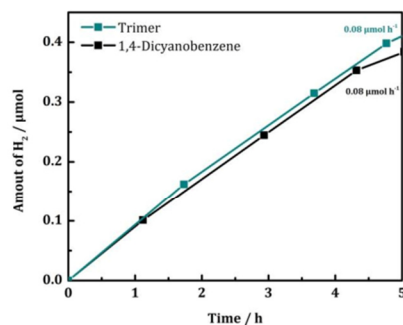


Fig. S14 Photocatalytic tests of the starting material 1,4-dicyanobenzene (black) and the trimer (cyan) using a buffered (pH 7, 0.5 M phosphate buffer) 10 vol% TEoA solution and platinum as co-catalyst during UV-Vis illumination (≥ 250 nm).

Table S8 Photocatalytic activity (with Pt as co-catalyst) versus the surface area.

Sample	BET SA [$\text{m}^2 \text{g}^{-1}$]	HER [$\mu\text{mol h}^{-1}$]	HER [$\mu\text{mol h}^{-1}$] / BET SA [$\text{m}^2 \text{g}^{-1}$]
PTO-300-1	116	1.45	0.01
PTO-300-2.5	12	6.91	0.58
PTO-300-5	19	3.36	0.18
PTO-300-10	13	9.00	0.69
PTO-300-15	21	9.40	0.48
CTF-1 as synthesized	610	0.02	0.00

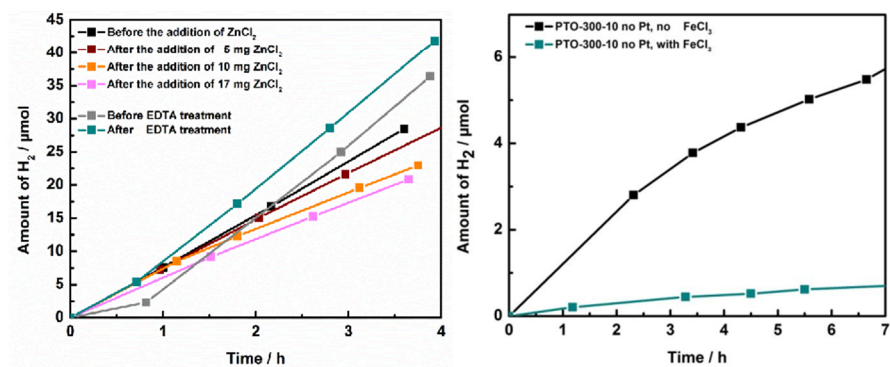


Fig. S15 Hydrogen evolution rates of Pt-PTO-300-10 before and after addition of several amounts (5, 10 or 17 mg) of ZnCl_2 and before and after stirring (for 2 days) / excessively washing the sample in EDTA (left). Hydrogen evolution rates (without the addition of H_2PtCl_6) of PTO-300-10 before and after stirring the sample in a FeCl_3 solution and an excessive washing procedure to achieve Fe^{3+} modification or, more accurately “poisoning” of the active site (likely the free electron pair at the nitrogen site of the nitrile group or the triazine) by coordination. However, the coordination mode is unclear, even if we can clearly

ascertain that iron is in the sample (see Table S9). The Fe^{3+} -treated sample showed a drastically decreased activity. The addition of platinum leads to an identical rate for both materials suggesting that not all active sites are poisoned by the Fe^{3+} or that platinum deposited on the Fe^{3+} site still promotes the electron transfer process.

Table S9 ICP data of the PTO-300-10 sample after/before EDTA treatment and Fe^{3+} poisoning.

Sample	Zn	Fe
PTO-300-10 before EDTA treatment	0.107	0.000
PTO-300-10 after EDTA treatment	0.079	0.000
PTO-300-10 after Fe^{3+} -poisoning	0.107	0.960

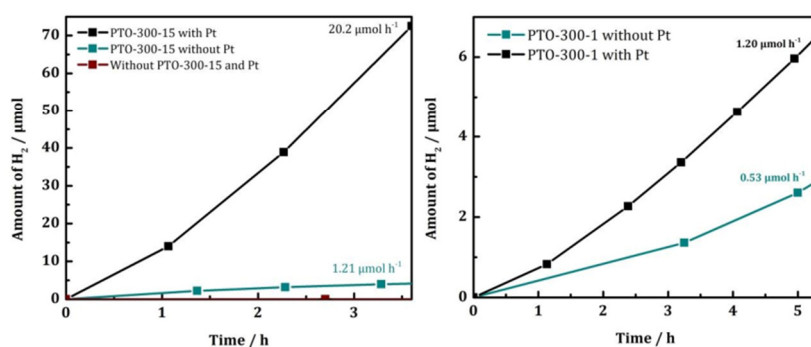


Fig. S16 Photocatalytic measurements (simulated sunlight) of dispersed PTO-300-15 (left) and PTO-300-1 (right) containing $6 \mu\text{L H}_2\text{PtCl}_6$ (black), in comparison to a photocatalysis run without the addition of platinum as co-catalyst (cyan). The red slope represents a control experiment showing the illuminated buffered TEoA solution without photocatalyst and platinum.

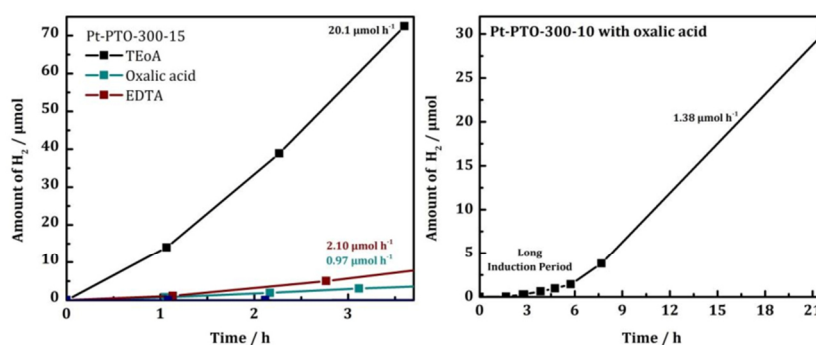


Fig. S17 Photocatalytic tests with Pt-PTO-300-15 (10 mL buffered - pH 7, 0.5 M phosphate buffer - electron donor solution, simulated sunlight, $6 \mu\text{L H}_2\text{PtCl}_6$) using different electron donors: TEoA (10 vol%;

black), oxalic acid (100 mg; cyan) and EDTA (10 vol%; red) (left). Stability test for more than 20 hours of Pt-PTO-300-10 using oxalic acid as electron donor (right).

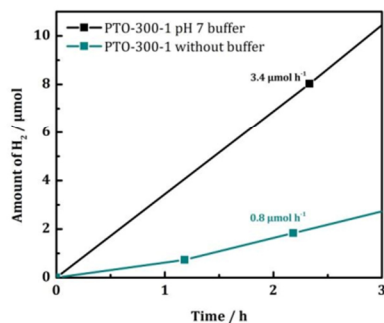


Fig. S18 Photocatalytic activity of Pt-PTO-300-1 dispersed in a phosphate buffered (pH 7, 0.5 M; black) compared to a non-buffered (cyan) 10 vol% TEoA solution illuminated with simulated sunlight.

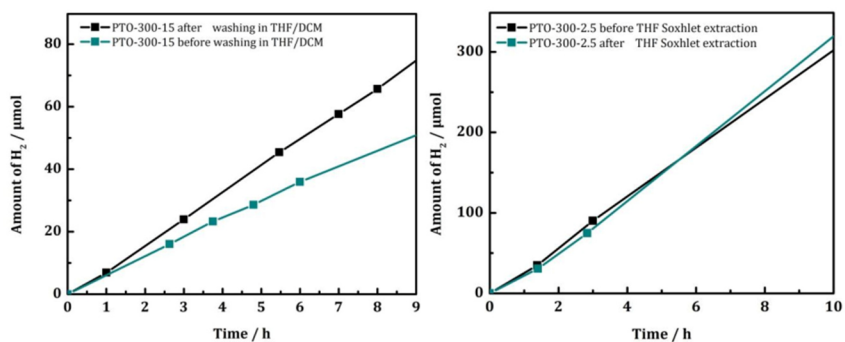


Fig. S19 Photocatalytic activity of Pt-PTO-300-15 before (cyan) and after (black) the first washing procedure with THF/DCM, showing that less active starting materials or rather small oligomers (such as trimers) are washed away (left). Photocatalytic activity of Pt-PTO-300-2.5 before (black) and after THF Soxhlet extraction (cyan) showing that the first washing procedure is sufficient to get rid of less active impurities (right).

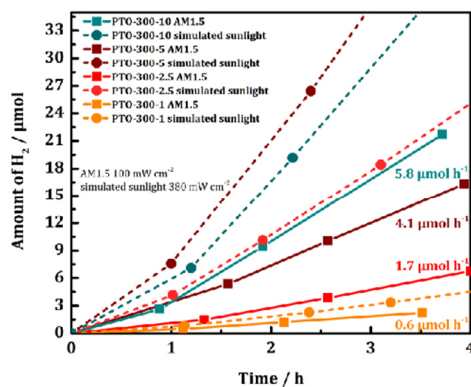


Fig. S20 Photocatalytic activity of four different PTO-300 samples under AM1.5 (100 mW cm^{-2}) vs. simulated sunlight conditions (380 mW cm^{-2}) (pH 7, 0.5 M phosphate buffer, 10 vol% TEoA solution, 2.2 wt% Pt).

Batch-to-Batch Variations

Table S10 Hydrogen evolution rates of several PTO-300 batches (Fig. S21). Colored values mark the “outlier” batches which were not used for the calculation of the “average” hydrogen evolution rate.

Sample	HER (several batches) / $\mu\text{mol h}^{-1}$ ^a
PTO-300-1	1.5, 1.5, 1.7
PTO-300-2.5	7.4, 8.0, 13.1, 15.6, 30.3
PTO-300-5	3.4 , 4.0 , 14.4, 15.8
PTO-300-10	8.3, 9.0, 9.9, 10.9
PTO-300-15	8.6, 8.7, 9.4, 11.6, 20.1

^aMeasurement error of 15%.

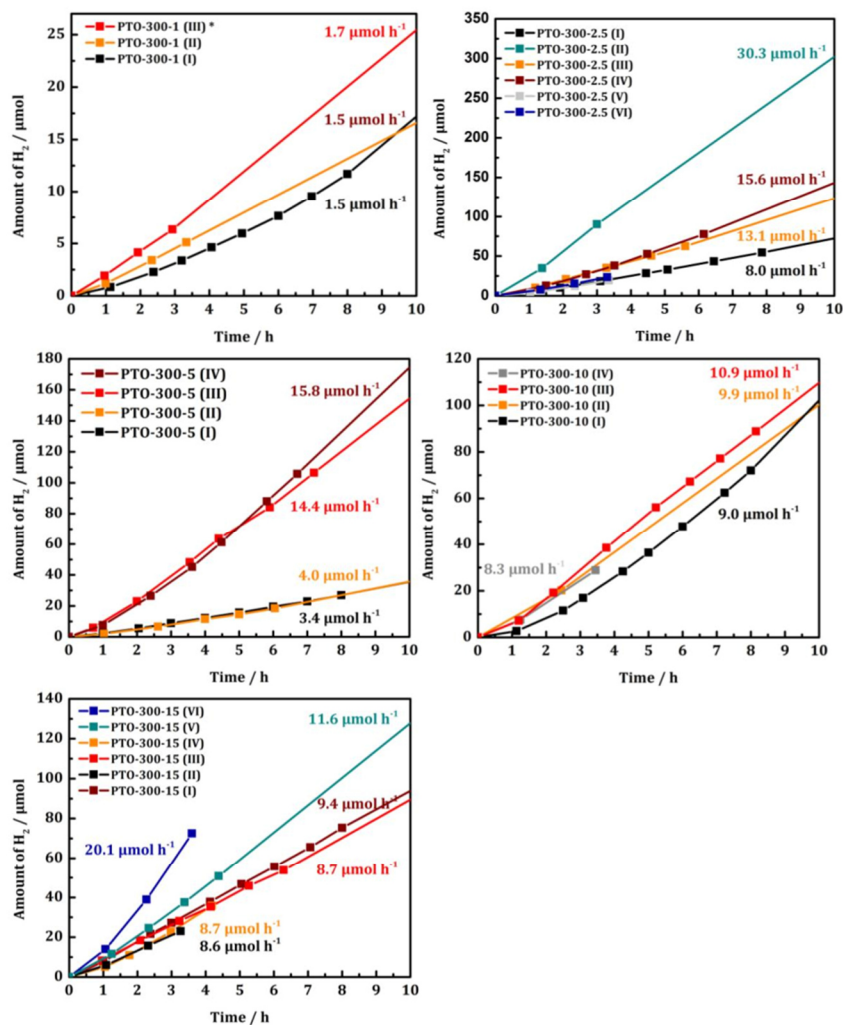


Fig. S21 Photocatalytic activity of various PTO-300 batches illuminated under simulated sunlight conditions (pH 7, 0.5 M phosphate buffer, 10 vol% TEoA solution, 2.2 wt% Pt) to illustrate batch-to-batch variations when synthesized in excess of ZnCl₂.

Characterization of the Photocatalyst after Photocatalysis

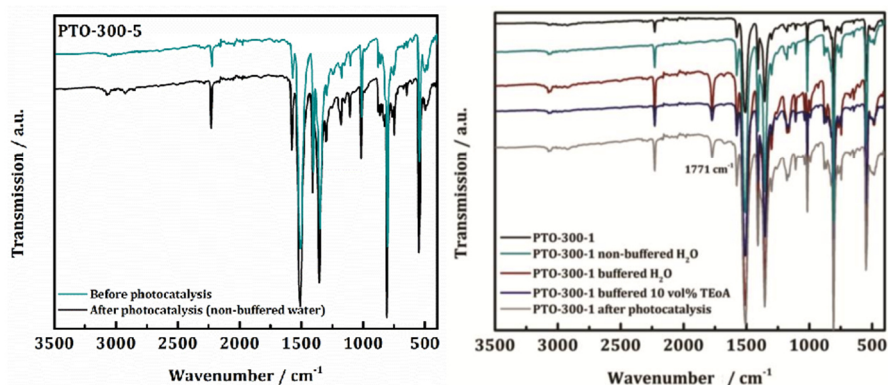


Fig. S22 IR spectroscopic characterization of the photocatalyst before (left: Pt-PTO-300-5; right: Pt-PTO-300-1) and after 24 hour of photocatalysis (left: in non-buffered water; right: in buffered water) as well as after each preparation step of the photocatalytic experiment: Stirring the photocatalyst in water or in pH 7 0.5 M phosphate buffer and after the addition of 10 vol% TEoA. A new band at 1771 cm⁻¹ appears due to the buffer. No changes caused by photodegradation.

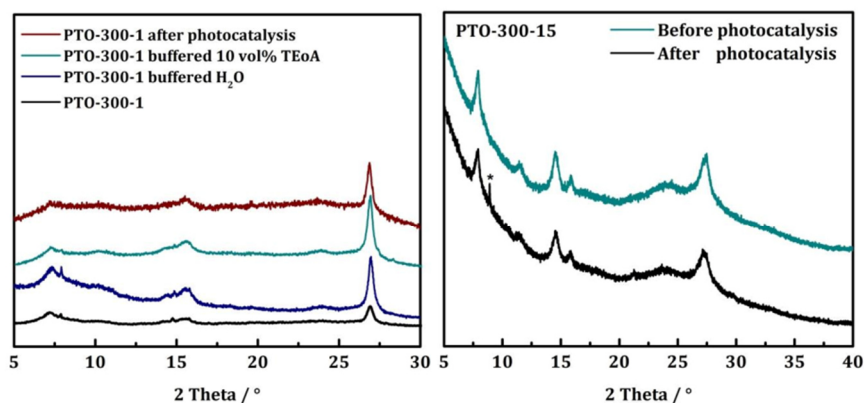


Fig. S23 PXRD of the photocatalyst PTO-300-1 (left) and PTO-300-15 (right) before and after 24 hour of photocatalysis in buffered water (left, Pt-PTO-300-1; right, Pt-PTO-300-15). In case of PTO-300-1, PXRD patterns are also shown after each preparation step of the photocatalytic experiment: Stirring the photocatalyst in pH 7 0.5 M phosphate buffer and after the addition of 10 vol% TEoA. The sharp reflection marked with an asterisk is an artefact due to the sample holder.

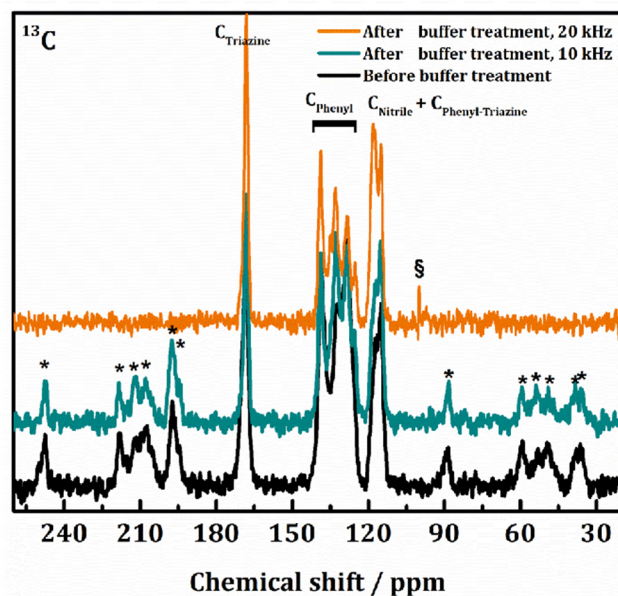


Fig. S24 Solid state NMR ^{13}C spectra (contact time 5 ms) of PTO-300-15 before (spinning speed 10 kHz) and after (spinning speed 10 and 20 kHz) stirring the photocatalyst three days in buffered water (pH 7, 0.5 M phosphate buffer). Bands marked with an asterisk are rotational side bands. The sharp peak marked with “S” is an artefact. No additional carbon signals are detected after buffer treatment which makes hydrolysis of the nitrile groups unlikely.

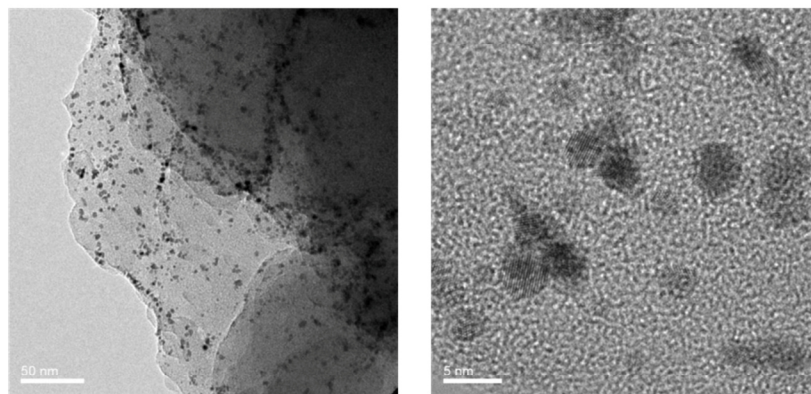


Fig. S25 TEM images of the Pt-modified PTO-300-1 sample after photocatalysis. Pt-nanoparticles around 4 nm of average size have been formed on the sample surface after photo-reduction of H_2PtCl_6 .

TEM Characterization

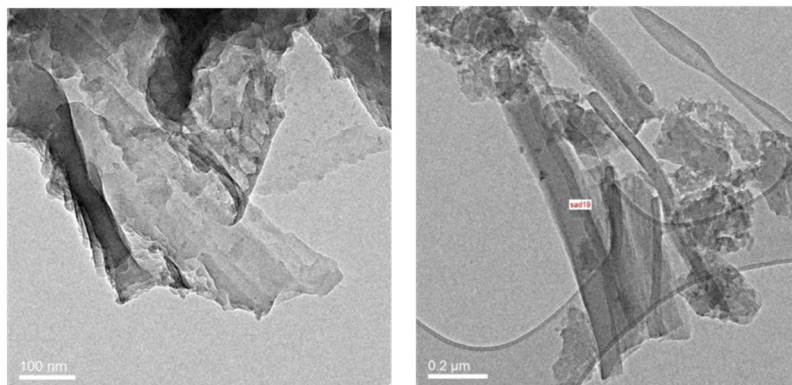


Fig. S26 TEM image of PTO-300-1 showing a layered-like material (left). TEM image of PTO-300-10 showing mixed phases of clusters and either fibers or furled layers (right).

References

- S1 P. Kuhn, M. Antonietti and A. Thomas, *Angew. Chem. Int. Ed.*, 2008, **47**, 3450.
- S2 H. Tanaka, K. Shizu, H. Nakanotani and C. Adachi, *Chem. Mater.*, 2013, **25**, 3766.
- S3 X. Wang, K. Maeda, A. Thomas, K. Takahabe, G. Xin, J. M. Carlsson, K. Domen and M. Antonietti, *Nat. Mater.*, 2009, **8**, 76.
- S4 K. Schwinghammer, B. Tuffy, M. B. Mesch, E. Wirnhier, C. Martineau, F. Taulelle, W. Schnick, J. Senker and B. V. Lotsch, *Angew. Chem. Int. Ed.*, 2013, **52**, 2435.
- S5 L. Stegbauer, K. Schwinghammer and B. V. Lotsch, *Chem. Sci.*, 2014, **5**, 2789.
- S6 K. Schwinghammer, M. B. Mesch, V. Duppel, C. Ziegler, J. Senker and B. V. Lotsch, *J. Am. Chem. Soc.*, 2014, **136**, 1730.
- S7 S. Ren, M. J. Bojdys, R. Dawson, A. Laybourn, Y. Z. Khimiyak, D. J. Adams, A. I. Cooper, *Adv. Mater.*, 2012, **24**, 2357.

6.2 Bestimmung der Länge von Heptazin-Oligomeren mittels 1D Spektren

Low-Molecular-Weight Carbon Nitrides for Solar Hydrogen Evolution

V. W. Lau,^{†,§} M. B. Mesch,[‡] V. Duppel,^{†,§} V. Blum,^{||} J. Senker,[‡] B. V. Lotsch^{*,†,§,¥}

Erschienen in:

Journal of the American Chemical Society 2015, 137, 1064

Reprinted with permission from Journal of the American Chemical Society 2015, 137, 1064. Copyright 2015 American Chemical Society.

[†] Max Planck Institute for Solid State Research, Heisenbergstr. 1, 70569 Stuttgart, Germany[‡] Department of Inorganic Chemistry III, University of Bayreuth, Universitätsstr. 30, 95447 Bayreuth, Germany[§] Department of Chemistry, University of Munich, Butenandtstr. 5-13, 81377 Munich, Germany^{||} Department of Mechanical Engineering and Materials Science and Center for Materials Genomics, Duke University, Durham, North Carolina 27708, United States[¥] Nanosystems Initiative Munich (NIM) and Center for Nanoscience, Schellingstr. 4, 80799 Munich, Germany^{*} B.Lotsch@fkf.mpg.de

6.2.1 Low-Molecular-Weight Carbon Nitrides for Solar Hydrogen Evolution

Low-Molecular-Weight Carbon Nitrides for Solar Hydrogen Evolution

Vincent Wing-hei Lau,^{†,§} Maria B. Mesch,[‡] Viola Duppel,^{†,§} Volker Blum,^{||} Jürgen Senker,[‡] and Bettina V. Lotsch^{*,†,§,⊥}

[†]Max Planck Institute for Solid State Research, Heisenbergstraße 1, 70569 Stuttgart, Germany

[‡]Department of Inorganic Chemistry III, University of Bayreuth, Universitätsstraße 30, 95447 Bayreuth, Germany

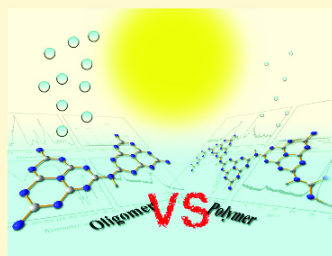
[§]Department of Chemistry, University of Munich, Butenandtstraße 5-13, 81377 Munich, Germany

^{||}Department of Mechanical Engineering and Materials Science and Center for Materials Genomics, Duke University, Durham, North Carolina 27708, United States

[⊥]Nanosystems Initiative Munich (NIM) and Center for Nanoscience, Schellingstraße 4, 80799 Munich, Germany

Supporting Information

ABSTRACT: This work focuses on the control of the polymerization process for melon ("graphitic carbon nitride"), with the aim of improving its photocatalytic activity intrinsically. We demonstrate here that reduction of the synthesis temperature leads to a mixture of the monomer melem and its higher condensates. We show that this mixture can be separated and provide evidence that the higher condensates are isolated oligomers of melon. On evaluating their photocatalytic activity for hydrogen evolution, the oligomers were found to be the most active species, having up to twice the activity of the monomer/oligomer mixture of the as-synthesized material, which in turn has 3 times the activity of the polymer melon, the literature benchmark. These results highlight the role of "defects", i.e., chain terminations, in increasing the catalytic activity of carbon nitrides and at the same time point to the ample potential of intrinsically improving the photocatalytic activity of "carbon nitride", especially through the selective synthesis of the active phase.



INTRODUCTION

Hydrogen production by photocatalytic water splitting is a promising technology for the storage and direct conversion of solar into chemical energy. The chemical energy can then be extracted using, for example, fuel cells with high efficiency, yielding only water as the byproduct. This cycle forms the basis of the energy paradigm known as the "hydrogen economy", a sustainable and environmentally benign alternative to the current practice based on the combustion of fossil fuels.¹ Following the seminal publication of Honda and Fujishima on TiO₂-photocatalyzed water splitting four decades ago,² many photocatalytic materials have been identified, of which the most active ones include La-doped NaTaO₃³ and the solid solution Ga_{0.88}Zn_{0.12}N_{0.88}O_{0.12}.⁴ However, none of these photocatalysts satisfies the requirements for commercial application, as they often require complex synthetic processes or are composed of rare and expensive elements, making their preparation uneconomical. Furthermore, many of these materials, especially the oxides, have low photocatalytic activity under visible light, the main constituent of solar irradiation at sea level.⁵

One new and promising class of photocatalysts is the so-called "graphitic carbon nitride", which are polymers based on the condensation products of melem (2,5,8-triamino-triazine, Scheme S1, Supporting Information).^{6–8} Note that the term "graphitic carbon nitride" or "g-C₃N₄" is used only to

keep consistency with the literature; it is in fact a misnomer considering that these materials do not possess the stoichiometric ratio C₃N₄, but always contain a sizable amount of hydrogen (≈2 wt %), consistent with the composition of Liebig's melon, C₆N₉H₃, a 1D carbon nitride polymer. Originally inspired by the "harder than diamond" postulate,⁹ this family of materials were thought to be a precursor to the predicted β-C₃N₄ and have been heavily investigated for their synthetic pathway and structure.^{10–16} The main advantages of these materials as photocatalysts are that they can be readily synthesized by heat treatment of inexpensive precursors (e.g., melamine or dicyandiamide), are active under visible light irradiation, and are chemically stable. Although their photocatalytic activity is low compared to the record holders mentioned above, there are still significant avenues for performance enhancement. Some strategies for improving their activity include texturization or morphology control to increase the surface area,^{17–22} chemical modification to red-shift the absorption edge,^{23–26} and band alignment by coupling with other semiconductors, photocatalysts, and cocatalysts to improve the electron–hole separation.^{27–34}

Received: April 9, 2014

Published: December 24, 2014

Despite the growing number of publications exploring these strategies, the literature has focused almost entirely on the polymer melon as the photocatalyst and overlooked the rich diversity of other related carbon nitride materials with different degrees of polymerization. For example, a change in synthesis conditions (temperature, pressure, atmosphere, or synthesis medium) can yield a variety of phases, including oligomers and polymers of triazine, adduct phases of melem, coordination and hydrogen-bonded compounds.^{15,35–38} Recent results have shown that not only are triazine polymers active for photocatalytic hydrogen and oxygen evolution, but also chemical modifications can enhance their activity to values even exceeding that of the heptazine polymer.^{39,40}

Another sparsely explored topic concerns the fundamental properties of these carbon nitride materials, particularly the nature of the active species, its mechanistic operation, and strategies to intrinsically improve their activity, rather than extrinsically by red-shifting the absorption through doping and increasing the surface area through morphology control. Since highly crystalline melem and melon, obtainable only by synthesis in closed ampoules under an autogenous pressure of ammonia (which induces partial de- and repolymerization, thereby leading to defect healing¹⁴), have negligible photocatalytic activity, the currently accepted postulate is that “surface terminations and defects seem to be the real active sites”.⁷ A more detailed understanding of its catalytic aspects can provide the guiding principles for bottom-up design and synthesis of carbon nitride photocatalysts, particularly when many synthetic modifications are now available for the heptazine skeleton.⁴¹

Thus, to gain further insights into the nature of the active sites and identify the criteria necessary for photocatalytic activity in the carbon nitride family, we direct our focus away from the polymer. Specifically, we investigate here the synthesis and characterization of a carbon nitride material with lower molecular weight than the polymer, and how its structural features affect its performance for photocatalytic hydrogen evolution when compared to the polymer.

RESULTS AND DISCUSSION

In our methodology, we selected synthetic conditions that favor the condensation of melamine into melem and higher condensation products but not completely to melon (temperatures between 380 and 490 °C based on results from temperature-programmed XRD and thermogravimetric analysis).^{15,42} We also employed an open vessel rather than a closed ampoule, such that the ammonolytic depolymerization did not occur, thus favoring the kinetically rather than thermodynamically driven formation of low condensed melem oligomers, in line with the increased formation of chain terminations.

The product obtained at the reduced synthesis temperature of 450 °C for 12 h of calcination at 5 °C min⁻¹ heating ramp, tentatively notated as “as-synthesized melem oligomer”, exhibited a photocatalytic activity more than twice that of melon in acidic, neutral, or alkaline conditions under AM 1.5 conditions (Figure 1 and Figure S2, Supporting Information). Here, the benchmark material melon was synthesized at 550 °C for 12 h in argon, corresponding to the typical literature protocols;⁴³ crystalline melon was not used, as we have verified its negligible activity. The photocatalytic activity of the as-synthesized melem oligomer was sustained for over 120 h without any decrease, demonstrating that the catalyst stability is comparable to melon. As will be shown and discussed in more

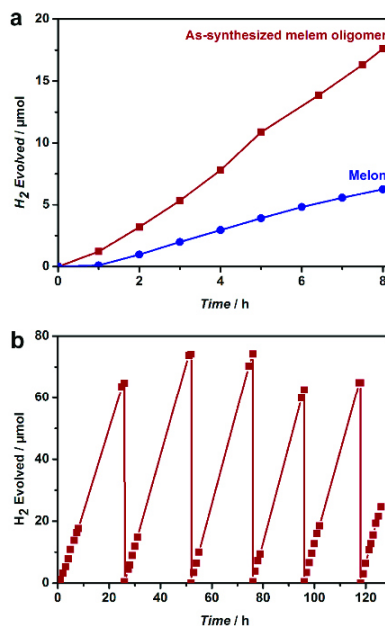


Figure 1. (a) Photocatalytic hydrogen evolution of the as-synthesized melem oligomer, compared with melon. (b) Extended photocatalytic test for 129 h of the as-synthesized melem oligomer, both in a pH 7 phosphate buffer system (PBS). After every overnight run, the reactor headspace was evacuated and purged with argon. Methanol (500 μL) was added on the 52nd and 118th hour after the overnight run.

detail below, the as-synthesized melem oligomer absorbs less in the visible spectrum than melon, indicating that its better activity is not due to collection of more photons but rather either due to improved charge separation or to interfacial charge transfer.^{44,45} We consider improved charge separation as an unlikely (albeit not ruled out) explanation for the better activity, since the photoexcited charge carriers in carbon nitrides have a short lifetime and appear to be confined to the individual heptazine unit without diffusing along the polymer or oligomer.^{46,47} The latter explanation appears more likely, and suggests that the melem oligomer contains features that accelerate the oxidation of methanol or reduction of hydrogen via the platinum centers. These encouraging photocatalysis results thus motivated us to determine the identity of this melem oligomer, with the aim of elucidating the properties or criteria for superior photocatalytic activity in carbon nitride materials.

The XRD pattern of the as-synthesized melem oligomer, depicted in Figure 2a, is similar to melem but shows various small shifts in the reflection positions, indicating that the crystalline portion of the oligomer sample contains a melem-related structure that has been observed and employed for synthesizing melem derivatives in the literature.⁴⁸ TEM analysis of the heat-treated melem oligomer (Figure S4, Supporting Information) showed the sample to have a sheet-like morphology, with lateral dimensions in the micron scale.

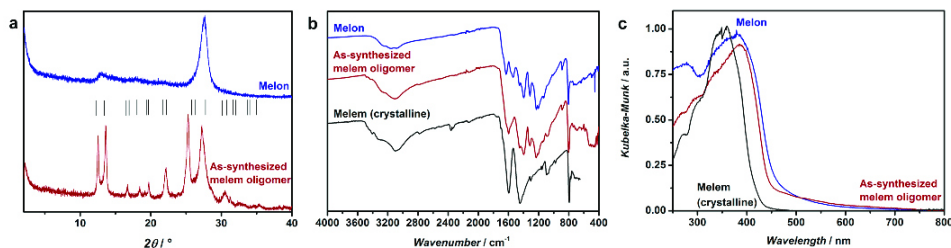


Figure 2. (a) XRD patterns, (b) ATR-IR, and (c) diffuse reflectance UV-vis spectra of the melem oligomer and melon in comparison with that of crystalline melem. The tick marks in the XRD show the prominent peaks of crystalline melem from the literature.

Electron diffraction analysis of this as-synthesized melem oligomer sample shows the presence of melem, an example given in the center image of Figure S4 (Supporting Information). An additional, melem-related phase was also observed by electron diffraction (Figure S4, Supporting Information, right) with slightly increased d -spacing for both 002 and 011, consistent with the melem-related phase in the XRD mentioned above. While carbon nitrides have been synthesized under similar conditions before, e.g., Guo et al. performed the synthesis under identical conditions except in air,^{49,50} we found that synthesis in air worsened the reproducibility of the XRD pattern and also reduced the photocatalytic activity (which may hint at the negative effect of oxygenated or oxidized functionalities).

Despite the fact that only the monomer is observed by crystallographic techniques in the as-synthesized melem oligomer sample, results from ATR-IR and diffuse reflectance UV-vis spectroscopy (Figure 2b and c), as well as elemental analyses (Table S1, Supporting Information), are consistent with those expected of higher condensation products of melem. In the IR spectra, the absorption bands at 1206 and 1235 cm^{-1} and 1316 cm^{-1} have been shown to be characteristic of the C–NH–C unit in melam (triazine–triazine dimer, Scheme S1, Supporting Information), and thus assigned to bridging secondary amine units.⁵¹ We also note that the UV-vis absorption for melem oligomer is between that of melem and melon. Assuming that melon behaves like a partially π -conjugated heptazine polymer,⁶ this result suggests that the aromatic system is larger than the monomer but smaller than the polymer. We however caution that recent optical investigations question this organic semiconductor model, with results from photoluminescence decay showing instead that the electronic structure of g- C_3N_4 can rather be described as that of a “quasi-monomer”, that is, a low degree of delocalization between the individual heptazine units.^{47,52} A separate explanation independent of the semiconductor model is that the melem oligomer contains an amount of reacted primary amines between that of the monomer and polymer, since derivatization of the amines on melem can also red-shift its absorption.⁴⁸

Lastly, the C:N atomic ratio of the as-synthesized melem oligomer sample lies between that of melem and the theoretical C_3N_4 , indicating an increased degree of condensation compared to melem. Combined with the XRD and TEM analyses, these results suggest that this melem oligomer sample contained a mixture of crystalline heptazine monomers (i.e., melem) and more highly condensed but less crystalline

products. While we do not rule out the possibility of forming triazine oligomers or oligomers between melem and melamine, we believe their presence to be improbable on thermodynamic considerations. For example, melam is a short-lived intermediate in the synthesis of melem,¹⁵ while polymers of triazine are not expected to form unless under ionothermal conditions.³⁹

Characterization of the spent as-synthesized catalyst after the photocatalytic reaction showed the formation of a melem hydrate phase,³⁸ as evident in the XRD patterns, but virtually no change in the IR spectra, from both the 8 h and the extended 129 h experiments (Figures S5 and S6, Supporting Information, respectively). The hydrate phase is likely formed from the recrystallization of the monomers present in the sample under the aqueous conditions of the photocatalytic reaction, rather than depolymerization of the higher condensation species, since the IR absorption bands corresponding to the bridging secondary amines are still present.

HRTEM analyses of the spent catalyst (Figure S7, Supporting Information) showed the formation of spherical platinum particles of diameter 1–2 nm on the catalyst surface as found previously.⁴³ X-ray photoelectron spectroscopy (XPS) of the spent catalyst shows the Pt $4f_{7/2}$ peak (Figure S8, Supporting Information, top right) to have a binding energy (B.E.) of around 71.3 eV, which is assigned to Pt⁰. This thus confirms the formation of metallic platinum, although HRTEM and XPS naturally do not allow us to determine the molecular binding sites of the metal particles to the light harvester. The integrity of the melem oligomer was also corroborated from spectra in the C 1s (Figure S8, Supporting Information, bottom left) and N 1s regions (Figure S8, Supporting Information, bottom right). The C 1s peak at 288.1 eV has been assigned to a C–N–C coordination, while the N 1s peaks at 398.6, 399.4, and 401.2 eV have been assigned to the C–N–C group, the tertiary nitrogen N–(C)₃ group, and the hydrogen-bearing amine group, respectively.⁵³ The larger intensity of the peak at 401.2 eV, compared to literature spectra, can be attributed to the presence of the monomer melem in the sample, which is in line with our observations outlined above.⁵⁴ No change is discernible when comparing the C 1s and N 1s spectra of this material before and after the photocatalytic reaction, other than the absence of platinum.

As we are interested in elucidating the structure–property–activity relationship in carbon nitride photocatalysts, it is thus necessary to separate these higher condensation species in the sample from the monomer, which has not been reported to possess photocatalytic activity. Since DMSO can solubilize

melem¹³ but does not affect the polymer chemically, we therefore can remove the majority of the monomer from the bulk melem oligomer sample and isolate the oligomer, which will have a lower solubility in DMSO. The insoluble component was further separated by differential centrifugation at RCF (relative centrifugal force) values of 10000 and 60000. Descriptions of the fractions are summarized in Table 1, and

Table 1. Fractions Obtained by Differential Centrifugation of a DMSO Suspension Containing Melem Oligomer (400 mg in 100 mL)

	amount recovered (mg)	appearance
DMSO soluble	175 (48%)	white
fraction RCF 60000	57 (16%)	off-white/light yellow
fraction RCF 10000	132 (35%)	light yellow

their characterizations by XRD, UV-vis, IR, MALDI-TOF-MS, and solid-state ¹³C and ¹⁵N magic angle spinning (MAS) NMR spectroscopy are shown in Figure 3. MALDI-TOF spectra of the fractions at lower mass ranges are shown in Figure S9 (Supporting Information). A summary of the BET surface areas, photocatalytic hydrogen evolution rate, and quantum efficiencies are given in Table S2 (Supporting Information).

In the DMSO soluble fraction, the most intense reflections in the XRD coincide with the 011 and 212 reflections of melem hydrate, the water likely originating from residual moisture in the DMSO. Thus, this fraction can be assigned to the hydrate phase, indicating that melem from the as-synthesized sample was reorganized into the hydrate phase during the separation procedure, while keeping the molecular structure and integrity of the triamino-heptazine. A small amount of sulfur (~1 wt %) was detected only in this fraction (but not the other two) by elemental analysis using energy dispersive X-ray spectroscopy (EDX), which we attribute to the minute presence of a DMSO-solvate of melem.⁵⁵ Its IR spectrum shows two broad bands at 1596 and 1442 cm⁻¹, again coinciding with those of melem, while the lack of absorption at around 1231 cm⁻¹ indicates the absence of the oligomeric species in this fraction. Its absorption onset in the UV-vis spectra, which is below 400 nm, suggests an underivatized monomeric structure. The ¹³C NMR spectrum exhibits two signal groups at 164 ppm and at 155 ppm which can be assigned to the amine-bearing and the remaining heptazine carbons, respectively. In crystalline melem, both signals exhibit a fine structure, due to different hydrogen bonding environments.¹⁰ Owing to the weak crystallinity, the signals for the present material are not as resolved and slightly shifted to lower ppm values similar to melem hydrate.³⁸ Three

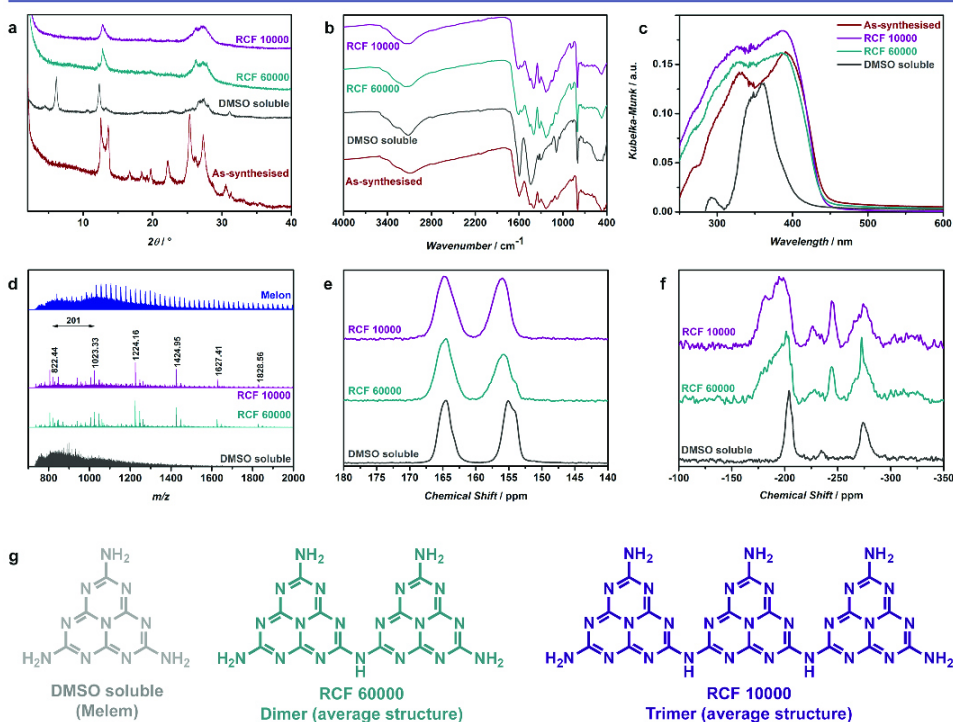


Figure 3. (a) XRD patterns, (b) ATR-IR, (c) diffuse reflectance UV-vis, (d) MALDI-TOF at mass range >850 amu in positive mode, (e) ¹³C and (f) ¹⁵N solid state CP-MAS NMR spectra, and (g) the postulated average structures of the three fractions from differential centrifugation.

peaks in the ^{15}N can thus be assigned: the broad signal in the range of -190 to -210 ppm corresponds to the peripheral nitrogens in the heptazine ring, -229 to -240 ppm to the center nitrogen of heptazine, and -265 to -285 ppm to the amine. The values of these shifts coincide with those of melem or melem hydrate.^{10,38} Lastly, the mass spectroscopy showed peaks at 219 and 420 amu (Figure S9, Supporting Information), corresponding to the protonated forms of the monomer and the dimer, respectively, but nothing of higher mass. It is possible that the dimer is somewhat soluble in DMSO, or may be present as a contaminant in minute amount below the detection limit of NMR ($\approx 5\%$). From this characterization, we can conclude that the DMSO-soluble fraction is predominantly melem, illustrating the separation of the monomer from the higher condensates.

The other two fractions showed similarities in their IR spectra with that of melon, the noteworthy feature being the bridging amine absorption at 1231 cm^{-1} , while their UV-vis absorption onsets are in the visible region. Compared with melon, their XRD patterns exhibit a relatively sharp reflection at $12.8^\circ 2\theta$ and broad reflections in the range $25\text{--}29^\circ 2\theta$, suggesting long-range order to some extent across the plane and largely turbostratic disorder in the stacking direction. These two fractions are however differentiated by their NMR spectra. In the ^{13}C spectrum, the RCF 60000 fraction is characterized by the same shoulder at 154 ppm as the DMSO soluble fraction, suggesting a more melem-like carbon environment. Nonetheless, both of these fractions are unequivocally not the monomer, as evidenced by the peak at -245 ppm in the ^{15}N spectrum, which coincides with the secondary amine (NH group) in melon. We also note the expansion of the signal of the peripheral heptazine nitrogens toward higher ppm values, being characteristic for melon;¹⁴ this peak is more intense for the RCF 10000 than the 60000 fraction. Lastly, we emphasize that the shift of the central heptazine nitrogen provides information regarding the extent of the polymerization, since this peak shifts from -234 ppm for melem to -225 ppm for the polymer.^{10,14} Although this peak is broad for both fractions, a comparison of the maxima revealed that the shift is at -226 ppm for the RCF 10000 fraction, whereas it is at -228 ppm for the RCF 60000 fraction, thus suggesting that this latter fraction is less melon-like than the former. An additional qualitative (but by no means quantitative, due to cross-polarization conditions) measure of polymerization is to compare the integral ratios of the $^{15}\text{NH}_2$: ^{15}NH peaks in the different spectra. In this case, this ratio is around 3.3 and 2.4 for the RCF 60000 and 10000 fractions, respectively, indicating that the former has more unreacted primary amine groups, i.e., less degree of polymerization. As the ratio depends on the chain length (Figure S10, Supporting Information), the size of the oligomer can thus be approximated. Therefore, the less dense fraction (RCF 60000) with a ratio of 3.3 will mainly consist of dimers with an average length of 2.3 melem units and only a small amount of higher condensates, whereas the denser fraction (RCF 10000) is shifted toward higher condensates, mostly trimers with an average length of 3.2 melem units. The postulated structures of these two fractions as linear polymers are shown in Figure 3g. Note that, as these fractions are inevitably mixtures, the oligomer lengths shown are average structures that are consistent with the NMR results. While we do not rule out the possibility of nonlinear structures (e.g., dendrimer or cyclic structures³⁵), no signal corresponding to a tertiary amine was detected from the ^{15}N NMR spectrum. We therefore surmise

that nonlinear structures involving a tertiary nitrogen are either absent or present only in negligible amounts. Regarding the possible presence of triazine moieties, we note that the spectral signatures of the ^{13}C and ^{15}N 1D spectra clearly fit better to a heptazine-based oligomer, rather than a triazine-based one.

As spectral overlap could mask the minute presence of such triazine species, we have performed matrix-assisted laser desorption/ionization time-of-flight (MALDI-TOF) mass spectrometry to corroborate the NMR results. Both samples exhibit peaks at mass corresponding to the protonated monomer (219 amu), dimer (420 amu) and trimer (621 amu); further increments of 201 amu corresponding to every additional monomer up to the nonamer (1627 amu) can be also clearly resolved. No triazine-containing oligomer was observed. These signals are unlikely to be fragments of the polymer, since the spectrum for melon does not contain these peaks. In contrast, in analyzing melon in the high mass range, a series of peaks with mass separated by 24 amu was observed. Note that this separation is also observed for the RCF 10000 fraction, and is assigned to the C_2 fragment resulting from the high laser power required to generate sufficient signal intensity. While we acknowledge previous MALDI-TOF analysis of heptazine polymers showing mass intervals of 201 amu,⁵⁶ we emphasize that the spectra in this work clearly show the molecular peaks at the exact masses expected for the oligomer, rather than the fragments. Although MALDI-TOF was unable to differentiate between these two fractions in terms of their oligomer length, it nonetheless verifies our hypothesis that these are indeed isolated oligomers of melem.

The thermal properties of these fractions and evolved volatiles were analyzed by thermogravimetric analysis coupled with mass spectroscopy under an argon atmosphere (Figure S11, Supporting Information). Melon has one mass loss step, beginning at around 520°C accompanied by evolution of HCN, before complete decomposition takes place at $620\text{--}700^\circ\text{C}$ with the evolution of C_2N_2 and small amounts of NH_3 . The DMSO soluble fraction—identified above to be melem—undergoes two mass loss steps, the first beginning at around 350°C with evolution of ammonia and small amounts of HCN, which we attribute to the condensation polymerization of the monomer. The second step is similar to melon decomposition, with HCN and C_2N_2 evolution onset at around 520 and 600°C , respectively. Both RCF 10000 and 60000 fractions have an identical mass loss profile with a single step mass loss at a temperature between that of the monomer and the polymer, consistent with the fact that these fractions are intermediates between the monomer and the polymer. The condensation reaction, as in melem, was not detected, and can be rationalized by the negligible presence of the monomer as a precursor.

The RCF 60000 fraction has a layered structure similar to the plate-like morphology observed in crystalline particles of melon,^{14,20} as shown in its SEM (Figure S12, Supporting Information) and TEM (Figure 4), with lateral dimensions in the micron regime. These fractions were tested for photocatalytic hydrogen evolution at pH 7 under irradiation from visible light ($>420\text{ nm}$), and the results are shown in Figure 5. The DMSO-soluble fraction, which we have assigned to melem, exhibited negligible activity as expected, since its absorption onset is in the UV region. The fractions collected at RCF 10000 and 60000, which together constitute about 50% of the total weight of the original sample, exhibited a hydrogen evolution rate of 4.8 and $5.4\ \mu\text{mol h}^{-1}$, respectively, with an apparent quantum efficiency (AQE) estimate at $400 \pm 25\text{ nm}$ of 0.087

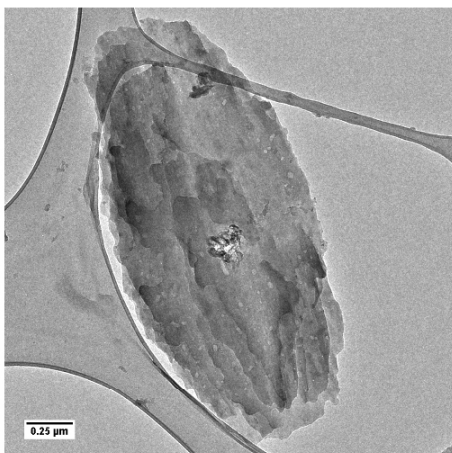


Figure 4. TEM image of the fraction obtained at RCF 60000.

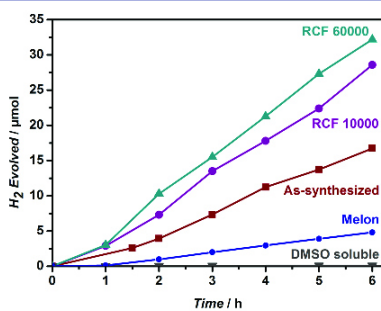


Figure 5. Photocatalytic activity under visible light irradiation ($\lambda > 420$ nm) of the fractions in PBS (18 mL of 0.1 M solution at pH 7) containing methanol (2 mL) and dihydrogen hexachloroplatinate (5 μ L of 8 wt % aqueous solution). The catalyst loading in all cases was 20 mg.

and 0.1%; these hydrogen evolution rates outperformed the as-synthesized sample by 1.66 and 1.71 times, respectively, and outperformed the polymer ($0.9 \mu\text{mol h}^{-1}$, AQE 0.015% at 400 ± 25 nm) by 5.9 and 6.1 times, respectively. The BET surface areas of these two active fractions are no more than 3 times that of the polymer (see Table S2, Supporting Information), nor does their morphology differ significantly from melon (other than having a small particle size in general as a result of the differential centrifugation). Solvent interaction and dispersibility of the polymer and the RCF 10000 fraction are also quite similar, as gauged by zeta potential measurements (Figure S13, Supporting Information), which show that the polymer and this fraction has zeta potentials of -18 and -28 mV at pH 6.6 and isoelectric points of pH 3.3 and pH 2.7, respectively. The values for the polymer are in broad agreement with literature values.²⁷ Thus, while textural properties, solvent effects, and mass transport may have an effect on the photocatalytic perform-

ances, the vast activity differences of the fractions indicate that these attributes are not the dominating contributors but point toward other intrinsic factors as the principal explanation for the large outperformances of the oligomeric fractions, i.e., increased activity per surface area. The separation procedure using DMSO does not affect the heptazine polymer chemically, thereby ruling this factor out as the source of the increased intrinsic activity. We then consider the common explanations for intrinsic increase in activity in photocatalysis, which are (1) improvement in light absorption, (2) lengthened lifetime of photogenerated charges, and/or (3) interfacial charge transfer rate. We can rule out the first factor immediately, as these active fractions absorb less in the visible region than the polymer, based on their diffuse reflectance UV–vis spectra. These active fractions are also poorly crystalline from the XRD, a factor usually associated with enhanced electron–hole recombination and impeded charge percolation.⁵⁷ Furthermore, the carrier lifetime and mobility of heptazine polymers are considered to be unfavorable for photocatalysis, due to strong carrier localization.^{47,58–60} The lifetime/mobility interplay may be varied slightly by changing the stacking separation, with the distance directly correlated with carrier lifetime but inversely correlated to mobility.⁴⁷ This relation however may not be applicable for oligomers due to differences in crystal structure and cofacial distances in the aromatic units.⁴⁷ We thus consider the second factor—increased activity due to more favorable carrier dynamics—an improbable explanation for the large difference in activity (even after normalizing the oligomers' activities to surface area; see below). Therefore, the remaining explanation, that the high activity of the as-synthesized melon oligomer is attributable to faster extraction of the photogenerated charges (i.e., faster kinetics for interfacial charge transfer), is considered the likeliest explanation. This step is typically the slowest and thus the bottleneck in most photocatalytic systems. Faster transfer kinetics can result from the catalyst having a larger number of exposed reactive sites, which may be a surface area effect. However, when the activities are normalized to the BET surface area, we see that the activity of the RCF 60000 fraction at $11 \mu\text{mol h}^{-1} \text{m}^{-2}$ has more than twice the activity of the polymer ($5.3 \mu\text{mol h}^{-1} \text{m}^{-2}$), thus illustrating that the surface area cannot be the principal factor in explaining this outperformance.

To understand the high activity of the oligomers, we have undertaken calculations of the HOMO/LUMO orbitals of the mono- and oligomers and their variation with conformation, employing van der Waals-corrected density functional theory^{61,62} for the structure and an optimized hybrid functional⁶³ to validate orbital energy trends, using the FHI-aims all-electron code^{64,65} (orbitals represented in Figure 6 and Table S4, Supporting Information; energies summarized in Table S3, Supporting Information; conformational variations in Table S4, Supporting Information; and additional discussions in the Supporting Information). The computational trends are corroborated with photoluminescence (PL) experiments (Figure S14, Supporting Information). Consistent with a previous study on the correlation of band gap with degree of polymerization,⁵² the energy gap was found to expand with shorter oligomer length. Current Kohn–Sham density functional approximations cannot be expected to give absolute band gap energies, but the trend of the band gap and HOMO/LUMO energies is consistent across different functionals. For the optimized functional (PBE⁶¹ functional), the gas-phase electronic gap increases from 7.83 (2.68) eV for the tetramer to

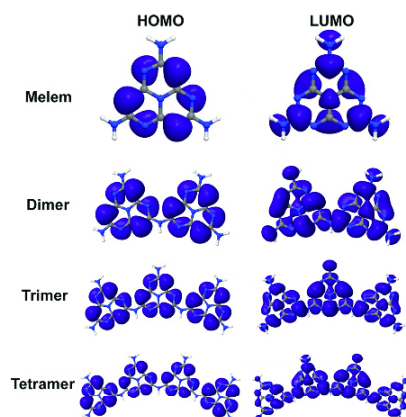


Figure 6. Highest occupied and lowest unoccupied orbitals of the monomer to the tetramer. Only the positive parts of the HOMO / LUMO orbitals are shown.

7.93 (2.77) eV for the trimer and 8.15 (2.95) eV and 8.98 (3.50) eV for the di- and monomer, respectively. From the PL spectra, both the oligomeric fractions and the polymer possess an emission state at about 375 nm but differ for the emission in the visible region. The polymer has an emission at 455 nm, while the spectra for the oligomers have a shoulder in the main emission peak at around 425 nm. The energy gap for these emissions corresponds to 2.7 eV for the polymer and 2.9 eV for the oligomers. While the absolute agreement with DFT-PBE is fortuitous, again the trend with length is in good agreement with the computational results. This shift in energy level is due to the LUMO shifting to more positive energy while the HOMO shifts much less with oligomer length, implying that the photoelectrons in the shorter oligomer are thermodynamically more reducing than the longer ones (i.e., more driving force for electron transfer), while the photoholes have largely invariant oxidizing ability. In relating this LUMO shift to the activity, we find that the absorption edge from the UV-vis spectra for the oligomeric fractions (440 nm, 2.8 eV) is blue-shifted by about 20 nm (0.1 eV) from the polymer (460 nm, 2.7 eV). Likewise for the PL, the emission is blue-shifted by 30 nm (0.2 eV) going from the polymer to the oligomer. In other words, the oligomer fraction has an over 5-fold increase in hydrogen evolution rate over melon (Figure 5; 2-fold on a per surface area basis) with only about 100–200 mV potential change. This variation is large, considering that semiconductor photocatalysts exhibit far less than a 2-fold variation in activity for a similar shift in band potential resulting from quantum confinement or by varying the composition of solid solution.^{66–69} Thus, in addition to the slightly higher reducing ability of the photoelectron due to the LUMO shift, we also considered factors related to kinetics, such as the location and distribution of the charge transfer sites. We find that for all oligomers the location of the HOMO, which is likely associated with the oxidation sites where the photoholes are quenched after interaction with methanol as the sacrificial electron donor, is localized exclusively on the tertiary heptazine nitrogen atoms for the small oligomers (Figure 6 and Table S4, Supporting

Information).^{6,58} Since these are the positions where direct hydrogen bonding interactions to methanol are most likely to occur, the HOMO location is therefore “ideal” for all oligomers. However, for all oligomers calculated, the LUMO, which typically is used as an approximation for the reducing sites,⁷⁰ is delocalized across the carbon and nitrogen atoms of the heptazine, including the central nitrogen and the bridging secondary amine, as well as localized on the primary amines. The LUMO is not equally spread across the multiple heptazine units of the oligomer, i.e., not entirely delocalized; even stronger localization effects are observed when conformational variations⁷¹ are accounted for (see Table S4, Supporting Information), consistent with the “quasi-monomer” description.⁴⁷ An explanation consistent with our empirical results would be to consider the primary and/or secondary amines to be the primary reducing sites, as they are not only more prevalent in the oligomeric than the polymeric case but better exposed on account of the stacking disorder and conformational flexibility for the less condensed oligomer, as observed in the broad XRD reflections. These amine groups would also be the preferred site for the in situ reduction of Pt⁰ from PtCl₆²⁻, given the numerous literature precedents on the encapsulation of platinum particles within photo- and electrocatalytic amine-bearing matrices (e.g., dendrimer^{72–75} and metal organic framework⁷⁶). These amines allow either better coordination to the platinum centers for efficient electron transfer (e.g., via inner sphere electron transfer mechanism), or for amine-mediated proton-coupled electron transfer,⁷⁷ or even as the actual site for recombination of the hydrogen atoms to molecular hydrogen.⁷⁸

These findings therefore lend evidence to the often-invoked relevance of “defects”, which are commonly considered to increase the photocatalytic activity of carbon nitrides, as the nature of such defects can in fact be associated with polymer terminations and increased exposure of the peripheral functional groups (e.g., –NH₂). It will therefore be key to explore whether the most NH₂-rich species—melon and its derivatives—possess photocatalytic activity, and how the modification of the heptazine skeleton affects the optoelectronic and photocatalytic properties. From a computational approach, it will be instructive to investigate conformer dependency, as observed in the preliminary calculations for the tetramer (Table S4, Supporting Information), where symmetry breaking and hydrogen bonding have been shown to shift both the HOMO/LUMO energy and location, and thus may offer alternative strategies for activity increase through altered photogenerated charge carrier location and separation.

The high activity of our experimentally resolved oligomer fractions highlights the potential of active site engineering as an alternative strategy to improve the intrinsic photocatalytic activity of carbon nitrides. The hydrogen evolution rates of these oligomers are quite competitive with values in the literature (after normalizing for catalyst loading and surface area), which are typically in the range of 1–4 μmol H₂ h⁻¹ m⁻² for g-C₃N₄ that is composited with other semiconductors.^{27,30,31,50} Note that a direct comparison is difficult on account of differences in reaction parameters (electron donor used, reactor configuration, and whether the catalyst loading is limited by mass transfer⁷⁹). Nonetheless, we expect the activity of the oligomer can be further enhanced on a per weight basis provided that the active phase can be selectively synthesized. We note that these two “oligomeric” fractions constitute approximately 50 wt % of the as-synthesized sample, with about

half of the melem remaining unreacted even after 12 h at 450 °C. We foresee that the yield and polymerization degree are far from optimized, and a simple fine-tuning of the synthesis parameters may already provide ample scope for further improvement in the photocatalytic activity of these heptazine-based polymers.

CONCLUSIONS

We have experimentally demonstrated that the length of the melon polymer chain can be reduced by decreasing the synthesis temperature, yielding a hydrogen evolution photocatalyst with 3 times the activity of the polymer under AM 1.5 conditions, despite absorbing less in the visible region. Through a separation procedure and detailed characterization, this photocatalyst was shown to be a mixture of the monomer and oligomers of melem. The former has negligible activity, while the latter has nearly twice the activity of the as-synthesized material on a per weight basis, resulting in a total increase in activity of 6 times the polymer. Moreover, the photocatalytic activity appears to increase with shorter oligomer length to a certain point, consistent with the periphery of the heptazine moiety being involved in the catalytic reaction, which has been corroborated by DFT calculations. The successful isolation of the active component(s) demonstrated in this work provides a platform for future investigations into the catalytic properties of carbon nitride photocatalysts. Furthermore, these results illustrate a strategy based on active site engineering for intrinsically improving carbon nitride photocatalysts, thus highlighting the need for developing synthetic protocols selective to the active species.

EXPERIMENTAL SECTION

Detailed descriptions of the characterization techniques are provided in the Supporting Information.

A sample tentatively notated as “melem oligomer” was prepared as follows. Melamine (1.00 g, Carl Roth, >99%) was loaded into a loosely covered alumina boat and was placed into a quartz tube furnace. After complete removal of air by an extended argon purge, the furnace was heated under a slow argon flow to 450 °C for 12 h at a 5 °C min⁻¹ ramp and then allowed to cool to ambient temperature at an unrestricted rate. The resulting light yellow solid (390 mg) was then thoroughly ground with an agate mortar and pestle prior to characterization and photocatalytic evaluation. The crystallinity of the product can be improved by further heat treatment at 300 °C for 24 h in argon.

For comparison, a sample of melon was prepared in an identical fashion, except that melamine was heated to 550 °C.

Separation of the melem oligomer into different fractions was carried out by stirring 400 mg of the ground solid in DMSO (100 mL) for 1 week. The resulting suspension was centrifuged at a relative centrifugal force (RCF) of 10000. The precipitate (notated as “fraction RCF 10000”) was washed with acetone and dried at 100 °C. The supernatant was centrifuged again at a RCF of 60000, and the precipitate (fraction RCF 60000) was washed and dried as in the previous fraction. For the supernatant, the DMSO was completely evaporated off at 70 °C *in vacuo* and the resulting white powder was subjected to the same acetone wash and drying procedure as described above for the two other fractions.

ASSOCIATED CONTENT

Supporting Information

Details of the Experimental Section and theoretical calculations, and additional characterizations (XPS, elemental analyses, surface areas, TGA-MS, SEM, and PL) of the melem oligomer and of the isolated species from differential centrifugation. This

material is available free of charge via the Internet at <http://pubs.acs.org>.

AUTHOR INFORMATION

Corresponding Author

*b.lotsch@fkf.mpg.de

Notes

The authors declare no competing financial interest.

ACKNOWLEDGMENTS

V.W.-h.L. gratefully acknowledges a postdoctoral scholarship from the Max Planck Society. This work was supported by the Deutsche Forschungsgemeinschaft (projects LO1801/1-1, SE1417/5-1), the Max Planck Society, the cluster of excellence Nanosystems Initiative Munich (NIM), the Fonds der Chemischen Industrie (FCI), and the Center for Nanoscience (CeNS). The authors would like to thank Dr. Stephan Rauschenbach for assistance in the preparation and analysis of the samples for MALDI-TOF measurements. The authors would also like to thank Ms. Marie-Luise Schreiber for the elemental analyses, Dr. Konuma for the XPS analyses, and Mr. Daniel Weber for the TGA-MS experiments. This work is dedicated to Prof. Arndt Simon on the occasion of his 75th birthday.

REFERENCES

- (1) Rand, D. A. J.; Dell, R. M. *Hydrogen Energy: Challenges and Prospects*; RSC Publishing: Cambridge, U.K., 2008.
- (2) Fujishima, A.; Honda, K. *Nature* **1972**, *238*, 37.
- (3) Kato, H.; Asakura, K.; Kudo, A. *J. Am. Chem. Soc.* **2003**, *125*, 3082.
- (4) Lu, D.; Takata, T.; Saito, N.; Inoue, Y.; Domen, K. *Nature* **2006**, *440*, 295.
- (5) Maeda, K.; Domen, K. *J. Phys. Chem. C* **2007**, *111*, 7851.
- (6) Wang, X.; Maeda, K.; Thomas, A.; Takanabe, K.; Xin, G.; Carlsson, J. M.; Domen, K.; Antonietti, M. *Nat. Mater.* **2009**, *8*, 76.
- (7) Wang, Y.; Wang, X.; Antonietti, M. *Angew. Chem., Int. Ed.* **2012**, *51*, 68.
- (8) Cao, S.; Yu, J. *J. Phys. Chem. Lett.* **2014**, *5*, 2101.
- (9) Liu, A. Y.; Cohen, M. L. *Science* **1989**, *245*, 841.
- (10) Jürgens, B.; Irran, E.; Senker, J.; Kroll, P.; Müller, H.; Schnick, W. *J. Am. Chem. Soc.* **2003**, *125*, 10288.
- (11) Lotsch, B. V.; Schnick, W. *Chem. Mater.* **2005**, *17*, 3976.
- (12) Lotsch, B. V.; Schnick, W. *Chem. Mater.* **2006**, *18*, 1891.
- (13) Sattler, A.; Schnick, W. *Z. Anorg. Allg. Chem.* **2006**, *632*, 238.
- (14) Lotsch, B. V.; Döblinger, M.; Sehnert, J.; Seyfarth, L.; Senker, J.; Oeckler, O.; Schnick, W. *Chem.—Eur. J.* **2007**, *13*, 4969.
- (15) Lotsch, B. V.; Schnick, W. *Chem.—Eur. J.* **2007**, *13*, 4956.
- (16) Seyfarth, L.; Seyfarth, J.; Lotsch, B. V.; Schnick, W.; Senker, J. *Phys. Chem. Chem. Phys.* **2010**, *12*, 2227.
- (17) Chen, X.; Jun, Y.-S.; Takanabe, K.; Maeda, K.; Domen, K.; Fu, X.; Antonietti, M.; Wang, X. *Chem. Mater.* **2009**, *21*, 4093.
- (18) Wang, X.; Maeda, K.; Chen, X.; Takanabe, K.; Domen, K.; Hou, Y.; Fu, X.; Antonietti, M. *J. Am. Chem. Soc.* **2009**, *131*, 1680.
- (19) Li, X.-H.; Zhang, J.; Chen, X.; Fischer, A.; Thomas, A.; Antonietti, M.; Wang, X. *Chem. Mater.* **2011**, *23*, 4344.
- (20) Niu, P.; Zhang, L.; Liu, G.; Cheng, H.-M. *Adv. Funct. Mater.* **2012**, *22*, 2763.
- (21) Wu, G.; Thind, S. S.; Wen, J.; Yan, K.; Chen, A. *Appl. Catal., B* **2013**, *142–143*, 590.
- (22) Yang, S.; Gong, Y.; Zhang, J.; Zhan, L.; Ma, L.; Fang, Z.; Vajtai, R.; Wang, X.; Ajayan, P. M. *Adv. Mater.* **2013**, *25*, 2452.
- (23) Liu, G.; Niu, P.; Sun, C.; Smith, S. C.; Chen, Z.; Lu, G. Q. M.; Cheng, H.-M. *J. Am. Chem. Soc.* **2010**, *132*, 11642.
- (24) Zhang, J.; Sun, J.; Maeda, K.; Domen, K.; Liu, P.; Antonietti, M.; Fu, X.; Wang, X. *Energy Environ. Sci.* **2011**, *4*, 675.

- (25) Zhang, G.; Zhang, J.; Zhang, M.; Wang, X. *J. Mater. Chem.* **2012**, *22*, 8083.
- (26) Zhang, J.; Zhang, G.; Chen, X.; Lin, S.; Möhlmann, L.; Dolega, G.; Lipner, G.; Antonietti, M.; Blechert, S.; Wang, X. *Angew. Chem., Int. Ed.* **2012**, *51*, 3183.
- (27) Di, Y.; Wang, X.; Thomas, A.; Antonietti, M. *ChemCatChem* **2010**, *2*, 834.
- (28) Ding, Z.; Chen, X.; Antonietti, M.; Wang, X. *ChemSusChem* **2011**, *4*, 274.
- (29) Xiang, Q.; Yu, J.; Jaroniec, M. *J. Phys. Chem. C* **2011**, *115*, 7355.
- (30) Ge, L.; Zuo, F.; Liu, J.; Ma, Q.; Wang, C.; Sun, D.; Bartels, L.; Feng, P. *J. Phys. Chem. C* **2012**, *116*, 13708.
- (31) Kang, H. W.; Lim, S. N.; Song, D.; Park, S. B. *Int. J. Hydrogen Energy* **2012**, *37*, 11602.
- (32) Sun, L.; Zhao, X.; Jia, C.-J.; Zhou, Y.; Cheng, X.; Li, P.; Liu, L.; Fan, W. *J. Mater. Chem.* **2012**, *22*, 23428.
- (33) Cao, S.-W.; Yuan, Y.-P.; Barber, J.; Loo, S. C. J.; Xue, C. *Appl. Surf. Sci.* **2014**, *319*, 344.
- (34) Chen, J.; Shen, S.; Guo, P.; Wang, M.; Wu, P.; Wang, X.; Guo, L. *Appl. Catal., B* **2014**, *152–153*, 335.
- (35) Döblinger, M.; Lotsch, B. V.; Wack, J.; Thun, J.; Senker, J.; Schnick, W. *Chem. Commun.* **2009**, 1541.
- (36) Sattler, A.; Pagano, S.; Zeuner, M.; Zurawski, A.; Gunzelmann, D.; Senker, J.; Müller-Buschbaum, K.; Schnick, W. *Chem.—Eur. J.* **2009**, *15*, 13161.
- (37) Wirnhier, E.; Döblinger, M.; Gunzelmann, D.; Senker, J.; Lotsch, B. V.; Schnick, W. *Chem.—Eur. J.* **2011**, *17*, 3213.
- (38) Makowski, S. J.; Köstler, P.; Schnick, W. *Chem.—Eur. J.* **2012**, *18*, 3248.
- (39) Ham, Y.; Maeda, K.; Cha, D.; Takane, K.; Domen, K. *Chem.—Asian J.* **2013**, *8*, 218.
- (40) Schwinghammer, K.; Tuffy, B.; Mesch, M. B.; Wirnhier, E.; Martineau, C.; Taulelle, F.; Schnick, W.; Senker, J.; Lotsch, B. V. *Angew. Chem., Int. Ed.* **2013**, *52*, 2435.
- (41) Schwarzer, A.; Saplinova, T.; Kroke, E. *Coord. Chem. Rev.* **2013**, *257*, 2032.
- (42) Bojdy, M. J. Ph.D. Thesis, Max-Planck Institut für Kolloid- und Grenzflächenforschung, Potsdam, Germany, 2009.
- (43) Maeda, K.; Wang, X.; Nishihara, Y.; Lu, D.; Antonietti, M.; Domen, K. *J. Phys. Chem. C* **2009**, *113*, 4940.
- (44) Sabio, E. M.; Chamousis, R. L.; Browning, N. D.; Osterloh, F. E. *J. Phys. Chem. C* **2012**, *116*, 3161.
- (45) Osterloh, F. E. *Chem. Soc. Rev.* **2013**, *42*, 2294.
- (46) Yang, F.; Kuznetsov, V.; Lublow, M.; Merschjann, C.; Steigert, A.; Klaer, J.; Thomas, A.; Schedel-Niedrig, T. *J. Mater. Chem. A* **2013**, *1*, 6407.
- (47) Merschjann, C.; Tyborski, T.; Orthmann, S.; Yang, F.; Schwarzbach, K.; Lublow, M.; Lux-Steiner, M.-C.; Schedel-Niedrig, T. *Phys. Rev. B* **2013**, *87*, 205204.
- (48) Schwarzer, A.; Böhme, U.; Kroke, E. *Chem.—Eur. J.* **2012**, *18*, 12052.
- (49) Guo, Y.; Chu, S.; Yan, S.; Wang, Y.; Zou, Z. *Chem. Commun.* **2010**, *46*, 7325.
- (50) Yuan, Y.-P.; Xu, W.-T.; Yin, L.-S.; Cao, S.-W.; Liao, Y.-S.; Tng, Y.-Q.; Xue, C. *Int. J. Hydrogen Energy* **2013**, *38*, 13159.
- (51) Komatsu, T. *J. Mater. Chem.* **2001**, *11*, 799.
- (52) Tyborski, T.; Merschjann, C.; Orthmann, S.; Yang, F.; Lux-Steiner, M.-C.; Schedel-Niedrig, T. *J. Phys.: Condens. Matter* **2012**, *24*, 162201.
- (53) Thomas, A.; Fischer, A.; Goettmann, F.; Antonietti, M.; Müller, J.-O.; Schlägl, R.; Carlsson, J. M. *J. Mater. Chem.* **2008**, *18*, 4893.
- (54) Ishii, A.; Habu, K.; Kishi, S.; Ohtsu, H.; Komatsu, T.; Osaka, K.; Kato, K.; Kimura, S.; Takata, M.; Hasegawa, M.; Shigesato, Y. *Photochem. Photobiol. Sci.* **2007**, *6*, 804.
- (55) Lotsch, B. V. Ph.D. Thesis, Ludwig Maximilians Universität, München, Germany, 2006.
- (56) Komatsu, T. *Macromol. Chem. Phys.* **2001**, *202*, 19.
- (57) Xing, J.; Fang, W. Q.; Zhao, H. J.; Yang, H. G. *Chem.—Asian J.* **2012**, *7*, 642.
- (58) Huda, M. N.; Turner, J. A. *J. Appl. Phys.* **2010**, *107*, 123703.
- (59) Meek, G. A.; Baczewski, A. D.; Little, D. J.; Levine, B. G. *J. Phys. Chem. C* **2014**, *118*, 4023.
- (60) Reshak, A. H.; Khan, S. A.; Auluck, S. *RSC Adv.* **2014**, *4*, 6957.
- (61) Perdew, J. P.; Burke, K.; Ernzerhof, M. *Phys. Rev. Lett.* **1996**, *77*, 3865.
- (62) Tkatchenko, A.; Scheffler, M. *Phys. Rev. Lett.* **2009**, *102*, 073005.
- (63) Atalla, V.; Yoon, M.; Caruso, F.; Rinke, P.; Scheffler, M. *Phys. Rev. B* **2013**, *88*, 165122.
- (64) Blum, V.; Gehrke, R.; Hanke, F.; Havu, P.; Havu, V.; Ren, X.; Reuter, K.; Scheffler, M. *Comput. Phys. Commun.* **2009**, *180*, 2175.
- (65) Ren, X.; Rinke, P.; Blum, V.; Wieferink, J.; Tkatchenko, A.; Sanfilippo, A.; Reuter, K.; Scheffler, M. *New J. Phys.* **2012**, *14*, 053020.
- (66) Lee, H.-S.; Woo, C.-S.; Youn, B.-K.; Kim, S.-Y.; Oh, S.-T.; Sung, Y.-E.; Lee, H.-I. *Top. Catal.* **2005**, *35*, 255.
- (67) Datta, A.; Priyam, A.; Bhattacharyya, S. N.; Mukherjee, K. K.; Saha, A. *J. Colloid Interface Sci.* **2008**, *322*, 128.
- (68) Luo, W.; Li, Z.; Jiang, X.; Yu, T.; Liu, L.; Chen, X.; Ye, J.; Zou, Z. *Phys. Chem. Chem. Phys.* **2008**, *10*, 6717.
- (69) Zhang, G.; Monllor-Satoca, D.; Choi, W. *Catal. Sci. Technol.* **2013**, *3*, 1790.
- (70) Ceroni, P.; Balzani, V. In *The Exploration of Supramolecular Systems and Nanostructures by Photochemical Techniques*; Ceroni, P., Ed.; Springer: Dordrecht, The Netherlands, 2012.
- (71) Butchosa, C.; Guigliori, P.; Zwijnenburg, M. A. *J. Phys. Chem. C* **2014**, *118*, 24833.
- (72) Ye, H.; Scott, R. W. J.; Crooks, R. M. *Langmuir* **2004**, *20*, 2915.
- (73) Esumi, K.; Suzuki, A.; Yamahira, A.; Torigoe, K. *Langmuir* **2000**, *16*, 2604.
- (74) Yang, L.; Luo, Y.; Jia, X.; Ji, Y.; You, L.; Zhou, Q.; Wei, Y. *J. Phys. Chem. B* **2004**, *108*, 1176.
- (75) Zhao, M.; Crooks, R. M. *Adv. Mater.* **1999**, *11*, 217.
- (76) Wen, M.; Mori, K.; Kamegawa, T.; Yamashita, H. *Chem. Commun.* **2014**, *50*, 11645.
- (77) DuBois, M. R.; DuBois, D. L. *Chem. Soc. Rev.* **2009**, *38*, 62.
- (78) Joo, J. B.; Dillon, R.; Lee, I.; Yin, Y.; Bardeen, C. J.; Zaera, F. *Proc. Natl. Acad. Sci. U.S.A.* **2014**, *111*, 7942.
- (79) Maschmeyer, T.; Che, M. *Angew. Chem., Int. Ed.* **2010**, *49*, 1536.

6.2.2 Supporting Information

Supporting information

Low molecular-weight carbon nitrides for solar hydrogen evolution

Vincent Wing-hei Lau^{†§}, *Maria B. Mesch*[‡], *Viola Duppel*^{†§}, *Volker Blum*^{||}, *Jürgen Senker*[‡], *Bettina V. Lotsch*^{*†§⊥}

[†] Max Planck Institute for Solid State Research, Heisenbergstraße 1, 70569 Stuttgart, Germany

[‡] Department of Inorganic Chemistry III, University of Bayreuth, Universitätsstraße 30, 95447 Bayreuth, Germany

[§] Department of Chemistry, University of Munich, Butenandtstraße 5-13, 81377 Munich, Germany

^{||} Department of Mechanical Engineering and Materials Science and Center for Materials Genomics, Duke University, Durham, North Carolina 27708, United States

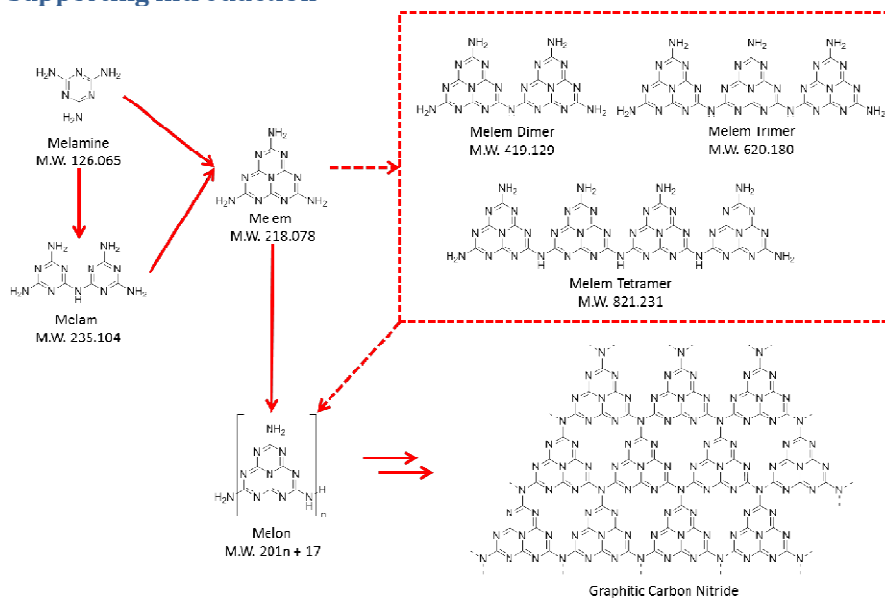
[⊥] Nanosystems Initiative Munich (NIM) and Center for Nanoscience, Schellingstraße 4, 80799 Munich, Germany

Table of content

Contents

Supporting introduction	2
Experimental section.....	3
Computational details & additional discussions	6
Characterization of as-synthesized melem oligomer	7
Characterization of as-synthesized melem oligomer after the photocatalytic reaction.....	9
Characterization of the fractions separated from the as-synthesized melem oligomer.....	12

Supporting introduction



Scheme S1 Route of condensation from melamine to melem, directly or via melam, then to the linear polymer melon. The idealized structure of graphitic carbon nitride is also shown as a hypothesised product of complete melem condensation, as indicated by the double arrow. Scheme adapted from Schwarzer *et al.*¹

Experimental section

Syntheses were carried out by loading the precursor in an alumina boat (volume 1.8 cm³) covered with alumina crucibles (not airtight) to prevent excess sublimation of the precursor (headspace ≈ 3 cm³). The alumina boat was placed in the centre of a quartz tube (diameter 28 mm, length 650 mm) inside a tube furnace operated by a temperature controller (Eurotherm 2408) using resistive heating. Air was removed by extended flushing of the quartz tube with argon. Argon flow was reduced to about 0.5 cm³ s⁻¹ prior to the heating program.

X-ray diffraction patterns were collected using a STOE Stadi P diffractometer (Cu K α 1) in transmission mode. ATR-IR spectra were collected with a PerkinElmer UATR TWO spectrometer equipped with a diamond crystal. Diffuse reflectance UV-Vis spectra were collected on a Cary 5000 spectrometer (referenced to PTFE or barium sulfate) and the spectra in percentage reflectance were converted using the Kubelka Munk function. CHN elemental analyses were performed with a Vario El element analyzer (Elementar Analysensysteme GmbH). Oxygen content analyses were performed using a carrier gas heat extraction analyzer (TC-436, LECO) as follows. The sample in a metallic flux (nickel and tin) was heated in a graphite crucible to 2500 °C under helium flow and the oxygen was quantified by IR absorption as CO₂. Surface areas were calculated using Brunauer–Emmett–Teller (BET) theory from the argon adsorption isotherms of the samples. Samples were outgassed for 6–12 h overnight at 100 °C to a vacuum of 10⁻⁷ mbar. Isotherms were collected on a Quantachrome Autosorb iQ gas sorption analyzer using argon as the sorbent at 87.45 K.

Solid-state magic angle spinning NMR was performed at ambient temperature on an Avance III HD 600 and an Avance III HD 400 solid state NMR spectrometer (Bruker) with an external magnetic field of 14.1 T and 9.4 T, respectively. The operating frequencies of the two spectrometers are 600.1 MHz, 150.9 MHz, 60.8 MHz and 400.1 MHz, 100.6 MHz, 40.6 MHz for ¹H, ¹³C and ¹⁵N, respectively. The samples were contained either in 1.9 mm or 4 mm ZrO₂ rotors, which were mounted in standard triple or double resonance MAS probes (Bruker). The spinning speed was set to 15 kHz for the 1.9 mm rotor, or 5 kHz for the 4 mm rotor. ¹³C and ¹⁵N spectra were recorded using standard or ramped amplitude cross polarization (CP) with contact times of 10 and 15 ms, respectively. The recycle delay was set to 4s for ¹³C and to 3s for ¹⁵N measurements. All spectra were referenced to TMS for the ¹³C and nitromethane for ¹⁵N. During acquisition of ¹³C and ¹⁵N proton decoupling was carried out using SPINAL64 with an rf field between 70 and 80 kHz.

MALDI-TOF (matrix-assisted laser desorption/ionization-time of flight) was performed on a Shimadzu Axima Resonance mass spectrometer. Calibration was carried out using neat fullerene and using CsI ground with trans-2-[3-(4-*tert*-butylphenyl)-2-methyl-2-propenylidene]malononitrile as the matrix. Each sample was ground with tetracyanoquinodimethane (TCNQ) as the matrix and deposited on a steel sample holder. The spectra were collected in raster mode and the laser power was progressively increased until a suitable signal-to-noise ratio was achieved. The spectra presented are averaged from 100 profiles.

Transmission electron microscopy (TEM) was performed with a Philips CM30 ST (300 kV, LaB6 cathode). The samples were suspended in *n*-butanol and drop-cast onto a lacey carbon film (Plano). Scanning electron microscopy (SEM) was performed on a Vega TS 5130MM (Tescan) microscope equipped with an energy dispersive detector for X-ray spectroscopy (EDX, Oxford Instrument). Each

sample was deposited onto a carbon tab (Leco) and sputtered with gold for imaging. No sputtering was used for elemental analysis by EDX.

Zeta potential was measured using a Malvern Zetasizer Nano ZS. The sample was dispersed with sonication in NaCl solution (10 mM) of different pH (adjusted with HCl or NaOH) and allowed to stand prior to measurements in disposable cuvettes (Malvern). Measurements were conducted as four replicates; average results were quoted using the standard deviation as the error.

For X-ray photoelectron spectroscopy (XPS), samples were pressed onto indium foil and the spectra were collected on an Axis Ultra (Kratos Analytical, Manchester) X-ray photoelectron spectrometer with charge neutralization. The spectra were processed using the software OriginPro 8.5.1. All peaks were fitted using a Gaussian function with baseline correction, except for platinum, where a Gaussian-Lorentzian function was used. The spectra were referenced with the adventitious carbon 1s peak at 284.80 eV. Binding energies were compared with the NIST Standard Reference Database 30 (Version 4.1) unless otherwise specified.

Thermogravimetric analysis coupled with mass spectroscopy (TGA-MS) was performed with the instrument STA 409 C (Netzsch GmbH, Selb, Germany) connected with a quadrupole mass spectrometer QMS 422 (Balzers, Hudson, USA). Samples were loaded in alumina crucibles and heated under argon (100 mL min^{-1}) from ambient temperature to $900 \text{ }^\circ\text{C}$ at a ramp rate of $1 \text{ }^\circ\text{C min}^{-1}$. To separate the contributions of ammonia and hydroxide (from background moisture) of the $m/z = 17$ signal, a blank, reference measurement was carried out to determine the ratio of the water to hydroxide signal. The ammonia contribution to the $m/z = 17$ signal was then calculated by subtracting the $m/z = 18$ signal multiplied by the water-hydroxide ratio.

Photoluminescence (PL) spectra were collected in excitation mode with a Horiba FluoroLog F3-22 spectrophotometer at 90° to the excitation source. The powder samples ($1.0 \pm 0.1 \text{ mg}$) were suspended with sonication in an aqueous methanol solution (10 vol%, 3 mL) and the suspension was measured in a quartz cuvette. Excitation wavelengths employed were 260 nm for the melon sample and 250 nm for the oligomeric samples. These wavelengths were identified to maximize the PL signal using emission mode.

Photocatalytic experiments were performed in a double-walled glass reactor (Figure S1), where the outer compartment is circulated with thermostated water ($25 \text{ }^\circ\text{C}$). The reactor was top-irradiated through a quartz window with a xenon lamp (Newport, 300 W) equipped with a water filter and either a dichroic mirror that allows only visible light ($\lambda > 420 \text{ nm}$) to pass or a full spectrum mirror ($2000 \text{ nm} > \lambda > 200 \text{ nm}$). An air mass (AM) 1.5 filter was also used where specified. For each experiment, the catalyst powder (20 mg) was suspended in a phosphate buffer solution (PBS, 18 mL of 0.1 M solution at pH 3, 7 or 11) containing methanol (2 mL). Dihydrogen hexachloroplatinate (5 μL , 8 wt% aqueous solution, Aldrich) was added for the *in-situ* formation of platinum as the cocatalyst, which yields a loading of around 2 wt%. The headspace was subjected to several cycles of evacuation and argon backfill prior to the experiment. In the course of the experiment, the headspace of the reactor was periodically sampled and the components were quantified by gas chromatography (Thermo Scientific TRACE GC Ultra) equipped with a TCD detector using argon as the carrier gas. After the photocatalytic experiment, the catalyst was recovered by centrifugation, washed with water, then dried at $100 \text{ }^\circ\text{C}$. Experiments for the estimation of quantum efficiencies were conducted using band pass filters with band centers at 400 nm and 500 nm with full width half

maximum of 50 nm (Thorlab). Irradiance of the incident light was measured using a thermopile (Thorlabs). The apparent quantum efficiency was then calculated as:

$$AQE [\%] = \frac{2 \times \text{Hydrogen evolution rate} [\text{mol } h^{-1}]}{\text{Photon flux} [\text{mol } h^{-1}]}$$

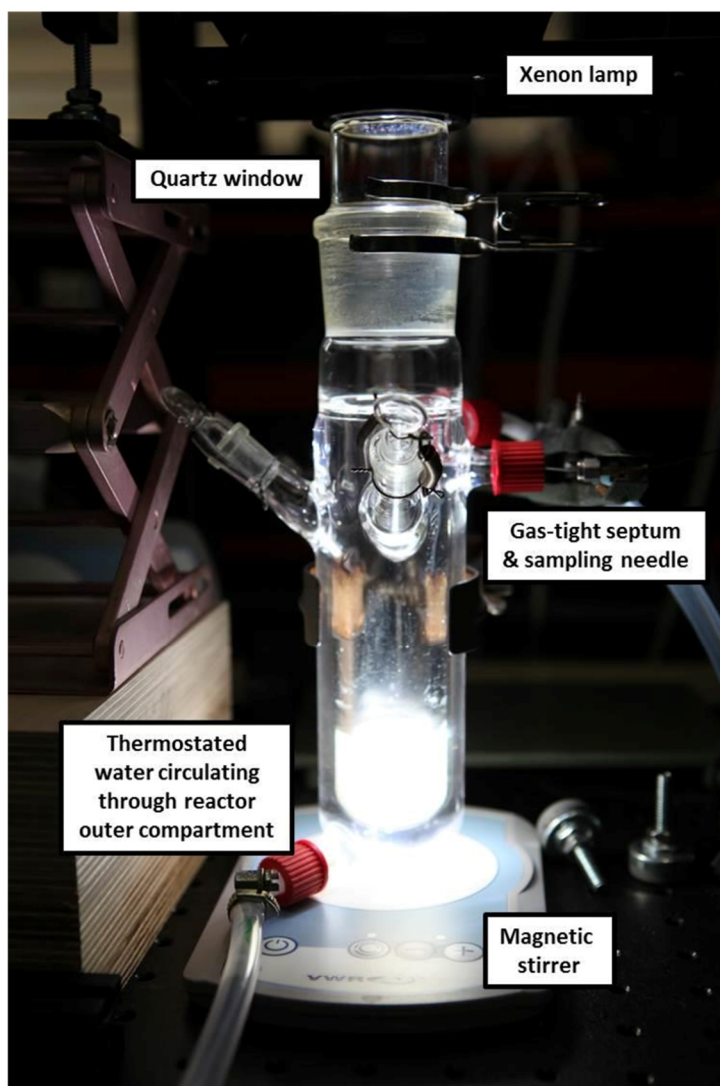


Figure S1 Reactor set-up used for evaluating photocatalysts for hydrogen evolution.

Computational details & additional discussions

Calculations were performed with the FHI-aims all-electron electronic structure code.^{2,3} For the heptazine monomer, dimer, trimer, and tetramer, minimum-energy geometries were calculated using the van der Waals corrected DFT-generalized gradient approximation (GGA) with the PBE functional^{4,5} and "tight" numerical settings ("tier 2" basis sets in FHI-aims). The isolated tetramer allows for significant conformation flexibility, as exemplified by four specific prototypes in Table S4.

For the calculation of HOMO and LUMO levels of the isolated conformers (vacuum), a recently developed, approximate approach⁶ to parameterize the PBE hybrid (PBEh) density functional⁷ for molecular systems was employed. In brief, so-called G^0W^0 -level many-body perturbation theory (MBPT) calculations³ were carried out for effective single quasi-particle levels of the monomer, based on the electronic structure derived from PBEh functional with different exact exchange mixing parameters $0 \leq \alpha \leq 1$ and using highly converged NAO-VCC-5Z basis sets,⁸ developed specifically for reliable convergence of the unoccupied-state sums necessary for MBPT. Following reference 6, a value $\alpha=0.6882$ was determined, for which the monomer HOMO level as evaluated by the PBEh functional and by the G^0W^0 calculation agree. This optimized PBEh functional ($\alpha=0.6882$) was then used to calculate HOMO and LUMO orbitals and energy levels for the isolated (vacuum) conformers of the dimer, trimer, and tetramer, using FHI-aims "tight" settings and a tier 2 basis set.

The effective single-quasiparticle levels of isolated gas phase molecules cannot be directly compared to UV-Vis absorption spectra or PL spectra obtained in the condensed phase, but the relative development of the HOMO/LUMO levels with conformer length and conformation can be compared as a trend. Table S3 lists HOMO, LUMO, and band gap values as calculated for the isolated conformers shown in Figure 6 in the main paper (optimized PBEh values; PBE values in brackets). Table S4 shows examples of types of tetramer conformers and their HOMO, LUMO, and gap values. The orbital isosurfaces shown were calculated using the optimized PBEh functional. As these calculations were carried out for an isolated molecule in vacuum, they serve to illustrate how conformation and inter/intramolecular variations can lead to changes in HOMO/LUMO distribution and energy gap. More detailed calculations require other factors (solvent effect, electron-phonon coupling, excitonic effects) to be taken into account to fully reflect the material under photocatalytic conditions.

The two different treatments yield very different absolute values for the gas phase frontier orbital energy levels, with the optimized PBEh values likely closer to the truth for the isolated molecules. In contrast, the experimentally measured UV-Vis gaps contain a variety of other effects due to the condensed phase, including the effect of the surrounding medium (solvent shift), renormalization by electron-phonon coupling or excitonic effects, etc. The trend of the HOMO, LUMO, and gap values with conformer length (smaller gap with increasing length) is consistent between both density functional descriptions used and also with the experiments. We stress that the overall shape (geometry) of the HOMO, LUMO, and molecular conformation are much less affected by the choice of functional than the actual eigenvalues.

Characterization of as-synthesized melem oligomer

Values for the quantum efficiencies were estimated using the incident photon across the entire AM 1.5 spectrum up to where the water filter cuts off the infrared portion. The melem oligomer and the melon have a quantum efficiency of approximately 0.015% and 0.0051%, respectively. The apparent deactivation of the photocatalysts in alkaline solution is attributed to the formation of CO in the oxidation of methanol in a basic environment, which can irreversibly bind to the platinum co-catalyst.⁹

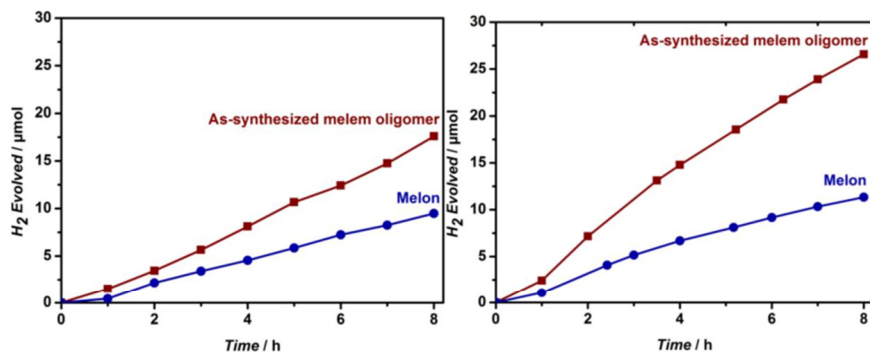


Figure S2 Photocatalytic hydrogen evolution of the melem oligomer, compared with melon, in PBS of pH 3 (left) and pH 11 (right). The full spectrum of the xenon lamp, together with the AM 1.5 filter, was used.

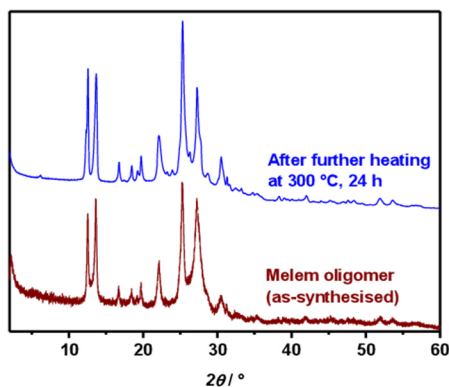


Figure S3 XRD pattern of melem oligomer after further heat treatment.

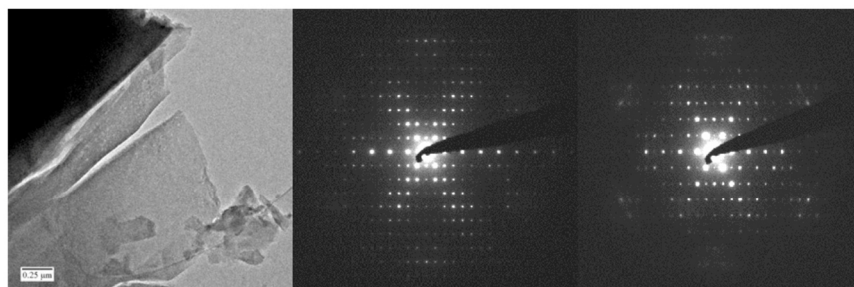


Figure S4 TEM image (left) and precession electron diffraction patterns (center and right) of the as-synthesized melem oligomer sample after heat treatment for improved crystallinity. The pattern in the center can be assigned to melem, viewed along the [100] zone axis. The pattern on the right is an unknown phase and has a unit cell slightly elongated in the [001] direction and contracted in the [010] direction compared to melem.

Table S1 Elemental analyses of the melem oligomer and melon in comparison with theoretical values for melem and ideal C_3N_4 . The reported values and their uncertainties are the average and standard deviation, respectively, of three replicates.

	C (wt%)	N (wt%)	H (wt%)	O (wt%)	C:N atomic ratio
Melem (th.)	33.0	64.2	2.8	0	0.60
As-synthesized melem oligomer	33.78±0.05	58.9±0.5	2.5±0.1	1.75±0.04	0.67
Melon	35.40±0.08	60.6±0.5	1.83±0.05	0.8±0.1	0.68
Melon (th. 1D polymer)	35.8	62.7	1.5	0	0.66
C_3N_4 (th.)	39.1	60.9	0	0	0.75

Characterization of as-synthesized melem oligomer after the photocatalytic reaction

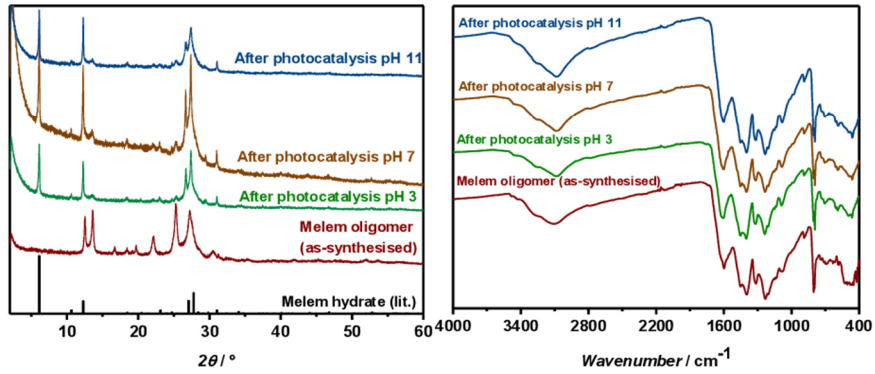


Figure S5 XRD patterns (left) and ATR-IR spectra (right) of melem oligomer before and after photocatalysis.

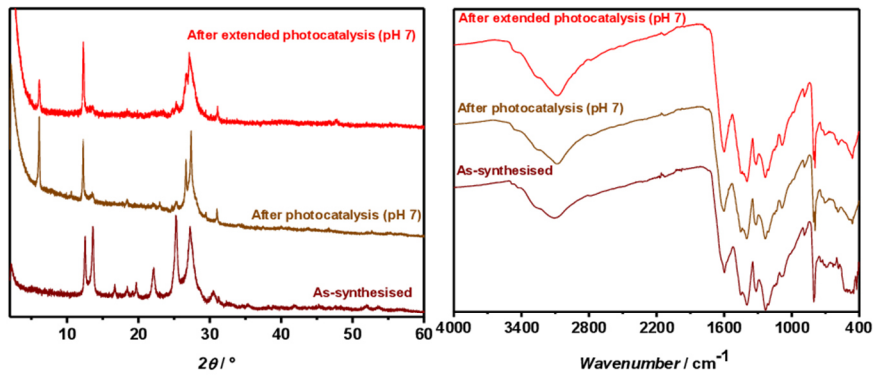


Figure S6 Characterization of the melem oligomer after the 129 h extended photocatalytic test (Figure 1b) by XRD (left) and ATR-IR (right).

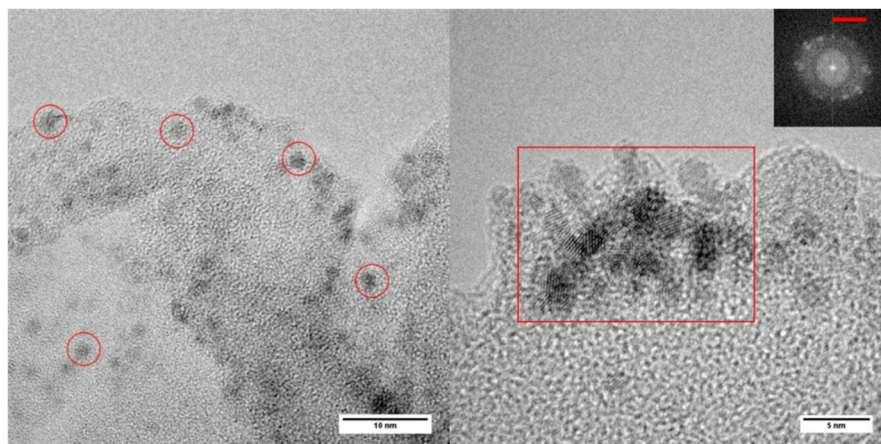


Figure S7 HRTEM images of the as-synthesized melem oligomer after the extended (>120 h) photocatalytic reaction. The left image shows an overview with some platinum particles marked; these spherical particles are generally less than 2 nm in diameter. The right image is a magnified view showing a cluster of platinum particles; the fast fourier transform of the region inside the red box is shown in the inset, where the red line shows the radius of the ring is $\approx 2.3 \text{ \AA}$, corresponding to the (111) d -spacing of platinum.

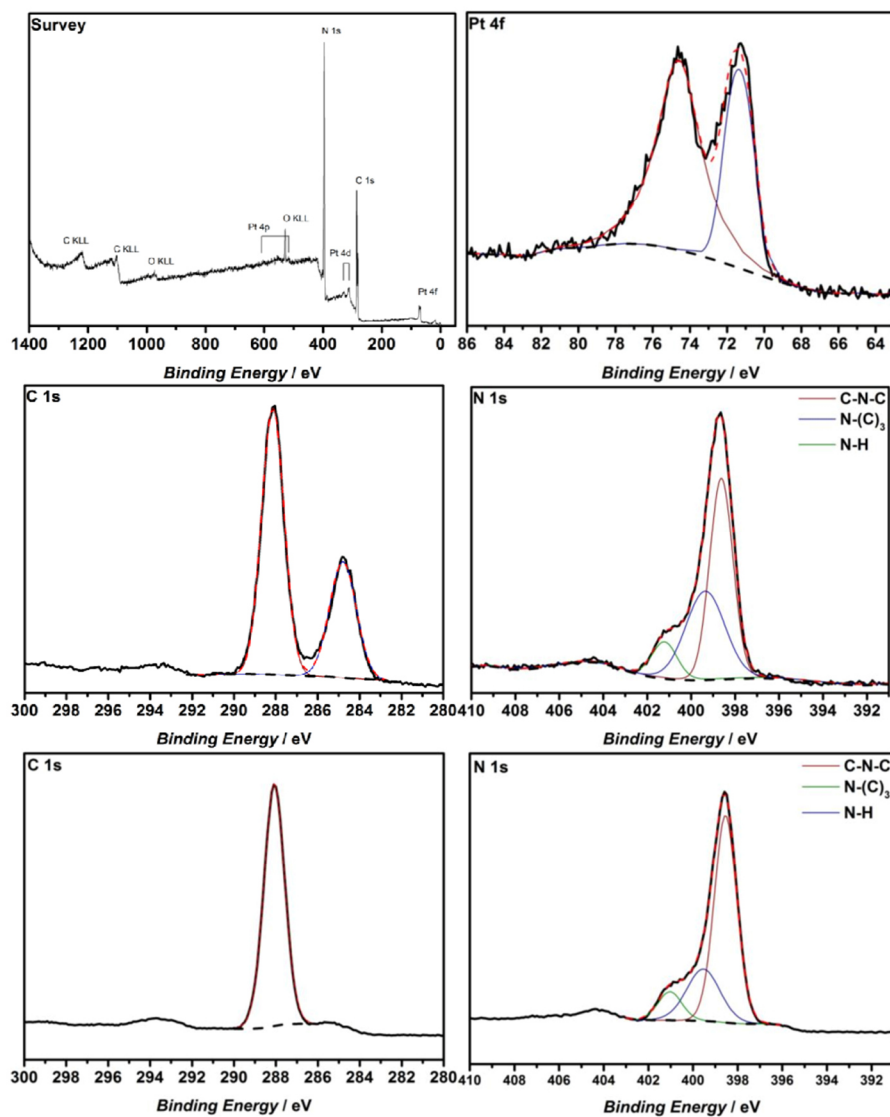


Figure S8 XPS spectra of the as-synthesized melem oligomer after extended (>120 h) photocatalytic reaction: survey spectrum (top left); Pt 4f region (top right); C 1s and N 1s regions (middle left and right respectively). For comparison, the C 1s and N 1s regions of the sample before the catalytic reactions are shown in the bottom left and right, respectively. Note that the C 1s peak at the lower binding energy is assigned to the adventitious carbon and is calibrated to 288.4 eV.

Characterization of the fractions separated from the as-synthesized melem oligomer

Table S2 BET surface areas, hydrogen evolution rates and apparent quantum efficiencies of the fractions, compared with the as-synthesized sample and melon.

	BET surface area (m ² g ⁻¹)	H ₂ evolution rate (μmol h ⁻¹)	Apparent quantum efficiency at 400 (±25) nm (%)
Melem oligomer (as-synthesised)	14.0 ± 0.5	2.8	*
DMSO soluble fraction	14.7 ± 0.5	0.0	*
RCF 10000 fraction	23.3 ± 0.3	4.8	8.7×10 ⁻²
RCF 60000 fraction	24.6 ± 1.4	5.4	1.0×10 ⁻¹
Melon	9.0 ± 0.2	0.6	1.5×10 ⁻²

*Not measured

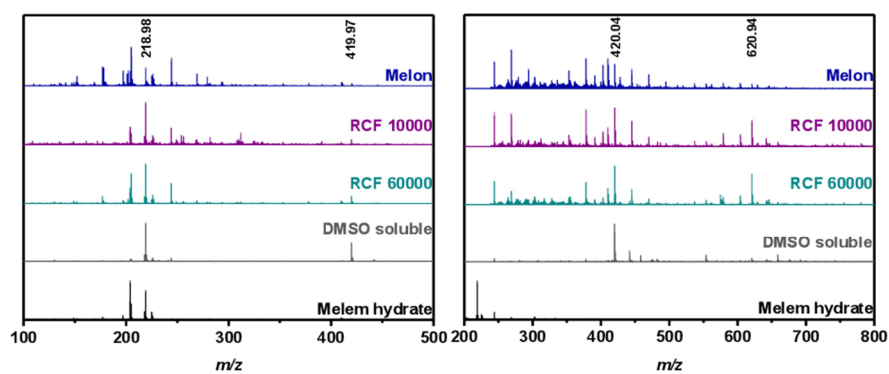


Figure S9 MALDI-TOF spectra of the fractions, compared with melem and melon, measured in the mass range >100 (left) and >300 (right). The signal at 203.94 corresponds to the matrix.

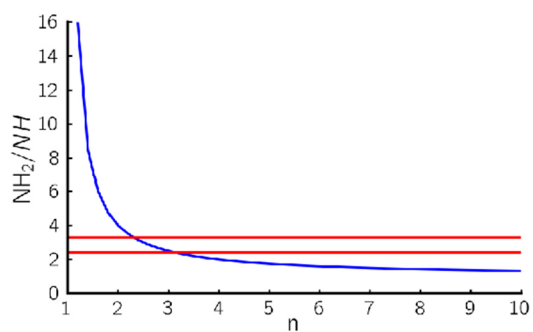


Figure S10 Plot of the integral ratio $^{15}\text{NH}_2 : ^{15}\text{NH}$ against the chain length n . Red lines indicate the experimental values. The ratio was calculated according to the formula $\frac{\text{NH}_2}{\text{NH}} = \frac{n+2}{n-1}$.

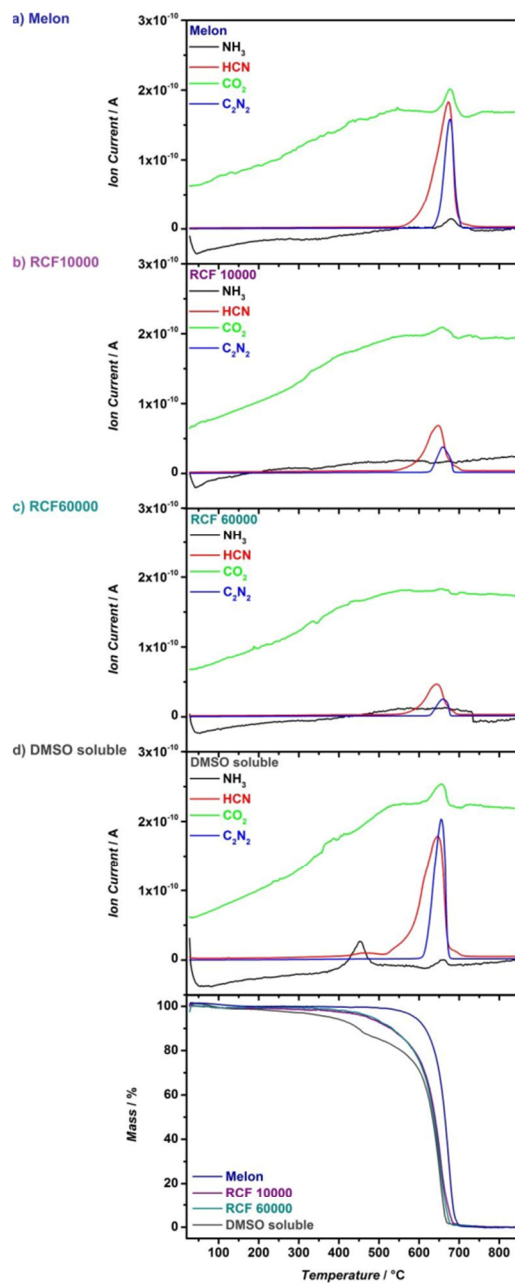


Figure S11 TGA-MS analyses of: a) melon; b) RCF 10000 fraction; c) 60000 fraction; and d) the DMSO soluble fraction. Samples were heated at 1 °C min^{-1} under argon.

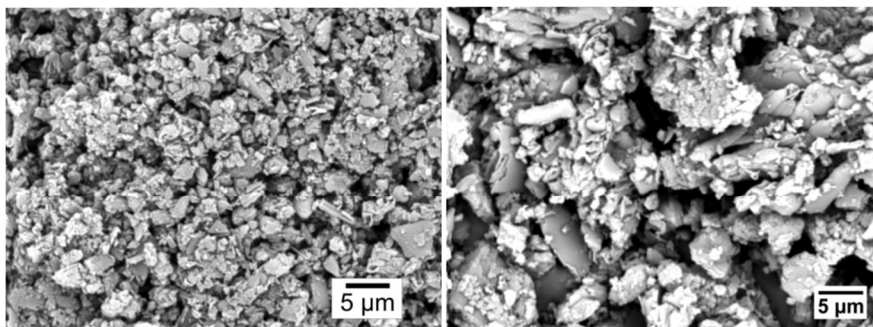


Figure S12 SEM image of the fraction obtained at RCF 60000 (left) and melon (right).

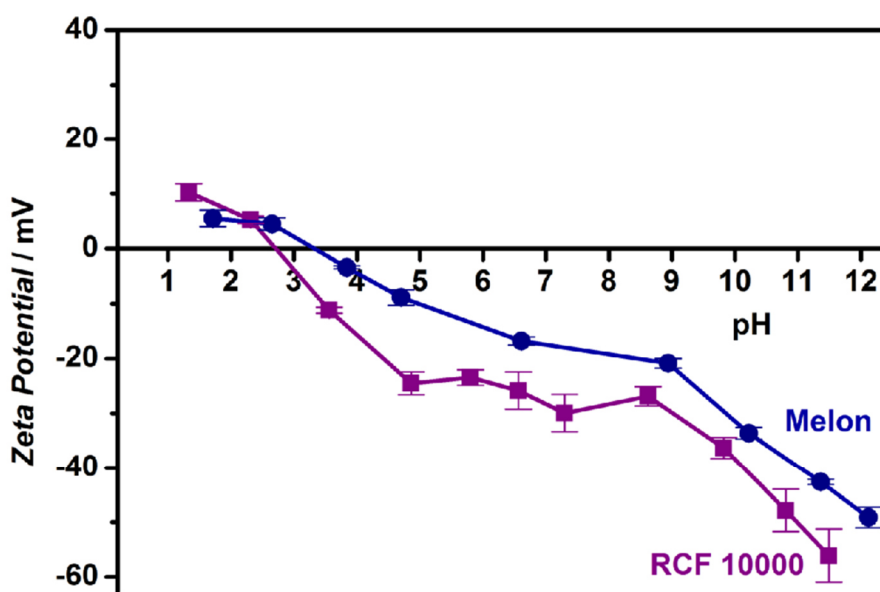


Figure S13 Plot of zeta potential versus pH for the fraction RCF 10000 compared to the polymer melon. Isoelectric points for this fraction and melon are at pH 2.7 and 3.3, respectively.

Table S3 Orbital energies for the calculated structures in Figure 7. Potential energies are referenced to vacuum. Optimized PBEh functional eigenvalues (PBE values in brackets).

	HOMO (eV)	LUMO (eV)	Energy Gap (eV)
Monomer	-8.695 (-5.602)	+0.285 (-2.105)	8.980 (3.497)
Dimer	-8.783 (-5.711)	-0.638 (-2.776)	8.145 (2.935)
Trimer	-8.825 (-5.760)	-0.894 (-2.984)	7.931 (2.776)
Tetramer	-8.847 (-5.780)	-1.014 (-3.085)	7.833 (2.695)

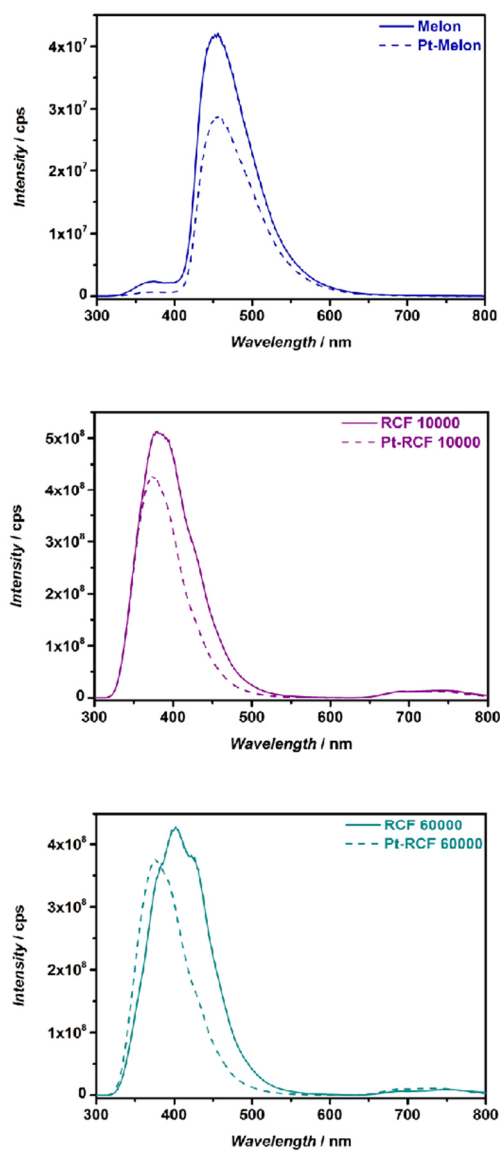
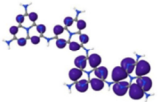
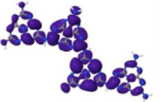
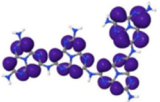
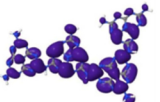
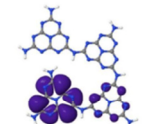
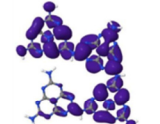
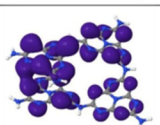
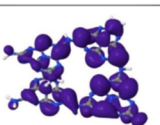


Figure S14 Photoluminescence spectra of melon and the oligomeric fractions suspended in aqueous methanol (10 vol%) with and without platinum loading.

Table S4 Variations of energy levels (versus vacuum) and gaps depending on tetramer conformation and hydrogen bonding. The potential values provided are derived from the optimized PBEh hybrid density functional with $\alpha = 0.6882$, while the values in brackets are derived using the PBE functional. Only the positive parts of the HOMO and LUMO orbitals are shown. The negative parts are located on the respective opposite sides of the heptazine planes and are omitted in order to show the locations of individual atoms more clearly.

Conformer	HOMO	LUMO	HOMO (eV)	LUMO (eV)	Energy Gap (eV)
Planar staggered			-8.834 (-5.762)	-1.012 (-3.084)	7.822 (2.678)
Twisted			-8.851 (-5.780)	-1.013 (-3.091)	7.838 (2.689)
Hydrogen bonded			-8.635 (-5.548)	-1.040 (-3.139)	7.595 (2.409)
Helical π -stacked			-8.841 (-5.708)	-0.987 (-3.084)	7.854 (2.624)

- (1) Schwarzer, A.; Saplinova, T.; Kroke, E. *Coord. Chem. Rev.* **2013**, *257*, 2032
- (2) Blum, V.; Gehrke, R.; Hanke, F.; Havu, P.; Havu, V.; Ren, X.; Reuter, K.; Scheffler, M. *Comput. Phys. Commun.* **2009**, *180*, 2175
- (3) Ren, X.; Rinke, P.; Blum, V.; Wieferink, J.; Tkatchenko, A.; Sanfilippo, A.; Reuter, K.; Scheffler, M. *New J. Phys.* **2012**, *14*, 053020
- (4) Perdew, J. P.; Burke, K.; Ernzerhof, M. *Phys. Rev. Lett.* **1996**, *77*, 3865
- (5) Tkatchenko, A.; Scheffler, M. *Phys. Rev. Lett.* **2009**, *102*, 073005
- (6) Atalla, V.; Yoon, M.; Caruso, F.; Rinke, P.; Scheffler, M. *Phys. Rev. B* **2013**, *88*, 165122
- (7) Perdew, J. P.; Ernzerhof, M.; Burke, K. *Journal of Chemical Physics* **1996**, *105*, 9982
- (8) Zhang, I. Y.; Ren, X.; Rinke, P.; Blum, V.; Scheffler, M. *New J. Phys.* **2013**, *15*, 123033
- (9) Spendelov, J. S.; Goodpaster, J. D.; Kenis, P. J. A.; Wieckowski, A. *Langmuir* **2006**, *22*, 10457

6.3 Strukturaufklärung eines heptazin-basierten Netzwerks mittels 1D Spektren

Donor-Acceptor Type Heptazine-Based Polymer Networks for Photocatalytic Hydrogen Evolution

K. Kailasam,^{*,†,‡} M. B. Mesch,[§] L. Möhlmann,^{||} M. Baar,^{||} S. Blechert,^{||} M. Schwarze,[¥] M. Schröder,[¥] R. Schomäcker,[¥] J. Senker,[§] A. Thomas^{*,†}

Erschienen in:

Energy Technology 2016, DOI: 10.1002/ente.201500478

Abdruck mit Genehmigung, Copyright (2016) Wiley-VCH Verlag GmbH & Co. KGaA

[†] Department of Chemistry, Functional Materials, Technische Universität Berlin, Hardenbergstr. 40, 10623 Berlin, Germany

[‡] Institute of Nano Science and Technology (INST), Habitat Centre, Phase-10, Sector-64, 160062 Mohali, Punjab, India

[§] Inorganic Chemistry III, Universität Bayreuth, Universitätsstr. 30, 95447 Bayreuth, Germany

^{||} Department of Chemistry, Technische Universität Berlin, Straße des 17. Juni 135, 10623 Berlin, Germany

[¥] Department of Chemistry, Technische Universität Berlin, Straße des 17. Juni 124, 10623 Berlin, Germany

* kamal@inst.ac.in, arne.thomas@tu-berlin.de

6.3.1 Donor-Acceptor Type Heptazine-Based Polymer Networks for Photocatalytic Hydrogen Evolution

Energy Technology

DOI: 10.1002/ente.201500478

FULL PAPER

Donor–Acceptor-Type Heptazine-Based Polymer Networks for Photocatalytic Hydrogen EvolutionKamalakannan Kailasam,^{*[a, b]} Maria B. Mesch,^[c] Lennart Möhlmann,^[d] Moritz Baar,^[d] Siegfried Blechert,^[d] Michael Schwarze,^[e] Marc Schröder,^[e] Reinhard Schomäcker,^[e] Jürgen Senker,^[c] and Arne Thomas^{*[a]}

A heptazine-based polymer network (HMP-3) with a donor–acceptor (D–A) structure was prepared and tested as catalyst for photocatalytic hydrogen evolution from water. Compared to other heptazine-based materials, which are typically prepared at high temperatures and have recently received much interest as metal-free photocatalysts, the low-temperature protocol applied here allows the defined introduction of organic functional groups within the polymer backbone. The

structure of HMP-3 contains alternating heptazine and benzothiadiazole moieties as electron acceptors connected by aminobenzene bridges as electron donors. The resulting material leads to enhanced hydrogen evolution compared to graphitic carbon nitride materials prepared at high temperatures (> 500 °C) most probably because of the stabilization of photogenerated charge carriers in the D–A structure.

Introduction

The generation of “green” fuels, such as hydrogen from water, using sunlight is one of the most important challenges in this century.^[1] One pathway to generate hydrogen from water is the application of semiconductor photocatalysts that are able to reduce protons to hydrogen by light excitation.^[2] A number of metal-based photocatalysts have been reported that can fulfill the task of photocatalytic hydrogen production from water or even overall water splitting.^[3] Recently, a polymeric carbon nitride (CN, frequently also denoted as g-C₃N₄) composed of amine-bridged heptazine (C₆N₇) units, which assemble in 2D sheets and a graphite-like stacking, has been reported as a metal-free system to catalyze both half reactions, that is, hydrogen or oxygen evolution from water, if a suitable sacrificial reagent is present.^[4] Besides their high potential as heterogeneous metal-free photocatalysts, heptazine-based polymeric carbon nitrides are easy to synthesize from inexpensive precursor molecules, which explains why these materials have been the subject of tremendous research activity over recent years.^[5]

In general, CN materials are prepared by the pyrolysis of nitrogen-rich precursors such as cyanamide, urea, dicyandiamide, or melamine.^[6] As bulk CN shows just moderate photocatalytic activity, numerous attempts have been made to improve its performance, for example, by controlling the degree of polymerization, the introduction of porosity and high surface areas, metal or heteroatom doping, or the formation of CN composites.^[5,7] Indeed, such modifications have been reported to influence and often enhance the catalytic performance of CNs. However, the high condensation temperatures involved (> 500 °C) make the incorporation of defined organic moieties into the CN structure in a controlled manner difficult if not impossible.

Therefore, it would be interesting to develop low-temperature strategies to synthesize CN materials. As CNs are composed of amine-bridged s-heptazine (C₆N₇) units, one possible pathway would be the use of functionalized heptazines that can be polymerized to generate new polymeric CN structures. An amine-functionalized heptazine, also called “melem”, is an intermediate in the thermal condensation of N-rich molecules towards CN materials.^[8] However, even

[a] Prof. Dr. K. Kailasam, Prof. Dr. A. Thomas
Department of Chemistry, Functional Materials
Technische Universität Berlin
Hardenbergstraße 40
10623 Berlin (Germany)
E-mail: kamal@inst.ac.in
arne.thomas@tu-berlin.de

[b] Prof. Dr. K. Kailasam
Institute of Nano Science and Technology (INST)
Habitat Centre, Phase-10, Sector-64
160062 Mohali, Punjab (India)
Fax: (+ 49) 303-142-9271

[c] M. B. Mesch, Prof. Dr. J. Senker
Universität Bayreuth
Inorganic Chemistry III
Universitätsstr. 30
95447 Bayreuth (Germany)

[d] Dr. L. Möhlmann, M. Baar, Prof. Dr. S. Blechert
Technische Universität Berlin
Department of Chemistry
Straße des 17. Juni 135
10623 Berlin (Germany)

[e] Dr. M. Schwarze, M. Schröder, Prof. Dr. R. Schomäcker
Department of Chemistry
Technische Universität Berlin
Straße des 17. Juni 124
10623 Berlin (Germany)

Supporting information for this article can be found under <http://dx.doi.org/10.1002/ente.201500478>.

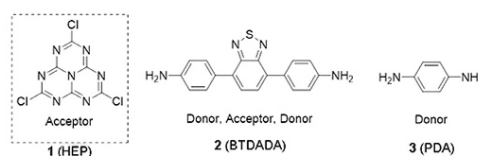
though melem can be isolated, it is hardly soluble in any solvent and the electron-deficient structure of the heptazine ring makes the amine groups nearly inaccessible to electrophilic attack. Cyameluric chloride ($C_6N_7Cl_3$), which can be synthesized from melem in two simple steps, seems to be a much more feasible monomer for the synthesis of heptazine-based polymers as it is easily soluble in organic solvents, and the chloride groups are highly reactive for nucleophilic substitutions.^[9] Recently, we introduced heptazine-based microporous polymer networks (HMPs) synthesized at room temperature by the polycondensation of aryl diamines with cyameluric chloride.^[10] The resulting HMPs showed activity as photocatalysts for hydrogen evolution under visible light. Furthermore, because of the rigid structure of the trigonal planar heptazine moiety, dense packing of the polymer chains is avoided, and therefore, the polymer networks exhibit intrinsic porosity, a concept that has been exploited recently for a wide range of microporous high-surface-area polymers.^[11] Similarly, an imine-linked covalent organic framework (COF) prepared at ambient temperatures and pyrene-based CMPs (conjugated microporous polymers) have been reported to exhibit photocatalytic activity for hydrogen generation from water.^[12] In general porous polymers are currently receiving increasing interest in the construction of green energy devices.^[13]

Tuning of band gaps in such organic semiconductors is a promising pathway to enhance their photocatalytic activity. Furthermore, the synthesis of structures that allow the formation of relatively stable charge carriers (i.e., excited electrons and holes) is of major importance. The same principles are applied in organic electronic devices, especially in organic solar cells. In this field, donor-acceptor (D-A) type polymers are of major interest and thus it is certainly desirable for these two fields of polymer research to stimulate each other.

In this article, we introduce the D-A concept for the generation of improved polymer network photocatalysts. An alternating $-D-A_1-D-A_2-$ polymer network was prepared from heptazine (A_1) and benzothiadiazole (A_2) subunits as electron acceptors and aminobenzene (D) as the electron donor under mild reaction conditions.

Results and Discussion

The monomers cyameluric chloride (**1**) and 4,4'-(benzo[*c*][1,2,5]thiadiazole-4,7-diyl)dianiline (BTDADA; **2**) used in this study are presented in Scheme 1 along with the monomer phenylenediamine (PDA) (**3**) used in our earlier study to prepare HMP-1.^[10] Notably, in the case of HMP-1, heptazine units were bridged by diaminobenzene moieties, which in principle already form a D-A-type structure.^[10] However, in HMP-3 another strong electron acceptor, benzothiadiazole, used frequently in organic electronics, was introduced into the structure to investigate the influence on the photocatalytic activity for water splitting.^[14] Recently, microporous poly(benzothiadiazole) networks have been reported and employed as a photocatalyst to generate singlet oxygen.^[15]

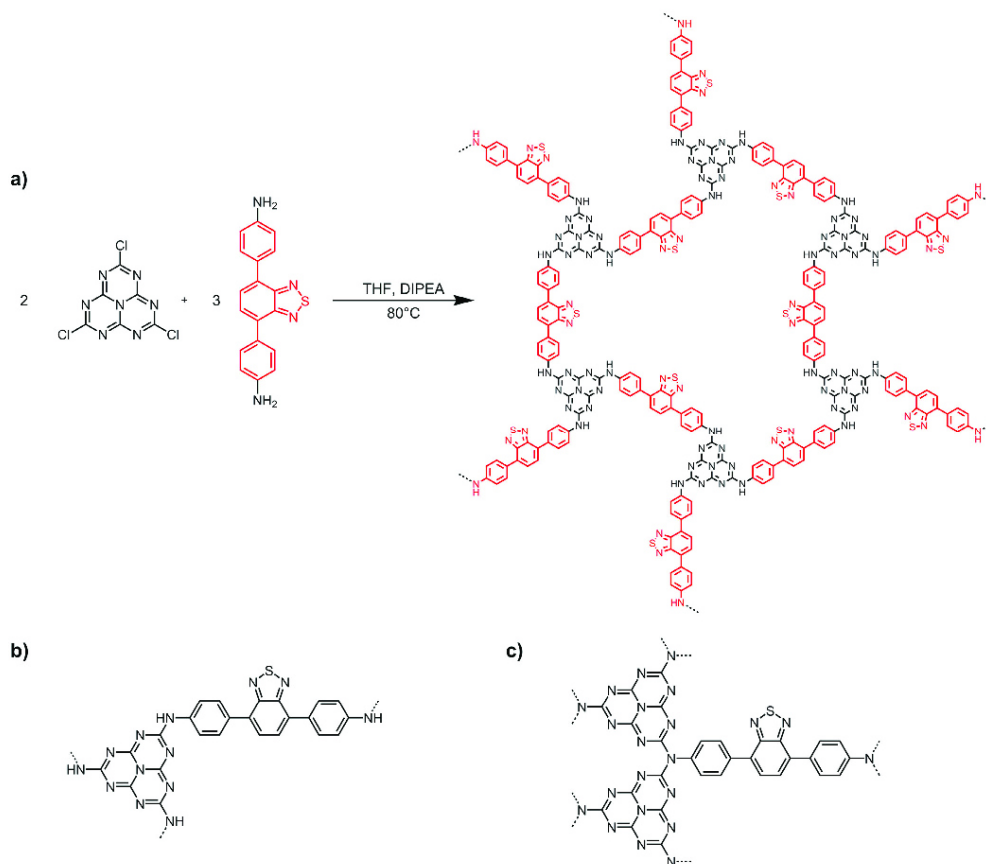


Scheme 1. Structures of **1** and **2** used in this study. Monomer **3** was used in our recent study to prepare HMP-1.

The D-A-type heptazine-based polymer network HMP-3 was prepared by the copolymerization of **1** with **2** in different monomer ratios in THF under basic conditions. (Scheme 2 a). This approach also enables the formation of homogeneous thin films on any conductive substrates, which we demonstrated previously.^[10] In principle, the heptazine core and the BTDADA linker can be connected either through secondary or tertiary amines and these connectivity patterns can, in theory, be achieved by changing the molar ratio of the monomers. Therefore, two different molar ratios of heptazine chloride to BTDADA were used, which would in principle allow the formation of either a network in which all aromatic moieties are connected through secondary amines (molar ratio = 2:3; Scheme 2 b) or through tertiary amines (4:3; Scheme 2 c) if we assume a quantitative and homogeneous condensation. Indeed, a strong color change from yellow/orange (HMP-3_4:3) to dark red (HMP-3_2:3) was observed for networks with increasing amount of benzothiadiazole units (Figure S1, Supporting Information), which indicates that this approach enables the incorporation of functional D-A units with adjustable amounts into heptazine-based networks.

The C and S atomic ratios derived from elemental analysis match well with the calculated values a quantitative and homogeneous condensation according to Scheme 2 is assumed (Table S1). As expected, the S content increases if more benzothiadiazole units are used in the initial monomer ratio (HMP-3_2:3). The observed N content is significantly lower, which is an often reported issue for N-rich and highly condensed polymers, probably because incomplete combustion makes a quantitative assessment of this element challenging.^[16] The non-quantitative yields of the polymerization reactions also indicate some amounts of unreacted end-groups, which, in case of the chloride groups on the heptazine, can further hydrolyze, making verifiable statements from elemental analysis even more difficult.

Thermogravimetric analysis (TGA) under inert atmosphere (Figure S2) shows that HMP-3_2:3 has a high thermal stability, with a weight loss of only around 5% at 500 °C. Indeed, the stability of HMP-3_2:3 is quite similar to that of polymeric carbon nitrides prepared at high temperatures. However, HMP-3_4:3, which should possess a higher cross-linking density, showed a lower thermal stability with a constant weight loss with increasing temperature. The decrease in thermal stability is, however, explained convincingly by a detailed study of the chemical structure and connectivity in these two polymers, provided by quantitative ¹³C NMR spec-



Scheme 2. (a) Reaction scheme and structure of HMP-3_2:3 prepared by the copolymerization of **1** and **2** in a 2:3 molar ratio. Possible repeating unit of (b) HMP-3_2:3 and (c) HMP-3_4:3.

trosopy, as these measurements show that indeed HMP-3_2:3 forms the more robust structure with improved connectivity between the monomers (see below).

XRD patterns of HMP-3 for both monomer ratios show just broad peaks at around $2\theta = 27^\circ$, which excludes crystalline structures (Figure S3). This is comparable to previous reports on the formation of amorphous polymeric networks that are inevitably formed under kinetically controlled polymerization conditions.^[11a]

To gain a deeper insight into the chemical structure of the HMP-3 networks, solid-state ^{13}C and ^{15}N NMR spectra were collected (Figure 1). In the ^{15}N cross-polarization magic-angle spinning (CP-MAS) spectra (Figure 1, left) of both samples a resonance for the benzothiadiazole linker is observed at approximately $\delta = -55$ ppm. This peak overlaps with a spinning sideband. The signal at around $\delta = -190$ ppm is characteristic of the outer heptazine N atoms. The shift of

the inner N atom is quite characteristic and depends on the substituents on the heptazine unit. For example, in cyameluric acid it is observed at $\delta = -245$ ppm and shifts to $\delta = -225$ ppm in melon.^[8,17] For the HMP-3 samples, the signal for the inner N atom is found at approximately $\delta = -227$ ppm, which indicates NH-bridged heptazine units. The remaining signal for HMP-3_2:3 between $\delta = -250$ and -260 ppm is typical for those NH groups. For HMP-3_4:3, the NH signals are downfield shifted by approximately 10 ppm probably because it has a slightly modified structure with a different hydrogen bond pattern. Furthermore, a signal at $\delta = -160$ ppm is observed that might suggest the presence of additional heptazine species. The group of signals at around $\delta = -240$ ppm observed only for HMP-3_4:3 is assigned to cyameluric acid, which could result from the hydrolysis of unreacted cyameluric chloride during the washing procedure.

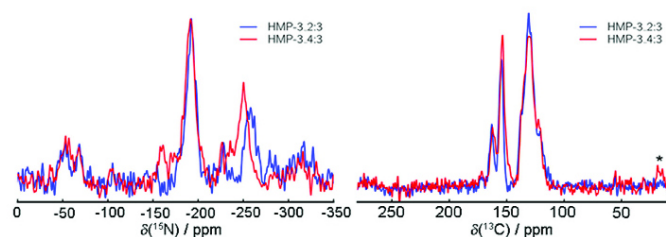


Figure 1. ^{15}N CP (left) and ^{13}C one-pulse (right) MAS NMR measurements of D-A-type heptazine-based porous polymer networks (* spinning side bands).

To confirm these results and obtain further details, quantitative ^{13}C MAS NMR spectra (Figure 1 right) were recorded. As expected, the ^{13}C NMR spectra of the two polymers are quite similar, and the signals can be assigned considering the ^{13}C NMR signals of the monomers (Figures S4 and S5). The signal at $\delta=110\text{--}140$ ppm is assigned to C atoms in the benzene rings of the BTDADA moiety. The C atoms attached directly to the benzothiadiazole moiety provide a signal at $\delta=154$ ppm along with the C atoms of the heptazine moiety. Finally, the peak at $\delta=162$ ppm corresponds to C atoms in the heptazine ring connected to the amino linkers. The C signals of cyameluric acid are found at approximately $\delta=150$ ppm for the inner C atoms and at approximately $\delta=155$ ppm for the O-bearing C atoms. The shoulder at $\delta=150$ ppm for HMP-3_4:3, which can be removed by the treating the sample with a KOH solution (see Figure S6), confirms the presence of cyameluric acid only for this sample and is in agreement with the ^{15}N NMR data.

Quantitative analysis of the ^{13}C NMR measurements (Figures S7 and S8) yields a ratio of 0.76 for heptazine to BTDADA units for HMP-3_2:3 (theoretical value = 0.67), whereas for HMP-3_4:3 a ratio of 0.95 for the polymeric part of the sample is found (theoretical value = 1.33; for further details see Supporting Information). We corrected the heptazine/BTDADA ratio of the latter sample for the free cyameluric acid, resulting in a ratio of 1.17, which is still considerably lower than the expected value of 1.33. This demonstrates that a fully condensed network, in which bridging amines are connected to one benzothiadiazole linker and two heptazine units (Scheme 2c), cannot be achieved under the chosen synthesis conditions. For the HMP-3_2:3 sample the value is closer to the expected heptazine/linker ratio (Scheme 2b), which points to secondary amines as the main connections within the networks. The slightly higher ratio of heptazine to linker for HMP-3_2:3 can be explained by incomplete condensation, that is, heptazine moieties connected just to one or two instead of three BTDADA units. This is also supported by the observation of unreacted chloride functionalities, which are detected as carbonyl functions after hydrolysis, introduced upon washing the polymers as described above.

To quantify the remaining unreacted chloride sites of the heptazine units that are incorporated into the polymer by at

least one or two covalent bonds, we made use of the intensity ratios of the peaks between $\delta=162$ and 150 ppm (for further details see Supporting Information). For HMP-3_2:3 and HMP-3_4:3 ~90 and ~80%, respectively, of the chloride groups reacted to form amine bridges. These relatively high values show that the HMP-3 networks are highly crosslinked.

From our analysis of the ^{13}C and ^{15}N NMR spectra, we conclude that both samples consist of a polymeric structure in which the heptazine units are connected through NH bonds and the benzothiadiazole linkers. For HMP-3_4:3, additionally, free cyameluric acid was observed. The quantitative assessment of the spectral intensities of the ^{13}C NMR spectra allows us to derive the stoichiometric formula as $(\text{Hep-3})_{0.52}(\text{Hep-2})_{0.24}(\text{BTDADA})_{1.0}$ for HMP-3_2:3 and $(\text{Hep-3})_{0.38}(\text{Hep-2})_{0.57}(\text{Hep-0})_{0.21}(\text{BTDADA})_{1.0}$ for HMP-3_4:3 (in which x in Hep-x stands for the number of covalent bonds from the respective heptazine core to BTDADA units, see Supporting Information). The stoichiometric formula confirms that HMP-3_2:3, which has a smaller heptazine/linker ratio, exhibits less unreacted chloride sites to give a more condensed network than HMP-3_4:3.

FTIR spectroscopy also confirms the successful reaction of **1** and **2** (Figure 2). Several strong bands at $\tilde{\nu}=1200\text{--}1600$ cm^{-1} correspond to the typical stretching modes of ar-

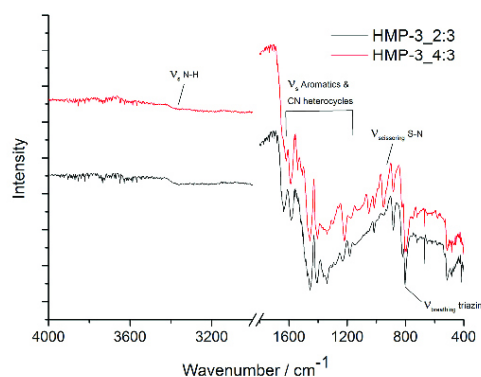


Figure 2. FTIR spectra of HMP-3.

matic groups and CN heterocycles. The characteristic breathing mode of the triazine units is observed at $\tilde{\nu}=800\text{ cm}^{-1}$, and the scissoring mode of S–N is found at around $\tilde{\nu}=950\text{ cm}^{-1}$, which prove the successful incorporation of the heptazine and benzothiadiazole moieties into the networks. The weak and broad signals at $\tilde{\nu}=3300\text{ cm}^{-1}$ represent N–H vibrations for secondary amine bridges and/or unreacted/terminal amino groups.

N₂ sorption measurements reveal BET surface areas of 85 and 24 m² g⁻¹ for HMP-3_2:3 and HMP-3_4:3, respectively (Table 1 and Figure S9). These surface areas are much lower than those observed for highly crosslinked microporous poly-

Sample	$S_{\text{BET}}^{[a]}$ [m ² g ⁻¹]	$V_{\text{p}}^{[b]}$ [cm ³ g ⁻¹]
HMP-3_2:3	85	0.2
HMP-3_4:3	24	0.03
HMP-1	185	0.39
g-CN	8	0.01

[a] S_{BET} : surface area calculated using the Brunauer–Emmett–Teller method. [b] V_{p} : total pore volume.

mer networks and the heptazine-based polymer networks reported previously (HMP-1 and HMP-2).^[11a, 18] This can be explained by the relatively long BTDA linker between the heptazine tectones and the presence of secondary amines that hinder the formation of high-surface-area networks because of their flexibility and ability to form H bonds.^[19] Furthermore, it is expected that the heptazine groups, which have just partially reacted, are detrimental to the formation of high surface areas. The low surface area of HMP-3_4:3 confirms again that tertiary amine connections (Scheme 2c) are not or just rarely formed.

It should be noted that the surface area and pore volume of HMP-3_2:3 are considerably higher than those of bulk polymeric carbon nitrides (g-CN) prepared at 550 °C (Table 1).

This can be however also attributed to an increased outer surface area due to the formation of small interconnected particle networks for HMP-3_2:3 (Figure 3a), with larger and denser particles for HMP-3_4:3 (Figure 3b) as shown in the transmission electron microscopy (TEM) measurements (Figures 3 and S10).

UV/Vis diffuse reflectance spectra of the polymer networks indicate the successful incorporation of –D–A₁–D–A₂– structures as a strong absorption in the visible region (Figure 4) with an onset of absorption of $\lambda=580\text{ nm}$ for HMP-3_4:3 and $\lambda=625\text{ nm}$ for HMP-3_2:3 is observed, which reflects the higher amount of incorporated BTDA monomers within the latter networks. The absorption edge is, therefore, considerably red-shifted compared to that of polymeric carbon nitrides, which typically absorb light just below $\lambda=450\text{ nm}$. The optical band gaps (2.0 and 2.1 eV) derived from the absorption band edge for the HMP-3 polymers

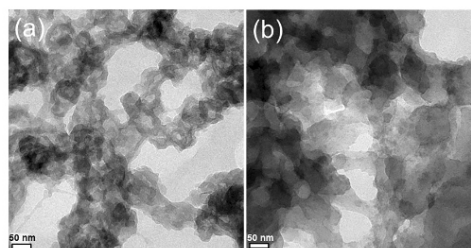


Figure 3. Transmission electron micrographs of (a) HMP-3_2:3 and (b) HMP-3_4:3 (scale bars correspond to 50 nm).

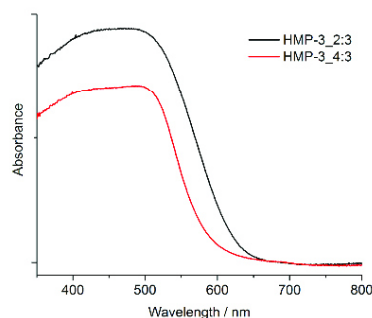


Figure 4. Diffuse reflectance UV/Vis spectrum of HMP-3.

Sample	E_g [eV] ^[a]	H ₂ evolution [$\mu\text{mol h}^{-1}$] ^[b]	H ₂ evolution [L m ⁻² h ⁻¹]
HMP-3_2:3	1.99	32	0.76
HMP-3_4:3	2.13	31	0.74
HMP-1	2.40	4	0.10
g-CN	2.70	10	0.24

[a] E_g : band gap calculated using the Kubelka–Munk equation. [b] H₂ evolution measured with 20 mg catalyst, 5 wt% Pt loading, 10% TEOA, 300 W Xe lamp, and $\lambda > 395\text{ nm}$ filter.

(Table 2) are indeed well below the band gap of carbon nitrides (2.7 eV).

These properties and the structural similarity to polymeric carbon nitride make HMP-3 an interesting material for photocatalytic applications. Photocatalytic measurements were performed for water reduction catalyzed by the HMP-3 networks using 5 wt% Pt as a co-catalyst and 10 vol% triethanolamine (TEOA) as a sacrificial electron donor at $\lambda > 395\text{ nm}$. The hydrogen evolution obtained by using the same amount of catalysts under similar conditions is summarized in Table 2. With the use of 20 mg of HMP-3_2:3 and 4:3 as photocatalysts, a high and stable H₂ evolution of 32 and

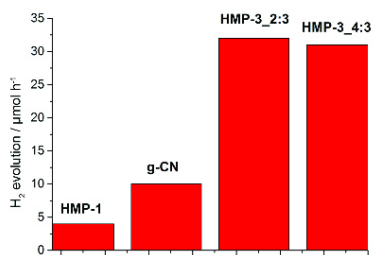


Figure 5. Photocatalytic H₂ generation of HMPs compared to bulk g-CN tested under similar conditions (20 mg catalyst, 5 wt% Pt loading, 10 wt% TEOA, 300 W Xe lamp, and > 395 nm filter).

31 μmol_{H₂} h⁻¹, respectively, is observed (Table 2 and Figure 5), which is significantly higher than that of HMP-1 and bulk g-CN. The hydrogen evolution values correspond to an amount of 1600 and 1550 μmol h⁻¹ g⁻¹ under the reaction conditions used here. However, even though these are high values, especially compared to other conjugated polymers prepared at low temperatures, we refrain from a direct comparison with other reported materials. Especially, the above stated hydrogen value per mass of catalyst, which is often used to compare catalytic activities, has to be handled with care, as hydrogen evolution values per catalyst mass are far from linear relationships.^[20] Furthermore, the values reported are highly dependent on reaction conditions, such as the reactor type, light source, and amount of co-catalyst and sacrificial agent.^[7,21] Nevertheless, it can be concluded that the introduction of alternating D–A moieties into polymeric photocatalysts can indeed be used to enhance their photocatalytic activity significantly.

The photocatalytic mechanism in these HMP-3 polymers follows the conventional electron–hole separation process, in which electrons in the conduction band are transferred to Pt nanoparticles that in turn reduce the H⁺ to H₂, whereas holes in the valence band oxidize the triethanolamine. HMP-3_2:3 was analyzed by TEM after the photocatalysis experiment (Figure S11). Pt nanoparticles of 5–15 nm are distributed homogeneously on the sample, and the polymer morphology remains unchanged after the experiment.

Isotope-labeling experiments (D₂O) were performed to ensure that H₂ formation is indeed caused by water splitting and not by the decomposition of the HMP-3 network. MS analysis revealed a mixture of 69.9% D₂, 20.3% HD, and 9.3% H₂. The high fraction of D₂ proves that the hydrogen is obtained from water splitting. The high values of HD and H₂ are because D₂O was used in excess together with H₂O. The H₂ evolution activity of the –D–A₁–D–A₂– heptazine polymers were further investigated under visible-light irradiation (λ > 420 nm). To our surprise, the H₂ evolution values are low (1 μmol_{H₂} h⁻¹ for HMP-3_2:3) despite their absorbance in the far-visible region. However, a long-term measurement of HMP-3_2:3 showed the steady evolution of hydrogen even after a run of 40 h (Figure S12). Therefore, we can con-

clude that the reduced band gap is not a crucial factor for the photocatalytic activity and that, most probably, the enhanced charge separation enabled by the D–A structure is the key factor to attain a high photocatalytic activity. Indeed, photoluminescence (PL) measurements of the HMP-3 polymers with an excitation at λ = 370 nm show significant quenching of the fluorescence compared to that of g-CN and HMP-1 (Figure S13). The fluorescence intensity is related to the recombination of photogenerated electron–hole pairs in CN polymers, which reduces the photocatalytic activity.^[22] The very low fluorescence intensity for HMP-3 indicates that photogenerated electrons and holes are stabilized in the –D–A₁–D–A₂– structures.

Conclusions

Donor–acceptor (D–A) type heptazine-based conjugated polymer networks have been synthesized under mild reaction conditions. Analysis of extensive ¹⁵N and ¹³C solid-state NMR spectroscopy showed that the copolymerization of cyameluric chloride and amine-functionalized 4,4'-(benzo[c][1,2,5]thiadiazole-4,7-diyl)dianiline (BTADADA) give mainly secondary amine bridges even if a large excess of cyameluric chloride was used. Polymer networks with the composition (Hep-3)_{0.52}(Hep-2)_{0.24}(BTADADA)_{1.0} for HMP-3_2:3 and (Hep-3)_{0.38}(Hep-2)_{0.57}(Hep-0)_{0.21} (BTADADA)_{1.0} for HMP-3_4:3 were observed. These –D–A₁–D–A₂– heptazine networks show only moderate porosity but an exceptionally high activity in photocatalytic hydrogen evolution especially compared to bulk polymeric carbon nitrides prepared at high temperatures. This can be attributed to the introduction of D–A moieties, which increase the lifetime of photogenerated electron–hole pairs.

The approach shown here for the low-temperature polycondensation of heptazine chloride with a diamine can, in principle, be used to prepare a variety of different D–A heptazine-based polymer networks and allow the design of metal-free photocatalysts. Consequently, further work will be dedicated to the development and optimization of new polymeric systems for photocatalysis applications. For example, a variety of other D–A structures can be incorporated into such networks inspired by abundant studies in organic electronics. Furthermore, other functional organic compounds can be envisaged that might be beneficial for photocatalysis applications, such as dyes to increase light harvesting or even ligands to incorporate molecular water reduction or water oxidation co-catalysts.

Experimental Section

Synthesis of –D–A₁–D–A₂– heptazine-based networks (HMP-3)

The monomers **1** and **2** were prepared according to previous reports (Figures S4 and S5).^[10,23] Different amounts of **2** (for a final molar ratio of **1** to **2** of 4:3, 60 mg and 2:3, 120 mg) were dissolved in THF (25 mL) in a glovebox. A solution of heptazine chloride (69 mg) in THF (25 mL) was added dropwise to the solution of **2**. This solution was stirred at RT, diisopropylethyla-

mine (DIPEA; for 4:3, 104 mg and 2:3, 52 mg) in THF (10 mL) was added dropwise, and the reaction solution was heated to reflux at 80 °C for 3 h under an Ar atmosphere. Subsequently, the orange to red turbid solution was poured into ice cold water, the precipitate was collected by filtration, washed successively with cold water, THF, and CHCl₃, and dried under vacuum overnight. The HMP-3 polymers were obtained in 72% (2:3) and 88% (4:3) yield (based on the respective ideal structure).

Photocatalytic tests

Photocatalytic reactions were performed in a quartz-glass-sided irradiation reaction vessel (irradiation area approximately 10.2 cm²) connected to a thermostat, and the evolved hydrogen was measured from the gas phase by using GC after the reaction. H₂ production was performed by dispersing catalyst powder (20 mg) in an aqueous solution (15 mL) that contained triethanolamine (10 vol%) as a sacrificial electron donor. Pt (5 wt %) was loaded onto the respective photocatalysts by the in situ photodeposition method using chloroplatinic acid solution (H₂PtCl₆, 8 wt %, Sigma–Aldrich). The reaction solution was evacuated several times to remove air completely before irradiation under a 300 W Xenon lamp (L.O.T. Oriol Quantum Design) equipped with a 395 nm cut-off filter to remove UV light.

Isotope-labeling experiments (D₂O) were performed to ensure that the hydrogen was formed from water. An OmniStar GSD 301C quadrupole mass spectrometer from Pfeiffer Vacuum equipped with a tungsten filament was used to detect the different hydrogen species (H₂, HD, and D₂) in the gas phase after the reaction. The voltage of the secondary electron multiplier was 1050 V.

Acknowledgements

We acknowledge the European Research Council (grant number 278593_ORGZEO) and the BMBF-funded “Light2-Hydrogen” project (03IS2071D) for financial support.

Keywords: donor–acceptor systems • hydrogen • photochemistry • polymers • water splitting

- [1] N. Armadori, V. Balzani, *ChemSusChem* **2011**, *4*, 21–36.
- [2] N. Serpone, A. V. Emeline, *J. Phys. Chem. Lett.* **2012**, *3*, 673–677.
- [3] A. Kudo, Y. Miseki, *Chem. Soc. Rev.* **2009**, *38*, 253–278.
- [4] X. Wang, K. Maeda, A. Thomas, K. Takanabe, G. Xin, J. M. Carlsson, K. Domen, M. Antonietti, *Nat. Mater.* **2009**, *8*, 76–80.
- [5] Y. Wang, X. Wang, M. Antonietti, *Angew. Chem. Int. Ed.* **2012**, *51*, 68–89; *Angew. Chem.* **2012**, *124*, 70–92.
- [6] a) A. Thomas, A. Fischer, F. Goettmann, M. Antonietti, J.-O. Muller, R. Schlögl, J. M. Carlsson, *J. Mater. Chem.* **2008**, *18*, 4893–4908; b) B. V. Lotsch, M. Döblinger, J. Sehnert, L. Seyfarth, J. Senker, O. Oeckler, W. Schnick, *Chem. Eur. J.* **2007**, *13*, 4969–4980.
- [7] a) X. Wang, K. Maeda, X. Chen, K. Takanabe, K. Domen, Y. Hou, X. Fu, M. Antonietti, *J. Am. Chem. Soc.* **2009**, *131*, 1680–1681; b) K. Kailasam, J. D. Epping, A. Thomas, S. Losse, H. Junge, *Energy Environ. Sci.* **2011**, *4*, 4668–4674.
- [8] B. Jürgens, E. Irran, J. Senker, P. Kroll, H. Müller, W. Schnick, *J. Am. Chem. Soc.* **2003**, *125*, 10288–10300.
- [9] a) C. E. Redemann, H. J. Lucas, *J. Am. Chem. Soc.* **1940**, *62*, 842–846; b) H. Schroeder, E. Kober, *J. Org. Chem.* **1962**, *27*, 4262–4266; c) E. Kroke, M. Schwarz, E. Horath-Bordon, P. Kroll, B. Noll, A. D. Norman, *New J. Chem.* **2002**, *26*, 508–512; d) A. Schwarzer, E. Kroke, *New J. Chem.* **2011**, *35*, 953–958.
- [10] K. Kailasam, J. Schmidt, H. Bildirir, G. Zhang, S. Blechert, X. Wang, A. Thomas, *Macromol. Rapid Commun.* **2013**, *34*, 1008–1013.
- [11] a) A. Thomas, *Angew. Chem. Int. Ed.* **2010**, *49*, 8328–8344; *Angew. Chem.* **2010**, *122*, 8506–8523; b) P. M. Budd, B. S. Ghanem, S. Makhseed, N. B. McKeown, K. J. Msayib, C. E. Tattershall, *Chem. Commun.* **2004**, 230–231; c) N. B. McKeown, P. M. Budd, *Chem. Soc. Rev.* **2006**, *35*, 675–683; d) J. Weber, Q. Su, M. Antonietti, A. Thomas, *Macromol. Rapid Commun.* **2007**, *28*, 1871–1876; e) G. Cheng, B. Bonillo, R. S. Sprick, D. J. Adams, T. Hasell, A. I. Cooper, *Adv. Funct. Mater.* **2014**, *24*, 5219–5224.
- [12] a) L. Stegbauer, K. Schwinghammer, B. V. Lotsch, *Chem. Sci.* **2014**, *5*, 2789–2793; b) R. S. Sprick, J.-X. Jiang, B. Bonillo, S. Ren, T. Ratvijitvech, P. Guignon, M. A. Zwijnenburg, D. J. Adams, A. I. Cooper, *J. Am. Chem. Soc.* **2015**, *137*, 3265–3270.
- [13] a) D. Wu, F. Xu, B. Sun, R. Fu, H. He, K. Matyjaszewski, *Chem. Rev.* **2012**, *112*, 3959–4015; b) X. Zhuang, D. Gehrig, N. Forler, H. Liang, M. Wagner, M. R. Hansen, F. Laquai, F. Zhang, X. Feng, *Adv. Mater.* **2015**, *27*, 3789–3796; c) X. Zhuang, F. Zhang, D. Wu, X. Feng, *Adv. Mater.* **2014**, *26*, 3081–3086; d) X. Zhuang, F. Zhang, D. Wu, N. Forler, H. Liang, M. Wagner, D. Gehrig, M. R. Hansen, F. Laquai, X. Feng, *Angew. Chem. Int. Ed.* **2013**, *52*, 9668–9672; *Angew. Chem.* **2013**, *125*, 9850–9854.
- [14] a) R. C. Coffin, J. Peet, J. Rogers, G. C. Bazan, *Nat. Chem.* **2009**, *1*, 657–661; b) S. H. Park, A. Roy, S. Beaupre, S. Cho, N. Coates, J. S. Moon, D. Moses, M. Leclerc, K. Lee, A. J. Heeger, *Nat. Photonics* **2009**, *3*, 297–302.
- [15] K. Zhang, D. Kopetzki, P. H. Seeberger, M. Antonietti, F. Vilela, *Angew. Chem. Int. Ed.* **2013**, *52*, 1432–1436; *Angew. Chem.* **2013**, *125*, 1472–1476.
- [16] P. Kuhn, A. L. Forget, D. Su, A. Thomas, M. Antonietti, *J. Am. Chem. Soc.* **2008**, *130*, 13333–13337.
- [17] V. W.-h. Lau, M. B. Mesch, V. Duppel, V. Blum, J. Senker, B. V. Lotsch, *J. Am. Chem. Soc.* **2015**, *137*, 1064–1072.
- [18] M. G. Schwab, B. Fassbender, H. W. Spiess, A. Thomas, X. Feng, K. Müllen, *J. Am. Chem. Soc.* **2009**, *131*, 7216–7217.
- [19] J. Weber, M. Antonietti, A. Thomas, *Macromolecules* **2008**, *41*, 2880–2885.
- [20] M. Schröder, K. Kailasam, S. Rudi, M. Richter, A. Thomas, R. Schomäcker, M. Schwarz, *Int. J. Hydrogen Energy* **2014**, *39*, 10108–10120.
- [21] M. Schwarze, D. Stellmach, M. Schroder, K. Kailasam, R. Reske, A. Thomas, R. Schomäcker, *Phys. Chem. Chem. Phys.* **2013**, *15*, 3466–3477.
- [22] D. Hollmann, M. Karnahl, S. Tschierlei, K. Kailasam, M. Schneider, J. Radnik, K. Grabow, U. Bentrup, H. Junge, M. Beller, S. Lochbrunner, A. Thomas, A. Brückner, *Chem. Mater.* **2014**, *26*, 1727–1733.
- [23] T. Ishi-i, N. Nakamura, T. Mine, S. Imamura, M. Shigeiwa, H. Gorohmaru, S. Maeda, *Chem. Lett.* **2009**, *38*, 1042–1043.

Received: November 20, 2015
Published online on ■■■ ■■, 0000

6.3.2 Supporting Information

Energy Technology

Supporting Information

Donor–Acceptor-Type Heptazine-Based Polymer Networks for Photocatalytic Hydrogen Evolution

Kamalakannan Kailasam,^{*,[a, b]} Maria B. Mesch,^[c] Lennart Möhlmann,^[d] Moritz Baar,^[d]
Siegfried Blechert,^[d] Michael Schwarze,^[e] Marc Schröder,^[e] Reinhard Schomäcker,^[e]
Jürgen Senker,^[c] and Arne Thomas^{*,[a]}

ente_201500478_sm_miscellaneous_information.pdf

– Supporting Information –

Experimental Details

Characterization

Nitrogen sorption analyses were carried out using an Autosorb-1 instrument after evacuating the samples at 180 °C overnight. The surface areas are determined by applying the Brunauer – Emmett – Teller (BET) method in the relative pressure range of 0.05-0.25. The pore volume is calculated at the relative pressure 0.95. Elemental analysis was performed on a Vario Micro setup.

¹³C and ¹⁵N solid-state magic-angle spinning (MAS) NMR spectra were recorded at ambient temperature on an Avance III HD 400 solid-state NMR spectrometer (Bruker) with an external magnetic field of 9.4 T. The operating frequencies are 400.1 MHz, 100.6 MHz, 40.6 MHz for ¹H, ¹³C and ¹⁵N, respectively. The samples were contained in 4 mm ZrO₂ rotors which were mounted in a standard double resonance MAS probe (Bruker). The spinning speed was adjusted to 14 kHz (¹³C) and 5 kHz (¹⁵N). The spectra are referenced relative to TMS (¹³C) and nitromethane (¹⁵N). Quantitative ¹³C measurements were recorded using a single pulse experiment. For full relaxation a recycle delay of 900 s was used and 272 scans were executed. To remove the background signal, an empty rotor was measured and its signal was subtracted from the spectrum. The ¹H¹⁵N cross-polarization (CP) MAS spectra were measured using a square excitation on both channels with a contact time of 15 ms and nutation frequencies of about 40 kHz (¹⁵N) and 45 kHz (¹H). During acquisition of ¹³C and ¹⁵N proton decoupling was carried out using SPINAL64 with an rf field of 70 kHz.

TGA measurements were done on PerkinElmer STA 6000 instrument in ambient conditions with the heating rate of 10 °C / min. UV-Visible measurement was carried out on a Varian Cary 300 scan UV-Visible spectrophotometer in diffuse reflectance mode by using barium sulfate reference. Infrared spectroscopic analyses were carried out on Varian 640 MID-IR spectrophotometer by using the ATR (Attenuated Total Reflectance) mode. Photoluminescence (PL) measurements were performed on LS-50B Perkin Elmer instrument and the excitation wavelength of the PL spectra set at 370 nm. The X-ray diffraction (XRD) measurements were performed on a Bruker D8 Advance X-ray diffractometer using CuK α_1 irradiation ($\lambda = 0.154$ nm). Transmission electron microscopy (TEM) images were obtained from a FEI Tecnai 20 microscope, using carbon-coated copper grids.

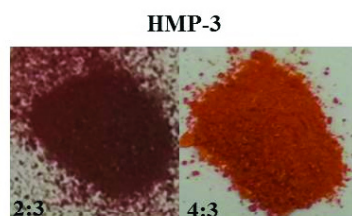


Figure S1: Pictures of the "Donor-Acceptor" (D-A) type heptazine based porous polymer networks prepared in this study.

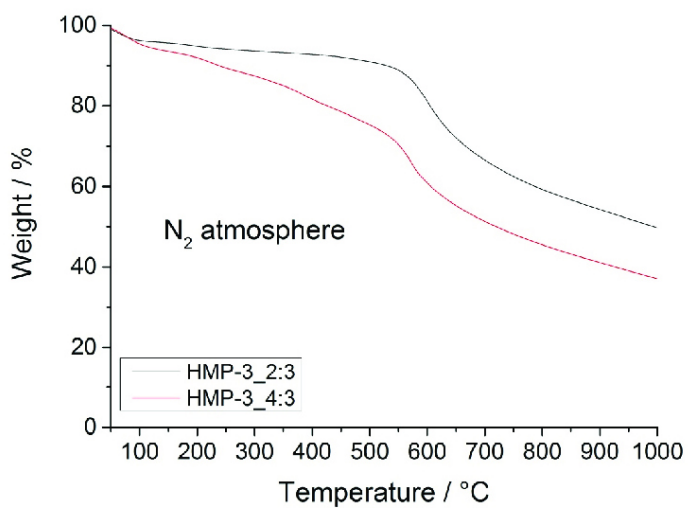


Figure S2: Thermogravimetric (TGA) analysis of HMP-3

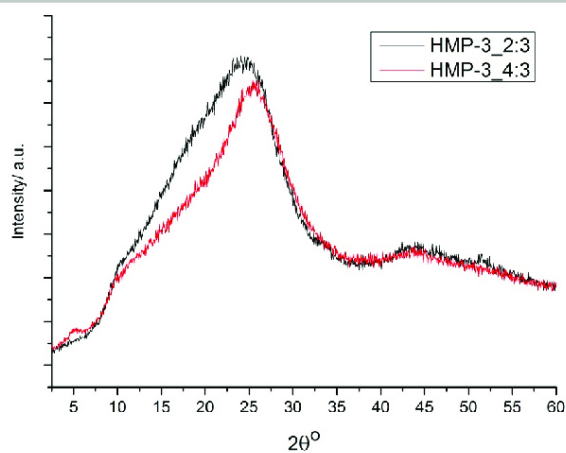


Figure S3: XRD patterns of the samples HMP-3_4:3 and HMP-3_2:3.

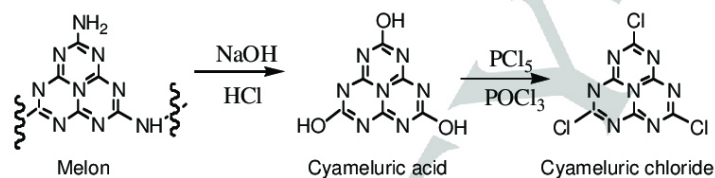


Figure S4: Reaction sequence for the synthesis of cyameluric chloride.

Cyameluric acid:

^{13}C CP-MAS NMR: δ 149.2 ($\text{CN}_2(\text{NH})$), 152.5, 153.7, 156.0 ($\text{CNO}(\text{NH})$) (tautomeric form in solid-state) ^[S1]

^{15}N CP-MAS NMR: δ -189.0, -194.0 ($N_{\text{rep,outer}}$), -243.0 (NH), -245.0 ($N_{\text{rep,c}}$) ^[S1]

FTIR (ATR, cm^{-1}): 3483, 3426, 3322, 3195, 2980, 2850, 2775, 1588, 1471, 1376, 1304, 1166, 940, 823, 785;

TGA: Prominent weight loss about 30 % begins with an endothermic event begins at around 400 °C, total decomposition starting around 650 °C.

Cyameluric chloride:

^{13}C NMR: δ 159.55 (CN_3), 176.29 (CCIN_2); FTIR (ATR, cm^{-1}): 1600, 1500, 1300, 1200, 938, 823, 648.

Reference:

S1. L. Seyfarth, J. Sehnert, N. E. A. El-Gamel, W. Milius, E. Kroke, J. Breu, J. Senker, *J. Mol. Struct.* **2008**, *889*, 217–228.

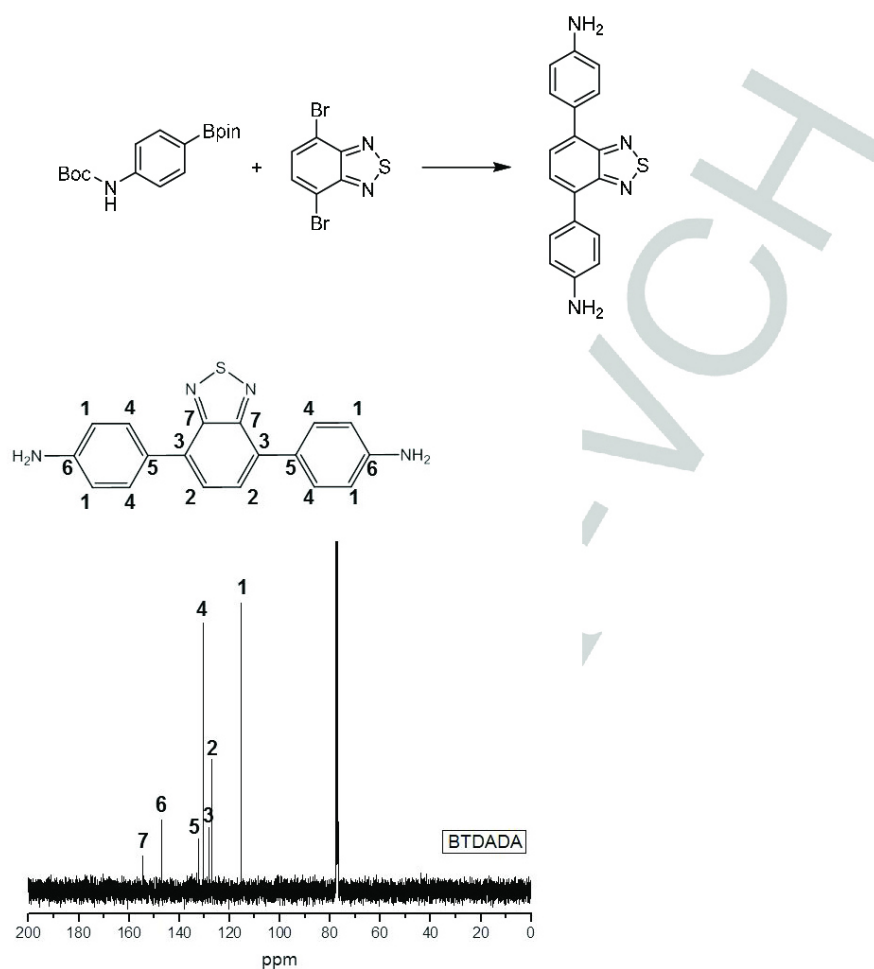
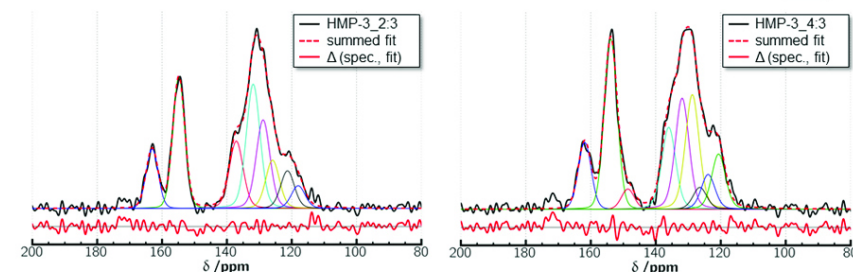


Figure S5: Synthesis of BTADADA. ^{13}C NMR of BTADADA. The carbon signals are indicated in numbers and compared to the structure.

To estimate the influence of the polymerization on the chemical shifts, a calculation with ACD/NMR Predictor Suite was performed. The only significant change occurs for carbon 6 which shifts below 140 ppm upon polymerization.

Determination of the ratio from heptazine units to linker from quantitative ^{13}C NMR measurements

Deconvolution of the two carbon spectra and the integrals are shown in Figure S6. An overview of the signal assignment as described in the main section is given in Figure S7.



	162 ppm	154 ppm	150 ppm	140-110 ppm
HMP-3_2:3	1.00	2.21	0.00	7.84
HMP-3_4:3	1.00	2.65	0.28	6.97

Figure S6: Deconvolution and integrals of ^{13}C -NMR peaks for the two HMP-3 polymers.

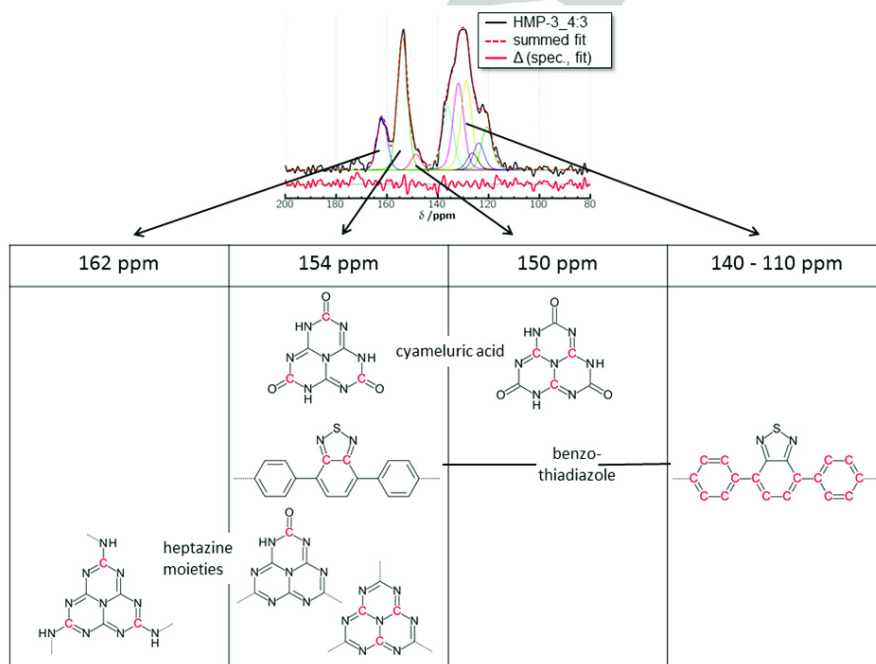


Figure S7: Signal assignment of ^{13}C -NMR peaks to carbon atoms in the HMP-3 polymers.

As shown in Figure S7, the signals of the different species are overlapping. To be able to calculate the ratio of heptazine moieties to BTDADA in the polymer, the contribution of cyameluric acid, which is present in HMP-3_4:3, has to be taken into account, as cyameluric acid can't polymerize. Based on this assignment, the amount of linker can be calculated from the signal at 140-110 ppm (corresponding to 16 C-atoms) and the contribution of the two benzothiadiazole carbons to the signal 154 ppm was subtracted. Now, as the amount of O-terminated heptazine units is unknown, we can sum the intensities of the signal at 154 ppm and 162 ppm which are then corresponding to 6 C-atoms of the heptazine unit. In the last step, the ratio from heptazine units to linker in the polymers is calculated. Taking into account that there are additional heptazine units in form of cyameluric acid in the HMP-3_4:3 sample, two values are calculated. One for the complete sample, including cyameluric acid and a second one for the polymeric part of the sample only (e.g. excluding cyameluric acid, as it can't be bound to the polymeric structure).

Heptazine/ BTADADA	Theoretical value	Experimental value
HMP-3_2:3	0.67	0.76
HMP-3_4:3	1.33	0.95 (polymeric structure) 1.17 (whole sample, including cyameluric acid)

The presence of cyameluric acid was further confirmed by treating HMP-3_4:3 with a KOH solution (2M, 100°C, 0.5h), as cyameluric acid is soluble herein. After washing the sample with distilled water and THF and drying under vacuum, ^{13}C CP-MAS NMR spectra were recorded (Figure S8). In comparison to the MAS spectra of the as synthesised material, the signal at 150 ppm is not observed anymore and the intensity of the resonance at 154 ppm is significantly reduced. This supports the signal assignment and proves the existence of cyameluric acid in sample HMP-3_4:3.

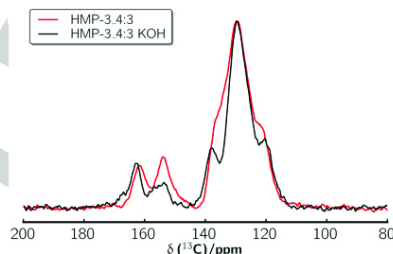


Figure S8: ^{13}C CP-MAS NMR spectra of HMP-3_4:3 (red) and the KOH treated sample (black).

Experimental Details:

^{13}C cross-polarization (CP) MAS NMR spectra were recorded with a contact time of 1.1 ms at ambient temperature on an Avance III HD 400 solid-state NMR spectrometer (Bruker) with an external magnetic field of

FULL PAPER

WILEY-VCH

9.4 T. The ^{13}C nutation during the Hartman Hahn block was set to 60 kHz with a square excitation. For the proton channel a ramped excitation where the rf field was linearly varied from 50 to 100% was used.

Determination of reacted sites using quantitative ^{13}C NMR measurements

For the determination of reacted sites a very similar approach can be chosen, assuming that every unreacted chloride site transforms into a carbonyl functionality during the washing procedure. To determine the percentage of reacted sites, the contribution of the benzothiadiazole to the intensity of the signals from 162-150 ppm has to be removed. The remaining intensity arises from the different heptazine species, which contribute to the signals according to the following scheme:

Heptazine unit with		162 ppm	154 ppm	150 ppm
3 reacted sites	Hep-3	$3 \cdot x$	$3 \cdot x$	
2 reacted sites	Hep-2	$2 \cdot y$	$4 \cdot y$	
Free cyameluric acid	Hep-0		$3 \cdot z$	$3 \cdot z$

With x = fraction of Hep-3
 y = fraction of Hep-2
 z = fraction of Hep-0 (cyameluric acid)

Hep-1 isn't listed, as we can't distinguish between Hep-1 and Hep-2. Anyway, to be able to calculate the amount of reacted chloride sites this is not necessary as the contribution of Hep-1 is considered in form of Hep-2. That means that in reality it is possible that two Hep-2 stand for one Hep-1 and one Hep-3.

After solving the above equations we derive

	x	y	z
HMP-3_2:3	69 %	31%	0%
HMP-3_4:3	33 %	49%	18%

Recalculation from heptazine units to chlorine sites gives 90 % reacted Cl-sites for HMP-3_2:3 and 66 % for HMP-3_4:3. As cyameluric acid is a three times terminated molecule, it can't be part of the polymer. Therefore, if only the polymeric part of HMP-3_4:3 is taken into account, 80 % of the chlorine sites have reacted.

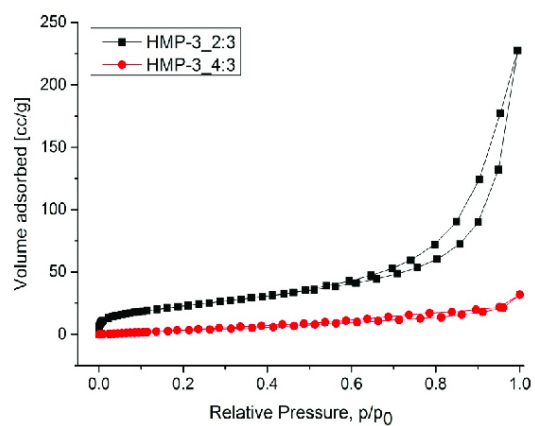


Figure S9: Nitrogen sorption isotherms of HMP-3 networks.

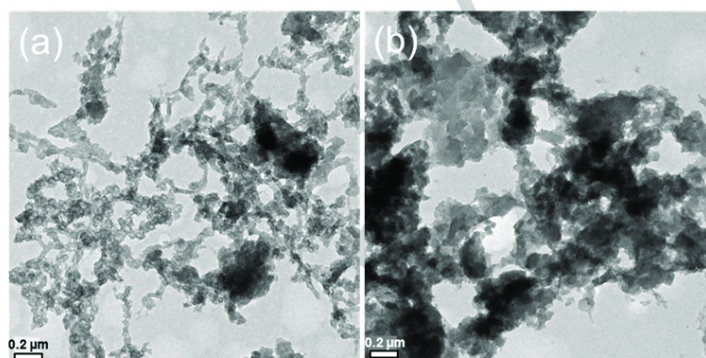


Figure S10: Higher magnification transmission electron micrographs of a) HMP-3_2:3 and b) HMP-3_4:3.

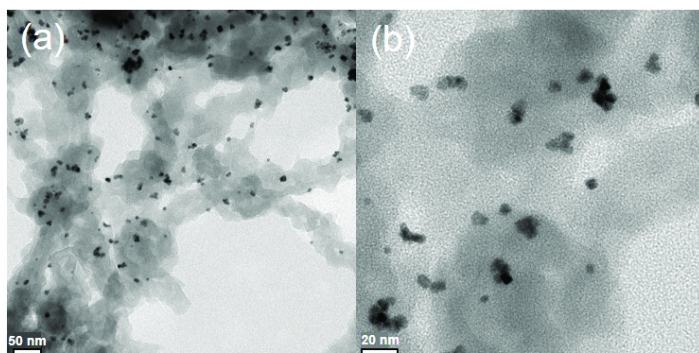


Figure S11: Transmission electron micrographs of HMP-3_2:3 sample after the photocatalytic experiments.

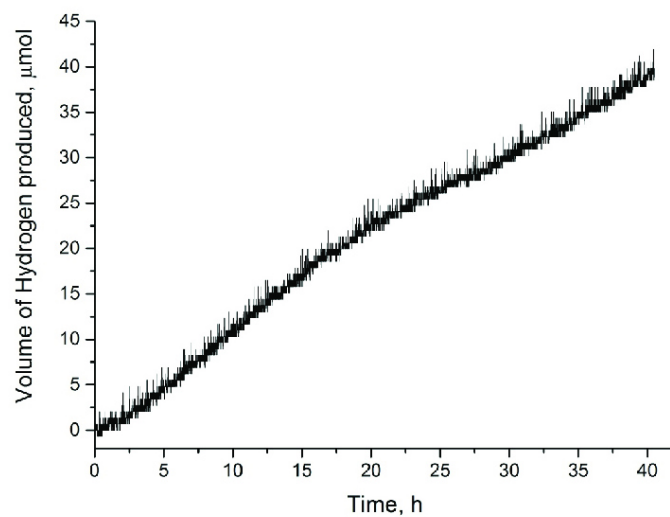


Figure S12: Long term photocatalytic H₂ generation using HMP-3_2:3 (50 mg catalyst, 3 wt% Pt loading, 10 wt% TEOA, 300 W Xe-lamp and $\lambda > 420$ nm filter).

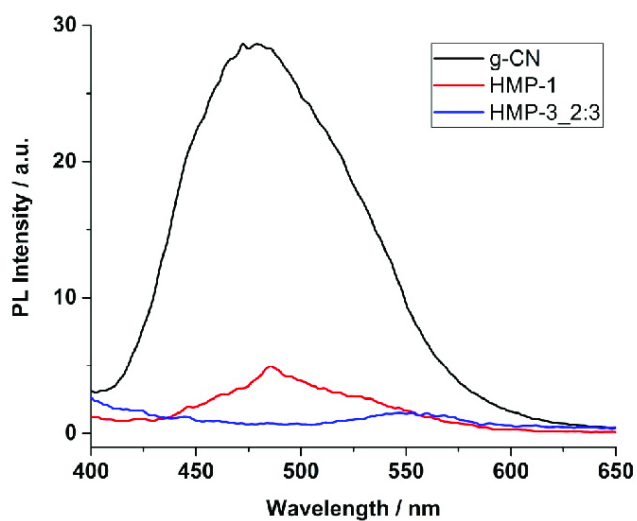


Figure S13: Photoluminescence spectra of the heptazine based porous polymer networks compared to graphitic carbon nitride.

Table S1: Elemental analysis of the HMP-3 networks.

Sample description	N %	C %	H %	S %
HMP-3_2:3	25.45	58.07	2.99	6.90
HMP-3_2:3 (calculated)	34.54	54.65	1.70	9.11
HMP-3_4:3	25.80	51.63	3.51	4.67
HMP-3_4:3 (calculated)	40.35	51.87	0.86	6.92

6.4 Spectral-editing zur Strukturlösung eines PTI-Derivates

Triazine-based Carbon Nitrides for Visible-Light-Driven Hydrogen Evolution

K. Schwinghammer,^{†,‡} B. Tuffy,^{†,‡} M. B. Mesch,[§] E. Wirnhier,[‡] C. Martineau,^{||} F. Taulelle,^{||} W. Schnick,[‡] J. Senker,[§] B. V. Lotsch^{*,†,‡}

Erschienen in:

Angewandte Chemie International Edition 2013, 52 (9), 2435

Abdruck mit Genehmigung, Copyright (2013) Wiley-VCH Verlag GmbH & Co. KGaA

[†] Max Planck Institute for Solid State Research, Heisenbergstr. 1, 70569 Stuttgart, Germany

[‡] Department of Chemistry, University of Munich, LMU, Butenandtstr. 5-13, 81377 Munich, Germany

[§] Department of Inorganic Chemistry III, University of Bayreuth, Universitätsstr. 30, 95447 Bayreuth, Germany

^{||} Tectospin, Institut Lavoisier de Versailles (ILV), UMR CNRS 8180, Université de Versailles Saint-Quentin-en-Yvelines, 45 Avenue des Etats-Unis, 78035 Versailles cedex, France

* B.Lotsch@fkf.mpg.de

6.4.1 Triazine-based Carbon Nitrides for Visible-Light-Driven Hydrogen Evolution

Photocatalysis
Triazine-based Carbon Nitrides for Visible-Light-Driven Hydrogen Evolution**

Katharina Schwinghammer, Brian Tuffy, Maria B. Mesch, Eva Wirnhier, Charlotte Martineau, Francis Taulelle, Jürgen Schnick, Jürgen Senker, and Bettina V. Lotsch*

The development of catalysts that enable the direct conversion of solar energy into chemical energy has been defined as one of the major challenges of modern materials chemistry. Hydrogen generated by photochemical water splitting has been identified as a promising energy carrier that offers a high energy density while being environmentally clean.^[1] Nevertheless, to realize a light-driven hydrogen-based economy, the exploration of new materials for highly efficient, stable, economically viable, and environmentally friendly photocatalysts is required.

To date, numerous inorganic semiconductors have been developed for water splitting, most of them being transition metal compounds containing heavy metals such as La, Bi, Ta, or Nb, which impede scalability, increase cost, and add complexity.^[2] Recently, attention has been attracted to a new class of metal-free photocatalysts, comprising polymeric melon-type carbon nitrides (CNs) based on imide-bridged heptazine units (see Figure 1 a).^[3] CNs are readily accessible, lightweight, stable, and low-cost compounds that offer an attractive alternative to metal-rich catalysts while still maintaining efficient photoactivity.^[4] Thermal condensation of CNs forms a wide variety of chemical species that differ substantially with respect to their degree of condensation, hydrogen content, crystallinity, and morphology.^[5,6] The chemical modification of CNs by molecular “dopants” has resulted in a number of CN materials with improved photo-

catalytic activity.^[7] Although the evidence is largely empirical, the property enhancement presumably originates from subtle modifications of the parent structures by incorporation of heteroatoms as well as structural defects, to give rise to enhanced absorption in the visible light range and a more complete exploitation of the solar energy spectrum.

In contrast to all known CN photocatalysts, which are composed of heptazine building blocks, poly(triazine imide) (PTI/Li⁺Cl⁻) is the only structurally characterized 2D CN network featuring imide-linked triazine units (see Figure 1 b).^[8,9] Owing to its high level of crystallinity, PTI/Li⁺Cl⁻ lends itself as an excellent model system to study photocatalytic activity towards water splitting as a function of the number of building blocks, the composition, and the degree of structural perfection of the system. Herein, we present a new generation of CN photocatalysts based on triazine building blocks and demonstrate their enhanced photocatalytic activity in comparison to heptazine-based CNs. Moreover, we show that their performance can be amplified by small-molecule doping, thus rendering them the most active nonmetal photocatalysts for the hydrogen evolution reaction that have been reported to date.

As a starting point, we synthesized crystalline PTI/Li⁺Cl⁻ as a model structure for triazine-based CNs in a two-step ionothermal synthesis according to the procedure of Wirnhier et al.^[8,9] To study the effect of crystallinity on the photocatalytic activity, we also synthesized an amorphous variant of PTI (aPTI), through a one-step ionothermal synthesis involving a LiCl/KCl salt melt. We used 4-amino-2,6-dihydroxypyrimidine (4AP; Figure 1 d) as the dopant because of its structural similarity to melamine and higher carbon and oxygen content. The photocatalytic activity of the as-prepared CNs was compared with that of crystalline PTI/Li⁺Cl⁻ and of heptazine-based raw melon (see the Supporting Information).

The XRD patterns of the aPTI samples confirm their amorphous character by the absence of sharp reflections (see the Supporting Information, Figure S1), which are present in the XRD patterns of crystalline PTI/Li⁺Cl⁻. However, the FTIR spectra of the synthesized aPTI CNs are still largely similar to that of PTI/Li⁺Cl⁻ (Figure 2 d and Figures S2–5 in the Supporting Information), as they contain a band at 810 cm⁻¹ (ring sextant out of plane bending) and a fingerprint region between 1200 and 1620 cm⁻¹ that is dominated by $\nu(\text{C-NH-C})$ and $\nu(\text{C=N})$ stretching vibrations.^[5,10] Doping with 4AP gives rise to less well-defined IR bands, thereby indicating a decrease in the structural order. In addition, in the spectra of 16% and 32% doped PTI there is a band at 914 cm⁻¹ that can be assigned to aromatic C–H bending vibrations of the dopant (see the Supporting Information,


[*] K. Schwinghammer, B. Tuffy, Prof. B. V. Lotsch
Max Planck Institute for Solid State Research
Heisenbergstr. 1, 70569 Stuttgart (Germany)
E-mail: B.Lotsch@fkf.mpg.de
Homepage: <http://www.cup.uni-muenchen.de/ac/lotsch/>

K. Schwinghammer, B. Tuffy, E. Wirnhier, Prof. W. Schnick,
Prof. B. V. Lotsch
Department of Chemistry, University of Munich, LMU
Butenandstr. 5–13, 81377 Munich (Germany)

M. B. Mesch, Prof. J. Senker
Department of Inorganic Chemistry III, University of Bayreuth
Universitätsstr. 30, 95447 Bayreuth (Germany)

C. Martineau, Prof. F. Taulelle
Tectospin, Institut Lavoisier de Versailles (ILV), UMR CNRS 8180
Université de Versailles Saint-Quentin-en-Yvelines
45 Avenue des Etats-Unis, 78035 Versailles cedex (France)

[**] Financial support by the Deutsche Forschungsgemeinschaft (projects LO1801/1-1, SCHN377/15-1, SE1417/5-1), the cluster of excellence “Nanosystems Initiative Munich” (NIM), and the Center for NanoScience (CeNS) is gratefully acknowledged. We thank V. Duppel, C. Minke, A. Ranft, S. Hug, M. Schreiber, and W. König for their assistance with the experimental work.

 Supporting information for this article is available on the WWW under <http://dx.doi.org/10.1002/anie.201206817>.

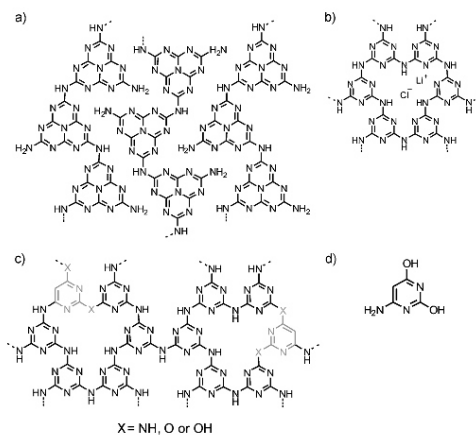


Figure 1. Chemical structures of a) melon, b) PTI/Li⁺Cl⁻ (idealized structure), c) aPTI_{4AP16%} (proposed structure), and d) the dopant 4AP.

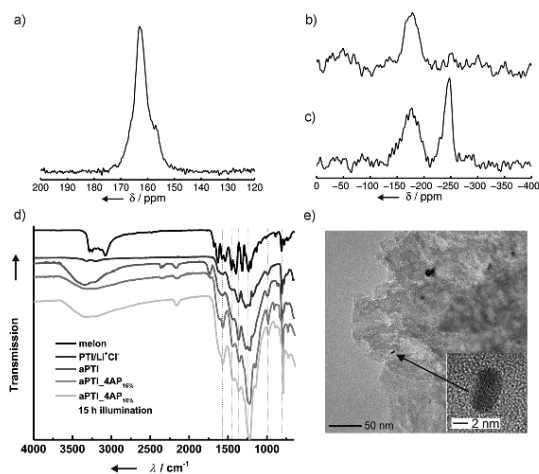


Figure 2. a) ¹³C CP-MAS NMR spectrum (10 kHz), b) ¹⁵N CPPI MAS NMR spectrum (6 kHz, inversion time = 400 μs) and c) ¹⁵N CP-MAS NMR spectrum (10 kHz) of aPTI_{4AP16%}. d) FTIR spectra of aPTI_{4AP16%} synthesized at 550 °C before and after 15 h illumination, compared to crystalline PTI/Li⁺Cl⁻, aPTI_{500°C}, and melon. e) A typical image of 2.3 wt% Pt-loaded aPTI_{4AP8%} after illumination for 3 h under visible light (λ > 420 nm) and at higher magnification (inset).

Figure S5). Interestingly, the bands at 2160 cm⁻¹, 1730 cm⁻¹, and around 1200 cm⁻¹, which are seen in the spectrum of aPTI and partially in those of the doped samples, point to the presence of terminal nitrile groups as well as oxygen-containing functionalities, such as C=O and C–O.

Elemental analysis (EA) indicates the atomic ratio C/N = 0.68 for PTI/Li⁺Cl⁻, whereas the C/N ratios of the aPTI

samples are slightly increased for those synthesized at elevated temperatures, indicating either a higher degree of condensation or an increase of oxygen incorporation (see the Supporting Information, Table S1). Notably, the amount of Li and Cl is lower in doped and nondoped aPTI than in crystalline PTI/Li⁺Cl⁻, whereas the oxygen content is significantly higher, consistent with the IR results. This finding is worth noting as the amount of carbon and oxygen atoms in CNs is likely to play an essential role in the activity of CN photocatalysts.^[11] By increasing the amount of 4AP incorporated in the doped PTI from 2% to 64% the C/N ratio increases from 0.69 to 1.13, respectively (see the Supporting Information, Table S2). In summary, the EA and IR results suggest that both carbon and oxygen atoms are incorporated into the amorphous materials, most likely through replacement of one of the ring or bridging nitrogen atoms, as proposed in Figure 1c.

The ¹³C and ¹⁵N cross-polarization magic-angle spinning (CP-MAS) NMR spectra (Figure 2a and c) for aPTI doped with 16% 4AP and synthesized at 550 °C (aPTI_{4AP16%}) provide additional information about the structural composition of the material derived from copolymerization with 4AP. Both spectra are similar to those of PTI/Li⁺Cl⁻ (see the Supporting Information, Figure S6),^[8,9] albeit with significantly increased line width (full width at half maximum (FWHM)) of 1.5 kHz compared to 600 Hz) owing to the less ordered character of the materials (see the Supporting Information, Figure S1). The ¹⁵N CP-MAS spectrum shows two broad signal groups centered around -175 and -245 ppm. The former group is typical for tertiary ring nitrogen atoms (N_{ter}, from the outer ring nitrogen atoms of heptazine or triazine rings), whereas the latter is characteristic of bridging NH groups. A very weak signal around -280 ppm indicates that only a small amount of terminal NH₂ groups is present, hence a melon-type structure seems very unlikely. However, to further corroborate this hypothesis and identify the type of heterocycle formed under the conditions used—triazine versus heptazine—we recorded a ¹⁵N cross polarization polarization inversion (CPPI)^[12] NMR spectrum of aPTI_{4AP16%} (Figure 2b) with an inversion time of 400 μs. Under such conditions, resonances of the NH groups are reduced to zero intensity whereas signals of NH₂ units will be inverted. In contrast, the ¹⁵N signals of tertiary nitrogen atoms are expected to remain largely unaffected. Hence, the unique signal for the central nitrogen atom, N_c of a heptazine ring between -220 and -240 ppm can unequivocally be identified.^[5] The absence of any signals in the ¹⁵N CPPI spectrum (Figure 2b) in the region between -200 and -300 ppm therefore strongly suggests the absence of heptazine units within the detection limit of roughly 10–15%. The markedly different intensity ratios in the ¹³C CP-MAS spectrum of aPTI_{4AP16%} (Figure 2a) compared to those in the ¹³C CP-MAS spectrum of PTI/Li⁺Cl⁻, and the broad asymmetric high-field flank of the signal between -140 and -170 ppm in the ¹⁵N CP-MAS spectrum (Figure 2c) may indicate partial incorporation of

pyrimidine into the PTI framework during copolymerization, which is not observed for PTI/Li⁺Cl⁻.^[8,9]

The brown color of crystalline PTI/Li⁺Cl⁻ indicates substantial absorption in the visible range of the spectrum. More specifically, the material absorbs largely in the UV region, yet additional absorption takes place in the blue part of the visible region and there is a gradual decrease in absorption toward higher wavelengths (Figure 3 and Fig-

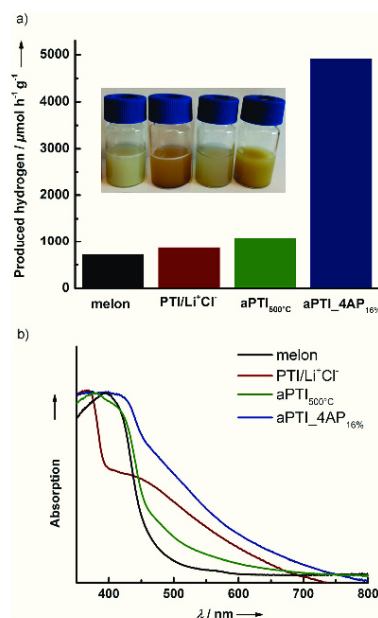


Figure 3. Photocatalytic activity towards hydrogen production (a). UV-Vis spectra (b) and color of the water/TEoA suspensions (inset in a) of aPTI_{4AP}_{16%} synthesized at 550 °C compared to crystalline PTI/Li⁺Cl⁻, aPTI synthesized at 500 °C, and melon.

ure S7 in the Supporting Information). The absorption spectra of aPTI synthesized at 400–600 °C show bands that are comparable to those in the spectrum of melon, thus rendering the color of the materials similar to that of melon (see the Supporting Information, Figures S7 and S10). When the reaction temperature is increased, the color of aPTI changes from cream (400 °C) to yellow (500 °C), suggesting enhanced absorption in the visible region. The absorption of aPTI_{500°C}, which is synthesized at a reaction temperature of 500 °C, is strongly red-shifted compared to that of crystalline PTI/Li⁺Cl⁻, thereby representing further improvement in the visible-light absorption (see the Supporting Information, Figure S7 (1)). With increasing amounts of dopant the color of the 4AP-doped CNs gets darker, changing from yellow (2%) to red-brown (64%); this color change correlates well with the red-shift observed in the absorption spectra (see the Supporting Information, Figure S8).

The inherent 2D architecture of crystalline PTI/Li⁺Cl⁻ gives rise to an expanded π -electron system, lower band-gap, and enhanced absorption as compared to the 1D polymer melon, and thus renders PTI/Li⁺Cl⁻ a promising photocatalyst that may even outperform the heptazine-based semiconductors. In fact, hydrogen production of 864 $\mu\text{mol h}^{-1} \text{g}^{-1}$ (ca. 15% error) was measured for crystalline PTI/Li⁺Cl⁻ in the presence of a Pt co-catalyst and triethanolamine (TEoA) as sacrificial electron donor; this result equates to an enhancement of approximately 20% compared to synthesized raw melon (see the Experimental Section; 722 $\mu\text{mol h}^{-1} \text{g}^{-1}$) and is comparable to “g-C₃N₄” synthesized at 600 °C (synthesis according to Zhang et al.;^[7a] 844 $\mu\text{mol h}^{-1} \text{g}^{-1}$). The photocatalytic activity of the amorphous CNs synthesized in an open system in the temperature range 400–600 °C showed that the highest activity was achieved for the CN synthesized at a reaction temperature of 500 °C (1080 $\mu\text{mol h}^{-1} \text{g}^{-1}$); this activity corresponds to an approximately 50% enhancement compared to that of raw melon (see Table 1).

Table 1: Physicochemical properties and photocatalytic activity of different Pt/CN_x species for the hydrogen evolution reaction driven by visible light.

Catalyst	Surface area [m ² g ⁻¹]	C/N molar ratio	Hydrogen evolution rate [$\mu\text{mol h}^{-1} \text{g}^{-1}$]	Quantum efficiency [%]
PTI/Li ⁺ Cl ⁻	37	0.68	864	0.60
Melon	18	0.62	722	0.50
aPTI _{500°C}	122	0.69	1080	0.75
aPTI _{4AP} _{16%}	60	0.82	4907	3.40

Although the above results show a moderate improvement of the photocatalytic activity of PTI-derived materials compared to melon-based ones, when PTI is doped with 4AP the increase in the photoactivity of PTI is a function of the doping level and synthesis temperature. By increasing the temperature from 400 to 600 °C, an optimum photocatalytic activity was measured for the material synthesized at 550 °C (see the Supporting Information, Figure S13). When the content of 4AP was increased from 2 to 64%, the highest photocatalytic activity of 4907 $\mu\text{mol h}^{-1} \text{g}^{-1}$ (3.4% quantum efficiency) was detected for 16% doped aPTI, synthesized at 550 °C (aPTI_{4AP}_{16%}; Figure S14 in the Supporting Information and Table 1). In essence, the photocatalytic activity of PTI/Li⁺Cl⁻ can be enhanced by 5–6 times upon doping with 4AP in a simple one-pot reaction. 4AP doping of crystalline PTI/Li⁺Cl⁻ leads to no apparent photocatalytic activity. Also, as a control experiment, pure 4AP was shown to be photocatalytically inactive by itself and under ionothermal or thermal treatment. Water oxidation experiments in which O₂ evolution was measured, carried out in the presence of a Co₃O₄ co-catalyst, did not yield substantial amounts of oxygen, thus suggesting that either water oxidation is thermodynamically unfeasible or that the reaction conditions need to be further optimized.

A typical TEM micrograph shows that the surface morphology of doped aPTI is layered and platelet-like

(Figure 2d and S11 in the Supporting Information). The crystallite size and composition of the platinum nanoparticles deposited on the carbon nitride catalyst in situ were studied by TEM and EDX. The results reveal that the photoinduced reduction of the co-catalyst results in well-dispersed nanoparticles roughly 5 nm in diameter.

N_2 sorption measurements allow us to quantify the impact of the surface area (SA) of the catalysts on the photocatalytic activity. In Table 1, the measured specific Brunauer–Emmett–Teller (BET) SAs indicate a weak correlation between SA and activity, but the increased photoactivity in the doped species cannot be rationalized by an increased SA alone.

As seen in Figure 3, the aPTI_4AP_{16%} photocatalyst yields an orange-brown suspension and its diffuse reflectance spectrum spans across the visible region. It is therefore instructive to examine the wavelength-specific hydrogen production to determine which wavelengths actively contribute to the H_2 evolution. In the wavelength dependence graph (Figure 4), the absorption is overlaid with the wavelength-

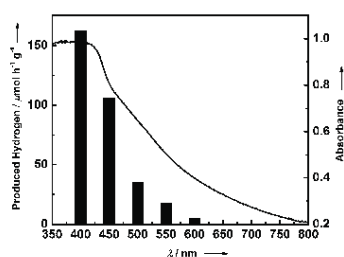


Figure 4. Overlay of UV-Vis spectrum and wavelength-specific hydrogen production (black bars) of aPTI_4AP_{16%} using 40 nm FWHM band-pass filters.

specific hydrogen evolution. The hydrogen production rate falls off at 450–500 nm, thus indicating that the majority of photons contributing to the hydrogen production are at $\lambda < 500$ nm. It is suggested that the active absorption follows the band edge observed between 430 and 440 nm. This band is similar to that seen for the other PTI compounds although red-shifted by the 4AP doping. The broad absorption profile suggests the existence of intra band-gap electronic states at various energies, which could arise from the incorporated 4AP (see the Supporting Information, Figure S4 and S5). However, as Figure 4 infers, not all electronic states—especially those associated with absorption at higher wavelengths—contribute to the hydrogen evolution but may rather act as traps and quenching sites for excitons. We therefore envision that through active control of the number and position of defects in the material, photocatalysts with further enhanced activity can rationally be designed. Nevertheless, the increased visible-light activity up to approximately 500 nm in doped PTI results in a significant improvement over its undoped or crystalline counterparts and is a contributing factor to its high photoactivity.

In conclusion, we have reported a new family of 2D triazine-based carbon nitrides that shows substantial visible-light-induced hydrogen production from water, and in this regard rivals the benchmark heptazine-derived photocatalysts. With external quantum efficiencies as high as 3.4%, the amorphous carbon- and oxygen-enriched poly(triazine imide) species not only outperform melon-type photocatalysts, but also crystalline PTI by 5 to 6 times. Consistent with previous results,^[13] we have demonstrated that a rather low level of structural definition and the introduction of defects up to a certain doping level (16% for 4-amino-2,6-dihydroxypyrimidine) tend to enhance the photoactivity of the catalysts. We believe that the diverse range of available organic and inorganic dopants will allow the rational design of a broad set of triazine-based CN polymers with controlled functions, thus opening new avenues for the development of light-harvesting semiconductors. The easily adjustable structural and electronic properties of CN polymers render them particularly versatile for solar energy applications.

Received: August 22, 2012

Published online: January 22, 2013

Keywords: carbon nitrides · copolymerization · photocatalysis · triazines · water splitting

- [1] X. Chen, S. Shen, L. Guo, S. S. Mao, *Chem. Rev.* **2010**, *110*, 6503–6570.
- [2] H. Tong, S. Ouyang, Y. Bi, N. Umezawa, M. Oshikiri, J. Ye, *Adv. Mater.* **2012**, *24*, 229–251.
- [3] a) X. Wang, K. Maeda, A. Thomas, K. Takanabe, G. Xin, J. M. Carlsson, K. Domen, M. Antonietti, *Nat. Mater.* **2009**, *8*, 76–80; b) E. Kroke, M. Schwarz, E. Horath-Bordon, P. Kroll, B. Noll, A. D. Norman, *New J. Chem.* **2002**, *26*, 508–512.
- [4] a) Y. Wang, X. Wang, M. Antonietti, *Angew. Chem.* **2012**, *124*, 70–92; *Angew. Chem. Int. Ed.* **2012**, *51*, 68–89; b) Y. Zheng, J. Liu, J. Liang, M. Jaroniec, S. Z. Qiao, *Energy Environ. Sci.* **2012**, *5*, 6717–6731.
- [5] a) B. V. Lotsch, M. Döblinger, J. Sehnert, L. Seyfarth, J. Senker, O. Oeckler, W. Schnick, *Chem. Eur. J.* **2007**, *13*, 4969–4980; b) L. Seyfarth, J. Seyfarth, B. V. Lotsch, W. Schnick, J. Senker, *Phys. Chem. Chem. Phys.* **2010**, *12*, 2227–2237; c) B. Jürgens, E. Irran, J. Senker, P. Kroll, H. Müller, W. Schnick, *J. Am. Chem. Soc.* **2003**, *125*, 10288–10300.
- [6] a) D. Mitoraj, H. Kisch, *Chem. Eur. J.* **2010**, *16*, 261–269; b) E. Kroke, M. Schwarz, *Coord. Chem. Rev.* **2004**, *248*, 493–532; c) G. Goglio, D. Foy, G. Demazeau, *Mater. Sci. Eng. R* **2008**, *58*, 195–227; d) X. Li, J. Zhang, L. Shen, Y. Ma, W. Lei, Q. Cui, G. Zou, *Appl. Phys. A* **2009**, *94*, 387–392.
- [7] a) J. Zhang, X. Chen, K. Takanabe, K. Maeda, K. Domen, J. D. Epping, X. Fu, M. Antonietti, X. Wang, *Angew. Chem.* **2010**, *122*, 451–454; *Angew. Chem. Int. Ed.* **2010**, *49*, 441–444; b) Q. Li, B. Yue, H. Iwai, T. Kako, J. Ye, *J. Phys. Chem. C* **2010**, *114*, 4100–4105; c) Y. Zhang, A. Thomas, M. Antonietti, X. Wang, *J. Am. Chem. Soc.* **2009**, *131*, 50–51; d) H. Yan, Y. Huang, *Chem. Commun.* **2011**, *47*, 4168–4170.
- [8] E. Wirmhier, M. Döblinger, D. Gunzelmann, J. Senker, B. V. Lotsch, W. Schnick, *Chem. Eur. J.* **2011**, *17*, 3213–3221.
- [9] M. J. Bojds, J.-O. Müller, M. Antonietti, A. Thomas, *Chem. Eur. J.* **2008**, *14*, 8177–8182.
- [10] a) B. V. Lotsch, W. Schnick, *Chem. Mater.* **2006**, *18*, 1891–1900; b) A. I. Finkel'shtein, *Opt. Spektrosk.* **1959**, *6*, 33; c) M. Takimoto, *Kogyo Kagaku Zasshi* **1961**, *64*, 1452–1454; d) M.

- Takimoto, *Nippon Kagaku Zasshi* **1964**, *85*, 159–168; e) D. A. Long, *J. Raman Spectrosc.* **2004**, *35*, 905–905; f) B. V. Lotsch, W. Schnick, *Chem. Eur. J.* **2007**, *13*, 4956–4968.
- [11] a) P. Niu, G. Liu, H.-M. Cheng, *J. Phys. Chem. C* **2012**, *116*, 11013–11018; b) A. Thomas, A. Fischer, F. Goettmann, M. Antonietti, J.-O. Müller, R. Schlögl, J. M. Carlsson, *J. Mater. Chem.* **2008**, *18*, 4893–4908; c) A. V. Semenchka, L. N. Blinov, *Glass Phys. Chem.* **2010**, *36*, 199–208; d) X. Q. Gong, A. Selloni, M. Batzill, U. Diebold, *Nat. Mater.* **2006**, *5*, 665–670; e) M. K. Nowotny, L. R. Sheppard, T. Bak, J. Nowotny, *J. Phys. Chem. C* **2008**, *112*, 5275–5300.
- [12] a) X. Wu, K. W. Zilm, *J. Magn. Reson. Ser. A* **1993**, *102*, 205–213; b) C. Gervais, F. Babonneau, J. Maquet, C. Bonhomme, D. Massiot, E. Framery, M. Vaultier, *Magn. Reson. Chem.* **1998**, *36*, 407–414.
- [13] a) X. Chen, L. Liu, P. Y. Yu, S. S. Mao, *Science* **2011**, *331*, 746–750; b) M. Alvaro, E. Carbonell, V. Fornés, H. García, *Chem-PhysChem* **2006**, *7*, 200–205; c) G. Zhang, J. Zhang, M. Zhang, X. Wang, *J. Mater. Chem.* **2012**, *22*, 8083–8091.
- [14] While this paper was in review, complementary data on the photocatalytic water splitting of crystalline PTI were published: Y. Ham, K. Maeda, D. Cha, K. Takanabe, K. Domen, *Chem. Asian J.* **2013**, *8*, 218–224.

6.4.2 Supporting Information



Supporting Information

© Wiley-VCH 2013

69451 Weinheim, Germany

Triazine-based Carbon Nitrides for Visible-Light-Driven Hydrogen Evolution**

*Katharina Schwinghammer, Brian Tuffy, Maria B. Mesch, Eva Wirnhier, Charlotte Martineau, Francis Taulelle, Wolfgang Schnick, Jürgen Senker, and Bettina V. Lotsch**

anie_201206817_sm_miscellaneous_information.pdf

Experimental Section

Photocatalysis. 1 mg mL⁻¹ aqueous solutions of carbon nitride catalyst were prepared and dispersed with an ultrasonic bath for 30 min. Triethanolamine (TEoA) was used as a sacrificial electron donor and H₂PtCl₆ (8 wt% in H₂O) was used as the Pt co-catalyst precursor which was photo-reduced during the reaction. Suspensions with 10 vol% TEoA and 6 μL H₂PtCl₆ (2.3 wt% Pt) were illuminated in 24 mL glass vials in an argon atmosphere with PTFE/Teflon septa. Samples were side-illuminated with a 300 W Xenon lamp with a water filter and dichroic mirror blocking wavelengths < 420 nm. The evolved gas was measured by gas chromatography with an online injection system and using a thermal conductivity detector with argon as carrier gas.

Synthesis of PTI/Li⁺Cl⁻ according to Wirnhier et al.^[S1-2] Dicyandiamide (0.20 g, 2.38 mmol) and an eutectic mixture of lithium chloride (59.2 mol%, 0.90 g, 21.33 mmol) and potassium chloride (40.8 mol%, 1.01 g, 14.70 mmol) were ground together in a glovebox. The reaction mixture was transferred into a dried thick-walled silica glass tube (ø_{ext.} 15 mm, ø_{int.} 11 mm). The tube was placed in a vertical tube furnace and heated under atmospheric argon pressure at 6°C min⁻¹ to 400°C. This temperature was held for 12 h and afterwards the sample was cooled to room temperature at 20°C min⁻¹. After this procedure, the tube was evacuated and sealed at a length of 120 mm. In a second step the ampoule was placed in a vertical tube furnace and heated at 1°C min⁻¹ to 600°C at which the sample was held for 24 h. After cooling down to room temperature the ampoule was broken and the sample was isolated and washed with boiling water to remove residual salt. The resulting material PTI/Li⁺Cl⁻ was obtained as a brown powder (80 mg, 50%).

Synthesis of aPTI using a modified procedure reported by Wirnhier et al.^[S1-2] Dicyandiamide (1.00 g, 11.90 mmol) and an eutectic mixture of lithium chloride (59.2 mol%, 2.26 g, 53.56 mmol) and potassium chloride (40.8 mol%, 2.74 g, 39.88 mmol) were ground together in a glovebox. The reaction mixture was transferred in open porcelain crucibles which were heated either in an argon-purged tube- or muffle furnace at 12°C min⁻¹ to 400 – 600°C. The temperature was held for 6 h and afterwards the samples were cooled down to room temperature. The samples were isolated and washed with boiling water to remove residual salts. The resulting materials yielded beige (0.70 g, 88%) to yellow colored powders (0.30 g, 38%).^[a]

Synthesis of doped amorphous PTI using a modified procedure reported by Wirnhier et al.^[S1-2] Dicyandiamide (0.50 g, 5.95 mmol), an eutectic mixture of lithium chloride (59.2 mol%) and potassium chloride (40.8 mol%) and 4AP as doping agent (2, 8, 16, 32 or 64%) were ground and transferred in open porcelain crucibles, which were heated in a muffle furnace at 12°C min⁻¹ to 400 – 600°C for 6 hours. The syntheses yielded yellow (0.30 g, 75%) to dark orange colored products (0.16 g, 40%).^[a]

^[a] Yields in percentage are based on crystalline PTI and can be considered as an approximate value.

Synthesis of raw melon according to Sattler et al.^[S3] A porcelain crucible was loaded with melamine (20 g) and covered with a porcelain lid. The crucible was placed in a muffle furnace and maintained at 490°C for 4 days. The product was ground to a powder and homogenized after the first day.

Synthesis of "g-C₃N₄" according to Zhang et al.^[S4] A porcelain crucible was loaded with dicyandiamide and heated in a muffle furnace at 600°C for 4 hours. The synthesis yielded a yellow colored powder.

Methods

X-ray powder diffraction. X-ray powder diffraction experiments were carried out on a *Huber G670* diffractometer in Guinier geometry using Ge(111)-monochromatized Cu-K α_1 -radiation ($\lambda = 1.54051 \text{ \AA}$). The specimen was ground in a mortar and evenly spread between two chemplexfoils (*Breitlänger GmbH*).

IR-spectroscopy. FTIR spectra were recorded on a *Perkin Elmer Spektrum BX II* spectrometer with an attenuated total reflectance unit.

NMR-spectroscopy. The ^{13}C and ^{15}N MAS NMR spectra were recorded at ambient temperature on an *Avance 500* solid-state NMR spectrometer (*Bruker*) with an external magnetic field of 11.7 T, operating at frequencies of 500.1 MHz, 125.7 MHz and 50.7 MHz for ^1H , ^{13}C and ^{15}N , respectively. The sample was contained in a 4 mm ZrO_2 rotor which was mounted in a standard double resonance MAS probe (*Bruker*). The ^{13}C and ^{15}N chemical shifts were referenced relative to TMS and nitromethane.

The $^1\text{H}^{15}\text{N}$ and $^1\text{H}^{13}\text{C}$ cross-polarization (CP) MAS spectra were recorded at a spinning speed of 10 kHz using a ramped-amplitude (RAMP) CP pulse on ^1H , centered on the $n = +1$ Hartmann-Hahn condition, with a nutation frequency ν_{nut} of 55 kHz (^{15}N) and 40 kHz (^{13}C). During a contact time of 7 ms the ^1H RF field was linearly varied about 20%.

The ^{15}N cross polarization combined with polarization inversion (CPPI) NMR spectrum was recorded at a spinning frequency of 6 kHz using a contact time of 7 ms and an inversion time of 400 μs . Constant amplitude CP pulses were applied on ^{15}N ($\nu_{\text{nut}} = 55 \text{ kHz}$) and ^1H ($\nu_{\text{nut}} = 50 \text{ kHz}$).

In all ^{15}N NMR experiments, a flip-back (FB)^[55] pulse was applied on ^1H after the acquisition of the FID, so that the recycle delay becomes less dependent of the ^1H T_1 relaxation time. ^1H continuous wave (CW) decoupling (ca 70 kHz RF field) was applied during the acquisition of the ^{15}N signal. The recycle delay was set to 1.5 s. About 47500 and 121000 transients were accumulated for the CP and CPPI experiments, respectively.

Diffuse reflectance measurements. Optical diffuse reflectance spectra were collected at room temperature with a UV/VIS diffuse reflectance spectrometer (*Varian, Cary 500*). Powders were prepared between two quartz discs at the edge of the integrating sphere with BaSO_4 as the optical standard. Absorption spectra were calculated from the reflectance data with the Kubelka-Munk function.

TEM. HRTEM was performed with a *Philips CM 30 ST* microscope (LaB $_6$ cathode, 300 kV, CS = 1.15 mm). Images were recorded with a CCD camera (*Gatan*) and *Digital Micrograph 3.6.1* (*Gatan*) was used as evaluation software. Chemical analyses (EDX) were performed with a Si/Li detector (*Thermo Fisher, Noran System Seven*).

Adsorption measurements. Nitrogen adsorption measurements were performed at 77 K with an *Autosorb iQ* instrument (*Quantachrome Instruments*, Boynton Beach, Florida, USA). Samples were outgassed in vacuum at 300°C for 12 h. For BET calculations pressure ranges were chosen with the help of the BET Assistant in the *ASiQwin software* (version 2.0). In accordance with the ISO recommendations multipoint BET tags equal or below the maximum in $V \cdot (1 - P/P_0)$ were chosen.

Quantum efficiency. The quantum efficiency was calculated according to $\text{QE}\% = (2 \times H)/P \times 100/1$, where H = number of evolved H_2 molecules and P = incident number of photons on the sample. The incident light was

measured with a thermopile power meter with a constant efficiency response across the visible spectrum. Wavelength specific hydrogen evolution was measured with 40 nm FWHM light filters (Thor labs) and with the same incident light and filter transmission efficiency for each filter.

Elemental analysis. Elemental analysis of the elements C, H, N and S is accomplished by high temperature digestion coupled with dynamic gas components separation. The samples are burned explosively at 1150°C in a highly oxygenated helium atmosphere. The combustion products are CO₂, H₂O, H₂, NO, NO₂, SO₂ and SO₃. The detection of the gases is done by a thermal conductivity measurement cell. The accuracy is 0.30 %. Measurements were done on an *Elementar vario EL*. The determination of oxygen was done under inert conditions at high temperature (1200 – 1400°C).

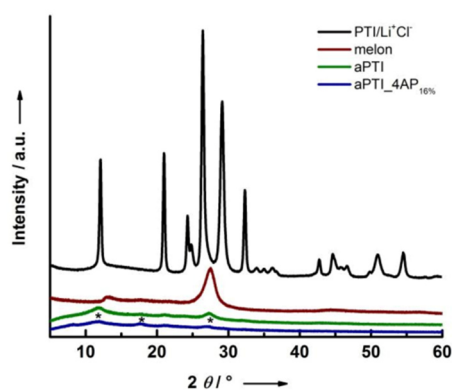


Figure S1. PXRD patterns of aPTI_{4AP16%} synthesized at 550°C, compared to crystalline PTI/Li⁺Cl⁻, aPTI_{500°C} and melon. The reflections marked with an asterisk are assigned to artifacts caused by the plastic sample holder.

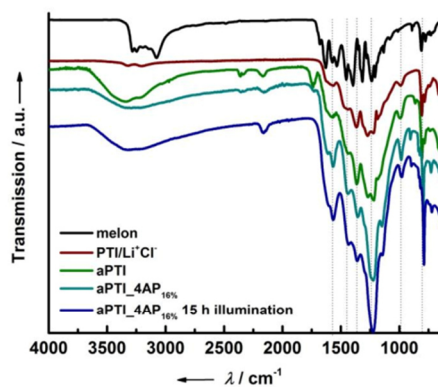


Figure S2. FTIR spectra of aPTI_{4AP16%} synthesized at 550°C before and after 15 h illumination, compared to crystalline PTI/Li⁺Cl⁻, aPTI_{500°C} and melon.

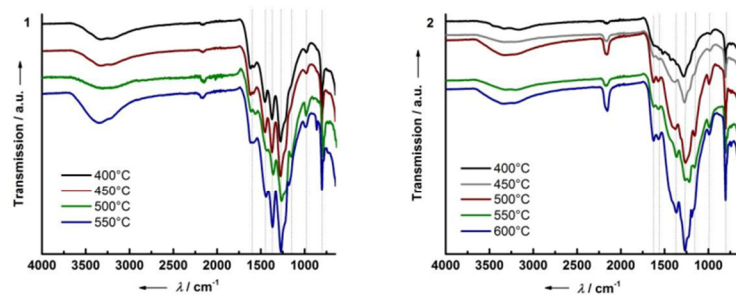


Figure S3. FTIR spectra of aPTI synthesized at 400 – 600°C in 1) air and 2) inert atmosphere.

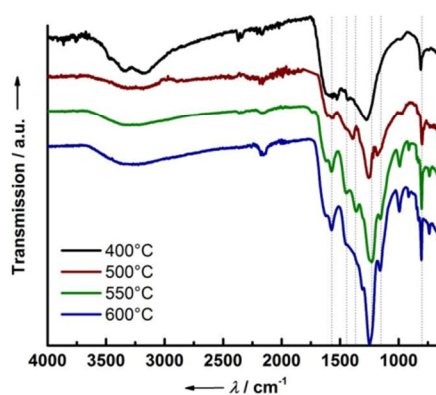


Figure S4. FTIR spectra of aPTI_4AP_{16%} synthesized at 400 – 600°C.

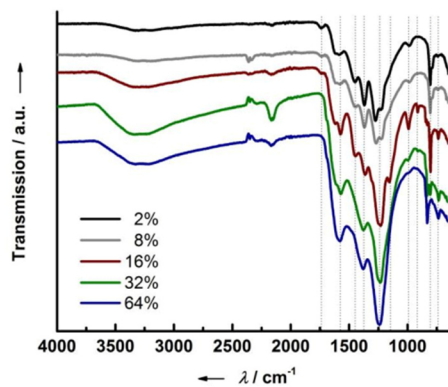


Figure S5. FTIR spectra of aPTI_4AP_{2-64%} synthesized at 550°C.

Table S1. Elemental analysis of aPTI synthesized air (muffel) or inert atmosphere (Ar-tube) at 400 – 600°C compared to PTI/Li⁺Cl⁻ and melon. The arrow indicates an increasing C/N atomic ratio.

Sample	Oven	Temperature [°C]	C [wt%]	N [wt%]	H [wt%]	C/N/H	C/N
PTI/Li ⁺ Cl ⁻	tube	600	29.6	50.4	1.3	C _{3.0} N _{4.4} H _{1.6}	0.68
melon	muffel	490	33.2	62.7	1.8	C _{3.0} N _{4.9} H _{1.9}	0.62
aPTI _{400°C}	muffel	400	26.9	46.6	2.8	C _{3.0} N _{4.5} H _{3.7}	0.67
aPTI _{450°C}	muffel	450	27.1	46.6	3.0	C _{3.0} N _{4.4} H _{4.0}	0.68
aPTI _{500°C}	muffel	500	24.7	41.9	2.5	C _{3.0} N _{4.2} H _{3.6}	0.69
aPTI _{550°C}	muffel	550	22.0	36.6	2.8	C _{3.0} N _{4.3} H _{4.6}	0.70
aPTI _{400°C}	Ar-tube	400	27.9	50.8	3.2	C _{3.0} N _{4.7} H _{4.1}	0.64
aPTI _{450°C}	Ar-tube	450	21.6	36.5	2.6	C _{3.0} N _{4.3} H _{4.3}	0.69
aPTI _{500°C}	Ar-tube	500	25.9	43.8	2.4	C _{3.0} N _{4.4} H _{3.3}	0.69
aPTI _{550°C}	Ar-tube	550	26.5	45.3	2.0	C _{3.0} N _{4.4} H _{2.7}	0.68
aPTI _{600°C}	Ar-tube	600	26.8	45.4	2.1	C _{3.0} N _{4.4} H _{2.8}	0.69

Table S2. Elemental analysis of aPTI_4AP synthesized at 400 – 600°C compared to PTI/Li⁺Cl⁻ and melon. The arrows indicate an increasing C/N atomic ratio.

Sample	Temperature [°C]	4AP [%]	C [wt%]	N [wt%]	H [wt%]	C/N/H	C/N
PTI/Li ⁺ Cl ⁻	600	0	29.6	50.4	1.3	C _{3.0} N _{4.4} H _{1.6}	0.68
melon	490	0	33.2	62.7	1.8	C _{3.0} N _{4.9} H _{1.9}	0.62
aPTI_4AP _{16%}	400	16	28.7	46.7	2.6	C _{3.0} N _{4.2} H _{3.2}	0.72
aPTI_4AP _{16%}	450	16	30.3	47.4	2.5	C _{3.0} N _{4.0} H _{3.0}	0.74
aPTI_4AP _{16%}	500	16	29.8	46.3	2.4	C _{3.0} N _{4.0} H _{2.9}	0.75
aPTI_4AP _{16%}	550	16	30.5	43.5	2.6	C _{3.0} N _{3.7} H _{3.1}	0.82
aPTI_4AP _{16%} ^[a]	550	16	30.1	42.2	2.9	C _{3.0} N _{3.6} H _{3.5}	0.83
aPTI_4AP _{2%}	550	2	29.2	49.0	2.4	C _{3.0} N _{4.3} H _{2.9}	0.69
aPTI_4AP _{8%}	550	8	29.8	48.3	2.3	C _{3.0} N _{4.2} H _{2.8}	0.72
aPTI_4AP _{16%}	550	16	30.5	43.5	2.6	C _{3.0} N _{3.7} H _{3.1}	0.82
aPTI_4AP _{32%}	550	32	28.2	35.9	2.7	C _{3.0} N _{3.3} H _{3.4}	0.92
aPTI_4AP _{64%}	550	64	35.5	36.8	2.6	C _{3.0} N _{2.7} H _{2.6}	1.13

[a] After illumination for 15 hours.

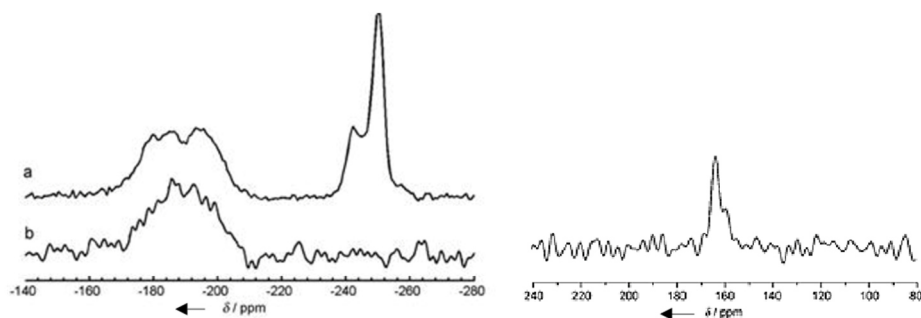


Figure S6. Left: a) ¹⁵N CP-MAS NMR spectrum of PTI/Li⁺Cl⁻ and b) a ¹⁵N CPPI experiment with attenuation of NH₄⁺ signals. Right: ¹³C CP-MAS NMR spectra recorded with 0.5 ms contact time.

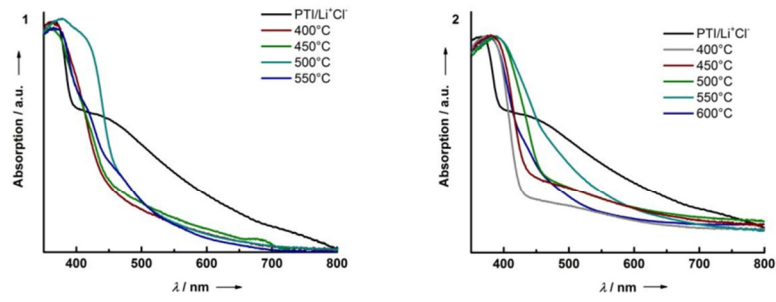


Figure S7. UV/Vis diffuse reflectance absorption spectra of aPTI synthesized at 400 – 600°C in 1) air and 2) inert atmosphere compared to crystalline PTI/Li⁺Cl⁻.

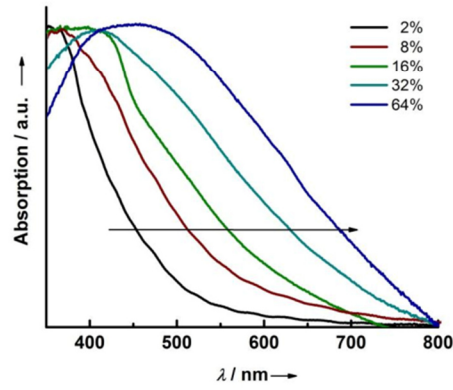


Figure S8. UV/Vis diffuse reflectance absorption spectra of aPTI_{4AP}_{2-6-4%} synthesized at 550°C.

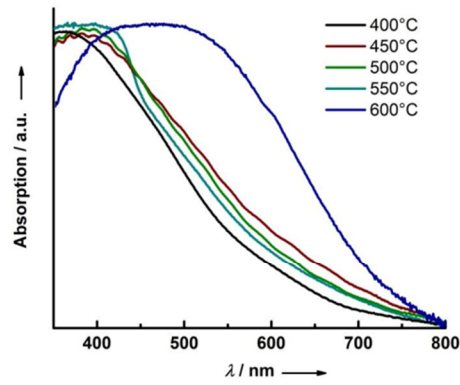


Figure S9. UV/Vis diffuse reflectance absorption spectra of aPTI_{4AP}_{18%} synthesized at 400 – 600°C.

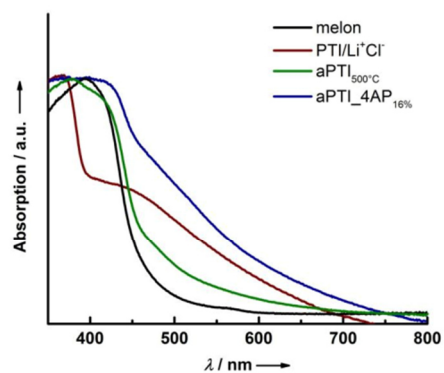


Figure S10. UV/Vis diffuse reflectance absorption spectra of aPTI_{4AP}_{16%} synthesized at 550°C, compared to crystalline PTI/Li⁺Cl⁻, aPTI synthesized at 550°C and melon.

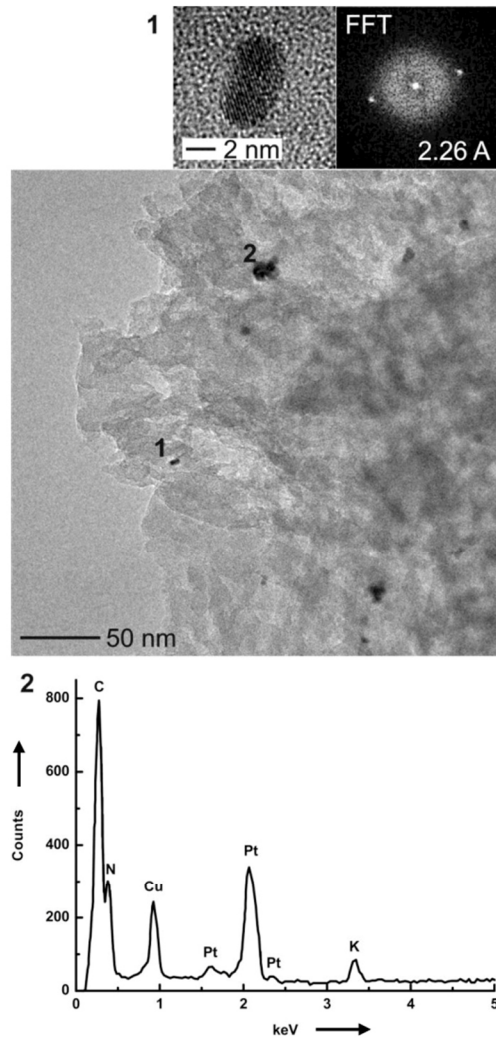


Figure S11. 1) A typical image of 2.3 wt% Pt-loaded aPTI_4AP after illumination for 3 h under visible light ($\lambda > 420$ nm), at higher magnification (top left) and its corresponding FFT (top right). The lattice planes correspond to elemental Pt. 2) The EDX spectrum of sample location 2 is shown below.

Synthesis of aPTI at elevated reaction temperatures (550 – 600°C) under inert atmosphere resulted in better photocatalytic activity of CNs than in air. On the other hand, synthesis at lower temperatures (400 – 500°C) in air resulted in marginally better photocatalytic activity compared to inert atmosphere conditions (Figure S12).

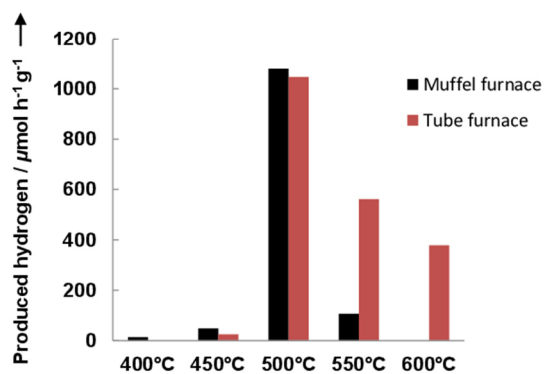


Figure S12. Photocatalytic activity of aPTI synthesized at 400 – 600°C in air (muffle furnace) or argon atmosphere (tube furnace).

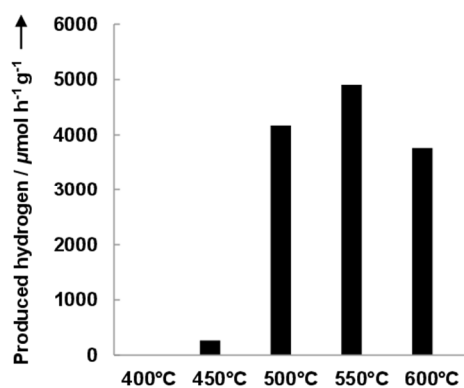


Figure S13. Photocatalytic activity towards hydrogen production of aPTI_{4AP10%} synthesized at 400 – 600°C.

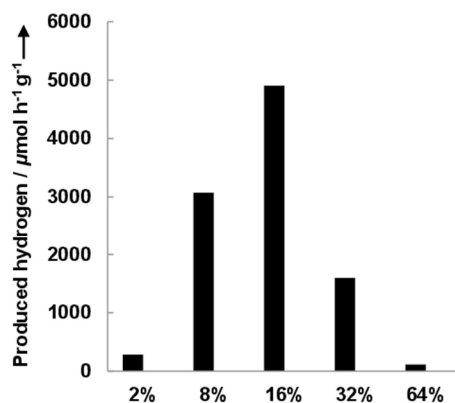


Figure S14. Photocatalytic activity towards hydrogen production of aPTI_4AP_{2-64%} synthesized at 550°C.

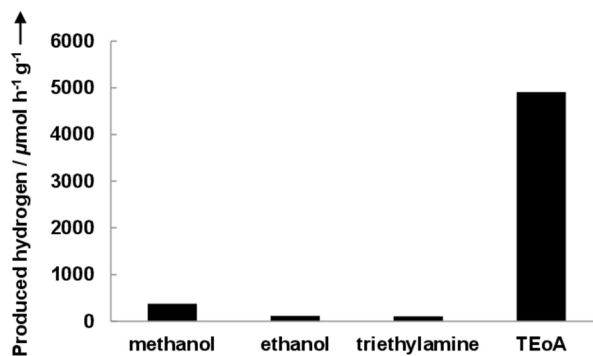


Figure S15. Steady rate of hydrogen production from water containing various electron donors (triethylamine, methanol, ethanol, triethanolamine TEOA; 10 vol%) under visible light ($\lambda > 420 \text{ nm}$) by 2.3 wt% Pt-loaded aPTI_4AP_{16%}.

- [S1] E. Wirnhier, M. Döblinger, D. Gunzelmann, J. Senker, B. V. Lotsch, W. Schnick, *Chem. Eur. J.* **2011**, *17*, 3213-3221.
- [S2] M. J. Bojdys, J.-O. Müller, M. Antonietti, A. Thomas, *Chem. Eur. J.* **2008**, *14*, 8177-8182.
- [S3] A. Sattler, Doctoral Thesis, University of Munich (LMU), **2010**.
- [S4] J. Zhang, X. Chen, K. Takanabe, K. Maeda, K. Domen, J. D. Epping, X. Fu, M. Antonietti, X. Wang, *Angew. Chem. Int. Ed.* **2010**, *49*, 441-444.
- [S5] a) J. Tegenfeldt, U. Haebleren, *J. Magn. Reson.* **1979**, *36*, 453-57; b) K. Saito, C. Martineau, G. Fink, F. Taulelle, *Solid State Nucl. Mag.* **2011**, *40*, 66-71.

6.5 Strukturaufklärung von PTI Nanoschichten: 1D und 2D Spektren

Crystalline Carbon Nitride Nanosheets for Improved Visible-Light Hydrogen Evolution

K. Schwinghammer,^{†,‡} M. B. Mesch,^{||} V. Duppel,[†] C. Ziegler,^{†,‡,§} J. Senker,^{||} B. V. Lotsch*^{†,‡,§}

Erschienen in:

Journal of the American Chemical Society 2014, 136, 1730

Reprinted with permission from Journal of the American Chemical Society 2014, 136, 1730. Copyright 2014 American Chemical Society.

[†] Max Planck Institute for Solid State Research, Heisenbergstr. 1, 70569 Stuttgart, Germany

[‡] Department of Chemistry, University of Munich, LMU, Butenandtstr. 5-13, 81377 Munich, Germany

[§] Nanosystems Initiative Munich (NIM) and Center for Nanoscience, Schellingstr. 4, 80799 Munich, Germany

^{||} Department of Inorganic Chemistry III, University of Bayreuth, Universitätsstr. 30, 95447 Bayreuth, Germany

* B.Lotsch@fkf.mpg.de

6.5.1 Crystalline Carbon Nitride Nanosheets for Improved Visible-Light Hydrogen Evolution

Crystalline Carbon Nitride Nanosheets for Improved Visible-Light Hydrogen Evolution

Katharina Schwinghammer,^{†,‡} Maria B. Mesch,^{||} Viola Duppel,[†] Christian Ziegler,^{‡,†,§} Jürgen Senker,^{||} and Bettina V. Lotsch^{*,†,‡,§}[†]Max Planck Institute for Solid State Research, 70569 Stuttgart, Germany[‡]Department of Chemistry, University of Munich, LMU, 81377 Munich, Germany[§]Nanosystems Initiative Munich (NIM) and Center for Nanoscience, 80799 Munich, Germany^{||}Inorganic Chemistry III, University of Bayreuth, 95447 Bayreuth, Germany

Supporting Information

ABSTRACT: Nanosheets of a crystalline 2D carbon nitride were obtained by ionothermal synthesis of the layered bulk material poly(triazine imide), PTI, followed by one-step liquid exfoliation in water. Triazine-based nanosheets are 1–2 nm in height and afford chemically and colloiddally stable suspensions under both basic and acidic conditions. We use solid-state NMR spectroscopy of isotopically enriched, restacked nanosheets as a tool to indirectly monitor the exfoliation process and carve out the chemical changes occurring upon exfoliation, as well as to determine the nanosheet thickness. PTI nanosheets show significantly enhanced visible-light driven photocatalytic activity toward hydrogen evolution compared to their bulk counterpart, which highlights the crucial role of morphology and surface area on the photocatalytic performance of carbon nitride materials.

The exploration of highly efficient photocatalysts has been fuelled by the prospect of converting sustainable solar energy into clean chemical fuels.¹ In this context, carbon nitrides have emerged as promising metal-free visible-light photocatalysts owing to their abundance, stability, and chemical tunability.² Recently, we³ and others⁴ independently discovered a new type of carbon nitride photocatalyst, poly(triazine imide) (PTI/Li⁺Cl⁻),^{5a,b} which rivals the benchmark carbon nitride based on heptazine building blocks, known as melon⁶ and often loosely called graphitic carbon nitride, *g*-C₃N₄.^{2,7} In contrast to melon (*g*-C₃N₄ⁿ), PTI is a crystalline species and represents the only structurally characterized two-dimensional (2D) carbon nitride network known to date.⁵ The layers are composed of imide-linked triazine units (Figure 1a) and are stacked in an ABA-type fashion, separated by weak van der Waals forces, with lithium and chloride ions situated in channels running along the stacking direction (Figure 1b).^{5b} In the past, various strategies, such as doping with heteroatoms⁸ or organic molecules,^{3,9} interfacing with other semiconductors or dyes to create heterojunctions,¹⁰ and morphology-tuning^{8c,11} have been used to increase the photocatalytic activity of carbon nitrides. In this regard, the exfoliation of carbon nitrides into ultrathin nanosheets has been shown to enhance the photocatalytic activity due to surface and quantum confinement effects.¹² Since the seminal discovery of

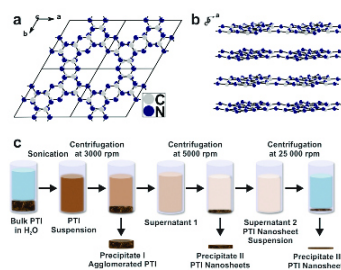


Figure 1. Idealized PTI structure (lithium/chloride intercalation omitted for clarity) viewed along the *c*-axis (a) and the slightly tilted *b*-axis (b). Scheme of the exfoliation process and product labeling (c).

graphene,¹³ it has been well-established that delamination of 2D layered materials such as MoS₂¹⁴ and WS₂¹⁵ may entail unique physicochemical properties, including ultrahigh charge carrier mobilities and pronounced changes in the band structure. Likewise, delamination of layered photocatalysts into 2D sheets may be advantageous for promoting photocatalytic efficiency, both via the exposure of active sites and optimized light harvesting, charge separation and percolation.^{12a–c,16} In contrast to melon-type carbon nitrides which have been exfoliated recently,^{12a} PTI is highly crystalline and a true 2D material,^{5b,12d} which lends itself as an excellent model system to explore both structural effects and photocatalytic activity as a function of the exfoliation state.

Layered materials such as graphite and boron nitride can be exfoliated when the enthalpy of mixing is minimized, which is the case when the surface energies of the nanosheet and solvent match.¹⁷ Zhang et al.^{12b} calculated the surface energy of *g*-C₃N₄ as 115 mJ/m², which matches well with the surface energy of water (~102 mJ/m²).^{17c} In addition, the terminal hydrogen atoms of the carbon nitrides prefer polar solvents, which upon hydrogen bond formation will cause swelling and exfoliation of the bulk carbon nitrides on a large scale.^{12b} Recently, Bojdy et al.

Received: November 6, 2013

Published: January 16, 2014

reported^{12d} that bromide intercalated PTI can be exfoliated by intercalation of potassium and subjecting the intercalate to water. The resulting thin sheets show large lateral sizes in the micrometer range, which however is expected to be unfavorable for photocatalysis due to the relatively small surface area and exposed number of active sites.

Here we demonstrate the one-step synthesis of crystalline PTI nanosheets by "green" liquid phase exfoliation in water, without the need for additives, toxic solvents or preintercalation steps. Remarkably, facile exfoliation in water leads to highly crystalline nanosheets of 1–2 nm in thickness, which show significantly increased photocatalytic efficiency for visible-light driven hydrogen evolution compared to bulk crystalline PTI.

Crystalline PTI/Li⁺Cl⁻ was suspended in water (2 mg/mL) and sonicated for 15 h at room temperature (Figure 1c). The dispersion was centrifuged at 3000 rpm to remove aggregates (Precipitate I), giving rise to a homogeneous dispersion of PTI nanosheets. To further separate the suspension according to the degree of exfoliation, a fraction of the aqueous suspension was further centrifuged at 5000 rpm (Precipitate II) to yield a nanosheet suspension with a higher degree of exfoliation compared to Precipitate I. The supernatant remaining after this centrifugation step, showing the maximum degree of exfoliation, was kept for analysis of the suspended nanosheets (Supernatant 2, 0.2 mg/mL). Finally, the nanosheets were precipitated by centrifugation at 25000 rpm and subjected to analysis in order to compare the suspended nanosheets (Supernatant 2) vs their restacked form (Precipitate III). The labeling scheme of the different nanosheet fractions is outlined in Figure 1c.

The well-dispersed PTI nanosheets (Supernatant 2) in water are negatively charged, with a zeta potential of -54.0 mV and a pH of 10.5. This observation is consistent with the fact that deprotonated, bridging imide moieties are present which are charge-compensated by Li ions, giving rise to dynamic lithium-proton exchange with water and, hence, to the observed basic character of the suspension caused by lithium hydroxide. The brownish dispersion is highly stable, showing no signs of precipitation even after being stored for 2 months, in line with the high negative surface charge. Interestingly, the surface charge is minimal (point of zero charge) at pH 5.4 and reversed at lower pH with a zeta potential of $+30$ mV at pH 2 (Figure S1). Thus, the nanosheets are stable both at low (<3) and high pH values (>8), which can be rationalized by the overall amphoteric character of the ring and bridging nitrogen functions in the PTI backbone.

Having ascertained the state of dispersion and stability of the suspensions, the thickness of as-prepared PTI nanosheets (Supernatant 2) was investigated by atomic force microscopy (AFM). According to Wirnhier et al. bulk PTI is built up from hollow microtubes whose walls are composed of an oriented assembly of hexagonal prismatic crystallites with lateral sizes of about 60 nm.^{5b} AFM images of the nanosheet suspension (Supernatant 2) and the corresponding height profile display exfoliated crystallites with lateral sizes of less than 100 nm and a height of 1–2 nm, indicating the exfoliated nanosheets are composed of only a few carbon nitride layers, taking into account a water shell likely surrounding the nanosheets (Figure 2a and discussion below).

AFM results were further confirmed by TEM investigations. HRTEM measurements reveal that the hexagonal shape of the crystallites is in fact retained, and the 2D sheets are well-separated and conformally spread across the substrate (Figure 2c). Selected area electron diffraction (SAED) patterns are fully

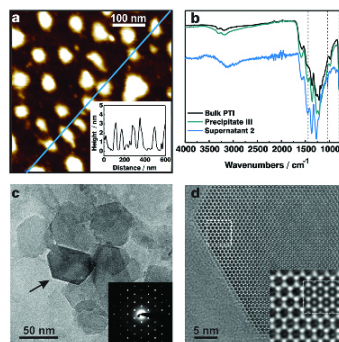


Figure 2. AFM image of exfoliated PTI nanosheets deposited on a Si/SiO₂ wafer (a) and the corresponding height image (inset). IR spectrum of bulk PTI (black) compared to Precipitate III (green) and Supernatant 2 (blue) (b). TEM image of exfoliated ultrathin PTI nanosheets (c), higher magnification of a PTI nanosheet edge viewed along [001] (d) marked in (c) and simulation (JEMS; $\Delta f = +50$ nm, $t = 2.70$ nm; inset).

consistent with the expected hexagonal symmetry of an individual PTI layer (Figures 2c (inset) and S2a).^{5b}

X-ray diffraction patterns (Figure S2b) confirm that both the restacked PTI nanosheets (Precipitate III) and the precipitates from the previous steps (Precipitate I and II) show reflections which are consistent with bulk PTI,^{5a,b} confirming that the structure of the parent bulk PTI is retained in the nanosheets. Interestingly, the presence of (*hkl*) reflections showing no obvious asymmetry or line broadening further suggests that the same stacking pattern is adopted after centrifugation, without the occurrence of turbostratic disorder in the restacked material.

The identity of the nanosheets was further confirmed by FTIR spectroscopy (Figure 2b). The characteristic IR spectrum of the nanosheet Precipitate II is largely reminiscent of that of the bulk material,^{5a,b} both having a band at 810 cm⁻¹ (triazine ring sextant out of plane bending) and a fingerprint region 1200–1620 cm⁻¹ which is dominated by the same ν (C–NH–C) and ν (C=N) stretching vibrations. Nevertheless, Precipitate II shows a more highly resolved band at 1440 cm⁻¹ and the intensity ratio of the ν (C–NH–C) vibrations at 1260 and 1210 cm⁻¹ is slightly shifted. The IR of the nanosheet suspension (Supernatant 2, measured in solution against a water background) shows slightly broadened and shifted bands in the region between 1000 and 1200 cm⁻¹ compared to the bulk material. These changes can be attributed to the water environment of the nanosheets in Supernatant 2.

The composition of the nanosheets (Precipitate III) was analyzed by elemental analysis (EA), revealing slight differences from the bulk material (Table S1). PTI nanosheets show a decreased lithium content compared to the starting material, suggesting that lithium ions are released during the exfoliation process, possibly by Li⁺–H⁺ exchange at the strongly basic bridging imide groups through reaction with water. The atomic C/N ratio of Precipitate II (0.62) is similar to the one in bulk PTI (0.64).

To further probe the chemical environment and bonding between the carbon and nitrogen atoms in the PTI nanosheets (Precipitate III), XPS measurements were conducted. No obvious shifts of the binding energy of C 1s and N 1s core electrons are observable, suggesting that the chemical states of

both carbon and nitrogen atoms in the nanosheets (Precipitate III) are the same as in bulk PTI (Supporting Information (SI)). Two oxygen peaks are observed for Precipitate III, which are due to air (O1 at 530.8 eV) and water (532.1 eV), respectively (Figure S4).¹⁸ Note that the bulk material contains only the first oxygen peak (O1).

To gain more insights into the local structure of the nanosheets relative to the one of bulk PTI, we performed solid-state NMR spectroscopy with ¹⁵N isotope-enriched samples of Precipitates I–III and bulk PTI in comparison (Figure 3). While being overall similar, both ¹³C and ¹⁵N spectra

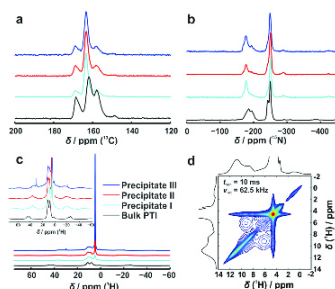


Figure 3. ¹³C (a) and ¹⁵N (b) CP–MAS NMR spectra and ¹H (c) MAS NMR spectra for Precipitates I–III and bulk PTI, respectively. ¹H¹H proton driven spin diffusion spectrum (d) for Precipitate III.

reveal subtle differences in the relative signal intensities on going from the bulk to the restacked nanosheets. These changes are predominantly attributed to a decrease in the lithium content in the channels and the resulting higher local symmetry of carbon and nitrogen environments in the restacked samples. As the Li content does not further decrease with increasing degree of exfoliation, it is likely determined initially by the sonication process and unaffected by the subsequent centrifugation-exfoliation steps. In contrast, the water content in the samples, apparent from ¹H spectra (signals at 6.2 and 4.6 ppm), tremendously increases from Precipitate I to III. Polarization exchange between the PTI protons and the ones of the water molecules as ascertained by ¹H¹H proton driven spin diffusion spectroscopy (Figures 3d and S6) is even faster than the exchange among the PTI protons. This points to a close vicinity of the nanosheets and water on a molecular scale. Assuming dense monolayers of water on the surface of the nanosheet stacks, we find that between 2 and 4 PTI layers are interspersed with two water layers, based on the relative proton signal intensities (SI and Figure S5). The derived height of the nanosheet stack (PTI)_{2,4} corresponds well to that measured by AFM (1–2 nm). Therefore, NMR presents a viable “bulk method” to indirectly determine the thickness of nanosheet stacks.

The brown color of the PTI nanosheet suspension indicates substantial absorption in the visible range of the spectrum, similar to bulk PTI. While the strong absorption edge just below 400 nm is likewise present in the nanosheet suspension, the broad band around 450 nm is less pronounced for Supernatant 2 (measured in water), which may be due to the absence of layer stacking or to solvation effects. Quantum confinement effects are not noticeable, since there are only minute changes in the absorption

properties for the precipitates (Figure S7) and nanosheet suspension (Figure 4d), respectively, compared to the bulk

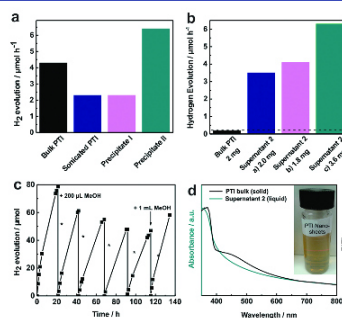


Figure 4. Photocatalytic activity toward H₂ production of the Pt-doped Precipitates (I and II) compared to sonicated PTI and bulk PTI (a), and of the nanosheet suspensions compared to bulk PTI (b), measured in a 10 vol% TEoA/water solution for 3 h illumination with visible light (>420 nm). Cyclic stability tests of the nanosheet suspension: Supernatant 1 with methanol as electron donor (c). The reactor was purged several times (marked with an asterisk) and methanol was reinjected twice. UV/vis spectrum of bulk PTI measured as solid in diffuse reflectance mode compared to Supernatant 2 measured as liquid in transmission mode (d).

material. More insights into the electronic band structure is given by Moewes and co-workers, who extracted a band gap of 2.2 eV for the LiCl-intercalated material.²⁰

Owing to their small particle size and, thus, higher exposed surface area and possibly higher number of active sites, the PTI nanosheets were tested for photocatalytic hydrogen evolution and compared to the water reduction activity of the bulk material. The photocatalytic activity of the PTI nanosheet suspension (Supernatant 2), of the bulk material as well as agglomerated PTI (Precipitate I) and partially exfoliated nanosheet fractions (Precipitate II) was measured in a water/triethanolamine (TEoA) solution (for details see SI) under visible light illumination (Figure 4a). Under the conditions applied, bulk PTI evolves 4.3 μmol H₂/h. Sonication of the material for 15 h in water lowers the activity of the suspension by about 43%. The formed agglomerates were centrifuged at 3000 rpm, redispersed and tested with regard to their photocatalytic activity, confirming the same low activity of Precipitate I compared to sonicated PTI. Precipitate II, containing partially exfoliated PTI, shows an improvement in hydrogen evolution by 28% (6.4 μmol H₂/h).

To examine the low concentrated PTI nanosheet suspensions (Supernatant 2), 2 mg of bulk PTI was tested and compared to three different suspensions (2a, 2b and 2c) containing 2.0, 1.8, and 3.6 mg of nanosheets, respectively. While bulk PTI shows an activity of 0.2 μmol H₂/h (Figure 4b), 2 mg of the PTI nanosheets (Supernatant 2a) exhibits a much higher hydrogen evolution rate, corresponding to an improvement by a factor of 18 (3.5 μmol H₂/h; 1.3% apparent quantum efficiency at 400 nm for nonoptimized conditions, see ref 21) as compared to the bulk material. As expected, the more concentrated nanosheet suspension (Supernatant 2c) shows an even higher photocatalytic activity, suggesting that hydrogen evolution is not yet diffusion limited under these conditions and light harvesting is not yet impeded by scattering effects.

Measurements probing whether sustained hydrogen evolution over extended periods of time is feasible were performed with Supernatant 1 and TEOA (Figure S8) or methanol as electron donor (Figure 4c). While with TEOA a decrease in activity was detected, which may be due to degradation of the material under basic conditions, long-term measurements in methanol show that the PTI nanosheets are steadily evolving hydrogen for at least 130 h. Note that after the sixth cycle (after addition of methanol), the hydrogen evolution rate of the first cycle (6.1 $\mu\text{mol H}_2/\text{h}$) could almost be recovered (5.4 $\mu\text{mol H}_2/\text{h}$). Furthermore, a strongly wavelength-dependent hydrogen evolution rate was observed (Figure S9).

In conclusion, triazine-based PTI nanosheets have been successfully synthesized through a simple and cost-effective aqueous exfoliation method starting with bulk PTI powder. The structure and morphology of the nanosheets was identified by complementary techniques including TEM, XRD, AFM and solid-state NMR spectroscopy, highlighting the close relationship between the parent PTI and the nanosheets. In agreement with AFM measurements revealing nanosheet thicknesses of 1–2 nm, NMR points to facile water incorporation in the restacked nanosheets, forming arrangements of 2–4 PTI layers interspersed with water layers. Exfoliated PTI is the first structurally well-defined, crystalline 2D carbon nitride showing high activity toward photocatalytic water-splitting, which is among the highest ever observed for pristine carbon nitrides, including mesoporous "g-C₃N₄"^{9a,12a,19}. The photocatalytic activity of the exfoliated sample is superior by a factor of >17 to both the nonexfoliated counterpart and melon (internal standard) and by a factor of >8 to "g-C₃N₄" (calculated for 2 mg).^{12a}

Our study draws on highly defined, structurally unambiguous carbon nitride nanosheets and thus paves the way for a better understanding of structure-property relationships in carbon nitrides and the factors influencing the photocatalytic activity in this promising, yet still largely ill-defined, class of photocatalysts.

■ ASSOCIATED CONTENT

Supporting Information

Experimental details and characterization data. This material is available free of charge via the Internet at <http://pubs.acs.org>.

■ AUTHOR INFORMATION

Corresponding Author

b.lotsch@fkf.mpg.de

Notes

The authors declare no competing financial interest.

■ ACKNOWLEDGMENTS

Financial support by the Deutsche Forschungsgemeinschaft (projects LO1801/1-1, SE1417/5-1), the cluster of excellence "Nanosystems Initiative Munich" (NIM), and the Center for NanoScience (CeNS) is gratefully acknowledged. We thank M. Konuma and M.-L. Schreiber for their assistance with the sample characterization and N. Popp for the synthesis of ¹⁵N-enriched PTI. Dedicated to Professor Ingo-Peter Lorenz on the Occasion of His 70th Birthday.

■ REFERENCES

- (1) (a) Hoffmann, M. R.; Scot, T. M.; Choi, W.; Bahnemann, D. W. *Chem. Rev.* **1995**, *95*, 69. (b) Linsebigler, A. L.; Lu, G.; Yates, J. T. *Chem. Rev.* **1995**, *95*, 735.
- (2) (a) Wang, X.; Maeda, K.; Thomas, A.; Takanahe, K.; Xin, G.; Carlsson, J. M.; Domen, K.; Antonietti, M. *Nat. Mater.* **2009**, *8*, 76.

- (b) Wang, Y.; Wang, X.; Antonietti, M. *Angew. Chem., Int. Ed.* **2012**, *51*, 68. (c) Zheng, Y.; Liu, J.; Liang, J.; Jaroniec, M.; Qiao, S. Z. *Energy Environ. Sci.* **2012**, *5*, 6717.

- (3) Schwinghammer, K.; Tuffy, B.; Mesch, M. B.; Wirnhier, E.; Martineau, C.; Taulelle, F.; Schnick, W.; Senker, J.; Lotsch, B. V. *Angew. Chem., Int. Ed.* **2013**, *52*, 2435.

- (4) Ham, Y.; Maeda, K.; Cha, D.; Takanahe, K.; Domen, K. *Chem.—Asian J.* **2013**, *8*, 218.

- (5) (a) Bojdys, M. J.; Müller, J.-O.; Antonietti, M.; Thomas, A. *Chem.—Eur. J.* **2008**, *14*, 8177. (b) Wirnhier, E.; Döbbling, M.; Gunzelmann, D.; Senker, J.; Lotsch, B. V.; Schnick, W. *Chem.—Eur. J.* **2011**, *17*, 3213. (c) Chong, S. Y.; Jones, J. T. A.; Khimyak, Y. Z.; Cooper, A. I.; Thomas, A.; Antonietti, M.; Bojdys, M. J. *J. Mater. Chem. A* **2013**, *1*, 1102.

- (6) Lotsch, B. V.; Döbbling, M.; Sehnert, J.; Seyfarth, L.; Senker, J.; Oeckler, O.; Schnick, W. *Chem.—Eur. J.* **2007**, *13*, 4969.

- (7) (a) Yu, J.; Wang, S.; Cheng, B.; Lin, Z.; Huang, F. *Catal. Sci. Technol.* **2013**, *3*, 1782. (b) Liao, G.; Chen, S.; Quan, X.; Yu, H.; Zhao, H. *J. Mater. Chem.* **2012**, *22*, 2721. (c) Bai, X.; Wang, L.; Zong, R.; Zhu, Y. *J. Phys. Chem. C* **2013**, *117*, 9952.

- (8) (a) Wang, Y.; Zhang, J.; Wang, X.; Antonietti, M.; Li, H. *Angew. Chem., Int. Ed.* **2010**, *49*, 3356. (b) Liu, G.; Niu, P.; Sun, C.; Smith, S. C.; Chen, Z.; Lu, G. Q.; Cheng, H.-M. *J. Am. Chem. Soc.* **2010**, *132*, 11642. (c) Lin, Z.; Wang, X. *Angew. Chem., Int. Ed.* **2013**, *52*, 1735.

- (9) (a) Zhang, J. H.; Chen, X. F.; Takanahe, K.; Maeda, K.; Domen, K.; Epping, J. D.; Fu, X. Z.; Antonietti, M.; Wang, X. C. *Angew. Chem., Int. Ed.* **2010**, *122*, 451. (b) Zhang, J.; Zhang, G.; Chen, X.; Lin, S.; Möhlmann, L.; Dolęga, G.; Lipner, G.; Antonietti, M.; Blechert, S.; Wang, X. *Angew. Chem., Int. Ed.* **2012**, *51*, 3183.

- (10) (a) Wang, Y.; Shi, R.; Lin, J.; Zhu, Y. *Energy Environ. Sci.* **2011**, *4*, 2922. (b) Zhang, Y.; Mori, T.; Ye, J.; Antonietti, M. *J. Am. Chem. Soc.* **2010**, *132*, 6294.

- (11) (a) Kiskan, B.; Zhang, J.; Wang, X.; Antonietti, M.; Yagci, Y. *ACS Macro Lett.* **2012**, *1*, 546. (b) Wang, X.; Maeda, K.; Chen, X.; Takanahe, K.; Domen, K.; Hou, Y.; Fu, X.; Antonietti, M. *J. Am. Chem. Soc.* **2009**, *131*, 1680.

- (12) (a) Yang, S.; Gong, Y.; Zhang, J.; Zhan, L.; Ma, L.; Fang, Z.; Vajtai, R.; Wang, X.; Ajayan, P. M. *Adv. Mater.* **2013**, *25*, 2452. (b) Zhang, X.; Xie, X.; Wang, H.; Zhang, J.; Pan, B.; Xie, Y. *J. Am. Chem. Soc.* **2013**, *135*, 18. (c) Niu, P.; Zhang, L.; Liu, G.; Cheng, H.-M. *Adv. Funct. Mater.* **2012**, *22*, 4763. (d) Bojdys, M. J.; Severin, N.; Rabe, J. P.; Cooper, A. I.; Thomas, A.; Antonietti, M. *Macromol. Rapid Commun.* **2013**, *34*, 850.

- (13) (a) Cai, M.; Thorpe, D.; Adamson, D. H.; Schniepp, H. C. *J. Mater. Chem.* **2012**, *22*, 24992. (b) Geim, A. K.; Novoselov, K. S. *Nat. Mater.* **2007**, *6*, 183.

- (14) Štengl, V.; Henych, J. *Nanoscale* **2013**, *5*, 3387.

- (15) Voiry, D.; Yamaguchi, H.; Li, J.; Silva, R.; Alves, D. C. B.; Fujita, T.; Chen, M.; Asefa, T.; Shenoy, V. B.; Eda, G.; Chhowalla, M. *Nat. Mater.* **2013**, *12*, 850.

- (16) (a) Ebina, Y.; Sakai, N.; Sasaki, T. *J. Phys. Chem. B* **2005**, *109*, 17212. (b) Ida, S.; Okamoto, Y.; Koga, S.; Hagiwara, H.; Ishihara, T. *RSC Adv.* **2013**, *3*, 11521. (c) Wang, W.; Yu, J. C.; Xia, D.; Wong, P. K.; Li, Y. *Environ. Sci. Technol.* **2013**, *47*, 8724.

- (17) (a) Coleman, J. N.; Lotya, M.; ÓNeill, A.; Bergin, S. D.; King, P. J.; Khan, U.; Young, K.; Gaucher, A.; De, S.; Smith, R. J.; et al. *Science* **2011**, *331*, 568. (b) Bergin, S. D.; Nicolosi, V.; Streich, P. V.; Giordani, S.; Sun, Z.; Windle, A. H.; Ryan, P.; Niraj, N. P. P.; Wang, Z.-T.; Carpenter, L.; et al. *Adv. Mater.* **2008**, *20*, 1876. (c) Since the surface tension of water equals 72.1 mJ/m², the surface energy of the nanosheet suspension (~102 mJ/m²) can be calculated considering the temperature and the entropy factor.^{17a,b}

- (18) George, G. A. *Polym. Int.* **1994**, *33*, 439.

- (19) Chen, X.; Jun, Y.-S.; Takanahe, K.; Maeda, K.; Domen, K.; Fu, X.; Antonietti, M.; Wang, X. *Chem. Mater.* **2009**, *21*, 4093.

- (20) McDermott, E. J.; Wirnhier, E.; Schnick, W.; Viridi, K. S.; Scheu, C.; Kauffmann, Y.; Kaplan, W. D.; Kurmaev, E. Z.; Moeves, A. *J. Phys. Chem. C* **2013**, *117*, 8806.

- (21) Ohtani, B. *J. Photochem. Photobiol., C* **2010**, *11*, 157.

6.5.2 Supporting Information

Supporting Information

Crystalline Carbon Nitride Nanosheets for Improved Visible-Light Hydrogen Evolution

Katharina Schwinghammer,^{†,‡} Maria B. Mesch,[‡] Viola Duppel,[†] Christian Ziegler,^{‡,†,§} Jürgen Senker[‡] and Bettina V. Lotsch^{*,†,‡,§}

[†]Max Planck Institute for Solid State Research, Heisenbergstr. 1, 70569 Stuttgart, Germany.

[‡]Department of Chemistry, University of Munich, LMU, Butenandtstr. 5-13, 81377 Munich, Germany.

[§]Nanosystems Initiative Munich (NIM) and Center for Nanoscience, Schellingstr. 4, 80799 Munich, Germany.

[‡]Department of Inorganic Chemistry III, University of Bayreuth, Universitätsstr. 30, 95447 Bayreuth, Germany.

Experimental Section

Photocatalysis. For testing the photocatalytic activity of the precipitates compared to bulk PTI and sonicated PTI, 10 mg of the carbon nitride catalysts were dispersed in 9 mL water (by 30 min of sonication). In case of the PTI nanosheet suspensions, 9 mL of the nanosheet suspensions (containing 2.0, 1.8 and 3.6 mg of PTI nanosheets) were directly used and compared to 2 mg of bulk PTI dispersed in 9 mL of water, which was dispersed by 30 min of sonication. Triethanolamine (TEoA, 1 mL, Roth) was used as a sacrificial electron donor and H₂PtCl₆ (8 wt% in H₂O, Sigma-Aldrich) was used as the Pt cocatalyst precursor which was photoreduced during the reaction (~ 2.2 wt% Pt). The suspensions were illuminated (0.4 W cm⁻²) in 24 mL glass vials in an argon atmosphere with PTFE/Teflon septa. The vials were purged with argon to remove any dissolved gases in the suspension. Samples were side-illuminated for 3 h with a 300 W xenon lamp with a water filter and dichroic mirror blocking wavelengths < 420 nm while stirring. For stability measurements and wavelength-specific measurements 9 mL of the PTI nanosheet suspension was filled in a 230 mL quartz glass reactor with a PTFE/Teflon septum under argon atmosphere. A sacrificial electron donor (1 mL) of either TEoA or methanol and the H₂PtCl₆ solution (~ 2.2 wt% Pt) was added. The flask was evacuated and purged with argon. The sample was simultaneously top-illuminated (top surface = 15.5 cm²) and cooled with a water jacket under the conditions described above. For wavelength-specific measurements and apparent quantum yield calculations, the full spectrum of the xenon lamp coupled with a band-pass filter (400, 450, 500, 550 or 600 nm; bandwidth ± 20 nm) was used. The average intensity of irradiation was measured as 4.0 mW cm⁻² and the irradiation area was 3.6 cm². The headspace of the reactor was periodically sampled with an online injection system and the gas components were quantified by gas chromatography using a thermal conductivity detector with argon as carrier gas.

Synthesis of $PTiLi^+Cl^-$ according to Wirnhier et al.⁵¹ Dicyandiamide (0.20 g, 2.38 mmol, Acros) and an eutectic mixture of lithium chloride (59.2 mol%, 0.90 g, 21.33 mmol, Roth) and potassium chloride (40.8 mol%, 1.01 g, 14.70 mmol, Roth) were ground together in a glovebox. The reaction mixture was transferred into a dried thick-walled silica glass tube (øext. 13 mm, øint. 10 mm). The tube was placed in a horizontal tube furnace and heated under atmospheric argon pressure at 6°C min^{-1} to 400°C . This temperature was held for 12 h and afterwards the sample was cooled to room temperature at $20^\circ\text{C min}^{-1}$. After this procedure, the tube was evacuated and sealed at a length of 120 mm. In a second step the ampule was placed in a slanted tube furnace and heated at 1°C min^{-1} to 600°C at which the sample was held for 24 h. After cooling down to room temperature the ampule was opened and the sample was isolated and washed with boiling water to remove residual salt. The resulting material PTi/Li^+Cl^- was obtained as a brown powder (80 mg, 50%). ^{15}N -enriched PTI was synthesized according to the procedure described above using ^{15}N -enriched dicyandiamide (Sigma-Aldrich).

Synthesis of a PTI nanosheet suspension. 40 mg of bulk PTi/Li^+Cl^- were dispersed in 20 mL of water. The ice-cooled suspension was sonicated for 15 h in an ultrasonic bath with an amplitude of 30%. The final suspension was centrifuged first at 3000 rpm and then at 5000 rpm to obtain the brown-colored PTI nanosheet suspension with a concentration of $\sim 0.2 \text{ mg mL}^{-1}$. DLS measurements, which theoretically give an idea about the hydrodynamic diameter of a spherical particle, resulted in an equivalent spherical diameter of 123 nm (98%). Non-exfoliated PTI shows a hydrodynamic diameter of 936 nm (100%).

Methods

Sonication. For sonication a *Sonorex Digital* DK 102 P of Bandelin with an ultrasonic frequency of 35 kHz and an ultrasonic power of 480 W was used.

Centrifugation. For centrifugation a bench top centrifuge *Sigma* 3-30K, with a maximum speed of 30000 rpm was used. The centrifugation speeds 3000, 5000 and 25000 rpm correspond to 795, 2208 and 55201 RCF, respectively.

X-ray powder diffraction. X-ray powder diffraction experiments were carried out with $\text{Cu-K}\alpha_1$ -radiation ($\lambda = 1.54051 \text{ \AA}$) on a *Bruker* D8 Advance diffractometer with a $\text{Ge}(111)$ -monochromator and a Dectris Mythen detector. The specimen was ground in a mortar and evenly spread by dispersing it with ethanol on a silicon carrier.

IR spectroscopy. FTIR spectra were recorded on a *Perkin Elmer* Spectrum Two spectrometer with an attenuated total reflectance unit.

UV/vis measurements. Optical diffuse reflectance spectra of the solids were collected at room temperature with a UV-Vis-NIR diffuse reflectance spectrometer (*Agilent Technologies*, Cary 5000) at a photometric range of 250 – 800 nm. Powders were prepared in a sample carrier with a quartz glass window at the edge of the integrating sphere with BaSO₄ as the optical standard. Kubelka-Munk spectra were calculated from the reflectance data.

AFM. Atomic force microscopy (AFM) measurements were performed on a diluted suspension of nanosheets allowed to dry on a silicon substrate, using an Asylum MFP3D Stand Alone AFM (*Asylum Research*, Santa Barbara, CA) using a Si micro cantilever (300 Hz resonant frequency and 26.1 N m⁻¹ spring constant) operated in tapping mode.

TEM. HRTEM was performed with a *Philips* CM 30 ST microscope (LaB₆ cathode, 300 kV, C_s = 1.15 mm). Images were recorded with a CCD camera (*Gatan*) and *Digital Micrograph* 3.6.1 (*Gatan*) was used as evaluation software. Chemical analyses (EDX) were performed with a Si/Li detector (*Thermo Fisher*, *Noran System Seven*).

Elemental analysis. Elemental analysis of the elements C, H, N and S is accomplished by high temperature digestion coupled with dynamic gas components separation. The samples are burnt explosively at 1150°C in a highly oxygenated helium atmosphere. The combustion products (CO₂, H₂O, H₂, NO, NO₂, etc) are detected by a thermal conductivity measurement cell. The accuracy is 0.30%. Measurements were done on an *Elementar vario EL*.

Solid-state NMR spectroscopy. The ¹H, ¹³C and ¹⁵N MAS-NMR spectra of ¹⁵N-enriched Precipitate I–III were recorded at ambient temperature on an AvanceIII HD 600 solid-state NMR spectrometer (Bruker) with an external magnetic field of 14.1 T, operating at frequencies of 600.1 MHz, 150.9 MHz and 60.8 MHz for ¹H, ¹³C and ¹⁵N, respectively. Additionally, the MAS-NMR spectra of the ¹⁵N-enriched bulk material were collected at ambient temperature on an Avance 300 solid-state NMR spectrometer (Bruker) with an external magnetic field of 7.0 T, operating at frequencies of 300.1 MHz, 75.5 MHz and 30.4 MHz for ¹H, ¹³C and ¹⁵N, respectively.

The samples were contained either in 1.3 mm, 1.9 mm or 4 mm ZrO₂ rotors which were mounted in standard triple resonance MAS probes (Bruker). The spinning speed was set to 62.5 kHz (1.3 mm), 15 kHz (1.9 mm) and 10 kHz (4 mm), respectively.

The ¹H spectra were recorded using one pulse and Hahn-echo experiments with a RF field of

125 and 83 kHz. The $^1\text{H}^{15}\text{N}$ cross-polarization (CP) MAS spectra were collected using a conventional sequence and contact times between 8 and 10 ms. The $^1\text{H}^{13}\text{C}$ cross-polarization (CP) MAS spectra were acquired with a ramped-amplitude (RAMP) CP sequence. During a contact time of 8 and 4 ms the ^1H RF field was linearly varied about 50%. During acquisition proton decoupling was carried out using SPINAL64 between 60 and 100 kHz. The recycle delay for all the spectra was set to 3 s and the spectra were referenced relative to TMS (^1H , ^{13}C) and nitromethane (^{15}N).

$^1\text{H}^1\text{H}$ 2D exchange experiments were conducted in a 1.3 mm ZrO_2 rotor on an Avance III HD 600 Bruker spectrometer using a NOESY-type three pulse experiment at a spinning speed of 62.5 kHz. Under these conditions the polarization transfer takes place by proton-driven spin-diffusion. Spectra with mixing times of 10 ms and 200 ms were recorded.

Dynamic Light Scattering. Dynamic light scattering measurements were performed with a Malvern Zetasizer Nano ZS with a maximum diameter size range of 0.3 nm to 10 μm and a molecular weight range of 342 Da to 2×10^7 Da.

pH-Meter. For the setting of the pH of the nanosheet suspension a *Mettler Toledo Seven Compact Labor-pH-meter* was used with a five point calibration system.

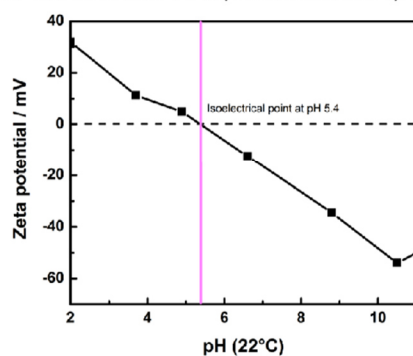


Figure S1. pH-dependent zeta potential measurements of Supernatant 2. The isoelectric point (IP) is at pH 5.4. Below pH 5.4 the nanosheets are positively charged, above the IP the nanosheets are negatively charged.

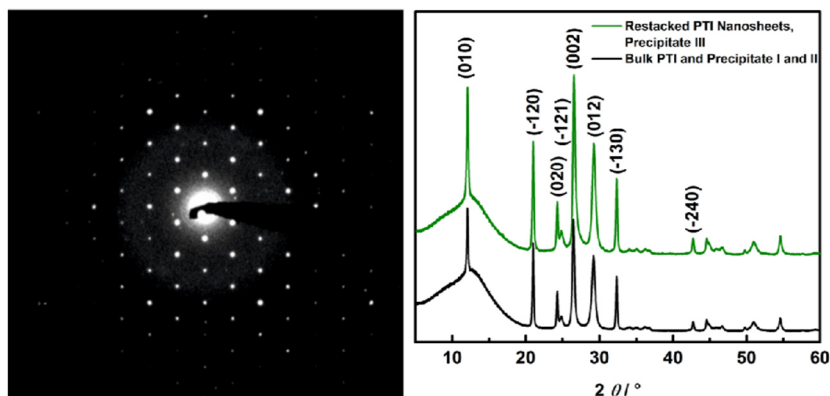


Figure S2. Electron diffraction pattern along [001] of a PTI nanosheet (left), shown in Figure 2c. The pattern is in agreement with the literature.⁵¹ Powder X-ray diffraction patterns of bulk PTI compared to the restacked PTI nanosheets (Precipitate III, right). The broad amorphous halo around $12^\circ 2\theta$ is caused by the sample carrier.

Table S1. Elemental analysis of bulk PTI compared to the restacked PTI nanosheets (Precipitate III).

Sample	C /wt%	N / wt%	H/wt%	Li/wt%
Bulk PTI/LiCl	30.7	47.7	1.5	4.1
Precipitate III	30.4	48.9	1.9	2.5

XPS measurements

The high-resolution N 1s spectra of both bulk PTI and Precipitate III were deconvoluted into two Gaussian-Lorentzian peaks at binding energies of 398.2/398.2 (N1 for bulk/III) and 399.8/399.7 eV (N2 for bulk/III) (Fig. S3b). For both materials, the dominant N1 is attributed to the sp^2 N atoms of the triazine rings,⁵²⁻³ while the smaller signal N2 is assigned to bridging N atoms in $NH(C_3N_3)_2 / LiN(C_3N_3)_2$.^{52,4} For bulk PTI and Precipitate III three different carbon atoms were found: 284.5/284.5 (C1), 286.2/285.9 (C2) and 287.7/287.6 (C3) (Fig. S3a). C1 is assigned to adventitious carbon (especially graphitic C=C and grease),^{52,4-5} while C3 and C2 originate from sp^2 C atoms bonded to N inside the triazine ring.^{54,6}

The chemical environment of the chlorine atoms is unchanged for the exfoliated material (Fig. S4): Both bulk and Precipitate III show one type of chlorine species (Cl1 at 197.7 eV (2p_{3/2}) and Cl2 at 199.4 eV (2p_{1/2})).

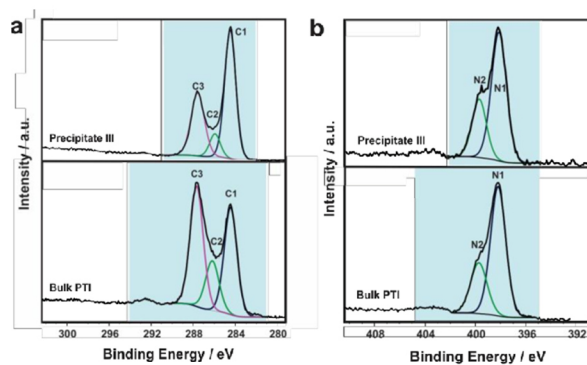


Figure S3. XPS spectra of C 1s (a) and N 1s (b) of bulk PTI compared to the PTI nanosheets (Precipitate III).

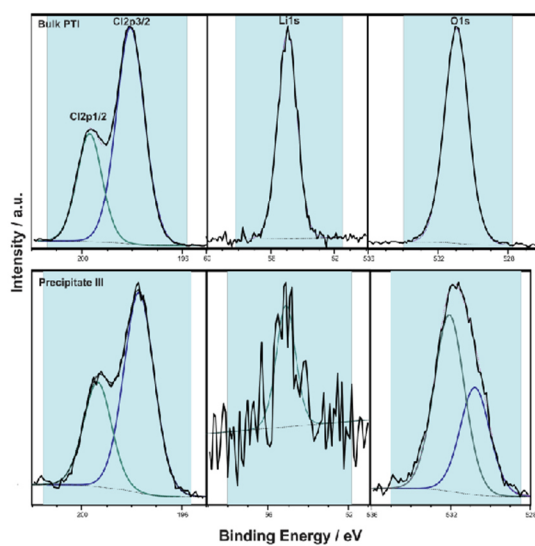


Figure S4. XPS spectra of Cl 2p, Li 1s and O 1s of bulk PTI (top) compared to PTI nanosheets (Precipitate III, bottom).

Calculation of the Water Content

Due to their negative zeta potential the PTI nanosheets or stacks of nanosheets carry a water shell in the suspension. Assuming that only the first hydration sphere is bonded strongly enough to be restacked together with the PTI nanosheets during the centrifugation process, the Precipitates I–III will consist of alternating PTI stacks separated by two monolayers of water. In this scenario the ratio of the PTI protons (signals at 8.9 and 10.8 ppm of Fig. S5) and the water protons (peaks at 4.6 and 6.2 ppm of Fig. S5) might be used to estimate the mean number of PTI layers sandwiched by a water shell. Since the surface density of a monolayer of water for a PTI surface is unknown, we extrapolate from results of DFT and MD calculations^{S7-8} for different uncharged surfaces. The lowest surface water density was found on MgO (001) surfaces, where the area per water molecule amounts to 17.8 \AA^2 .^{S7} In contrast, on (100) silica surfaces, the highest surface density of 13.0 \AA^2 was derived.^{S8} For a PTI monolayer two protons occupy a unit cell with a surface area of 64.18 \AA^2 . Taking into account a bottom and a top water monolayer for each PTI stack, the ratio of PTI protons (H_{PTI}) to water protons (H_{water}) was calculated as a function of the number of stacked PTI layers (Tab. S2).

Table S2. Ratio between PTI protons (H_{PTI}) and water protons (H_{water}). Calculation based on the monolayer water density for MgO (column 1) and silica (column 2).

N° of PTI layers	$H_{\text{PTI}} : H_{\text{water(MgO)}}$	$H_{\text{PTI}} : H_{\text{water(silica)}}$
1	1 : 7.2	1 : 9.9
2	1 : 3.6	1 : 4.9
3	1 : 2.4	1 : 3.3
4	1 : 1.8	1 : 2.5
5	1 : 1.4	1 : 2.0

The deconvolution of a high-resolution ^1H MAS spectrum at ultrafast spinning (Fig. S5-6 and Tab. S3) leads to $H_{\text{PTI}} : H_{\text{water}} = 1:2.8$. The two signals at 8.9 and 10.8 ppm represent the typical resonances for the PTI protons and are independent of the water content (compare Fig. 3c and ref. 6 of the manuscript). The resonances for the two peaks at 4.6 and 6.2 ppm are typical for water, and they increase from Precipitate I to III and are in close vicinity to the PTI protons as proven by the $^1\text{H}^1\text{H}$ spin-diffusion exchange spectra (Fig. 3 and S6). We thus take both resonances as a measure for the relative amount of adsorbed water molecules. The residual signals at 1.0, 3.5 and 3.9 ppm (Fig. S5) do not exchange with the resonances for neither the PTI nor the water protons and are thus considered as small impurities. Within the limit of our model, for the lower water coverage of 17.8 \AA^2 per H_2O molecule the “nanosheet” consists, on average, of 2 to 3 PTI layers, whereas for the higher water surface density (13.0 \AA^2 per H_2O

molecule) a mean value between 3 to 4 layers is derived. This amounts to a mean number of PTI layers $N = 3(1)$.

Table S3. Relevant parameters for the deconvolution of the high-resolution ^1H MAS spectrum for Precipitate III at ultrafast spinning ($\nu_{\text{rot}} = 62.5$ kHz). The resonances were refined with pseudo-Voigt profiles.

$\delta_{\text{iso}} / \text{ppm}$	FWHM	G/L ratio ^a	Intensity
1.0	2.0	0.4	0.16
3.5	0.5	0.0	0.12
3.9	0.5	0.5	0.14
4.6	0.23	0.0	5.1
6.2	2.0	0.9	0.63
8.9	2.1	0.7	1.0
10.8	2.0	0.6	1.0

^a: With a value 0 the resonance is described by a Lorentzian. For the other limit 1 the peak is refined by a Gaussian profile.

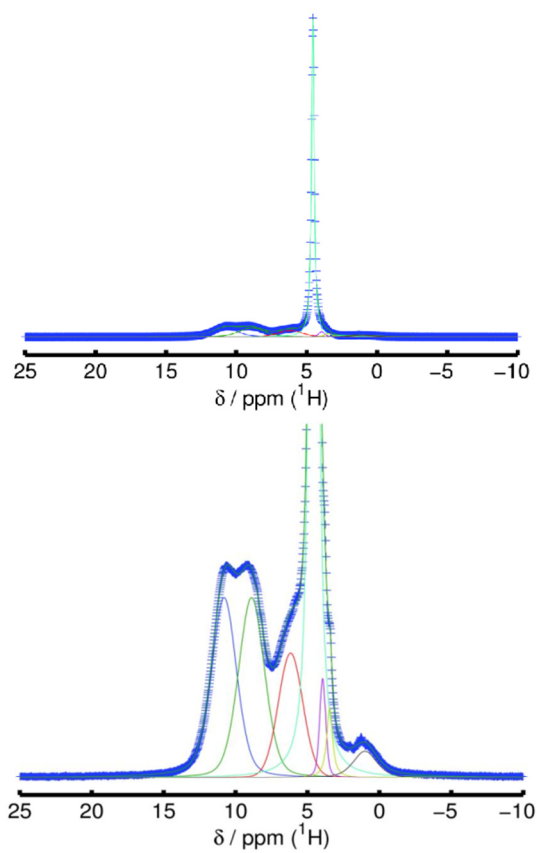


Figure S5. High-resolution ^1H MAS spectrum for Precipitate III at ultrafast spinning ($\nu_{\text{rot}} = 62.5$ kHz), together with the deconvolution using pseudo-Voigt profiles (compare also Tab. S3).

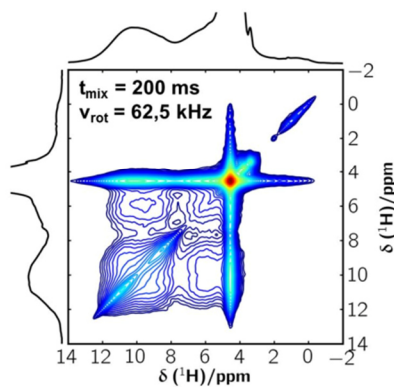


Figure S6. ^1H - ^1H proton driven spin diffusion spectrum for Precipitate III with a mixing time of 200 ms.

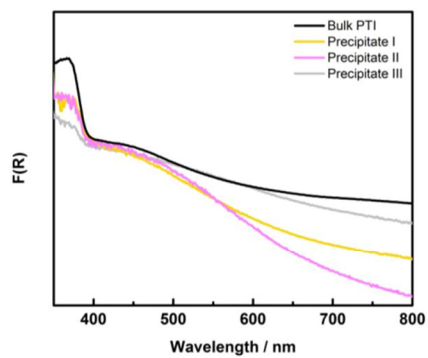


Figure S7. UV/vis F(R) spectrum of bulk PTI compared to the Precipitates I, II and III.

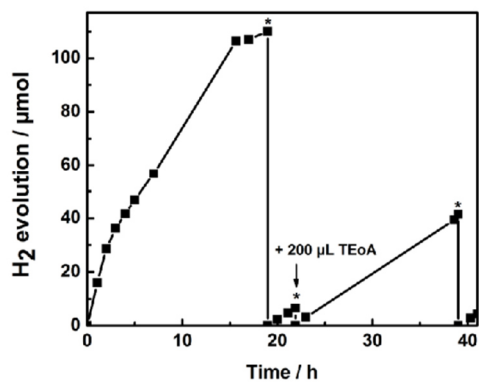


Figure S8. Long-term measurements of the PTI nanosheets (Supernatant 2) with TEoA as electron donor. The reactor was purged in moments marked with an asterisk.

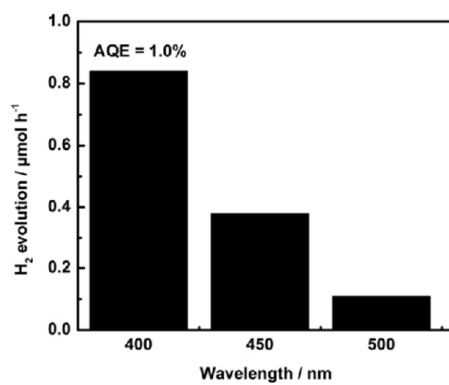


Figure S9. Wavelength-specific hydrogen production of PTI nanosheets (Supernatant 2) using 40 nm FWHM band-pass filters in a 10 vol% TEoA/water solution.

Control Experiments

Bulk PTI sonicated for 30 min

As a control experiment, bulk PTI was sonicated for 30 min in water (2.0 mg mL^{-1}) for dispersion and centrifuged at 5000 rpm (Supernatant, $< 0.1 \text{ mg mL}^{-1}$). Another reactor containing 30 min sonicated bulk PTI in water (1.0 mg mL^{-1}) was prepared and its photocatalytic activity was tested compared to the supernatant. The supernatant was characterized by TEM and AFM. Its concentration was very low and the suspension was only stable for several hours, in accordance with the low zeta potential of -24.4 mV (measured at a pH of 7.2). There was no photocatalytic improvement of the supernatant compared to the 30 min sonicated, uncentrifuged bulk PTI with similar concentration. Characterization showed that bulk PTI was not sufficiently exfoliated within 30 min of sonication (S10). The thickness of the obtained material was rather increased (TEM, AFM and DLS) compared to the dispersions sonicated for longer times (15 h) and the suspension contained agglomerates (320 nm in diameter for 87.4% of the crystallites compared to 123 nm for 98% of the nanosheets of Supernatant 2). TEM measurements show that the shape of the crystallites of the suspension sonicated for 30 min are rather rounded, whereas longer sonication with separation steps apparently leads to smaller and less aggregated crystallites with an edged shape which were homogeneously dispersed on the TEM grid. The AFM image (Fig. S10c) shows that sonication for 30 min yields essentially no exfoliated material. We find only one nanoparticle on a Si/SiO₂ wafer at a scan area of $5 \times 5 \mu\text{m}$ for the PTI suspension (supernatant) sonicated for 30 min and centrifuged at 5000 rpm.

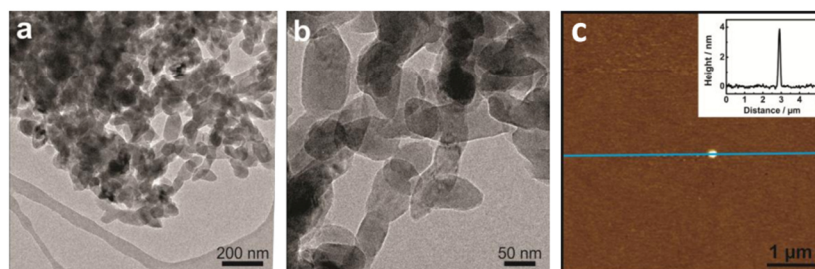


Figure S10. TEM measurements of bulk PTI sonicated for 30 min (and centrifuged at 5000 rpm) demonstrate agglomerates (a) and enlarged crystallites (b). The AFM image shows one PTI particle (very low concentration) found on the Si/SiO₂ wafer on a scan area of $5 \times 5 \mu\text{m}$, after centrifuging the PTI suspension sonicated for 30 min (c).

LiCl/LiOH Activation

Since we observed a loss in the lithium amount from bulk PTI (4.1 wt%) compared to Precipitate III (2.5 wt%), we tested the amount of lithium in Supernatant 3 to be about 10.7 mg L^{-1} (0.096 mg in 9 mL; corresponding to 0.6 mg LiOH monohydrate or LiCl). To exclude any lithium hydroxide / lithium chloride “activation” of the PTI nanosheet suspension (Supernatant 2), we performed further control experiments. Three reactors of 10 mg bulk PTI containing additionally 0.6 mg, 1.0 mg or 3.0 mg of lithium hydroxide monohydrate and two reactors containing additionally 2.0 or 6.0 mg lithium chloride, respectively, were prepared and their photocatalytic activity (10 mL 10 vol% TEoA solution; 2.5 wt% Pt) was tested compared to pristine bulk PTI. We also compared Supernatant 2 to the same PTI nanosheet suspension which was washed several times with water toward their water reduction ability. The addition of lithium hydroxide leads to a decrease in photocatalytic activity, which may arise from an increase in pH (11.3 vs. 10.5 for the pristine material). The addition of lithium chloride only leads to a decrease in activity when large amounts are used. Otherwise no difference is detected. The washed PTI nanosheet suspension (Supernatant 2 washed) shows a slightly decreased hydrogen evolution rate compared to the unwashed (LiOH added) suspension within the batch-to-batch error ($\sim 15\%$), which might be due to loss of material during the washing procedure.

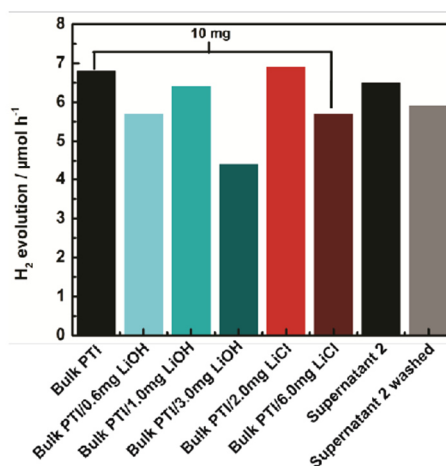


Figure S11. Photocatalytic activity of bulk PTI compared to LiCl and LiOH monohydrate contaminated bulk PTI samples (10 mg of photocatalyst, 10 vol% TEoA, 2.2 wt% Pt) and of Supernatant 2 ($\sim 0.2 \text{ mg mL}^{-1}$) compared to washed Supernatant 2 ($< 0.2 \text{ mg mL}^{-1}$).

- (S1) (a) Wirnhier, E.; Döblinger, M.; Gunzelmann, D.; Senker, J.; Lotsch, B. V.; Schnick, W. *Chem. Eur. J.* **2011**, *17*, 3213. (b) Bojdys, M. J.; Müller, J.-O.; Antonietti, M.; Thomas, A. *Chem. Eur. J.* **2008**, *14*, 8177.
- (S2) Yang, S.; Gong, Y.; Zhang, J.; Zhan, L.; Ma, L.; Fang, Z.; Vajtai, R.; Wang, X.; Ajayan, P. M. *Adv. Mater.* **2013**, *25*, 2452.
- (S3) (a) Xu, J.; Li, Y.; Peng, S.; Lu, G.; Li, S. *Phys. Chem. Chem. Phys.* **2013**, *15*, 7657-7665. (b) Aono, M.; Aizawa, S.; Kitazawa, N.; Watanabe, Y. *Thin Solid Films* **2008**, *516*, 648.
- (S4) Kim, M.; Hwang, S.; Yu, J.-S. *J. Mater. Chem.* **2007**, *17*, 1656.
- (S5) (a) Essafti, A.; Ijdiyaou, Y.; Azizan, M. *Sol. Energ. Mat. Sol. C* **2006**, *90*, 4. (b) Moulder, W. F. S. J. F.; Sobol, P. E.; Bomben, K. D. Handbook X-ray Photoelectron Spectroscopy. In *Physical Electronics*, Eden Prairie, MN, USA, **1995**.
- (S6) (a) Angleraud, B.; Mubumbila, N.; Tessier, P. Y.; Fernandez, V.; Turban, G. *Diam. Relat. Mater.* **2001**, *10*, 1142. (b) Roy, S. S.; McCann, R.; Papakonstantinou, P.; Maguire, P.; McLaughlin, J. A. *Thin Solid Films* **2005**, *482*, 145.
- (S7) Włodarczyk, R.; Sierka, M.; Kwapień, K.; Sauer, J.; Carrasco, E.; Aumer, A.; Gomes, J. F.; Sterrer, M.; Freund, H.-J. *J. Phys. Chem. C* **2011**, *115*, 6764.
- (S8) Yang, J.; Meng, S.; Xu, L. F.; Wang, E. G. *Phys. Rev. Lett.* **2004**, *92*, 146102-1-4.

6.6 Bestimmung von Atompositionen am Beispiel von PTI/LiCl

Solving the Hydrogen and Lithium Substructure of Poly (Triazine Imide)/LiCl Using NMR Crystallography

M. B. Mesch,[†] K. Bärwinkel,[†] Y. Krysiak,[‡] C. Martineau,[§] F. Taulelle,[§] R. Neder,^{||} U. Kolb,[‡] J. Senker^{*,†}

Manuskript vorbereitet zur Einreichung bei:

Chemistry – A European Journal

[†] Department of Inorganic Chemistry III, University of Bayreuth, Universitätsstr. 30, 95447 Bayreuth, Germany

[‡] Institute of Inorganic Chemistry and Analytical Chemistry, Johannes Gutenberg University Mainz, Jakob-Welder-Weg 11, 55128 Mainz, Germany

[§] Tectospin, Institut Lavoisier de Versailles (ILV), UMR CNRS 8180, Université de Versailles Saint-Quentin-en-Yvelines, 45 Avenue des Etats-Unis, 78035 Versailles cedex, France

^{||} Lehrstuhl für Kristallographie und Strukturphysik, Friedrich-Alexander-Universität Erlangen-Nürnberg, Staudtstr. 3, 91058 Erlangen (Germany)

* juergen.senker@uni-bayreuth.de

6.6.1 Solving the Hydrogen and Lithium Substructure of Poly (Triazine Imide)/LiCl Using NMR Crystallography

WILEY-VCH

FULL PAPER

Solving the Hydrogen and Lithium Substructure of Poly (Triazine Imide)/LiCl Using NMR Crystallography

Maria B. Mesch,^[a] Kilian Bärwinkel,^[a] Yaşar Krysiak,^[b] Charlotte Martineau,^[d] Francis Taulelle,^[d] Reinhard Neder,^{*[c]} Ute Kolb,^{*[b]} Jürgen Senker^{*[a]}

^[a] Inorganic Chemistry III, University of Bayreuth, 95447 Bayreuth (Germany)

^[b] Institute of Inorganic Chemistry and Analytical Chemistry, Johannes Gutenberg University Mainz, Jakob-Welder-Weg 11, 55128 Mainz (Germany)

^[c] Lehrstuhl für Kristallographie und Strukturphysik, Friedrich-Alexander-Universität Erlangen-Nürnberg, Staudtstr. 3, 91058 Erlangen (Germany)

^[d] Tectospin, Institut Lavoisier de Versailles (ILV), UMR CNRS 8180 Université de Versailles Saint-Quentin-en-Yvelines 45 Avenue des Etats-Unis, 78035 Versailles cedex (France)

* reinhard.neder@fau.de, kolb@uni-mainz.de, juergen.senker@uni-bayreuth.de

Abstract: Poly (triazine imide) with incorporated lithium chloride recently attracted substantial attention due to its photocatalytic activity for water splitting. However up to date, an apparent H/Li disorder prevents to derive structure property relations e.g. with respect to a band gap tuning. Here we show, that by combining one- and two-dimensional, multinuclear solid-state NMR spectroscopy, chemical modelling, automated electron diffraction tomography and X-ray pair distribution function we were finally able to resolve the H/Li substructure. In each cavity only one hydrogen is bound to a bridging nitrogen while a second one, surprisingly, protonates a triazine ring. The two lithium ions within each cavity are positioned between two nitrogen atoms of neighbouring triazine rings. The thereby induced local dipole moments cause buckling of the framework with a coherence length below 4 nm. Nevertheless, the average structure is described with the space group $P2_12_12_1$. In this way, we demonstrate that in particular, the above mentioned techniques allow for a smart interplay thus extending the repertoire of NMR crystallography.

Introduction

Poly (triazine imide) with incorporated lithium chloride (PTI/LiCl) was first reported in 2011.^[1] At that time it was described as a 2D layer structure with a planar framework of triazine rings connected via imide groups (Figure 1) and is thus a member of the larger family of carbon nitride materials with a strictly alternating arrangement of carbon and nitrogen atoms.^[2–6] The PTI layers are stabilized by incorporation of LiCl with chloride ions positioned between and Li⁺ ions occupying voids within the 2D layers (Figure 1).^[1] In this process, additionally, hydrogen atoms are partially exchanged against lithium ions maintaining charge neutrality, and leading to a pronounced, and up to now unknown, structural disorder. Elemental analysis and quantitative ¹⁵N SSNMR spectroscopy revealed that 1/3 of the NH-groups are deprotonated resulting in a chemical composition of $[(C_2N_3)_2(NH_xLi_{1-x})_2LiCl]$ with $x = 2/3$.^[1]

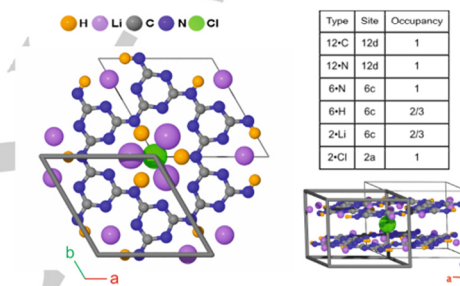


Figure 1. Structure solution of PTI/LiCl according to Wirthner et al. within space group $P6_3cm$. The Wyckoff positions together with the occupancy are given in the table (top right). For further crystallographic data refer to SI chapter 1. Projection of one layer with chlorine shifted out of plane in c direction by $1/4$ (left) and side view on the unit cell (right).

As for many graphitic carbon nitride materials, PTI/LiCl is a medium band gap semiconductor with a flat signature due to its layered character.^[7] Additionally, the electrochemical potential for the hydrogen electrode is positioned between valence and conduction band.^[8] This allows for an efficient hydrogen evolution from water under irradiation with visible light.^[8,9] The corresponding activity is comparable or exceeds the one observed for other CN materials.^[9,10] Furthermore, the LiCl and hydrogen content can be varied, with the latter controlling the amount of excess lithium in the structural cavities.^[7,8] Both effects seem to have a significant influence on the photocatalytic activity. This observation is supported by a study combining X-ray and electron loss spectroscopies with quantum mechanical calculations on DFT level revealing a correlation between the Li⁺ and Cl⁻ ion content and the size of the band gap.^[7] Since both ions influence the band gap individually, a low Li⁺ content, while maintaining full Cl⁻ loading, is expected to improve the hydrogen evolution reaction.^[7] We sug-

FULL PAPER

gest that this effect is connected to changes in the electron density of the framework upon protonation or deprotonation. Consequently, the lacking knowledge of the H/Li substructure prevented the development of structure property relations, thus hindering a tailored band gap design.

Despite of the quantum mechanical calculations,^[7] the most obvious indications for the H/Li disorder are revealed by the ¹³C and ¹⁵N MAS solid-state NMR (SSNMR) spectra already obtained by Wirnhier et al.^[1] While the crystallographic structure solution consists of only one carbon and two nitrogen atoms (Figure 1) the spectral signatures point to three carbon sites with equal multiplicities and at least five nitrogen sites – three nonprotonated and two protonated ones. The discrepancy between the X-ray powder diffraction and the SSNMR spectroscopic data might be understood by two fundamentally different scenarios. Either the split positions for H and Li (Figure 1) are a consequence of a lower symmetry resulting in an ordered scenario with as superstructure or the disorder is an intrinsic feature of the PTI/LiCl leading to a stochastic occupation of H⁺ and Li⁺ within the framework cavities.

Since both scenarios will influence the band structure and thus the macroscopic properties of PTI/LiCl in different ways, we focus on unravelling the H/Li substructure of the title compound for this work. Lithium, as well as hydrogen, are lightweight atoms and any attempt to resolve the H/Li disorder by X-ray powder diffraction failed due to the low scattering forces of both elements compared to the framework atoms. However, similar problems were solved successfully recently, relying on NMR crystallographic strategies.^[11,12] In this way the structures of cyameluric acid,^[13,14] melem^[2,15,16] and melon^[3,17] were unraveled showing that the N-H...N hydrogen bond network is the main driving force for the crystallization in all cases.

For resolving the H/Li disorder of PTI/LiCl, we rely on 1D and 2D multinuclear SSNMR experiments to derive chemical units, their connectivity pattern, as well as quantitative information based on heteronuclear dephasing experiments. In particular, hydrogen and lithium with their large gyromagnetic ratios and high natural abundances pose a main advantage for the structure solution. To be able to assign and interpret the NMR data, additionally, structure predictions and modelling on DFT level were carried out. To exclude modulations within the chemical composition of different crystallites and to determine the real structure, structure solutions based on automated diffraction tomography (ADT) and analyses of the pair distribution function (pdf) were used. Although the combination of X-ray diffraction and NMR spectroscopy is widely used nowadays, the combination of the here presented techniques for structure solution has not been reported so far. Nevertheless, in our case, only by combining these three techniques finally the H and Li substructure could be probed.

Results and Discussion

1D and 2D NMR Spectra of PTI/LiCl

PTI/LiCl was ¹⁵N-enriched starting from ¹⁵N-dicyandiamide according to the synthesis described by Wirnhier et al.^[1] The enriched sample was characterized using EA, PXRD, and SSNMR

spectroscopy. EA and PXRD data are similar to the ones published, therefore support the successful synthesis of PTI/LiCl and are discussed in more detail in the experimental part and in the SI chapter 2.

We recorded 1D ¹H, ¹³C, ¹⁵N and ⁷Li MAS NMR spectra. The ¹H spectrum displays two well-resolved proton signals at about 8 ppm (H¹) and 11 ppm (H²) with an intensity ratio of 1:1 (Figure 2a). The ¹³C and ¹⁵N CP MAS spectra (Figure 2b and c) exhibit the same characteristics as described by Wirnhier et al.^[1] Three different carbon signals in the shift range of triazine carbons, at 158 (C¹), 162 (C²), and 168 ppm (C³), which have equal intensities, derived from a spectrum with direct excitation (Figure S2 (left), Table S1). The ¹⁵N signals are split into two groups: two sharp lines at -250 ppm and -242 ppm corresponding to two NH groups (N¹H and N²H) and a broad signal at around -180 ppm representing tertiary nitrogen atoms (N_{tert}) assigned by Wirnhier et al.^[1] For the here presented sample their intensity ratio (NH:N_{tert}) is 1:3.55 (from single pulse experiment, Figure S2 (right), Table S1), which is well in agreement with the previously reported ratio for PTI/LiCl.^[1] In the ⁷Li MAS spectrum only one resonance including sidebands, with a shift of 0.8 ppm was detected and deconvolution yields a quadrupolar coupling constant of 180 kHz and an asymmetry parameter of 0.8.

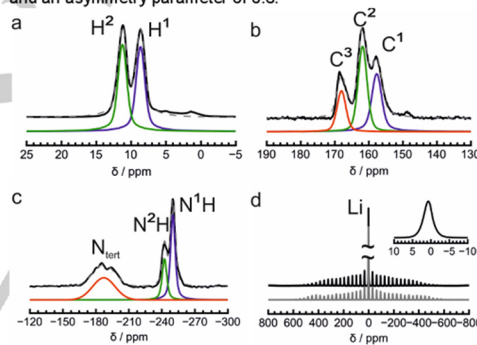


Figure 2. 1D SSNMR MAS spectra of PTI/LiCl a) ¹H Hahn-echo at 20 kHz b) ¹³C cross-polarization (CP) at 10 kHz. c) ¹⁵N CP at 6 kHz, and d) ⁷Li single pulse at 5 kHz. The experiment is plotted in black, the profile of the refinement in grey, and the individual resonances of the refinement in colour.

To determine connectivities 2D SSNMR correlation spectra were recorded (Figure 3) and a connectivity pattern is derived (Scheme 1). Depending on the experiment, hetero- or homonuclear correlations are depicted. The pulse sequences and mixing times were chosen, so that only the relevant structural features, e.g. direct bonds (Scheme 1, black lines), are displayed.

Therefore the ¹H-¹⁵N HETCOR spectrum (Figure 3a) was recorded using a PRESTO-II^[18] pulse sequence to display directly bonded NH groups selectively. Consequently, it is only plotted in the shift range of the NH groups. The two different NH signals correlate with two different proton signals and give rise to two

FULL PAPER

main correlation peaks demonstrating the connectivities N^1H-H^1 and N^2H-H^2 .

As known from the crystallographic solution the only direct bonds, besides NH, are CN bonds, which are probed using a ^{15}N - ^{13}C HETCOR spectrum (Figure 3b) recorded with an *i*DCP pulse sequence.¹⁹⁾ C^1 exhibits a correlation peak with N^2H and N_{tert} , whereas C^2 correlates to N^1H and N_{tert} resulting in two $(NH)_x-C-(N_{tert})_y$ groups with $x+y=3$. The third carbon signal C^3 does not have a correlation peak with any NH, only with N_{tert} giving $C^3-(N_{tert})_3$.

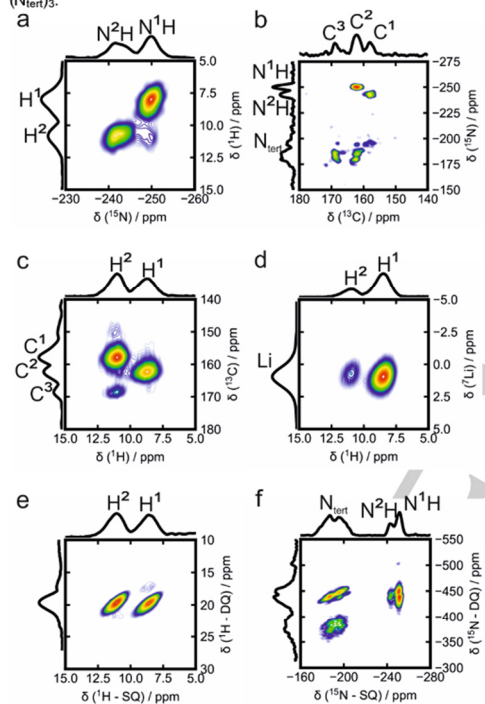


Figure 3. 2D SSNMR spectra of PT/LiCl. a) 1H - ^{15}N PRESTO-II with $\tau_{rec} = 107 \mu s$ b) ^{15}N - ^{13}C *i*DCP with $\tau_{rec} = 2 ms$ c) ^{13}C - 1H HMQC with $\tau_{rec} = 448 \mu s$ d) 7Li - 1H HMQC with $\tau_{rec} = 96 \mu s$ e) 1H - 1H DQ-SQ with $\tau_{rec} = 50 \mu s$ f) ^{15}N - ^{15}N DQ-SQ with $\tau_{rec} = 6 ms$.

Besides direct bonds also spatial proximities between 1H and ^{13}C or 7Li (Scheme 1, orange dashed lines) are detected using a *D*-HMQC²⁰⁾ pulse sequence as the sensitivity is enhanced, due to indirect detection.

The 1H - ^{13}C correlation spectrum (Figure 3c) shows two main peaks (C^1-H^2 and C^2-H^1) and an additional weak correlation of C^3-H^2 . This is well in agreement with the correlations described before, as C^1 and C^2 correlate with N^1H and N^2H , whereas C^3 only correlates to N_{tert} . This indicates a proton rich environment or

short C-H distances for C^1 and C^2 and a proton poor environment or long C-H distances for C^3 . This supports the CP measurements by Wirnhier et al.¹¹⁾, which suggested that C^3 does not have protons nearby.

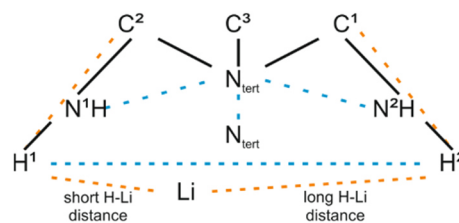
The 7Li - 1H HETCOR spectrum (Figure 3d) displays a correlation signal for both protons with lithium. At a mixing time of $96 \mu s$ the H^2 -Li correlation is less pronounced, whereas at longer recoupling time ($704 \mu s$) the intensities of both signals interchange (Figure S3). This suggests a different lithium environment for the two protons with H^1 displaying a shorter H-Li distance or less atoms in the vicinity.

To get an idea about homonuclear correlations, 1H - 1H and ^{15}N - ^{15}N DQ-SQ spectra (Figure 3e and f) were recorded using symmetry based pulse sequences²¹⁾ with the advantage to also gain information about self-correlations (Scheme 1, blue dashed lines). The 1H - 1H DQ-SQ spectrum with a short DQ build-up time ($50 \mu s$) only shows the cross correlation peaks between H^1 and H^2 . At longer mixing time ($225 \mu s$, Figure S4) the self-correlation peaks are developed as well. Therefore, a short distance is derived for H^1 - H^2 , whereas the H^1 - H^1 and H^2 - H^2 distances are expected to be significantly longer.

The ^{15}N - ^{15}N DQ-SQ spectrum (Figure 3f) displays a self-correlation peak for N_{tert} , and strong cross correlation peaks between NH and N_{tert} . The self-correlation peaks of the NH groups are almost invisible. Due to the known network structure, the spatial proximity of NH and N_{tert} as well as of N_{tert} and N_{tert} is almost inevitable, whereas the absence of the self-correlation of the NH groups adds valuable knowledge as it excludes neighboring NH groups in the structure and therefore $(NH)_x-C-(N_{tert})_y$ is restricted to $x=1$ and $y=2$.

All connectivities are summarized schematically in Scheme 1. There are two different directly bonded N_{tert} -C-NH-C- N_{tert} patterns, which have different H-Li distances (N_{tert} - C^2 - N^1H - C^1 - N_{tert} and N_{tert} - C^1 - N^2H - C^2 - N_{tert} , indicated by black lines in Scheme 1). Additionally, both show spatial proximities within the pattern, whereas between the two groups the protons are close, and the nitrogen atoms are not.

There are several ways to fit this structure fragment in the framework (Figure S5), which cannot be distinguished by the presented NMR experiments. To address this uncertainty, computational modelling is carried out in a next step.



Scheme 1. Schematic connectivity patterns for PT/LiCl derived from 2D SSNMR spectra. Black lines indicate direct bonds, whereas orange dashed lines indicate heteronuclear and blue dashed line homonuclear spatial proximities.

FULL PAPER

Model Building

Based on the information derived from 1D and 2D SSNMR spectra and the structure of the network, several structure models were developed. Two main scenarios are possible (Figure 4): homogeneous models in which two protons and two lithium ions share one cavity and heterogeneous models in which one cavity hosts four protons, another four lithium ions. All models are labelled with three numbers, the first and second being the number of unitcells along *a* and *b* direction, the third, standing for the number of layers within the model.

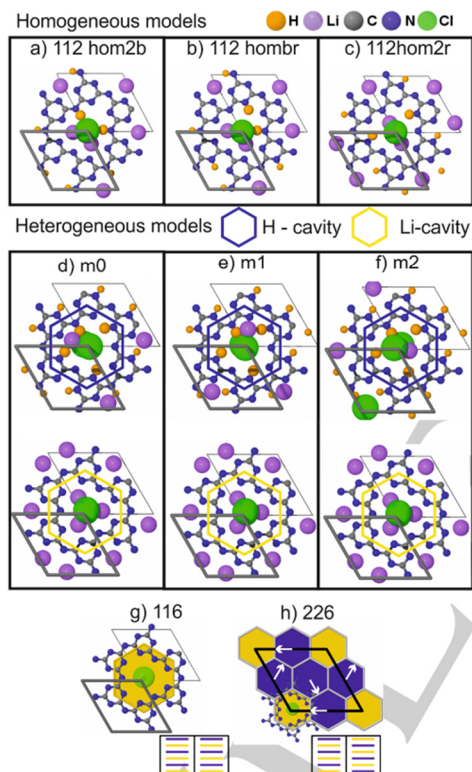


Figure 4. Overview over the structure models within this work. For each model, only one layer is shown. a)-c) The three homogeneous models with two bridge nitrogen atoms protonated a), protonation of one bridge and one ring nitrogen b), and two ring nitrogen atoms protonated c). d)-f) The three possible pairs of H-Li cavities and their arrangement within the layer (g) and h)) (for more details refer to the main text).

Within the class of homogeneous models, we present three different two-layer models. The first one, similar to the one which has been published beforehand^[7], exhibits two protons bound to two bridging nitrogen atoms (N_b) (model 112 hom2b). The second

one features one proton bound to N_b , the other one to a ring nitrogen (N_r) (model 112 hombr) and consequently, in the third model, both protons are bound to N_r (112 hom2r). Within each class of models, the proton positions are derived from DFT calculations. Therefore all possible models for one layer of the two were built and the structure of the energetic minimum was used (analogously as presented in reference [22]). Subsequently, preferable positions for the lithium atoms for all models were found by quantum chemical geometry optimizations. All homogeneous models are constructed in a way that the arrangement of proton and lithium positions within the cavities of the second layer is turned by exactly 180° . This is necessary to minimize the residual dipole moment within the structure, mainly due to ionic bonds. For the models 112 hom2b and 112 hom2r the lithium environment for both protons is the same. This is, as discussed before, not well in agreement with the 2D ^7Li - ^1H HETCOR spectra. Although they seem less likely, they cannot be excluded by just one method. Additionally, they are the most prominent representatives of the class of homogeneous models and therefore will be discussed further.

Further possibilities to design models with the predicted different H-Li environments are heterogeneous models. These are constructed in a way that they have a separation of protons and lithium resulting in protonated and lithiated cavities. For the protonated cavities, four protons have to be placed. Again all possible permutations within one cavity were built. Then, the energies were derived based on DFT calculations^[22] and the structure of the energetic minimum was used for protonated cavities. The protonated cavities have three protons bound to N_r ($N_r\text{H}$) and one to N_b ($N_b\text{H}$). All other combinations (2 $N_r\text{H}$ and 2 $N_b\text{H}$ or 1 $N_r\text{H}$ and 3 $N_b\text{H}$) were energetically less favored.

In the lithium cavity the positions of three of the four lithium atoms are derived from the structure solution by Wirnhier et al.^[1] and are stable during geometry optimizations. The fourth lithium atom was placed between two of the three lithium in *a/b* and set halfway between the layers, consequently giving three starting models. On these three models, a geometry optimization was performed giving three structures: m0, m1, and m2 (Figure 4d-f). For m0 and m1 the lithium maintained the position between the two layers along *c* and relaxed only slightly within *a/b*. In model m2, the lithium moved into the CN-layer, as there is more space beneath the lithium within the layer than in m0 and m1, due to the asymmetric protonation pattern.

These protonated and lithiated cavities were combined in two different ways (Figure 4g, h). First, in the 116 model one layer is fully protonated, while the other is fully lithiated. In this model, it is not possible to minimize the residual dipole moment within two layers. To achieve this, a threefold supercell structure along the *c*-axis has to be constructed with a 120° turn between the 112 unitcells resulting in six-layer models. Second, the 226 model, which has protonated and lithiated cavities within one layer. This is realized by constructing a supercell also along *a* and *b* (Figure 4i). In this model, a minimization of the dipole moment within the layer is possible by turning the cavities within *a/b*. This is indicated by the arrows. To fulfil charge compensation and stoichiometric requirements two layers always feature an inverse number of protonated

FULL PAPER

and lithiated cavities (Figure 4h, i, inset). As there is only one protonated cavity in the inverse layer to Figure 4h, a dipole moment remains in every second layer, which again makes a six-layer model with 120° turns inevitable.

Upon geometry optimization, a slight displacement of atoms along *c* with a standard deviation below 0.1 Å is observed, which is attributed to interactions of N-H groups with incorporated chlorine anions (for further information see SI chapter 5).

A subsequent symmetry search for all models with a maximum atom deviation of 0.3 Å yields triclinic, monoclinic, orthorhombic, and trigonal space groups (Table S3). The *a* and *b* axis vary between 8.424 and 8.513 Å for 11x models and slight deviations of the ideal angles up to 2% were observed, which result from geometry optimization in P1 (Table S3).

Model Evaluation

Energetic Considerations

The energy ranking for all geometry-optimized structures discussed until now is shown in Figure 5. The lithium position within the layer (m2) is preferred over the lithium position between the layers (m0, m1) for both 116 and 226 models. In addition, homogenous models are preferred energetically. We will regard the five models having the lowest energy, leaving 112 hom2b, 112 hombr, 112 hom2r, 116 m2, and 226 m2 for further discussion.

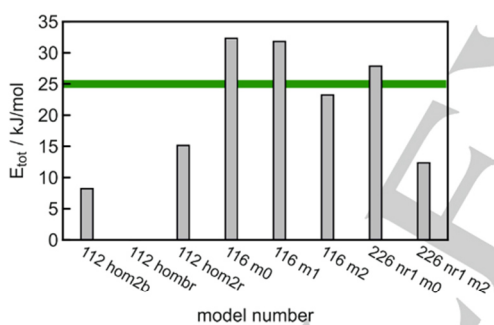


Figure 5. Energy ranking of different models. The values are presented in Table S4.

To evaluate these models, we chose a combined approach of several methods, as one method only resolves a separate piece of the whole picture. The combination is based on a cost function with an individual figure of merit for each method.

Therefore, a figure of merit for the energy is defined in accordance with Materials Studio® 5.0.

$$R_{Energy} = \tanh\left(0.3 \frac{E - E_{min}}{E_{tol}}\right) \quad (1)$$

with E_{tol} set to 25 kJ/mol, $E_{min} = E(112 \text{ hombr})$ and the prefactor set to 0.3 to fit to observed error ranges of all methods. The resulting *R*-values for the five models are presented in Table 1.

Chemical Shift Calculations

As a priori shift assignment of those complex models is not possible, chemical shift calculations were carried out, based on the quantum mechanical simulations. Though these allow for a shift assignment of the individual models, a joint assignment for all models is not possible. Consequently, to be able to compare the experimental spectra with the calculated shifts, it is required to calculate an envelope, based on a Pseudo-Voigt profile for each shift. The full widths at half maximum (FWHMs) were estimated by deconvoluting the experimental 1D ¹H, ¹³C, and ¹⁵N spectra to 1.5 ppm (¹H), 2.5 ppm (¹³C), and 6.0 ppm (¹⁵N), respectively. Assuming a similar T_2 for all chemical units within the sample, these FWHMs were applied for all resonances. The spectra and the envelopes for the five models are shown in Figure 6.

For the ¹H and ¹³C spectra, the envelope of 112 hombr fits quite well to the experiment. In addition, the model 226 m2 matches, although missing the resolution and being shifted about 2 ppm for ¹H. Moreover, for ¹³C the spectral width is too broad. All other models lack one signal in each spectrum, and therefore do not reproduce the spectral features. For the ¹⁵N spectrum, the picture is slightly different. Besides model 112 hombr, 112 hom2r fits nicely, whereas the shift range for N_{int} of 226 m2 is far too broad. To quantify the results again, a figure of merit for the shift calculations is defined. In this case, it is based on the deviation of the experimental and the calculated spectrum using the *rmsd*.

$$R_{x_{shift}} = rmsd = \sqrt{\frac{\sum_i (exp_i - sim_i)^2}{\sum_i (exp_i)^2}} \quad (2)$$

The resulting values are displayed in Figure 6 (right) and support the discussion above.

FULL PAPER

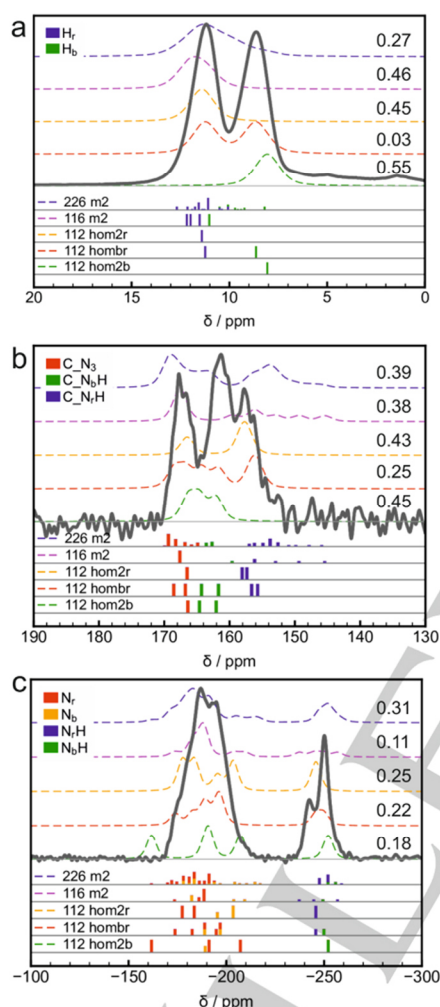


Figure 6. Comparison of quantitative 1D SSNMR spectra with the chemical shift calculations for the five models. a) ^1H ^{13}C and c) ^{15}N . The R_{xy} -values are displayed on the right side of each spectrum.

Distance Measurements

As we strive to determine the lithium and proton positions within the well-known CN-framework, distance measurements seem to be a promising approach. Hence, in general any distance information between the nuclei with uncertain (^1H , ^7Li) and certain (^{13}C ,

^{15}N) positions or between the nuclei with uncertain positions is relevant.

We restricted ourselves to the combination ^7Li - ^1H and ^7Li - ^{13}C for the following reasons. (a) In comparison to ^1H , there is only one ^7Li signal, whereby a restriction to a series of 1D spectra for combinations with lithium is feasible. For combinations with ^1H (e.g. ^1H - ^1H or ^1H - ^{13}C), a series of 2D spectra would have to be acquired. As there is no joint shift assignment for all models, the evaluation would be more complex and therefore time-consuming. (b) Compared to ^7Li - ^{13}C , ^7Li - ^{15}N couplings are weaker by about a factor of 2.5. As the CN-network structure is well defined, they are not expected to contribute additional insights. Leaving ^7Li - ^1H and ^7Li - ^{13}C for evaluation.

These selected heteronuclear combinations were examined using rotational-echo double-resonance (REDOR) giving dephasing curves whereby distance sums are accessible. The resulting dephasing curves are shown in Figure S9. For the $^1\text{H}\{^7\text{Li}\}$ REDOR, the signal at 8 ppm exhibits a faster dephasing than the one at 11 ppm, indicating a stronger coupling and consequently a shorter distance sum to Li. This is well in agreement with the 2D ^7Li - ^1H HETCOR spectra discussed before. For the $^{13}\text{C}\{^7\text{Li}\}$ REDOR, the differences between the three signals are smaller. Whereas the signal at 162 ppm shows the slowest dephasing, the signals at 158 and 168 ppm exhibit a faster dephasing with a similar trend, and in conclusion, have a denser lithium environment.

To allow for a matching of the experiments with the quantum chemical models, SIMPSON simulations were carried out (for parameters and convergences see experimental details and SI chapter 8). A REDOR curve for each ^1H or ^{13}C atom of the examined model was simulated including the four nearest lithium, resulting in up to 64 simulations per model.

As there is no common shift assignment for all models, an average curve for the simulations and the measurements were compared. These are, in case of $^{13}\text{C}\{^7\text{Li}\}$, almost the same for all models (Figure S9 (right column)), and therefore do not provide information for the differentiation. This confirms the importance of a correct chemical shift assignment for a meaningful and reliable analysis.

Without a shift assignment, we rely on the individual shifts from quantum chemical calculations and the envelope spectrum, as derived before (Figure 6). However, in this case, it is combined with the SIMPSON simulations to give a simulated, dephased spectrum at every point τ of the REDOR curve (for further details see SI chapter 9). For each τ , the $rmsd^x$ of the calculated to the measured dephased spectrum is extracted (Table S5 and S6). All $rmsd^x(\tau)$ -values of one nucleus were averaged and used as figure of merit (Table 1):

$$R_{shift}^{REDOR} = \overline{rmsd^x} = \frac{1}{N^x} \sum_{i=1}^{N^x} rmsd^x(\tau)_i \quad (3)$$

This approach to evaluate the $^1\text{H}\{^7\text{Li}\}$ and $^{13}\text{C}\{^7\text{Li}\}$ REDOR experiments without a shift assignment already includes the information of ^1H and ^{13}C shift calculations, which makes their individual R_{shift} -values obsolete.

FULL PAPER

Determination of the Structure

In total, four complementary R -values are provided, which are used to determine the structure. They are averaged to yield R_{av} according to the following equation

$$R_{av} = \frac{(R_{Energy} + R_{H_{shift}}^{REDOR} + R_{C_{shift}}^{REDOR} + R_{N_{shift}}^{15N})}{4} \quad (4)$$

An overview of all values is given in Table 1.

Table 1. Overview of all R -values for the cost function.

Model	R_{Energy}	$R_{H_{shift}}^{REDOR}$	$R_{C_{shift}}^{REDOR}$	$R_{N_{shift}}^{15N}$	R_{av}
112 hom2b	0.10	0.43	0.27	0.31	0.28
112 hombr	0.00	0.24	0.24	0.11	0.15
112 hom2r	0.18	0.34	0.54	0.25	0.33
116 m2	0.27	0.33	0.33	0.22	0.29
226 m2	0.15	0.26	0.28	0.18	0.22

Amongst the five models, 112 hombr is found to be the best. It outperforms the second best model by 0.07. The favored model up today, 112 hom2b, has a R_{av} of 0.28 and therefore does not fit to any NMR experiments. Noticeably, while the 112 hombr model is the best in all methods, the order of the other models varies between the methods. This supports the strength of a combined approach of several methods.

Shift Assignment for Model 112 hombr

As the model could be unambiguously derived, within the range of the models, to be 112 hombr, the shifts are assigned on that basis. Therefore the above presented shift calculations (Figure 6) are used. All experimental signals are labelled according to the shift at the maximum of the signal, according to experimental resolution.

The two proton signals at 8 ppm and 11 ppm are assigned to N_bH and N_rH , respectively (Figure 7). For the three carbon shifts, the protonation pattern of the adjacent nitrogen atoms represents the most important structural influence. If none of the three directly bound nitrogen is protonated (C_{N_3}), the carbon is shifted downfield and is therefore, assigned to the ^{13}C signal at about 168 ppm. Protonation of the bound bridging nitrogen, N_b (C_{N_bH}), shifts the carbon signal further upfield, consequently those C atoms are assigned to the signal at 162 ppm. An additional upfield shift is observed for protonation of the adjacent N_r (C_{N_rH}), whereby it is assigned to the signal at 158 ppm. In the ^{15}N shift calculation all N_{tert} exhibit a shift in the range of -160 to -210 ppm, whereas the NH groups are shifted upfield to about -246 ppm (Figure 7). The latter are additionally assigned: N_rH shifts slightly downfield (-242 ppm) compared to N_bH (-250 ppm).

In consequence, this structure realizes two different $N_{tert}-C-NH-C-N_{tert}$ patterns as described by 2D SSNMR spectra, with N_bH and N_rH (Figure S5). Additionally, the shortest $NH-NH$

distance (4.0 Å) is longer than the shortest $N_{tert}-NH$ or $N_{tert}-N_{tert}$ (2.3 Å) distances whereas H_b and H_r have a shorter distance (2.9 Å) than H_b-H_b (5.3 Å) and H_r-H_r (4.6 Å), respectively. Both facts are well in agreement with the information derived from homonuclear 2D DQ-SQ spectra before. In order to confirm model 112 hombr electron diffraction studies are undertaken.

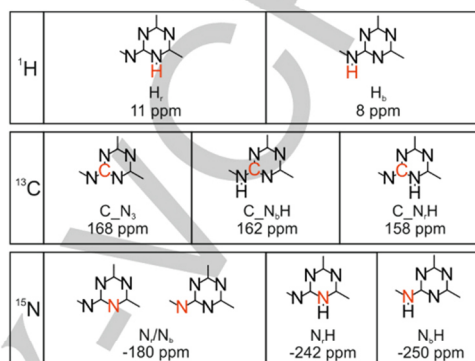


Figure 7. Chemical shift assignment and shift relevant structure fragments. The signals of the experiments are labelled according to the shift at the maximum of the signal, according to experimental resolution.

Electron Diffraction

The use of automated diffraction tomography (ADT), a new developed electron diffraction approach,^[23] delivers 3D diffraction intensities from single nanocrystals suitable for *ab initio* structure determination superior to the beforehand used in-zone data.^[24] The typical problems of oriented electron diffraction patterns, like changes in intensities by dynamical scattering and due to the spike function, are significantly reduced.

The plate-like crystals are oriented in general with the c^* direction of the hexagonal lattice perpendicular to the grid. Two independent ADT data sets are collected from one lying (CR I) and one upstanding crystal (CR II) and reconstructed in three-dimensional diffraction volumes (Figure 8a-d). Both diffraction volumes delivered as expected a primitive hexagonal lattice. Systematic absences (Figure 8e, f) for $l = 2n+1$ reflections of $0kl$ and $h0l$ zone patterns are observable. This observation leads to a c -glide plane orthogonal to a resp. b , which is present in both datasets. In dataset CR I the c^* is not detected. Only the CR II dataset includes the whole information of the $00l$ reflections and the expected screw axis along c could be observed by the absence of $00l$ reflections $l = 2n+1$. Analysis of symmetrically equivalent reflections like 100, 010 and 1-10 indicates the breakdown of the hexagonal symmetry. Even if the extinction rules of $P6_3cm$ are observable in both datasets, a violation through light scattering atoms possibly could not be visible. While the single datasets deliver the published structure in hexagonal $P6_3cm$ the completeness of the collected data is not sufficient for a reliable structure analysis in a

FULL PAPER

monoclinic symmetry. For further investigation, both datasets are merged.

In order to merge the data the chosen indices for the hexagonal case cannot be transformed directly. Apart from three possible choices for the axes a^* and b^* the direction of the c^* -axis needs to be taken into account. Therefore, intensities of data set CR II are taken as extracted and compared to all six possible intensity data sets of CR I after iteration of cell parameters. Intensities of the same hkl are plotted against each other (Figure S11) and linearly approximated by least squares using $y = a^*x$. Apart from Figure S11b the plots show strong scattered data indicating a violation of the hexagonal symmetry. Using data set CR I as basis the missing reflections were taken from CR II, scaled with 5.98, for merging.

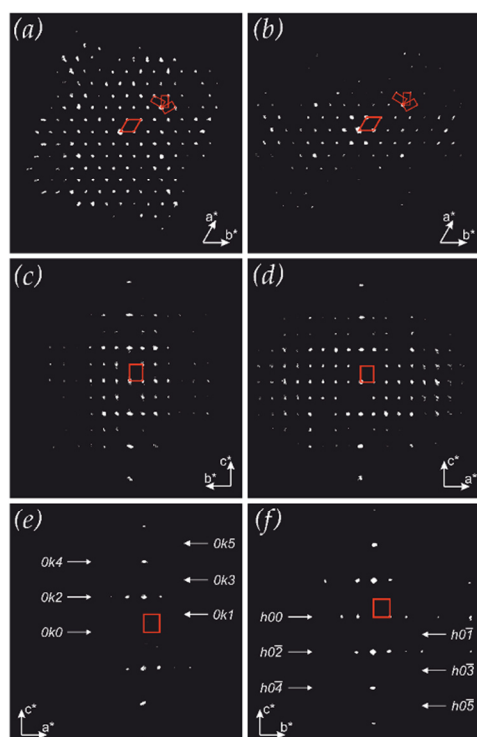


Figure 8. Reconstructed three-dimensional diffraction volumes obtained by ADT data. CR I and CR II reconstructed diffraction volume projected down c^* (a) and (b); CR II diffraction volume projected down a^* (c) and b^* (d). Sector of CR II diffraction volume projected down a^* (e) shows $0kl$, projected down b^* (f) $h0l$ in-zone patterns, where extinctions are marked with arrows and dotted lines. The three possible C-centered orthorhombic cells able to describe the diffraction of CR I and CR II are shown in the upper right corner of (a) and (b).

In general, the structure of PTI is solvable in the hexagonal space group $P6_3cm$. The network of PTI should be still describable with a hexagonal space group. More degrees of freedom for H/Li positions can be assigned by using subgroups as shown in Figure 9.

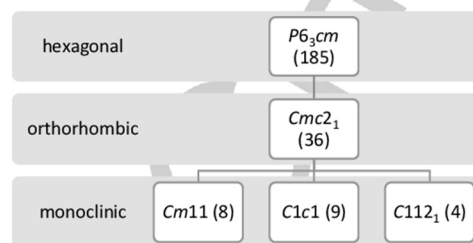


Figure 9. Scheme of possible *translationsgleiche* subgroups of $P6_3cm$ by reducing crystal class excluding trigonal space groups.

In order to use the lowest symmetry including not too many free parameters for structure solution the symmetry is reduced to $P112_1$. Stepping down from hexagonal to orthorhombic symmetry, the lattice points have to be indexed with a centered rectangular cell, as shown in Figure 8. Further reduction leads to a monoclinic crystal system. The space group $C112_1$ was chosen because the change to the primitive lattice with $P112_1$ (unique axis c) symmetry can be performed directly.

Structure solution, shown in Figure 10, with this space group converged to a final residual R_f of 0.150 with an intensity residual R_{int} of 0.166. The potential map shows 16 strong maxima (from 1.76 to 1.27 $e \text{ \AA}^{-3}$) corresponding to the CN network including chlorine.

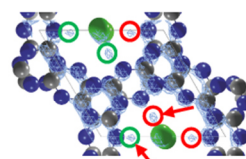


Figure 10. Three-dimensional potential map of structure solution in space group $P112_1$, combined with structure model projected down c^* . Chlorine atoms are represented in green, carbon in grey and nitrogen in blue. The red arrows mark two additional potentials. The projections include two layers. Red circles are $+1/2$ higher in z than green circles.

Two of the next six maxima (from 0.28 and 0.16) are corresponding to reasonable lithium ion positions. A third reasonable position is not obtained, which corroborates a belief of broken symmetry. Four faulty maxima (0.31 to 0.10 $e \text{ \AA}^{-3}$) show very high Debye-Waller factors ($U_{iso} = 0.74$ and 0.68 \AA^2) and/or chemically unreasonable atom positions. In a subsequent symmetry search, $C222_1/Cmc2_1$ is found with a maximum atom deviation of 0.20.3 \AA (for further information see SI chapter 10).

FULL PAPER

By selecting the higher detected symmetry, with its smaller parameter set, it is reasonable to use the non-merged data as well for structure solution. All three possibilities for cell transformations, as indicated in Figure S13, led to a structure solution. For both, CR I and CR II data, one of the three transformations proved best

structure solutions in both space groups (Table 2) supporting again the symmetry reduction.

All four structure solutions confirm the location of two lithium ions per cavity, four per two layers respectively (Figure S13).

Table 2. Experimental ADT details and crystallographic information.

c System	merged data		unmerged data		
	CR I and CR II		CR I		CR II
Experimental details					
Tilt range (°)	-40/+40 & -60/+60		-40/+40		-60/+60
No. of total sampled reflections	1651		668	697	1215
No. of independent reflections	581		175	184	280
Resolution (Å)	0.9		0.9	0.9	0.9
Independent reflection coverage (%)	92		50	50	82
R_{sym}	16.6		15.1	15.3	23.0
Overall U (Å ²)	0.046		0.038	0.036	0.053
Residual $R(F)$ (SIR2014)	0.150		0.092	0.104	0.136
Reflections/parameter ratio	4.6		2.75	2.91	4.4
Crystallographic information					
Space group	$P112_1$	$Ccm2_1$	$C222_1$	$Ccm2_1$	$C222_1$
a (Å)	8.468	8.468	8.468	8.468	8.468
b (Å)	8.468	14.6670	14.6670	14.6670	14.6670
c (Å)	6.750	6.750	6.750	6.750	6.750
α (°)	90	90	90	90	90
β (°)	90	90	90	90	90
γ (°)	120.0	90	90	90	90
No. of independent atoms	18	10	10	10	10

Structure Refinement

As electron diffraction revealed an orthorhombic cell with two lithium ions per cavity, model 112 hombr was setup orthorhombically to give model 112 o hombr I (Figure 11a). A symmetry search of the geometry-optimized structures, using Materials Studio 5.0 with a maximum atom deviation of 0.3 Å, consistently yields $P2_1/m$ for the hexagonal, as well as for the orthorhombic setup.

Nevertheless, from electron diffraction, we still could not derive hydrogen positions. As NMR spectroscopy is sensitive to hydrogen, consequently, a second model 112 o hombr II (Figure 11b) was designed and studied. Therefore, the second cavity within the orthorhombic cell, centered at $[1/2, 1/2, 0]$, is mirrored along the b -axis, compared to the cavity centered at $[0, 0, 0]$. Again, the second layer is constructed as described for all 112 models, which means that each cavity in the second layer is rotated by 180° compared to the first layer to minimize the residual dipole moment. On the geometry-optimized structure, again a symmetry search was performed, resulting in space group $P2_12_12_1$, which is in agreement with the space group from electron diffraction ($C222_1$) only that the C-center is broken.

Both models have a very similar energy. Additionally, the chemical shift calculations only allow a discrimination of models with different chemical groups. Within the chemical groups, the variation of the shifts is below the accuracy of about 2 ppm. However, this allows us to apply the chemical shift assignment derived before for both models.

Therefore, a shift-assigned analysis of $^1\text{H}\{^7\text{Li}\}$ and $^{13}\text{C}\{^7\text{Li}\}$ REDOR is possible. Again, an individual REDOR curve of each atom was simulated, but this time they were sorted according to the shift assignment and averaged within each chemical group (i.e. H_r and H_b or $\text{C}_{\text{N}_3\text{H}}$, C_{NH} and C_{N_3} , respectively). This results in one simulated curve for each measured curve and therefore, the $rmsd$ for each curve is calculated (Table S8, S9). The final R_X -value is then the sum of the $rmsd$ of each experimentally determined build-up curve for the REDOR experiment X (Table 3). Both experiments favor model 112 o hombr II as the R -values are lower. In the $^{13}\text{C}\{^7\text{Li}\}$ REDOR (Figure 11) this can be seen qualitatively as well. For both models the curve for C_{N_3} match nicely, whereas 112 o hombr II also resolves the trend of the remaining two curves, strongly suggesting different protonation patterns in neighboring cavities.

This is further corroborated by ^1H - ^{13}C CP build-up curves, as they are a very sensitive long-range probe to determine the proton substructure if the carbon positions are well known and the chemical shifts are assigned.^[16] The ^1H - ^{13}C CP build-up curves (Figure S15) reveal, as already suggested from the 2D spectrum, two different environments. The signals at 158 and 162 ppm have a faster build-up than the third at 168 ppm. This confirms a proton rich environment for these carbon atoms. The oscillation at short build-up times indicates at least one dominating short distance, which we attribute to the C-NH group with a ^1H - ^{13}C distance of approximately 2 Å.

FULL PAPER

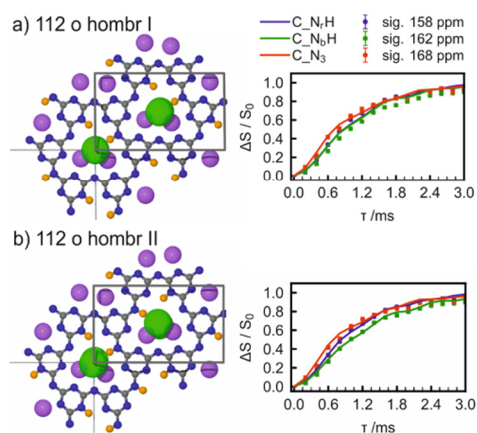


Figure 11. Structure and $^{13}\text{C}\{^7\text{Li}\}$ REDOR curves with signal assigned averaged simulations of the models used in the refinement. Experiments are marked with round symbols with error bars whereas the simulated curves are indicated with lines. a) model 112 o hombr I and b) model 112 o hombr II.

Exemplarily, the CP-build up curve for the signal at 158 ppm was fitted with 2 Å implementing the analytical description according to Peng Li et al. and Hawkes et al.^[25,26] The fit reveals that the dipole coupling is underestimated by about 50% if only this short distance is taken into account (Figure S16). Consequently, we rely on the simplest kinetic case^[18,27] to include many contributing I-S distances as described in the Experimental Section. Evaluation yields a R_{CP} -value for each model (Table 3). The ^1H - ^{13}C CP build-up supports the findings of the REDOR evaluation. The model 112 o hombr II with a R_{CP} of 0.07 fits better than 112 o hombr I (0.10).

Table 3. R -values for $^1\text{H}\{^7\text{Li}\}$ REDOR, $^{13}\text{C}\{^7\text{Li}\}$ REDOR and ^1H - ^{13}C CP build-up for the models of the structure refinement.

Model	$R_{^1\text{H}\{^7\text{Li}\}}$	$R_{^{13}\text{C}\{^7\text{Li}\}}$	R_{CP}	R_{av}
112 o hombr I	0.10	0.09	0.10	0.10
112 o hombr II	0.09	0.07	0.07	0.08

Overall, all quantitative methods favor model 112 o hombr II. Therefore, the original proposed structure model 112 o hombr I could be further refined. The resulting model 112 o hombr II, has a $P2_12_12_1$ symmetry, with $a = 14.558 \text{ \AA}$, $b = 8.603 \text{ \AA}$, and $c = 6.705 \text{ \AA}$ (the cif-file is shown in the SI chapter 13). There are two lithium, two hydrogen, six carbon, and nine nitrogen sites within the asymmetric unit without any partial occupancies, explaining 1D ^1H , ^{13}C , and ^{15}N NMR spectra.

Pair Distribution Function

Conclusion

We resolved the H/Li substructure of poly (triazine imide)/LiCl (PTI/LiCl) by a new NMR crystallographic strategy, combining NMR spectroscopy and chemical modelling with electron diffraction and the analysis of the pair distribution function.

Structure models were designed based on information of 1D ^1H , ^{13}C , ^{15}N and ^7Li MAS SSNMR spectra and homo- and heteronuclear 2D correlation experiments. The resulting models were evaluated by combining energy and shift calculations with $^1\text{H}\{^7\text{Li}\}$ and $^{13}\text{C}\{^7\text{Li}\}$ REDOR distance measurements using a cost function.

The derived structure model was confirmed by electron diffraction. With ADT it was possible to measure diffraction tilt series of two different orientated nm-sized crystals. Through intense analysis of the reconstructed three-dimensional diffraction volume and merging of two datasets, a significant absence of hexagonal symmetry was demonstrated. This could be confirmed by *ab initio* structure solution in an orthorhombic C-centered setting with two independent datasets, which revealed two lithium positions per cavity. However, electron diffraction only revealed the lithium and not the hydrogen positions. Therefore, the protonation pattern was subsequently refined on two orthorhombic models using NMR distance measurements, revealing a broken C-center. The resulting structure, 112 o hombr II, has a $P2_12_12_1$ symmetry with the lattice parameters $a = 14.56 \text{ \AA}$, $b = 8.60 \text{ \AA}$ and $c = 6.71 \text{ \AA}$. One proton is bound to a bridging nitrogen atom, whereas the second one is bound to a triazine ring nitrogen. Each of the two lithium ions is stabilized by two nitrogen atoms of two triazine rings. Additionally the analysis of the pair distribution function revealed a buckling of the framework with a coherence length below 4 nm, which is triggered by the local dipole moments.

In conclusion, it could be demonstrated that the H/Li substructure of PTI/LiCl could be resolved only by the combination of these methods. Whereas electron diffraction provides symmetry information, NMR crystallography allows resolving the hydrogen positions. The consistency of the structures derived from electron diffraction and NMR spectroscopy is demonstrated in Figure 12. Analysis of the pair distribution function adds information about buckling on a nanometer length scale. Therefore, each method contributes with its individual strength to resolve a complex structural problem.

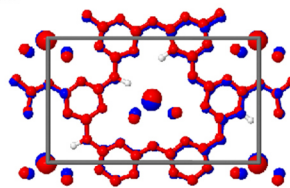


Figure 12. Superposition of the structure solved in $C222$, by electron diffraction (blue) and in $P2_12_12_1$, by NMR spectroscopy (red).

FULL PAPER

Experimental Section

Synthesis. The ^{15}N -enriched sample was synthesized according to the procedure described by Wirnhier et al.^[11] ^{15}N -dicyandiamide was heated in a LiCl/KCl salt melt in a two step procedure. The washed product was characterized using elemental analysis, powder X-ray diffraction (PXRD) and solid-state NMR spectroscopy (SSNMR). Elemental analysis (%): Wirnhier et al.: C 29.6, H 1.3, N 50.4, Cl 11.0, Li 4.6, this work: C 28.4, H 1.2, N 50.3, Li 4.6. PXRD is shown in Figure S1. NMR spectra are shown and discussed in the main part of the paper.

Solid-state NMR experiments. All SSNMR measurements were carried out on an Avancell 300, an Avancell HD 400, an Avance 500 or an Avancell HD 600 SSNMR spectrometer (Bruker). All measurements were conducted using standard double or triple resonance probes (Bruker) at room temperature and were referenced relative to TMS (^1H , ^{13}C), nitromethane (^{15}N) and a 1M LiCl solution (^7Li), respectively. The spectrometers have a B_0 field of 7.1, 9.4, 11.7 and 14.1 T, respectively. During acquisition of all ^{13}C and ^{15}N spectra proton decoupling was applied using a SPINAL64^[28] sequence and a RF field of 70–100 kHz. All 2D spectra were recorded using States-TPP1 for quadrature detection in the indirect dimension, except the ^1H - ^1H DQ-SQ and the ^1H - ^{15}N HETCOR spectra which were recorded using the States method.^{[29],[30]} The recycle delay for all experiments, which depend on proton relaxation, was chosen between 3 s and 10 s dependent on the B_0 field.

1D experiments. 1D ^1H measurements were recorded at a Larmor frequency (ω_0) of 600 MHz with a single pulse or Hahn-echo pulse sequence under magic-angle spinning (MAS) using a 1.9 mm rotor and a spinning frequency of 20 kHz. 1D ^7Li measurements were recorded on all spectrometers in different rotors, spinning between 5 kHz and 20 kHz using a single pulse experiment. ^1H - ^{13}C and ^1H - ^{15}N ramped-amplitude (RAMP)^[31] cross-polarization (CP)^[32] MAS experiments were carried out at $\omega_0(^1\text{H}) = 300$ MHz. The sample was contained in a 4 mm ZrO_2 rotor spinning at 10 kHz and 6 kHz, respectively. For ^1H - ^{13}C CP the RF field of ^1H was linearly varied about 50% during a contact time of 4 ms, whereas a square pulse of 8 ms was used for the ^1H - ^{15}N CP block. ^{13}C and ^{15}N single pulse experiments were recorded at $\omega_0(^1\text{H}) = 400$ MHz or 600 MHz using 4 mm and 1.9 mm rotors at a spinning speed of 10 kHz, respectively. The recycle delay was set to 600 s for the ^{13}C and 900 s (using a 45° pulse) for the ^{15}N measurement.

2D experiments. ^{13}C - ^1H and ^7Li - ^1H HETCOR experiments with inverse detection (F2: ^1H) were recorded at $\omega_0(^1\text{H}) = 600$ MHz in a 1.3 mm rotor spinning at 62.5 kHz using a D-HMQC pulse sequence.^[33] To transfer polarization between the nuclei the supercycled symmetry based SR4_r² sequence was applied.^[34] As the quadrupolar moment of ^7Li is quite small (<200 kHz), strong 90° pulses (RF field ~230 kHz) were used to excite the whole spectrum. For both spectra, the t_1 evolution was rotor synchronized using a dwell time of 128 μs . For the ^1H - ^{13}C spectrum, a recoupling time of 448 μs was chosen and for the ^1H - ^7Li HETCOR the recoupling time was set to 96, 320 and 704 μs . The ^1H - ^{15}N HETCOR experiment was recorded with direct detection (F2: ^{15}N) at $\omega_0(^{15}\text{N}) = 61$ MHz using a PRESTO-II pulse sequence^[18] in a 4 mm rotor spinning at 12.5 kHz. The applied symmetry based R-sequence^[21] is R18_r⁷ using 180° pulses in the R-block. The recoupling time was 107 μs . For the 2D ^{15}N - ^{13}C HETCOR experiment the DCP pulse sequence was applied as published.^{[17],[19]} For the measurement a 4 mm triple resonance probe was used, MAS with 10 kHz was applied and ^{13}C ($\omega_0 = 75$ MHz) was directly detected. For the first contact (^1H - ^{15}N) a contact time of 20 ms with a ramped pulse on ^1H was used. For the ^{15}N - ^{13}C contact an overall contact time with a square pulse of 2 ms was chosen. For the first half of the second contact the RF field was set to 35 kHz for ^{15}N and to 25 kHz for ^{13}C . For the second half, the RF fields were switched, and the phase was changed by 180°. During the second

CP (^{15}N - ^{13}C) contact, a continuous-wave (cw) decoupling of 100 kHz was applied on ^1H . ^1H - ^1H and ^{15}N - ^{15}N double-quantum-single-quantum (DQ-SQ) correlation spectra were recorded at $\omega_0(^1\text{H}) = 500$ MHz in a 2.5 mm rotor spinning at 26.666 kHz and at $\omega_0(^{15}\text{N}) = 30$ MHz in a 4 mm rotor spinning at 8 kHz, respectively. A rotor-synchronized symmetry based R-sequence^{[34],[21]} R12_r⁵ and SR18_r⁷ in a excitation-reconversion- $\pi/2$ -acquisition scheme was used. The R-block was implemented using 180° pulses for ^1H and a composite pulse scheme (90-270) for ^{15}N . The phase cycling was performed with a conventional 16-fold phase cycle to select the required coherence pathway $0 \pm 2 0 -1$. Recoupling times of 50 and 225 μs for ^1H and 6 ms for ^{15}N were chosen.

Pseudo 2D experiments. Rotational-Echo Double-Resonance (REDOR) measurements. ^1H (^7Li) and ^{13}C (^7Li), were conducted using a conventional REDOR pulse sequence with recoupling on the ^7Li channel.^{[35],[38]} Both REDOR experiments were recorded at $\omega_0(^7\text{Li}) = 233$ MHz in a 1.9 mm rotor spinning at 31.25 kHz and 10 kHz, respectively. The initial excitation was carried out using a 90° pulse on ^1H for ^1H (^7Li) and a ^1H - ^{13}C CP block for ^{13}C (^7Li) REDOR. The $S(\tau)$ and $S_0(\tau)$ spectra were recorded alternating. The dephasing pulses on ^7Li were chosen as strong as possible, giving a 180° pulse of 3.1 μs in double resonance mode for ^1H (^7Li) and of 3.9 μs in triple resonance mode for ^{13}C (^7Li). This ensures a proper dephasing, as they are shorter than 10% of the rotational period and as they excite the whole ^7Li spectrum. Errors of the experiment are approximated according to the scheme presented by Celinski et al.^[37] except that ΔS_0 and ΔS_0 were determined individually. ^1H - ^{13}C CP build-up curves were measured at $\omega_0(^{13}\text{C}) = 101$ MHz in a 4 mm rotor spinning at 4 kHz. For the polarization transfer a square excitation on both channels with a varying contact time between 0.05 and 20 ms in 26 steps was used. Nutation frequencies were experimentally adjusted to the +1 Hartmann-Hahn condition^[38] using Adamantane (58 kHz for ^{13}C and 54 kHz for ^1H , respectively).

Model building. All models treated in this paper were created using an in-house PYTHON library allowing for high-throughput structure generation and analysis. It relies on the Numpy/Scipy and LMFIT Packages.^[39-41] The library also implements automatic setup and read-in of CASTEP calculations, the extraction of spin systems for SIMPSON simulations, and allows calculation of second moments as well as analytical solutions for REDOR. Model building started with the CN positions taken from the structure published by Wirnhier et al.^[11] The models were treated in $P1$ symmetry to allow scanning any combination of lithium- and proton positions in the cell. Possible proton- or lithium positions are defined by the user. Supercells of the $P1$ cell were built as necessary, keeping the network structure intact. All structures are geometry-optimized in CASTEP before simulations are performed.

Solid-state NMR simulations. For all 1D SSNMR spectra the Fourier transform and baseline correction was carried out using the software TopSpinTM (Version 3.2, Bruker). The following deconvolution and integration based on Pseudo-Voigt Profiles was done using the in-house PYTHON library, described above. The quadrupolar parameters for ^7Li were estimated using a slow MAS (5 kHz) 1D spectrum and TopSpinTM (Version 3.2, Bruker). An additional $\sin(x)/x$ function with an FWHM of 1250 ppm was applied on the simulated spectrum to compensate artefacts due to the width of the probe and imperfect pulses. The Pseudo 2D spectra were treated using the same tools as for the 1D spectra. REDOR simulations shown in this paper were performed using the program SIMPSON (version 4.1.0).^[42] Each simulation implemented 168 pairs of α and β crystallite angles and 20 γ angles using the REPULSION^[43] scheme. An exemplary input file is shown in the SI chapter 8. The simulations were carried out using a five spin system after convergence was studied (SI chapter 8.2). Experimental details in the simulation were adjusted to the experiment. The RF field of the ^7Li pulses was simulated based on the experimental pulse

FULL PAPER

lengths. As C_q is small, the 180° pulse lengths for the simulation could be calculated using the RF field without any adjustment due to C_q . Quadrupolar and heteronuclear X-Li dipolar interactions have been accounted for, while both chemical shift anisotropy and homonuclear interactions have been found to have negligible influence on the simulations and were thus neglected (SI chapter 8.2). For scanning larger numbers of models, an analytical solution as outlined by Mueller et al. has been used.¹⁴⁴ To judge the quality of the simulations and calculations the *rmsd* value was calculated according to

$$rmsd = \sqrt{\frac{\sum_i (exp_i - sim_i)^2}{\sum_i (exp_i)^2}} \quad (5)$$

Evaluation of CP build-up. Quantitative information about the proton and carbon structure is obtained using CP build-up curves, as the magnetization is transferred from ^1H to ^{13}C . This has been used for several nuclei on several systems.^{116,17,27,48} The transfer obeys the exponential equation (6).

$$I(t) = I_0 \{1 - \exp[-(k_{CP}t)^b]\} \quad (6)$$

with k_{CP} being the CP transfer rate for the observed signal. The average k_{CP} can be determined from the initial slope of the CP build-up curve in a logarithmic plot as shown in Figure S17. It is defined as

$$\langle k_{CP} \rangle = c_{CP} \frac{\langle M_2^{XY} \rangle}{\sqrt{\langle M_2^{XX} \rangle}} \quad (7)$$

and depends on a constant c_{CP} and the second moments. c_{CP} depends only on physical constants and the experimental setup and should be the same for all signals. The second moment is calculated according to

$$M_2^{XY} = \left(\frac{1}{2\pi}\right)^2 \frac{4}{5} \left(\frac{1}{2}\gamma_X\gamma_Y\hbar\frac{\mu_0}{4\pi}\right)^2 \sum_i (r_i^{XY})^{-6} \quad (8)$$

and is proportional to the sum of all distances $(r_i^{XY})^{-6}$ and therefore conveys only structural information.¹⁴⁹ This strong dependency on the distance, as well as the precisely defined carbon positions in the system make CP build-up a valuable method to verify a suggested proton substructure. Eqs. (7) and (8) allow to calculate c_{CP} for each carbon in a given model structure using the second moments. Taking into account distances up to a radius of 30 \AA has been found to ensure convergence. For a perfect structure model, all c_{CP} give the same value. The quality factor used is defined as

$$R_{CP} = \sqrt{\frac{\sum_{i=1}^N (c_{CP,i} - \bar{c}_{CP})^2}{\sum_{i=1}^N c_{CP,i}^2}} \quad (9)$$

The values for the evaluation are given in Table S10, S11.

Computational methods. All calculations have been performed with the CASTEP code^{47–49} version 7.01, using ultrasoft pseudopotentials. Semi-empirical dispersion corrections using the TS scheme⁵⁰ have always been applied. The PBE⁵¹ functional with a plane wave basis set cut-off energy of 300 eV and a maximum spacing of k-points of 0.06 \AA^{-1} was chosen after checking for convergence. Shielding tensors were calculated with the gauge-including projector augmented-wave method⁴⁹, also using ultrasoft pseudopotentials. The same reference shift for the calculations presented was used for all calculations and was estimated from the best-fitting model.

Electron diffraction. For transmission electron microscopy (TEM), electron dispersive X-ray spectroscopy (EDX) and automated diffraction tomography (ADT) investigations, powdered samples were dispersed in hexane using an ultrasonic bath and sprayed on carbon-coated copper grid using a sonifier.²³ TEM, EDX and ADT measurements were carried out with a FEI TECNAI F30 STWIN transmission electron microscope equipped with a field emission gun and working at 300 kV. TEM images and nano electron diffraction (NED) patterns were taken with a CCD camera (16-bit 4,096 x 4,096 pixel GATAN ULTRASCAN4000) and acquired by Gatan Digital Micrograph software. Scanning transmission electron microscopy (STEM) images were collected by a FISCHIONE high-angular annular dark field (HAADF) detector and acquired by Emispec ES Vision software. Three-dimensional electron diffraction data were collected using an automated acquisition module developed for FEI microscopes (Kolb et al., 2007). For high tilt experiments, all acquisitions were performed with a FISCHIONE tomography holder. A condenser aperture of $10 \mu\text{m}$ and mild illumination settings were used in order to produce a semi-parallel beam of 50–100 nm in diameter on the sample. Crystal position tracking was performed in microprobe STEM mode and NED patterns were acquired sequentially in steps of 1° . Tilt series were collected within a total tilt range up to 120° , occasionally limited by overlapping of surrounding crystals or grid edges. ADT data were collected with electron beam precession (precession electron diffraction, PED; Vincent & Midgley, 1994). PED was used in order to improve reflection intensity integration quality.²³ PED was performed using a Digistar unit developed by NanoMEGAS Company. The precession angle was kept at 1.0° . The ADT3D software package was used for three-dimensional electron diffraction data processing (Kolb et al., 2011). *Ab initio* structure solution was performed assuming the kinematic approximation $I = F_{\text{int}}$ by direct methods implemented in the program SIR2014 (Burla et al., 2014). Difference Fourier mapping and least-squares refinement were performed with the software SHELX97 (Sheldrick, 2008). Scattering factors for electrons were taken from Doyle & Turner (1968).

Pair Distribution Function.

Acknowledgements

We thank Dr. Lothar Fink and Edith Alig for the X-ray powder measurements. We are grateful to the Stipendienstiftung Rheinland-Pfalz.

Keywords: NMR spectroscopy • electron diffraction • pair distribution function • poly (triazine imide) • structure elucidation • NMR crystallography

- [1] E. Wirthner, M. Döblinger, D. Gunzelmann, J. Senker, B. V. Lotsch, W. Schnick, *Chem. Eur. J.* **2011**, *17*, 3213–3221.
- [2] B. Jürgens, E. Irran, J. Senker, P. Kroll, H. Müller, W. Schnick, *J. Am. Chem. Soc.* **2003**, *125*, 10288–10300.
- [3] B. V. Lotsch, M. Döblinger, J. Sehnert, L. Seyfarth, J. Senker, O. Oeckler, W. Schnick, *Chem. Eur. J.* **2007**, *13*, 4969–4980.
- [4] M. Döblinger, B. V. Lotsch, J. Wack, J. Thun, J. Senker, W. Schnick, *Chem. Commun.* **2009**, 1541–1543.
- [5] Z. Zhang, K. Leinerweber, M. Bauer, L. A. J. Garvie, P. F. McMillan, G. H. Wolf, *J. Am. Chem. Soc.* **2001**, *123*, 7788–7796.

FULL PAPER

- [6] J. Sehnert, K. Baerwinkel, J. Senker, *J. Phys. Chem. B* **2007**, *111*, 10671–10680.
- [7] E. J. McDermott, E. Wirnhier, W. Schnick, K. S. Virdi, C. Scheu, Y. Kauffmann, W. D. Kaplan, E. Z. Kurmaev, A. Moewes, *J. Phys. Chem. C* **2013**, *117*, 8806–8812.
- [8] Y. Ham, K. Maeda, D. Cha, K. Takanabe, K. Domen, *Chem. Asian J.* **2013**, *8*, 218–224.
- [9] K. Schwinghammer, M. B. Mesch, V. Duppel, C. Ziegler, J. Senker, B. V. Lotsch, *J. Am. Chem. Soc.* **2014**, *136*, 1730–3.
- [10] K. Schwinghammer, B. Tuffy, M. B. Mesch, E. Wirnhier, C. Martineau, F. Taulelle, W. Schnick, J. Senker, B. V. Lotsch, *Angew. Chem. Int. Ed.* **2013**, *52*, 2435–9.
- [11] R. Harris, *Encycl. Magn. Reson.* **2008**, 1–13.
- [12] C. Martineau, J. Senker, F. Taulelle, *Annu. reports NMR Spectrosc.* **2014**, *82*, 1–57.
- [13] N. E. A. El-Gamel, L. Seyfarth, J. Wagler, H. Ehrenberg, M. Schwarz, J. Senker, E. Kroke, *Chem. Eur. J.* **2007**, *13*, 1158–1173.
- [14] L. Seyfarth, J. Sehnert, N. E. A. El-Gamel, W. Milius, E. Kroke, J. Breu, J. Senker, *J. Mol. Struct.* **2008**, *889*, 217–228.
- [15] A. Sattler, W. Schnick, *Zeitschrift für Anorg. und Allg. Chemie* **2006**, *632*, 238–242.
- [16] L. Seyfarth, J. Senker, *Phys. Chem. Chem. Phys.* **2009**, *11*, 3522–3531.
- [17] L. Seyfarth, J. Seyfarth, B. V. Lotsch, W. Schnick, J. Senker, *Phys. Chem. Chem. Phys.* **2010**, *12*, 2227–2237.
- [18] X. Zhao, W. Hoffbauer, J. Schmedt auf der Günne, M. H. Levitt, *Solid State Nucl. Magn. Reson.* **2004**, *26*, 57–64.
- [19] M. Bjerring, N. C. Nielsen, *Chem. Phys. Lett.* **2003**, *382*, 671–678.
- [20] O. Lafon, Q. Wang, B. Hu, F. Vasconcelos, J. Trébosc, S. Cristol, F. Deng, J. P. Amoureux, *J. Phys. Chem. A* **2009**, *113*, 12864–12878.
- [21] M. H. Levitt, *Encycl. Nucl. Magn. Reson.* **2002**, *9*, 165–196.
- [22] K. Bärwinkel, M. B. Mesch, J. Senker, **2016**, to be submitted.
- [23] E. Magnaioli, T. Gorelik, U. Kolb, *Ultramicroscopy* **2009**, *109*, 758–765.
- [24] T. E. Gorelik, J. Van De Streek, A. F. M. Kibinger, G. Brunklaus, U. Kolb, *Acta Crystallogr. Sect. B* **2012**, *68*, 171–181.
- [25] G. E. Hawkes, M. D. Mantle, K. D. Sales, S. Aime, R. Gobetto, C. J. Groombridge, *J. Magn. Reson. A* **1995**, *116*, 251–254.
- [26] P. Li, Q. Chen, S. Zhang, *J. Magn. Reson.* **2015**, *250*, 76–79.
- [27] W. Kolodziejski, J. Klinowski, *Chem. Rev.* **2002**, *102*, 613–628.
- [28] B. M. Fung, A. K. Khitrin, K. Ermolaev, *J. Magn. Reson.* **2000**, *142*, 97–101.
- [29] D. Marion, M. Ikura, R. Tschudin, A. Bax, *J. Magn. Reson.* **1989**, *85*, 393–399.
- [30] D. J. States, R. A. Haberkom, D. J. Ruben, *J. Magn. Reson.* **1982**, *48*, 286–292.
- [31] G. Metz, X. Wu, S. O. Smith, *J. Magn. Reson. A* **1994**, *110*, 219–227.
- [32] A. Pines, M. G. Gibby, J. S. Waugh, *J. Chem. Phys.* **1972**, *56*, 1776–1777.
- [33] Z. Gan, *J. Magn. Reson.* **2007**, *184*, 39–43.
- [34] A. Brinkmann, A. P. M. Kentgens, *J. Am. Chem. Soc.* **2006**, *128*, 14758–14759.
- [35] T. Gullion, J. Schaefer, *J. Magn. Reson.* **1989**, *81*, 196–200.
- [36] T. Gullion, *Concepts Magn. Reson.* **1998**, *10*, 277–289.
- [37] V. R. Celinski, J. Weber, J. Schmedt auf der Günne, *Solid State Nucl. Magn. Reson.* **2013**, *49–50*, 12–22.
- [38] R. S. Hartmann, E. L. Hahn, *Phys. Rev.* **1962**, *128*, 2042–2053.
- [39] F. Perez, B. E. Granger, *Comput. Sci. Eng.* **2007**, *9*, 21–29.
- [40] S. van der Walt, S. C. Colbert, G. Varoquaux, *Comput. Sci. Eng.* **2011**, *13*, 22–30.
- [41] M. Newville, T. Stensitzki, D. B. Allen, A. Ingargiola, *Zenodo* **2014**, DOI 10.5281/zenodo.11813.
- [42] M. Bak, J. T. Rasmussen, N. C. Nielsen, *J. Magn. Reson.* **2000**, *147*, 296–330.
- [43] M. Bak, N. Nielsen, *J. Magn. Reson.* **1997**, *125*, 132–139.
- [44] K. T. Mueller, *J. Magn. Reson. A* **1995**, *113*, 81–93.
- [45] C. A. Fyfe, D. H. Brouwer, *J. Am. Chem. Soc.* **2006**, *128*, 11860–11871.
- [46] J. H. van Vleck, *Phys. Rev.* **1948**, *74*, 1168–1183.
- [47] S. J. Clark, M. D. Segall, C. J. Pickard, P. J. Hasnip, M. I. J. Probert, K. Refson, M. C. Payne, *Zeitschrift für Krist.* **2005**, *220*, 567–570.
- [48] J. R. Yates, C. J. Pickard, F. Mauri, *Phys. Rev. B* **2007**, *76*, 024401(1–11).
- [49] C. J. Pickard, F. Mauri, *Phys. Rev. B* **2001**, *63*, 245101(1–13).
- [50] A. Tkatchenko, M. Scheffler, *Phys. Rev. Lett.* **2009**, *102*, 073005(1–4).
- [51] J. P. Perdew, K. Burke, M. Ernzerhof, *Phys. Rev. Lett.* **1996**, *77*, 3865–3868.

6.6.2 Supporting Information

Solving the Hydrogen and Lithium Substructure of Poly (Triazine Imide)/LiCl Using NMR Crystallography

Maria B. Mesch,^[a] Kilian Bärwinkel,^[a] Yaşar Krysiak,^[b] Charlotte Martineau,^[d] Francis Taulelle,^[d] Reinhard Neder,^{*,[c]} Ute Kolb,^{*,[b]} Jürgen Senker^{*,[a]}

^[a]Inorganic Chemistry III, University of Bayreuth, 95447 Bayreuth (Germany)

^[b]Institute of Inorganic Chemistry and Analytical Chemistry, Johannes Gutenberg University Mainz, Jakob-Welder-Weg 11, 55128 Mainz (Germany)

^[c]Lehrstuhl für Kristallographie und Strukturphysik, Friedrich-Alexander-Universität Erlangen-Nürnberg, Staudtstr. 3, 91058 Erlangen (Germany)

^[d]Tectospin, Institut Lavoisier de Versailles (ILV), UMR CNRS 8180 Université de Versailles Saint-Quentin-en-Yvelines 45 Avenue des Etats-Unis, 78035 Versailles cedex (France)

* reinhard.neder@fau.de, kolb@uni-mainz.de, juergen.senker@uni-bayreuth.de

SUPPORTING INFORMATION

1	cif-file of PTI/LiCl ⁽¹⁾	2
2	CHARACTERIZATION OF SAMPLE	4
3	SINGLE PULSE ¹³ C AND ¹⁵ N SPECTRUM	4
4	ADDITIONAL INFORMATION ON 2D SPECTRA	5
5	CORRUGATION BEHAVIOUR	6
6	CRYSTALLOGRAPHIC DATA OF MODELS	8
7	ENERGY VALUES	8
8	REDOR SIMULATIONS	9
8.1	Exemplary SIMPSON input file	9
8.2	Convergence studies for SIMPSON simulations	12
8.3	Analysis of REDOR	13
9	DETERMINATION OF <i>RXshiftREDOR</i> -values	14
10	Electron Diffraction	16
11	REDOR Refinement	18
12	CP-build up	19
13	Crystallographic data of 112 o hombr II	21
14	References	22

1 cif-file of PTI/LiCl^[1]

```

data_Template
_audit_creation_method 'TOPAS ACADEMIC 4.1 + PLATON'
_audit_creation_date 2013-06-06
_audit_update_record 2013-06-06
loop
_publ_author_name
'Wirnhier,, '
'Eva, '
'Doeblinger,, '
'Markus, '
'Gunzelmann,, '
'Daniel, '
'Senker,, '
'Juergen, '
'Lotsch,, '
'Bettina, '
'V., '
'Schnick,, '
'Wolfgang, '

_publ_section_title
;
Poly(triazine imide) (PTI) - A Crystalline 2D Carbon Nitride Network with
Intercalation of Alkali and Halide Ions
;
_chemical_formula_sum 'C12 C12 Li2 N18'
_chemical_name_common
;
Poly(triazine imide)with LiCl intercalation
;
_chemical_name_systematic
;
Poly(triazine imide)with LiCl intercalation
;
_chemical_formula_weight 481.026
_cell_length_a 8.4682(10)
_cell_length_b 8.4682(10)
_cell_length_c 6.7502(9)
_cell_angle_alpha 90.000
_cell_angle_beta 90.000
_cell_angle_gamma 120.000
_cell_volume 419.2(1)
_cell_formula_units_Z 1
_symmetry_int_tables_number 185
_symmetry_space_group_name_H-M 'P 63 c m'
_symmetry_space_group_name_Hall 'P_6c_-2'

loop
_symmetry_equiv_pos_site_id
_symmetry_equiv_pos_as_xyz
1 x,y,z
2 x-y,x,1/2+z
3 -y,x-y,z
4 -x,-y,1/2+z
5 -x+y,-x,z
6 y,-x+y,1/2+z
7 -x+y,y,1/2+z
8 x,x-y,1/2+z

```

```
9 -y, -x, 1/2+z
10 y, x, z
11 x-y, -y, z
12 -x, -x+y, z

loop_
  _atom_type_symbol
  _atom_type_oxidation_number
  _atom_type_radius_bond
  Cl ? 1.200
  Li ? 1.200
  C ? 1.200
  N ? 1.200

loop_
  _atom_site_label
  _atom_site_type_symbol
  _atom_site_fract_x
  _atom_site_fract_y
  _atom_site_fract_z
  _atom_site_occupancy
  _atom_site_symmetry_multiplicity
  _atom_site_Wyckoff_symbol
  _atom_site_attached_hydrogens
  _atom_site_calc_flag
  _atom_site_thermal_displace_type
  _atom_site_u_iso_or_equiv
  Cl Cl 0.0000 0.0000 0.4404 1.000 2 a ? d ? 5.54(25)
  Li Li 0.2200 0.0000 0.2050 0.333 6 c ? d ? 0.70000
  C2 C 0.6427 0.1580 0.2455 1.000 12 d ? d ? 0.70000
  N3 N 0.4926 0.1812 0.2203 1.000 12 d ? d ? 0.70000
  N4 N 0.6387 0.0000 0.2263 1.000 6 c ? d ? 0.70000

loop_
  _geom_bond_atom_site_label_1
  _geom_bond_atom_site_label_2
  _geom_bond_site_symmetry_1
  _geom_bond_site_symmetry_2
  _geom_bond_distance
  _geom_bond_publ_flag
  N3 C2 . . 1.3895 yes
  N3 C2 . 5_665 1.4159 yes
  N4 C2 . . 1.3278 yes
  N4 C2 . 11 1.3278 yes
  Cl Li . . 2.4486(2) no

loop_
  _geom_angle_atom_site_label_1
  _geom_angle_atom_site_label_2
  _geom_angle_atom_site_label_3
  _geom_angle_site_symmetry_1
  _geom_angle_site_symmetry_2
  _geom_angle_site_symmetry_3
  _geom_angle
  _geom_angle_publ_flag
  C2 N3 C2 . . 5_665 118.82 yes
  C2 N4 C2 . . 11 121.55 yes
  N3 C2 N4 . . . 124.47 yes
  N3 C2 N3 . . 3_655 118.29 yes
  N3 C2 N4 3_655 . . 113.43 yes
```


2 CHARACTERIZATION OF SAMPLE

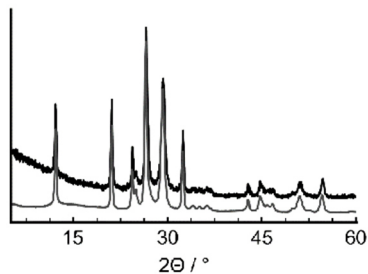


Figure S1. Powder X-ray diffractogram of PT/LiCl synthesized by Wirnhier (grey) and the ^{15}N -enriched sample (black).

3 SINGLE PULSE ^{13}C AND ^{15}N SPECTRUM

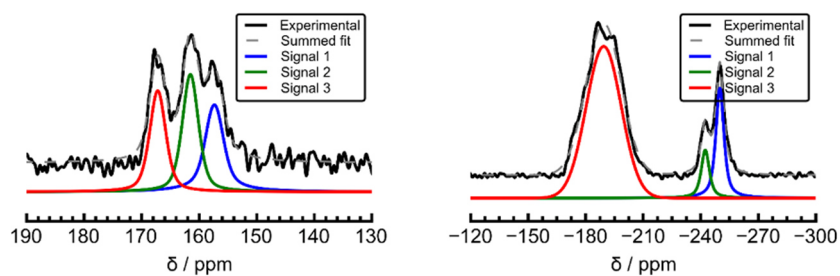


Figure S2. ^{13}C (left) and ^{15}N (right) MAS SSNMR single pulse spectrum. Spinning sidebands for ^{15}N signal 3 are not shown for clarity.

Table S1. Overview over the integrals of the signals displayed in Figure S2.

	Integrals ^{13}C	Integrals ^{15}N
Signal 1	1.10	0.70
Signal 2	1.16	0.30
Signal 3	1.00	3.55

4 ADDITIONAL INFORMATION ON 2D SPECTRA

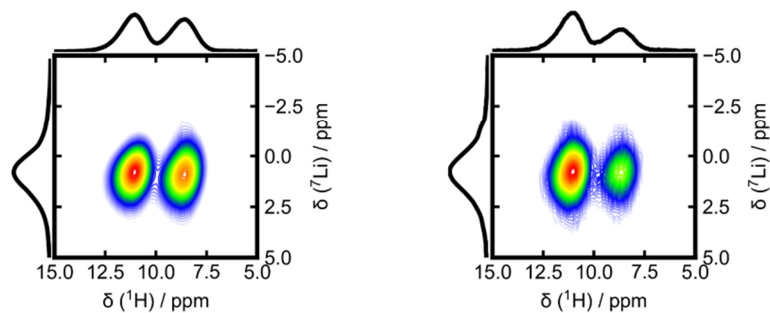


Figure S3. ${}^7\text{Li}$ - ${}^1\text{H}$ HMQC at mixing times of 320 (left) and 704 μs (right).

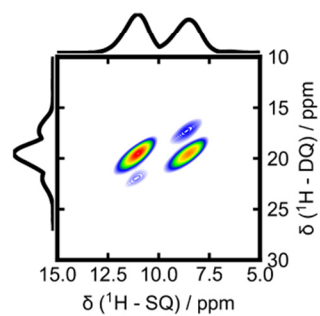


Figure S4. ${}^1\text{H}$ - ${}^1\text{H}$ DQ-SQ spectrum measured with a $\text{R}12_2^5$ pulse sequence and a recoupling time of 225 μs .

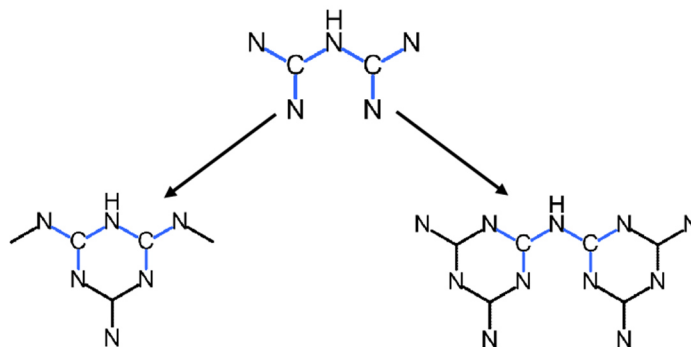


Figure S5. Possible structure fragments from 2D spectra.

5 CORRUGATION BEHAVIOUR

As described in the main part, upon geometry optimization, a slight displacement of atoms along c is observed, which is attributed to interactions of N-H groups with incorporated chlorine anions. The observed displacement for all models is displayed in **Figure S6**.

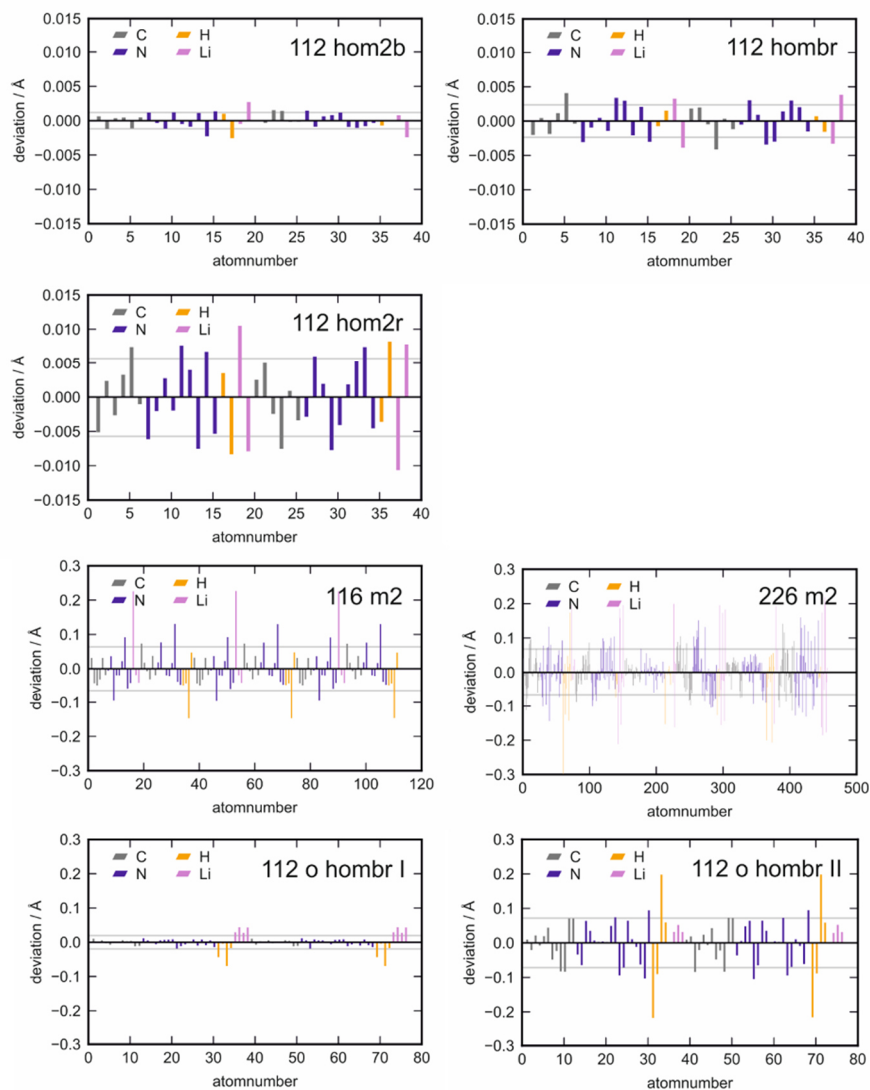


Figure S6. Deviation of each atom of all models from the average c -position of its layer. The grey line indicates the standard deviation s .

The standard deviation s is calculated according to the formula

$$s = \sqrt{\frac{1}{n-1} \sum_{i=1}^n (\bar{c} - c_i)^2}$$

with n being the number of atoms, \bar{c} being the average c -position within the layer and c_i being the c -position of atom i . All atoms within the layer (H, Li, N, C) are included to derive the standard deviations summarized in **Table S2**.

Table S2. Standard deviation s for the displacement of the atoms along c for all models.

Model	$s / \text{\AA}$
112 hom2b	0.0012
112 hombr	0.0023
112 hom2r	0.0049
116 m2	0.0402
226 m2	0.0543
112 hombr I	0.0081
112 hombr II	0.0554

Figure S7 shows the structures from model 112 o hombr I and II viewed along the b -axis to illustrate the difference in deviation.

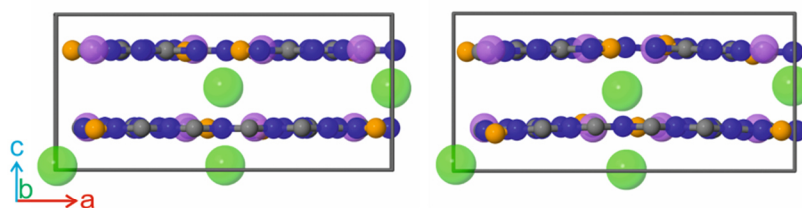


Figure S7. Structure of model 112 o hombr I (left) and 112 o hombr II (right) viewed along the b -axis to illustrate the deviation of the atoms from the average layer c -coordinate.

6 CRYSTALLOGRAPHIC DATA OF MODELS

Table S3. Summary of the crystallographic data of the geometry optimized models. All models were optimized in P1. The maximal symmetry found by a symmetry search in Material Studio with a maximum atom deviation of 0.3 Å is given in the table. The deviation of *b* compared to *a* is given in percent as well as the deviation of the angles from theoretical values (90/120).

Model	Space group	<i>a</i>	<i>b</i>	<i>c</i>	α	β	γ
112 hom2b	<i>Amm</i> 2 (38)	8.447	8.447 0.00%	6.701	89.95 0.06%	89.96 0.04%	117.75 1.88%
112 hombr	<i>P</i> 2 ₁ / <i>m</i> (11)	8.424	8.47 0.55%	6.746	90.11 0.12%	90.01 0.01%	118.75 1.04%
112 hom2r	<i>Cmcm</i> (63)	8.513	8.472 0.48%	7.003	90.23 0.26%	90.03 0.03%	119.84 0.13%
116 m2	<i>P</i> 3 ₁ (144)	8.448	8.448 0.00%	19.473	90.00 0.00%	90.01 0.01%	120.00 0.00%
226 m2	<i>P</i> 1 (1)	16.969	16.970 0.01%	20.316	90.36 0.40%	89.61 0.43%	120.00 0.00%
112 o hombr I	<i>P</i> 2 ₁ / <i>m</i> (11)	14.536	8.604 2.52%	6.719	90.00 0.00%	90.00 0.00%	90.39 0.43%
112 o hombr II	<i>P</i> 2 ₁ 2 ₁ 2 ₁ (19)	14.558	8.603 2.35%	6.705	89.97 0.01%	90.01 0.01%	90.04 0.04%

7 ENERGY VALUES

Table S4. Energy values for all models referenced to 112 hombr.

Model	Energy / (kJ/mol)
112 hom2b	8.21
112 hombr	0.00
112 hom2r	15.16
116 m2	23.23
226 m2	12.37
112 hombr I	-1.07
112 hombr II	-0.77

8 REDOR SIMULATIONS

8.1 Exemplary SIMPSON input file

```
spinsys {
channels 13C 7Li
nuclei 13C 7Li 7Li 7Li 7Li
  quadrupole 2 2 180000.0 0.8 0.0 1.5707963267948966 1.2643287808595876
  quadrupole 3 2 180000.0 0.8 -3.017447698938259 0.0 0
  quadrupole 4 2 180000.0 0.8 -3.017447698938259 0.0 0
  quadrupole 5 2 180000.0 0.8 -3.017447698938259 0.0 0
dipole 1 2 -402.48105328 0.0 90.0234025248 -10.4100381227
dipole 1 3 -356.211773415 0.0 90.0539759116 156.691006585
dipole 1 4 -194.322578361 0.0 30.7561378604 30.3394413359
dipole 1 5 -193.884960132 0.0 149.209418523 30.5452100435
}

par {
  proton_frequency 600e6
  spin_rate 10000
  sw spin_rate/2
  np 200
  crystal_file repl68
  gamma_angles 20
  start_operator Ilx
  detect_operator Ilp
  verbose 11110
  variable rf 71400
  variable rf2 124400
  variable t90_li 2.01
}

proc pulseseq {} {
  global par
  maxdt 0.5

  set t180 [expr 0.5e6/$par(rf)]
  set t180_2 [expr $par(t90_li)*2]
  set tr3 [expr (1.0e6/$par(spin_rate)-$t180-$t180_2)/2]
  set tr2 [expr 0.5e6/$par(spin_rate)-$t180_2]
  reset
  acq

  reset
  delay $tr2
  pulse $t180_2 0 x $par(rf2) x
  delay $tr2
  pulse $t180_2 0 x $par(rf2) y
  store 1
  reset

  reset
  delay $tr2
  pulse $t180_2 0 x $par(rf2) y
  delay $tr2
  pulse $t180_2 0 x $par(rf2) x
  store 2
  reset

  reset
```

```
delay $tr2
pulse $t180_2 0 x $par(rf2) x
delay $tr2
store 5
reset

reset
delay $tr2
pulse $t180_2 0 x $par(rf2) y
delay $tr2
store 6
reset

reset
delay $tr2
pulse $t180_2 0 x $par(rf2) x
delay $tr3
pulse $t180 $par(rf) x 0 x
delay $tr3
pulse $t180_2 0 x $par(rf2) x
delay $tr2
pulse $t180_2 0 x $par(rf2) y
store 3
reset

reset
delay $tr2
pulse $t180_2 0 x $par(rf2) y
delay $tr3
pulse $t180 $par(rf) x 0 x
delay $tr3
pulse $t180_2 0 x $par(rf2) x
delay $tr2
pulse $t180_2 0 x $par(rf2) y
store 4

reset
delay $tr2
pulse $t180_2 0 x $par(rf2) x
delay $tr3
pulse $t180 $par(rf) x 0 x
delay $tr3
pulse $t180_2 0 x $par(rf2) x
delay $tr2
acq
reset

reset
store 8
reset

for {set i 2} {$i < $par(np)} {incr i} {
  set q [expr $i % 4]
  if {$q == 2} {
    reset
    prop 1
    prop 8
    prop 3
    prop 8
    prop 5
    acq
  }
}
```

```
        reset
        prop 8
        prop 1
        store 8
    } elseif {$q == 3} {
        reset
        prop 1
        prop 8
        prop 4
        prop 8
        prop 6
        acq
        reset
        prop 8
        prop 2
        store 8
    } elseif {$q == 0} {
        reset
        prop 1
        prop 8
        prop 4
        prop 8
        prop 6
        acq
        reset
        prop 8
        prop 2
        store 8
    } elseif {$q == 1} {
        reset
        prop 1
        prop 8
        prop 3
        prop 8
        prop 5
        acq
        reset
        prop 8
        prop 1
        store 8
    }
}
}
}

proc main {} {
    global par
    # set $par(Dipol) [dist2dip 13C 15N $par(Abstand)]
    # set f [fsimpson [list [list dipole_1_2_aniso $Dipol ]]]
    set f [fsimpson]
    # puts "$Abstand"
    # fsave $f $par(name).fid
    # fexpr $f {$re} {$im}
    # fadddb $f 50 0
    fsave $f $par(name).dat -xreim
}
```


8.2 Convergence studies for SIMSPON simulations

For SIMPSON REDOR simulations, a convergence study for the spin system size was carried out, and the influence of different interactions was examined. This is exemplarily displayed for the $^{13}\text{C}\{^7\text{Li}\}$ REDOR measurement of one ^{13}C atom of model 112 hombr (Figure S8). The spin system size was tested for one carbon atom and one to four lithium atoms (Figure S8 (left)). The changes between the curves for three and four lithium atoms are negligible, therefore showing a clear convergence. All simulations within the paper were carried out with four lithium atoms. Additionally we tested the influence of the quadrupolar coupling of lithium (cq), of the chemical shift anisotropy of carbon (csa) and of the homonuclear dipolar coupling between lithium (hdd). The homonuclear dipolar coupling of carbon is not considered as the natural abundance of carbon is 1% and therefore makes coupling unlikely. The cq is extracted from the 1D ^7Li SSNMR experiment, whereas the csa and the hdd are derived from quantum mechanical calculations of model 112 hombr. The simulations, exemplarily carried out on a spin system with two lithium atoms are displayed in figure Figure S8 (right). It reveals that the influence of cq is very important, whereas all other interactions have no influence and are consequently neglected for the presented REDOR simulations.

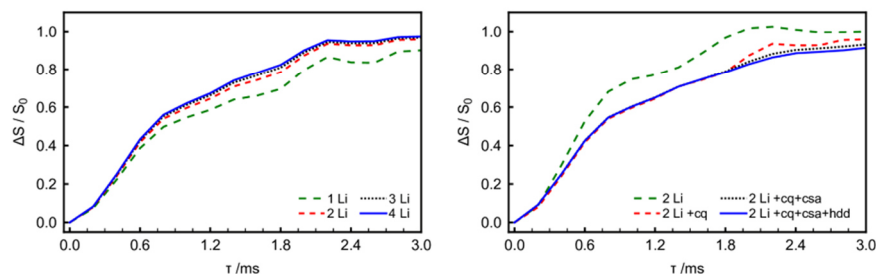


Figure S8. Convergence study for the REDOR simulations exemplarily displayed for the simulation of one ^{13}C atom of model 112 hombr for the $^{13}\text{C}\{^7\text{Li}\}$ REDOR measurement. The spin system size is varied between one and four lithium atoms (left) with a clear convergence starting at three atoms. Additionally, several spin systems (two lithium atoms) including different interactions were tested (right).

8.3 Analysis of REDOR

For a qualitative analysis, a REDOR curve for each ^1H or ^{13}C atom of the examined model was simulated (Figure S9).

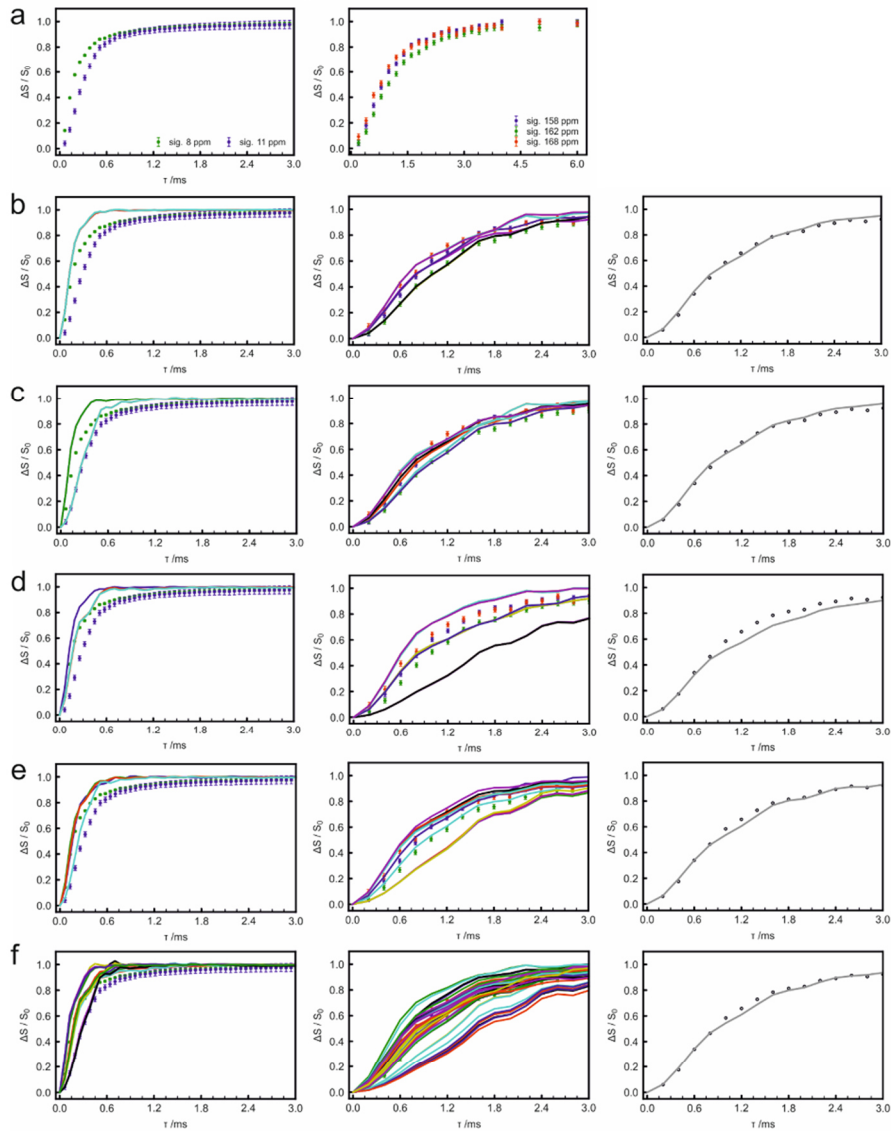


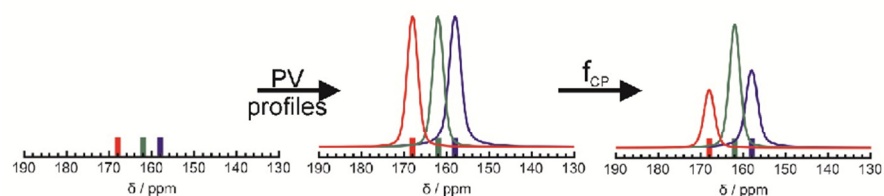
Figure S9. $^1\text{H}\{^{13}\text{C}\}$ REDOR and $^{13}\text{C}\{^{13}\text{C}\}$ REDOR experiment (a). $^1\text{H}\{^{13}\text{C}\}$ REDOR, single simulation for every atom (left column), $^{13}\text{C}\{^{13}\text{C}\}$ REDOR, single simulation for every atom (middle column) and $^{13}\text{C}\{^{13}\text{C}\}$ REDOR average over all signals and all simulations (right column) for 112 hom2b (b), 112 hombr (c), 112 hom2r (d), 116 m2 (e), and 226 m2 (f). Experiments are marked with round symbols with error bars whereas the simulated curves are indicated with lines.

9 DETERMINATION OF $R_{X_{shift}}^{REDOR}$ -values

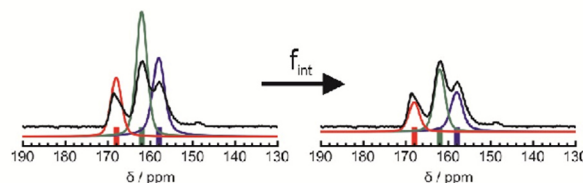
First, the dephased spectrum has to be determined at every point τ of the REDOR curve. Therefore, a Pseudo-Voigt (PV) profile is calculated for every shift and is weighted with several factors according to

$$spectrum_{calc}(\tau) = f_{int} \sum_{i=1}^N PV_i f_{CP,i} f_{REDOR,sim,i}(\tau)$$

f_{CP} : Only for ^{13}C : The experimental spectra are based on CP and therefore cannot be directly compared to the calculations. Consequently, each profile is multiplied with a weighting factor, which is derived from the comparison of the three signals of a direct excitation spectrum and the three signals of the first reference spectrum (158 ppm = 0.89, 162 ppm = 1.00, 168 ppm = 0.45). The weighting factors are assigned to the PV profiles according to the shift calculations.



f_{int} : A scaling factor to scale the whole spectrum. It is calculated by the ratio of the integral of the first reference spectrum and the integral of the (CP-scaled) spectrum of each model.



$f_{REDOR,sim}$: The factor for the SIMPSON simulated dephasing for every chemical shift at every time τ of the REDOR curve (Figure S10).

The resulting dephased $spectrum_{calc}(\tau)$ (Figure S10, green dashed line) is used to calculate the *rmsd* to the experimental dephased $spectrum_{exp}(\tau)$. The whole procedure is applied to both nucleus and to all models (Table S5 and Table S6). After 10 (1H), respectively 16 (^{13}C) points, the dephased spectra become quite small, giving small *rmsd*-values which have a negligible influence on the later calculated average value. Therefore, only the first 10 (1H) or 16 (^{13}C) spectra are considered.

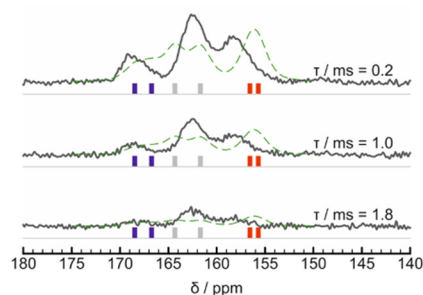


Figure S10. Calculated dephased $^{13}\text{C}\{^7\text{Li}\}$ REDOR spectra (dashed green line) and the experiment (grey line) at three different dephasing times shown exemplary for model 112 hombr. The calculated shift positions are displayed at the bottom of each spectrum.

Table S5. *rmsd*-values of $^1\text{H}\{^7\text{Li}\}$ REDOR curves for all models.

$\tau^{^1\text{H}} / \text{ms}$	rmsd 112 hom2b	rmsd 112 hombr	rmsd 112 hom2r	rmsd 116 m2	rmsd 226 m2
0.064	0.45	0.09	0.42	0.35	0.24
0.128	0.38	0.12	0.31	0.29	0.19
0.192	0.36	0.14	0.25	0.25	0.17
0.256	0.37	0.15	0.25	0.26	0.19
0.384	0.38	0.19	0.27	0.27	0.20
0.448	0.40	0.23	0.28	0.28	0.22
0.512	0.44	0.29	0.32	0.34	0.27
0.576	0.48	0.37	0.40	0.40	0.34
0.640	0.49	0.39	0.44	0.41	0.37
0.704	0.52	0.39	0.49	0.44	0.40

Table S6. *rmsd*-values of $^{13}\text{C}\{^7\text{Li}\}$ REDOR curves for all models.

$\tau^{^{13}\text{C}} / \text{ms}$	rmsd 112 hom2b	rmsd 112 hombr	rmsd 112 hom2r	rmsd 116 m2	rmsd 226 m2
0.2	0.34	0.24	0.40	0.37	0.32
0.4	0.32	0.25	0.41	0.37	0.32
0.6	0.30	0.23	0.42	0.35	0.30
0.8	0.29	0.23	0.45	0.35	0.30
1.0	0.29	0.23	0.48	0.35	0.29
1.2	0.30	0.23	0.53	0.35	0.30
1.4	0.29	0.23	0.57	0.35	0.30
1.6	0.28	0.23	0.61	0.34	0.28
1.8	0.23	0.21	0.56	0.31	0.26
2.0	0.27	0.24	0.65	0.34	0.29
2.2	0.22	0.21	0.59	0.31	0.25
2.4	0.21	0.22	0.56	0.29	0.24
2.6	0.24	0.25	0.63	0.33	0.28
2.8	0.21	0.23	0.54	0.29	0.24
3.0	0.27	0.29	0.60	0.36	0.32
3.2	0.28	0.28	0.58	0.32	0.27

10 Electron Diffraction

Table S7: Comparison of residues from orthorhombic structure solutions.

	CR I		CR II	
	R / %	R _{int} / %	R / %	R _{int} / %
<i>trans I</i> C222 ₁	11.6	17.9	14.4	20.4
<i>trans II</i> C222 ₁	12.2	14.8	16.8	20.4
<i>trans III</i> C222 ₁	10.4	15.3	14.1	23.3
<i>trans I</i> Cmc2 ₁	9.8	17.9	13.7	20.3
<i>trans II</i> Cmc2 ₁	11.5	14.7	15.9	20.2
<i>trans III</i> Cmc2 ₁	9.2	15.1	13.6	23.0

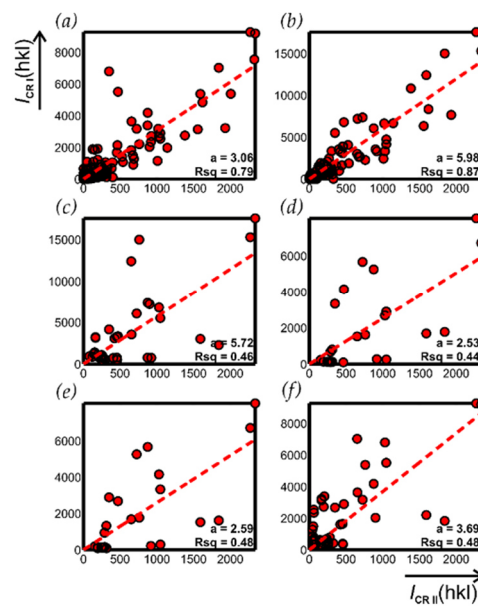


Figure S11. Merge of CR II hkl data with hkl data of CR I in six different orientations. The intensities of same hkl from CR I and CR II are plotted against each other. The resulting scaling factor of respective linear fits with error are shown in the lower right corner of each plot.

The structure solution in $C222_1/Cmc2_1$ is not surprising, because the structure, as well the literature structure, is in general very close to a centrosymmetric structure. Deduced from the centrosymmetric space group $P63/mcm$ by removing the inversion centre a structure description through $C222_1/Cmc2_1$ is conceivable (see **Figure S11**).

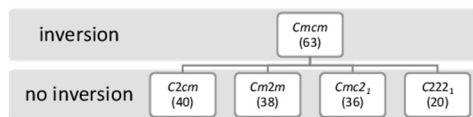


Figure S12. Scheme of *translationsgleiche* orthorhombic subgroups deduced from $Cmcm$ (orthorhombic subgroup of $P63/mcm$) by reducing symmetry elements.

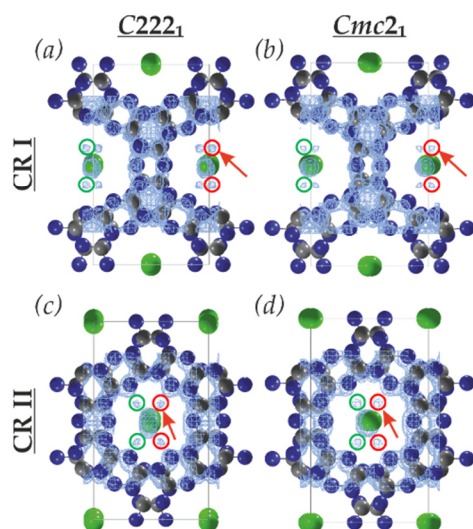


Figure S13. Three-dimensional potential maps of structure solutions in space groups $C222_1$ for CR I (a) CR II (c) and $Cmc2_1$ for CR I (b) CR II (d) combined with structure models projected down c^* . Chlorine atoms are represented in green, carbon in grey and nitrogen in blue. The red arrow marks an extra potential in (a) to (d). The projections include two layers. Red circles are $+1/2$ higher in z than green circles.

11 REDOR Refinement

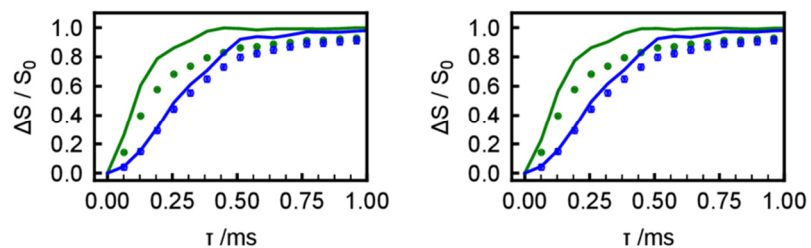


Figure S14. $^1\text{H}\{^7\text{Li}\}$ REDOR curves and simulations for 112 o hombr I (left) and 112 o hombr II (right). The signal at 8 ppm assigned to H_b is plotted in green, the one at 11 ppm, H_t , in blue.

Table S8. *rmsd*-values of the individual $^1\text{H}\{^7\text{Li}\}$ REDOR curves, and their sum, the $R^{^1\text{H}\{^7\text{Li}\}}$.

Model	8 ppm	11 ppm	$R^{^1\text{H}\{^7\text{Li}\}}$
112 o hombr I	0.0661	0.0320	0.0981
112 o hombr II	0.0626	0.0320	0.0946

Table S9. *rmsd*-values of the individual $^{13}\text{C}\{^7\text{Li}\}$ REDOR curves, and their sum, the $R^{^{13}\text{C}\{^7\text{Li}\}}$.

Model	158 ppm	162 ppm	168 ppm	$R^{^{13}\text{C}\{^7\text{Li}\}}$
112 o hombr I	0.0221	0.0455	0.0250	0.0926
112 o hombr II	0.0196	0.0224	0.0288	0.0708

12 CP-build up

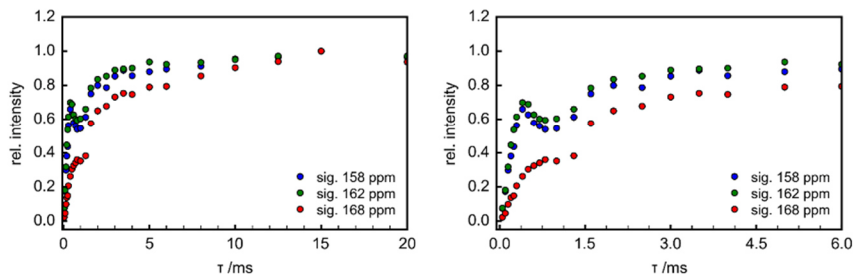


Figure S15. ^1H - ^{13}C CP-build up curves: Full x-range (left), first 6 ms (right).

The fits shown in **Figure S16** have been conducted by powder averaging over the analytical solution as outlined by Peng Li et. al. and Hawkes et. al.:^[2,3]

$$I(t) = I_0 \left[1 - \frac{1}{2} \exp(-Rt) - \frac{1}{2} \exp(-R_1 t) \cos(\theta_{1eff}(t)) \right]$$

R^{-1} = proton spin-diffusion rate

R_1^{-1} = dipolar dampening

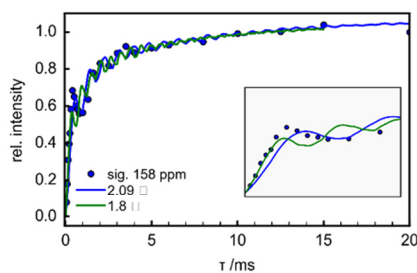
with the dipolar coupling constant d_0 under MAS rotation at ω_r expressed as $\theta_{1eff}(t)$. The Euler angles Θ and Ψ relate the orientation of the internuclear vector in the crystal axis system to the MAS frame:

$$\theta_{1eff}(t) = \frac{d_0}{4\omega_r} \{ 2\sqrt{2}\sin(2\Theta)[\sin(\omega_r t + \Psi) - \sin(\Psi)] - \sin^2\beta[\sin(\omega_r t + \Psi) - \sin(\Psi)] \}$$

with

$$d_0 = \left(\frac{\hbar\mu_0}{4\pi} \right) \frac{1}{r^3} \gamma_I \gamma_S$$

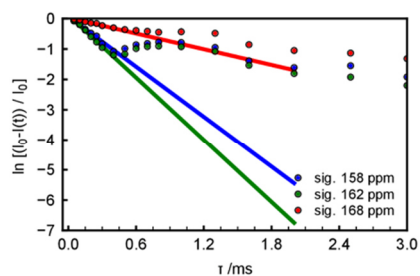
and \hbar being the Planck constant, μ_0 the permeability of vacuum and γ_X the gyromagnetic ratio of spin X.



d(C-H)	R	R ₁
2.09 Å	900 μs	8 ms
1.80 Å	900 μs	8 ms

Figure S16. Experimental ^1H - ^{13}C CP-build up curve for the signal at 158 ppm (blue) with fit according to Kolodziejcki and Klinowski.^[4] Spin diffusion rates are fitted to the experiment in the range from 3 to 20 ms. The C-H distance was set to 2.09 Å as extracted from the 112 hombr model for the C_NH and to 1.80 Å to fit the experiment.

Logarithmic Plot and k_{CP} -values.



Signal	$k_{CP} / 10^{-3} s^{-1}$
sig. 158 ppm	2.7558
sig. 162 ppm	3.4313
sig. 168 ppm	0.8624

Figure S17. Logarithmic plot of the experimental 1H - ^{13}C CP-build up curves and linear fit for the first four points (left). Slope k_{CP} of the linear fit for the three signals (right).

Second Moments calculated according to equation (7).

Table S10. C-H second moments for the three different carbon signals for the three different models (in $10^6 s^{-2}$).

Signal	M_2 112 o hombr I	M_2 112 o hombr II
sig. 158 ppm	9.6152	9.4551
sig. 162 ppm	1.1144	1.0985
sig. 168 ppm	2.3916	2.5130

c_{CP} -values calculated according to equation (6).

Table S11. c_{CP} for the three different carbon signals for the three different models and average values (in 10^{-6}).

Signal	c_{CP} 112 o hombr I	c_{CP} 112 o hombr II
sig. 158 ppm	2.8663	2.9148
sig. 162 ppm	3.0788	3.1233
sig. 168 ppm	3.6042	3.4302
$\overline{c_{CP}}$	3.1831	3.1561

13 Crystallographic data of 112 o hombr II

```

data_112_o_hombr_II
_audit_creation_date      2016-03-25
_audit_creation_method    'Materials Studio'
_symmetry_space_group_name_H-M 'P212121'
_symmetry_Int_Tables_number 19
_symmetry_cell_setting    orthorhombic
loop_
_symmetry_equiv_pos_as_xyz
  x,y,z
  -x+1/2,-y,z+1/2
  -x,y+1/2,-z+1/2
  x+1/2,-y+1/2,-z
_cell_length_a            14.5580
_cell_length_b            8.6030
_cell_length_c            6.7050
_cell_angle_alpha         90.0000
_cell_angle_beta          90.0000
_cell_angle_gamma         90.0000
loop_
_atom_site_label
_atom_site_type_symbol
_atom_site_fract_x
_atom_site_fract_y
_atom_site_fract_z
_atom_site_U_iso_or_equiv
_atom_site_adp_type
_atom_site_occupancy
H1      H      0.37131  0.13630  0.71909  0.00000  Uiso  1.00
H2      H      1.21057  0.33961  0.73893  0.00000  Uiso  1.00
Li3     Li     1.14051  0.90545  0.74597  0.00000  Uiso  1.00
Li4     Li     0.34071  0.85361  0.74993  0.00000  Uiso  1.00
C5      C      1.01013  0.40932  1.25127  0.00000  Uiso  1.00
C6      C      0.56584  0.14598  1.25313  0.00000  Uiso  1.00
C7      C      1.16599  0.44460  1.23840  0.00000  Uiso  1.00
C8      C      1.01315  0.61155  0.74679  0.00000  Uiso  1.00
C9      C      0.56895  0.84728  0.75679  0.00000  Uiso  1.00
C10     C      1.17049  0.57098  0.73840  0.00000  Uiso  1.00
N11     N      1.09294  0.34579  1.24474  0.00000  Uiso  1.00
N12     N      0.49499  0.04543  1.25026  0.00000  Uiso  1.00
N13     N      0.65449  0.08606  1.25891  0.00000  Uiso  1.00
N14     N      0.93498  0.31290  1.25932  0.00000  Uiso  1.00
N15     N      1.24577  0.36518  1.23523  0.00000  Uiso  1.00
N16     N      1.09945  0.67199  0.74038  0.00000  Uiso  1.00
N17     N      0.49207  0.93568  0.74985  0.00000  Uiso  1.00
N18     N      0.65668  0.89906  0.76249  0.00000  Uiso  1.00
N19     N      0.93619  0.69872  0.75153  0.00000  Uiso  1.00
C120    C1     1.24341  0.98204  1.01637  0.00000  Uiso  1.00

```

14 References

- [1] E. Wirnhier, M. Döblinger, D. Gunzelmann, J. Senker, B. V. Lotsch, W. Schnick, *Chem. Eur. J.* **2011**, *17*, 3213–3221.
- [2] G. E. Hawkes, M. D. Mantle, K. D. Sales, S. Aime, R. Gobetto, C. J. Groombridge, *J. Magn. Reson. Ser. A* **1995**, *116*, 251–254.
- [3] P. Li, Q. Chen, S. Zhang, *J. Magn. Reson.* **2015**, *250*, 76–79.
- [4] W. Kolodziejcki, J. Klinowski, *Chem. Rev.* **2002**, *102*, 613–628.

7 Publikationsliste

- (1) Wirnhier, E.; Mesch, M. B.; Senker, J.; Schnick, W. *Chem. Eur. J.* **2013**, *19* (6), 2041.
- (2) Schwinghammer, K.; Tuffy, B.; Mesch, M. B.; Wirnhier, E.; Martineau, C.; Taulelle, F.; Schnick, W.; Senker, J.; Lotsch, B. V. *Angew. Chem. Int. Ed.* **2013**, *52* (9), 2435.
- (3) Schwinghammer, K.; Mesch, M. B.; Duppel, V.; Ziegler, C.; Senker, J.; Lotsch, B. V. *J. Am. Chem. Soc.* **2014**, *136* (5), 1730.
- (4) Hug, S.; Mesch, M. B.; Oh, H.; Popp, N.; Hirscher, M.; Senker, J.; Lotsch, B. V. *J. Mater. Chem. A* **2014**, *2* (16), 5928.
- (5) Lau, V. W.; Mesch, M. B.; Duppel, V.; Blum, V.; Senker, J.; Lotsch, B. V. *J. Am. Chem. Soc.* **2015**, *137*, 1064.
- (6) Niefind, F.; Djamil, J.; Bensch, W.; Srinivasan, B. R.; Sinev, I.; Grünert, W.; Deng, M.; Kienle, L.; Lotnyk, A.; Mesch, M. B.; Senker, J.; Dura, L.; Beweries, T. *RSC Adv.* **2015**, *5* (83), 67742.
- (7) Schwinghammer, K.; Hug, S.; Mesch, M. B.; Senker, J.; Lotsch, B. V. *Energy Environ. Sci.* **2015**, *8*, 3345.
- (8) Kailasam, K.; Mesch, M. B.; Möhlmann, L.; Baar, M.; Blechert, S.; Schwarze, M.; Schörder, M.; Schomäcker, R.; Senker, J.; Thomas, A. *Energy Technol.* **2016** DOI: 10.1002/ente.201500478
- (9) Lau, V. W.; Moudrakovski, I.; Botari, T.; Weinburger, S.; Mesch, M. B.; Duppel, V.; Senker, J.; Blum, V.; Lotsch, B. V. *submitted to Nature Comm.* **2015**
- (10) Mesch, M. B.; Bärwinkel, K.; Krysiak, Y.; Martineau, C.; Taulelle, F.; Neder, R.; Kolb, U.; Senker, J. *to be submitted to Chem. Eur. J.*

8 Danksagung

Zum Abschluss meiner Doktorarbeit möchte ich die Gelegenheit nutzen und Danke sagen.

An erster Stelle möchte ich meinem Doktorvater Prof. Jürgen Senker für die Aufnahme in seinen Arbeitskreis danken. Durch ihn konnte ich meine Begeisterung für NMR in einem sehr attraktiven wissenschaftlichen Umfeld ausleben. Trotz allen Freiheiten die er mir ließ stand er jederzeit mit Rat und Tat zur Seite. Weiterhin möchte ich mich für die Möglichkeit bedanken an einem wissenschaftlichen Austausch mit Versailles teilzunehmen und meine Ergebnisse auf diversen internationalen Tagungen zu präsentieren.

Was wäre NMR-Spektroskopie ohne Proben? Daher möchte ich auch meinen Kooperationspartnern danken:

Viele meiner Projekte wurden zusammen mit Prof. Bettina V. Lotsch und ihrem Lehrstuhl realisiert. Für die gute, professionelle und produktive Zusammenarbeit bedanke ich mich ganz herzlich. Insbesondere möchte ich mich bei Katharina Schwinghammer bedanken, die mich immer wieder mit neuen Proben und Herausforderungen versorgte. Auch den Gruppenmitgliedern Dr. Vincent W. Lau und Dr. Stephan Hug danke ich für die Zusammenarbeit.

Des Weiteren möchte ich mich bei den Münchner CN-Partnern bedanken. Insbesondere Prof. Wolfgang Schnick und Dr. Eva Zeuner (geb. Wirnhier), die besonders zu Beginn meiner Arbeit die ersten Projekte mit mir durchführten.

Ein Dank geht auch nach Berlin, an Prof. Arne Thomas, und Prof. Kamalakannan Kailasam, die mich mit den porösen heptazin-basierten Materialien in Kontakt brachten.

Auch in Kiel möchte ich mich bei Prof. Wolfgang Bensch und Felix Niefind für die Zusammenarbeit bedanken, auch wenn die entstandene Publikation nicht Teil meiner Doktorarbeit wurde.

Danke möchte ich auch in Versailles sagen, wo ich in den ersten beiden Jahren meiner Promotion an einem wissenschaftlichen Austausch teilnehmen durfte. Prof. Francis Taulelle, Dr. Charlotte Martineau und Dr. Gerhard Fink haben mich sehr herzlich aufgenommen, mir die Möglichkeit gegeben viel Messerfahrung zu sammeln und mich immer wieder unterstützt und voran gebracht.

Auch möchte ich meinen Kooperationspartnern in Mainz, Prof. Ute Kolb und Yasar Krysiak, sowie Prof. Reinhard Neder danken, durch die die Strukturaufklärung von PTI nochmal neuen Schwung erhielt.

Dann möchte ich mich bei allen Kollegen der Lehrstühle AC I und AC III bedanken. Vor allem bei Denjenigen, die mit mir Praktikum betreuten, und mich besonders in der „ersten Runde“ gut eingelernt und unterstützt haben. Ein besonderer Dank geht auch an Alle, die die Kaffeepausen, Mittagessen und sonstige Veranstaltungen belebt und erheitert haben.

Auch möchte ich mich bei unseren technisch Angestellten Sonja, Beate und Lena und unseren Sekretärinnen Petra und Iris für ihre Unterstützung bedanken. Vor allem Beate hat mich im Labor und am Spektrometer entlastet.

Ein besonderer Dank geht auch an Dr. Renée Siegel. Sie war immer für einen Spaß zu haben und hat mich quasi zu jeder Tages- und Nachtzeit am Spektrometer unterstützt wenn es Probleme gab.

Außerdem möchte ich mich noch insbesondere bei Nadine und Christoph aka Klaus bedanken, die im Labor immer geholfen und synthetisiert haben, wenn der „NMR’ler“ mal wieder was brauchte. Bei Kilian möchte ich mich für seine Hilfe rund um den Computer, die Portion Geduld die er dafür brauchte und für die anregenden wissenschaftlichen Diskussionen bedanken.

Weiterhin möchte ich mich bei Julia, Paul und Helen bedanken, die mir sowohl wissenschaftlich als Mentor oder Praktikant weiter geholfen haben, die aber auch privat immer ein offenes Ohr hatten, wenn ich Gesprächsbedarf hatte.

Ein weiteres großes Dankeschön geht an die Freunde vom Dödel-Dienstag/Freunde-Freitag, dem Donnerstags-Stammtisch und Sina. Ihr habt während dem Master und der Promotion viel Abwechslung und Spaß in mein Leben gebracht. Danke auch an Johannes, als Freund und NMR’ler.

Der allergrößte Dank gilt meiner bald-erweiterten Familie, insbesondere meinen Eltern, die mich mit „chemischen Genen“ ausgestattet, mich immer unterstützt und an mich geglaubt haben. Ohne euch wäre dieser Weg undenkbar gewesen.

Zu guter Letzt geht mein Dank an denjenigen, der meine gesamte Promotion hautnah miterlebt hat, oder vielleicht besser musste. Lieber Philipp, du stehst immer voll hinter mir und hast an mich geglaubt hat, vor allem wenn ich es nicht getan habe. Du hast mich aufgefangen, wenn es nicht so lief und dich mit mir gefreut, wenn’s an der Zeit war. Danke!

9 Erklärung des Verfassers

(§ 8 S. 2 Nr. 6 PromO)

Hiermit erkläre ich mich damit einverstanden, dass die elektronische Fassung meiner Dissertation unter Wahrung meiner Urheberrechte und des Datenschutzes einer gesonderten Überprüfung hinsichtlich der eigenständigen Anfertigung der Dissertation unterzogen werden kann.

(§ 8 S. 2 Nr. 8 PromO)

Hiermit erkläre ich eidesstattlich, dass ich die Dissertation selbständig verfasst und keine anderen als die von mir angegebenen Quellen und Hilfsmittel benutzt habe.

(§ 8 S. 2 Nr. 9 PromO)

Ich habe die Dissertation nicht bereits zur Erlangung eines akademischen Grades anderweitig eingereicht und habe auch nicht bereits diese oder eine gleichartige Doktorprüfung endgültig nicht bestanden.

(§ 8 S. 2 Nr. 10 PromO)

Hiermit erkläre ich, dass ich keine Hilfe von gewerblichen Promotionsberatern bzw. -vermittlern in Anspruch genommen habe und auch künftig nicht nehmen werde.

.....

Ort, Datum, Unterschrift